UNIVERSITAT
JAUME·I

# Advanced studies on Dye-Sensitized Solar Cells

**Sonia Ruiz Raga**

Tesi Doctoral
*Programa de Doctorat en*
*Nanociència i Nanotecnologia*

**Directors**
Francisco Fabregat Santiago
Ivan Mora Seró

Departament de Física
Escola Superior de Tecnologia i Ciències Experimentals

Universitat Jaume I
Castelló de la Plana, abril 2013

GRUP DE DISPOSITIUS
FOTOVOLTAICS I
OPTOELECTRÒNICS

*Memòria presentada per aspirar al Grau de Doctor per:*

Sonia Ruiz Raga

*Vist i plau,*
*Els directors:*

Francisco Fabregat Santiago

Ivan Mora Seró

A Castelló de la Plana, Abril de 2013

“All in all it's just another brick in the wall”

# Abstract

The humanity has been increasingly aware to the environmental problems derived from the use of fossil fuels. Pollution originated from its combustion and limited resources require the development of renewable and clean energy sources. Among all alternative energy sources, those which profits the power received from the sun are highly promising. Within the family of photovoltaics, dye sensitized solar cells (DSC) have been presented as low cost devices. DSC mimics the photosynthesis basics, absorbing photons with a photoactive molecule and separating the charge in different media.

A standard DSC consist in a nanostructured wide band gap semiconductor film, generally $TiO_2$, deposited over a transparent conductive substrate (TCO) with adsorbed dye molecules on its surface. This electrode is sandwiched together with a platinized TCO substrate, the gap in between is filled with a redox-containing electrolyte. The photogenerated electrons are injected from the dye molecule to the semiconductor, transported to the TCO and extracted through the contact. The redox pair of the electrolyte is responsible of regenerating electrons to the dye molecules and with the incoming electrons from the platinized counter electrode, completing in this way the electrical circuit.

The analysis of the working principles of these devices is essential in order to achieve further improvements in cell efficiency. With this basis, the aim of this thesis is to deepen the understanding of the interactions between internal components and the final performance of the device. This will be done mainly by employing a robust and fast characterization technique which allows separating the different processes occurring in a DSC, the impedance spectroscopy (IS).

In this work we started with the analysis the origin of the open circuit voltage ($V_{oc}$), a key parameter affecting the efficiency of DSC. By definition, $V_{oc}$ is given by the difference between the Fermi levels of electrons and holes which, in turn, are affected by the recombination and chemical capacitance of the semiconductor. Analyzing the data obtained from impedance spectroscopy measurements we demonstrate how varying the electrolyte additives or dye molecule is translated in changes in recombination rates, conduction band shifts or photocurrent. The individual impact of these parameters on the $V_{oc}$ value and thus the final efficiency will be unraveled.

Taking into account that solar cells usually work in outdoor installations, it leads to think that a DSC will present different responses depending the external conditions. Taking the external temperature as a variable, a detailed study of its effect on DSC performance is given. Impedance spectroscopy measurements were applied to a single device, under dark and illumination conditions, in a range of attainable atmospheric temperatures. We demonstrate how employing a single characterization method we are able to explain variations in efficiency in terms of five different parameters which, in turn, present temperature dependence. This study will help to further compare the performance of different types of photovoltaic devices at different temperatures. In this section we conclude that, under normal operation cell temperatures, DSC present a maximum in the efficiency, very close to that of polycrystalline-Si solar cells at the same temperature.

Major efforts in the improvement of DSC efficiency have been focused in the development of sensitizers, improving their spectral response and stability. Electrolytes have also received a lot of attention in order to find new additives or non volatile ionic liquids. We proposed to enhance DSC efficiency by studying the suitability of one-dimensional porous photonic crystals (1DPC) for their application as light scatterers in DSC. For this purpose, diffusion resistance of ionic species in the electrolyte through these structures have been studied by *j*-*V* curves and IS. The aim was to determine if the increase of series resistance introduced by 1DPC could affect in a relevant way the series resistance of the complete device. This fact, eventually could compensate potential increases of photocurrent provided by the incorporation of these structures in a DSC.

Finally we analyze the problems arising from DSC upscaling, as the final step in DSC laboratory research. Three different module configurations are reviewed, and a detailed analysis of the working principles of one of them is given. It is concluding that the series connected modules behave in a different manner than conventional Si solar cells, as the DSC modules still retain a relevant power production when part of them is shaded. This represents a clear advantage that allows extracting solar energy under conditions in which conventional solar technologies drop their production to zero. It is shown that the structure of DSC modules naturally produces an integrated bypass channel on each unit capable of evacuating the current of the unshadowed cells working at full performance.

The results presented here provide a fertile base for further investigation, which will focus on quick characterization techniques for identifying and characterizing the electrical parameters affecting DSC efficiency.

**Keywords:** Renewable energy, photovoltaics, dye-sensitized solar cells, impedance spectroscopy, open circuit voltage, charge recombination, series resistances, photonic crystals, chemical capacitance, density of states.

# Resum

La humanitat és cada vegada més conscient dels problemes mediambientals què es deriven de l'ús dels combustibles fòssils. La pol·lució causada amb la combustió i el limitat nombre de recursos exigeixen el desenvolupament d'energies netes i renovables. D'entre totes les fonts d'energia alternatives, les que aprofiten l'energia del sol són altament prometedores. Entre la família de dispositius fotovoltaics, les cel·les solars de colorant (DSC) han sigut introduïdes com la versió de baix cost. Les DSC imiten els principis bàsics de la fotosíntesi, absorbint fotons mitjançant una molècula fotoactiva i separant posteriorment la càrrega generada en diferents medis.

Una DSC estàndard consisteix en una capa d'un semiconductor nanoestructurat amb una ampla banda prohibida, generalment $TiO_2$, dipositat sobre un substrat conductor i transparent (TCO), què en la seva superfície té adherides les molècules de colorant. Aquest elèctrode s'uneix cara a cara amb un altre TCO platinitzat i l'espai intermedi s'ompli amb un electròlit què conté un parell redox. Els electrons fotogenerats s'injecten des del colorant cap al semiconductor, aquí conduït fins al TCO i extret a través dels contactes. El parell redox s'encarrega de regenerar els electrons perduts de la molècula de colorant i alhora captar-los en el contra-electrode platinitzat, tancant, d'aquesta manera, el circuit elèctric.

Analitzar els principis de funcionament d'aquests dispositius és essencial per a assolir futures millores en eficiència. Amb aquest propòsit, l'objectiu d'aquesta tesi es aprofundir en el coneixement de les interaccions entre els components interns i el seu efecte en el rendiment final del dispositiu. Això es durà a terme emprant una ràpida i robusta tècnica de caracterització què ens permetrà separar els diferents processos què tenen lloc dintre de la DSC: l'espectroscòpia d'impedància (IS).

En aquest treball hem començat per analitzar l'origen del voltatge a circuit obert ($V_{oc}$), uns dels paràmetres clau què determinen l'eficiència final de les DSC. Per definició el $V_{oc}$ ve donat per la diferència entre els nivells de Fermi dels electrons i els buits què, a la vegada, estan determinats per la recombinació i la capacitat química del semiconductor. Analitzant les dades obtingudes mitjançant les mesures d'IS demostrem com la variació dels additius en l'electròlit o les molècules de colorant resulta en canvis en les taxes de recombinació, moviments de la banda de conducció o la fotocorrent. L'impacte individual d'aquests paràmetres en el valor de $V_{oc}$ i, per tant, l'eficiència final seran desxifrats.

Tenint en compte que les cel·les solars normalment operen en instal·lacions exteriors, du a pensar que una DSC tindrà diferents respostes depenent de les condicions externes. Prenent la temperatura externa com a variable, proposem un estudi detallat del seu efecte en el rendiment de les DSC. Mesures d'espectroscòpia d'impedància van ser aplicades a un únic dispositiu, en condicions de foscor i il·luminació, en un rang de temperatures assolibles en condicions atmosfèriques reals. Mitjançant un únic mètode de caracterització demostrem com es poden explicar les variacions d'eficiència en termes de cinc paràmetres diferents, els quals tenen dependència amb la temperatura. Aquest estudi ajudarà a comparar el rendiment de

diferents tipus de dispositius fotovoltaics a diferents temperatures. En aquesta secció concloem que, sota temperatures d'operació reals, les DSC presenten un màxim en l'eficiència, molt pròxim a la d'altres dispositius com el Si policristal·lí a la mateixa temperatura.

La major part dels esforços fets fins ara per a la millora de les DSC han estat centrats en el desenvolupament de colorants, millorant la seva resposta espectral i estabilitat. La composició dels electròlits també ha rebut especial atenció, investigant sobre nous additius o líquids iònics poc volàtils. Aquí hem proposat millorar l'eficiència de les DSC estudiant la idoneïtat de cristalls fotònics unidimensionals (1DPC) per a l'aplicació com a dispersors de llum en les DSC. Amb aquest objectiu, s'ha estudiat la resistència de difusió de les espècies iòniques en l'electròlit mitjançant corbes *j*-*V* i IS. El propòsit va ser determinar si l'increment de les resistències en sèrie produït pel 1DPC podria afectar d'alguna manera les resistències en sèrie del dispositiu. Aquest fet podria contrarestar l'increment en fotocorrent d'una DSC aportat pel cristall fotònic .

Finalment, com al pas final en la recerca de les DSC en el laboratori, analitzem els problemes sorgits a l'hora d'escalar les DSC en mòduls. Tres configuracions diferents de mòduls han sigut avaluades i el principi de funcionament d'una d'elles ha sigut analitzat. És concloent què els mòduls de DSC connectats en sèrie es comporten de manera diferent que, per exemple, les cel·les solars convencionals de Si. Els mòduls de DSC són capaços de conservar una bona part de la producció de potència encara que part del dispositiu estigui ombrejat. Això representa un clar avantatge què ens permet extraure energia del sol en condicions en les què cel·les convencionals de Si connectades en sèrie disminuïrien la seva producció a zero. Aquí es mostra que l'estructura dels mòduls DSC conté un canal de derivació de càrrega natural, capaç d'evacuar la corrent generada per les unitats què tenen màxim rendiment.

Els resultats presentats en aquest treball pretenen proveir d'una fèrtil base per a futures recerques, enfocades a tècniques de caracterització ràpides per a identificar i caracteritzar els paràmetres elèctrics que afecten l'eficiència de les DSC.

**Paraules clau:** Energia renovable, fotovoltaica, cel·les solars sensibilitzades amb colorant, espectroscòpia d'impedància, voltatge a circuit obert, recombinació de càrrega, resistències en sèrie, cristalls fotònics, capacitat química, densitat d'estats.

# Table of Contents

**APPENDIX**

# Chapter 1

## Introduction

## 1.1 Motivation

Demographic expansion of the earth population has exceeded 7000 million in 2012 and is expected to be 9000 million in 2040.[1] Continuous development of cities and industry following the population growth will increase the energy demand over all kind of resources. Considering that oil production will not be able of encompassing the future energy demand, it has yielded United Nations to site Energy as one of the top issues for Mankind on the 21st century, and the first issue for some other authors.[2,3] According to their predictions, economical, social and political problems may derive from fuel scarcity situation. Eventually this may derive in both local and international conflicts related to access and management of oil sources.

In parallel, the alternative combustible fossil fuels, carbon and gas, as oil produce tons of carbon dioxide each year, contributing to the global warming. Furthermore, air pollution has a direct effect in degradation of human health and plant growth. For all of these reason, it is clearly necessary to promote additional sources of renewable and clean energies in order to fulfill the 80% increase in electricity demand by 2040 with respect to 2010.[4]

Among the green energies developed in the last years, solar cells are probably the most attractive candidates. Taking into account that the amount of solar energy that reaches the earth every minute is equivalent to the amount of energy the world's population consumes in a year,[5] photovoltaic technology (PV) becomes a real alternative.

After A. E. Becquerel discovered the photovoltaic effect in 1839,[6,7] research in this field continued over the years since the first true PV cell was constructed by Charles Fritts in 1883 using junctions formed by coating selenium with a thin layer of gold.[8] Before the World War II, in 1938, a solar cell with record energy conversion efficiency of 1.1% was developed by B.T. Kolomiets using thallium sulfide.[9] It wasn’t until the early of the 1950s that first PV device of 5% efficiency appeared in the market by the hand of Chapin et al.[10] In the following years many semiconductor materials and junctions were developed, resulting in a continuous increasing of solar cell efficiencies and PV technologies, as detailed in Figure 1.1.

Nowadays, the most common commercial solar cells are based on inorganic materials such as monocrystalline silicon (27.6% efficiency), polycrystalline silicon (20.4%) or CdTe thin film (17.3%).[11] These efficiencies are determined for laboratory-scale devices, for larger devices or modules the efficiency decreases significantly to 17%, 15% and 11.8% respectively. However, high quality materials and complicate fabrication processes needed, convert these solar cells in an expensive energetic solution. Cheaper ways to convert solar energy have been investigated. The invention in 1991 of the Dye-sensitized Solar Cells (DSC) and the development of organic bulk heterojunction solar cells has opened new prospects to overcome this drawback.[12,13]

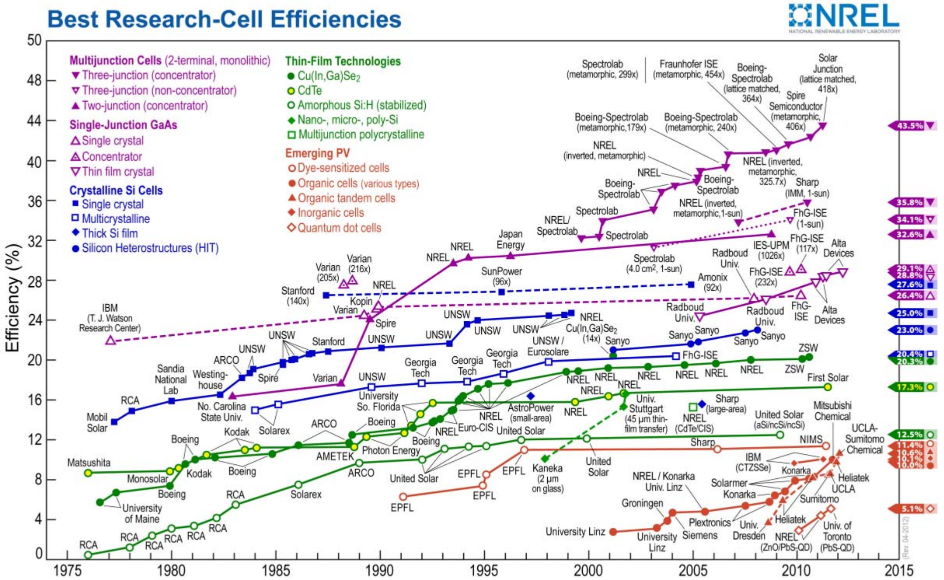

**Figure 1.1:** Evolution of efficiencies for different photovoltaic technologies reported by National Renewable Energy (NREL).[14]

The common materials employed and low temperatures needed for processing DSC and the organic solar cells convert this technologies into low-cost photovoltaics. The key point common for both technologies is that, immediately after light absorption, the generated charges are separated in different phases after photon collection. This allows minimizing charge losses and yields to reasonable efficiencies of these devices. Particularly in DSC, photosensible dye molecules absorb light, injecting electrons to the nanostructured inorganic semiconductor and holes to the acceptor species in a liquid electrolyte. After the report of the first DSC several new areas have been explored in the field of materials development in order to increase the overall efficiency. Mesoporous nanocrystalline layers [15,16], counter electrodes [17,18], light absorbers [19-21] electrolytes and hole transporters[22-24] have been improved in order to increase efficiency. Up to now the highest record in conversion efficiency reached is 12.3% under standard AM 1.5 G sunlight with porphyrin-sensitized $TiO_2$ and Cobalt(II/III)-based electrolyte. [25]

Looking at the relative efficiency differences between photovoltaic technologies it may be concluded that they should complement each other in order to make their way together into the energetic market. This is that, i.e., a DSC is never going to substitute a Si solar cell in applications such as solar fields. The idea is to replace combustible energy sources investing in renewable energies. The first step must be done in research field, laying the groundwork for further development. This is the main reason that encouraged the present work.

## 1.2 Photovoltaic market and applications

More than 80% of solar modules available in the market today is still based on crystalline or polycrystalline silicon (c-Si, pc-Si, respectively). The rated DC efficiencies of standard c-Si modules are about 14-16%.[26] The second majority group of PV are represented by thin film solar cells. Employing around 100 times less material than current c-Si cells and a simplified processing, thin-film solar cells represent a much more affordable PV technology. Nonetheless, low-cost is followed by lower efficiency, this is about 9%-12% for CdTe, 6%-9% for a-Si, and 8%-14% for CIGS.[26] In addition materials employed for thin-film PV are usually rare elements (such as In, Cd or Te) which are found globally in finite quantities and only in few locations. New cell architectures such as multi junction cells and the use of solar concentrators increasing the incident radiation in a factor of 50-1000 can improve significantly the efficiency of c-Si PV modules approaching theoretically 68.5%.[27] The last group of photovoltaic technologies in Fig. 1 are the emerging technologies. Besides, their efficiency is actually lower, such as 12% for Dye-sensitized Solar cells (DSC), 8% for organic solar cells (OSC) or 5.1% for Quantum-dot solar cells.

Since 1976, global module prices followed a decline trend of roughly 98% up to 2011, from about 60 \$/Wp to 0.97 \$/Wp for c-Si.[28] The costs are variable depending on the manufacturer and the scaling, varying up to 20%. Comparing different technologies, great differences are found with regard to materials, process and overhead cost, as reported by Kalowekamo et Baker.[29] Table 1.1 indicates the cost estimates in 2009 of four PV technologies in terms of materials, processing, overhead and manufacturing costs as well as the module cost in terms of energy output. It has been taken into account a 5% efficiency for OSC and DSC, 8% for Cd-Te and 15% for polycrystalline Silicon (pc-Si). A 98% module yield has been estimated for all.[29]

| Tech. | Materials cost | | | Process costs (\$/m$^2$) | Overhead costs (\$/m$^2$) | Module Manuf. (\$/m$^2$) | Module cost (\$/Wp) |
|---|---|---|---|---|---|---|---|
| | Active (\$/m$^2$) | Inactive (\$/m$^2$) | Total (%) | | | | |
| **pc-Si** | 150.6 | 57.5 | 57 | 95.8 | 23.3 | 343.5 | 2.34 |
| **CdTe** | 6.8 | 58.9 | 53 | 30.1 | 27.4 | 129.3 | 1.65 |
| **DSC 1** | 10.3-16.6 | 5.2-5.5 | 22-23 | 7.7-10.9 | 11.6 | 36.6-46.2 | 0.75-0.94 |
| **DSC 2** | 23.5 | 97.6 | 80 | 18.1 | 1.2-11 | 157.7 | 3.22 |
| **OSC** | 6.7-10 | 16.7-27.5 | 27-48 | 9.3-69.6 | 13.8-25.2 | 48.8-138.8 | 1-2.83 |

**Table 1.1:** Comparison of the estimated cost of four different PV technologies. DSC 1 and DSC 2 present a wide range of cost due to the uncertainty in estimating a process that has not been perfected in the laboratory, let alone transferred to industry.[26]

Nowadays, the global PV market presents an annual average rate growth of 53%, reaching 17.4 gigawatt (GW) in 2010 as seen in Figure 1.2(a). PV production up to 2006 was led by European and Japanese manufacturers, that have been progressively overwhelmed by the very intensive Chinese/Taiwanese industry growth, which was already taking a 53% share of the global production on 2010. Nevertheless, the shipments of PV modules are received majorly in the European Union, reaching the 80% of the total PV demand in 2010 Figure 1.2(b).[30,31]

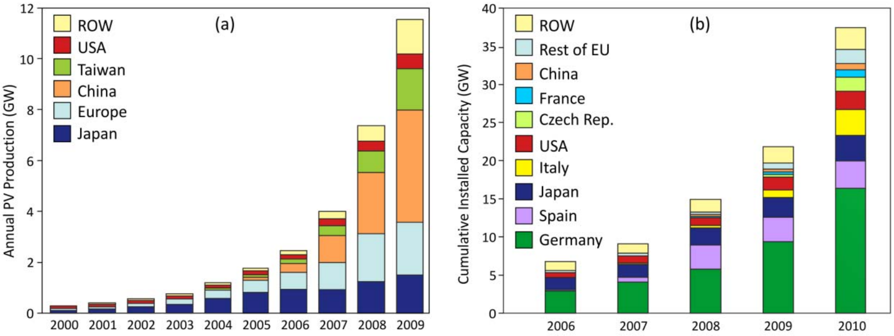

**Figure 1.2: (a)** Annual PV production (Mints, 2011a). **(b)** Cumulative installed PV capacity in the top eight countries (EPIA 2011).[32]

Major market segments served by this industry comprise consumer applications, remote industrial systems, developing countries, and grid-connected systems. This last represents the major part of the applications. At any rate, organic PV and dye-sensitized solar cells applications are restricted to indoor, gadgets or architectural ornament applications. Australian DSC developer, Dyesol, is seeking to exploit low-cost processing of this technology. Its last strategy is to integrate dye-based PV into building materials such as glass high-rise panels and steel roofing sheets. In example Timo Technologies, a Korean partner of Dyesol, installed glass panels on a building in Seoul while India’s Tata Steel is developing dye-solar-coated steel roofing.

## 1.3 Solar cells

Solar cell is the name given to photovoltaic devices employing sun radiation as source of energy conversion. The photovoltaic effect is the process of generating electricity (power) from light (photons) exciting an electron in a material from a low energy level to a higher energy level by absorbing a single photon. Traditional PV systems (first generation) are based on silicon p-n junctions, and are generally the most efficient. The second generation of solar cells are made of thin films of compounds formed by semiconductors with direct bandgap as CdTe, Cu(In,Ga)$Se_2$ or amorphous Si. Direct bandgap provides higher light absorption allowing than a thinner layer can harvest completely the incident light. Third generation of PV cells are based on nanostructures and molecular organic compounds. This technology introduce new physical mechanisms which can overcome the intrinsic constraints of existing materials.

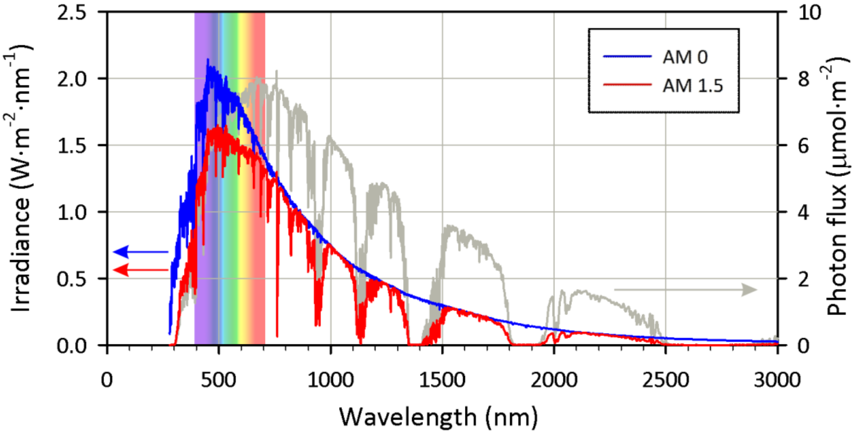

**Figure 1.3:** Extraterrestrial solar irradiance AM 0 compared with the global irradiance on surface earth standard AM 1.5 spectrum. The grey plot in the background indicates the photon flux corresponding to AM1.5 irradiance, at a given wavelength. Note that the maximum photon flux at the earth surface is displaced towards the infrared regarding to the peak in irradiance.

For understanding the working principle of solar cells we have to focus on the available energy coming from the Sun. The power density received outside the earth's atmosphere is about 1353 $Wm^{-2}$, and the irradiance spectra is similar to the radiation produced by a 6000K blackbody. This irradiance spectra is called Air Mass 0 (AM0), see Figure 1.3. Gases and water vapor contained in the atmosphere absorb specific wavelengths, diminishing the radiation received on the earth surface. The quantity of energy absorbed by the atmosphere depends on the latitude and the season of the year. For normalized measurements of solar cells efficiency, a standard value of AM 1.5 has been taken, see Figure 1.3. This corresponds to a power density of 1000 $W \cdot m^{-2}$ on the earth's surface. Air Mass (AM) indicates the amount of atmosphere crossed by trajectory of the solar light beam with an angle $\theta$ in respect to the zenith. Hence, the standard AM 1.5 corresponds to a solar incident angle of 48.2º relative to the normal surface.

Figure 1.3 shows that the major photon density is received between 400-1100 nm (from blue to near infrared (IR)) corresponding to energies between 2.47 to 3.2 eV. The materials chosen for a PV device as light absorbers should absorb in this energy range, *i.e.* Si has an 1.1eV bandgap, absorbing photons from 1.1 to 3.1 eV. For light absorbing materials any incoming photon with an energy equal or higher than the band gap energy ($E_g$) will excite an electron from the valence band (VB) to the conduction band (CB) creating a electron-hole pair. Photons with energy higher than $E_g$, will excite electrons higher into the CB for later being relaxed to the bottom of the CB in a thermalization process via phonon interactions in the form of heat.

In the case of semiconductor solar cells the pair electron-hole is separated before recombination using an asymmetric p-n junction structure. P-type or n-type doping of a material results when introducing donor or acceptor impurities into the crystal structure, respectively. A charge gradient is created in the junction of the doped materials, ensuring the flow of current in a specific direction.

## 1.4 Dye sensitized solar cells

### Background

Photocatalytic properties of titanium dioxide described by Fujishima and Honda in 1972 opened new prospects for photovoltaic applications of this abundant and cheap material.[33] Although $TiO_2$ is restricted to absorb only in ultraviolet range because of its wide band gap of 3 eV, it may be sensitized to the visible and even in the IR by functionalizing the surface with proper molecules absorbing in these bands. The ease processing of this semiconductor made possible to create nanostructured films increasing by a factor of 1000 it's active surface for dye adsorption. The resulting photoelectrochemical electrode was then adequate for the fabrication of low-cost solar cells, as discovered Grätzel et al. in 1991.[13] In this configuration, adsorbed dye on $TiO_2$ acts as light absorbing material, while $TiO_2$ provides a scaffold with very high effective area and playing the role of electron selective contact.

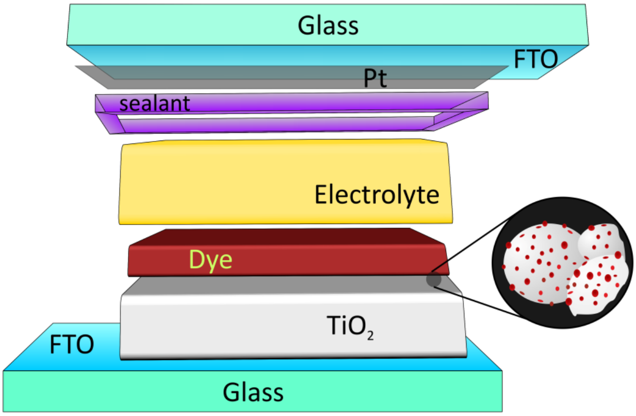

**Figure 1.4:** Schematic representation of a DSC sandwich configuration.

A transparent and conductive substrate (TCO) gives the sufficient conductivity and light transmission for ensuring good illumination of the dye and quick charge extraction through external circuit. Fluorine-doped Tin Oxide (FTO) layer over glass is commonly used as TCO substrate for both working and counter electrode. Catalytic properties of the counter electrode are achieved by platinizing its surface. Both electrodes are assembled together in a sandwich-type configuration using a thermoplastic polymer as spacer and sealant, see Figure 1.4. The gap in between is filled with a redox-containing electrolyte, embedding completely the nanoporous $TiO_2$.

### Operating principle

Figure 1.5 schematizes the basic mechanisms for the photon-to-electron conversion in a DSC as follows: (1) electron-hole photogeneration in sensitizer molecules, (2) electron injection from dye to $TiO_2$ CB, (3) electron diffusion through $TiO_2$ nanoparticles, (4) charge collection at TCO substrate, (5) extraction through an external circuit up to the counter electrode, (6) reduction of acceptor species in the electrolyte ($I_3^-$) catalyzed by Pt particles on TCO, (7) diffusion of ionic species between counter electrode and $TiO_2$ surface, (8) regeneration of the oxidized sensitizer by donor species in the electrolyte. (9) Internal voltage reached under illumination and open circuit conditions and (10) photogenerated charge loss caused by recombination processes.

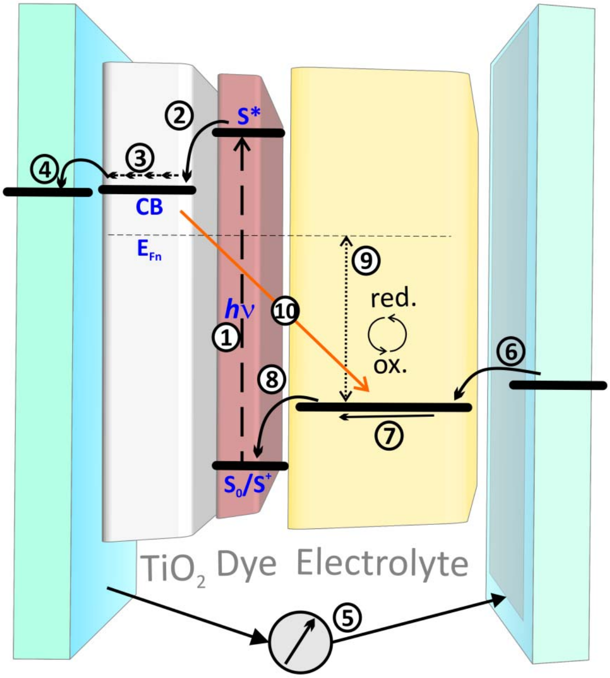

**Figure 1.5:** Principle of operation and energy levels of a DSC. (1) Photon collection, (2) electron injection, (3) electron diffusion through $TiO_2$, (4) electron extraction, (5) external circuit, (6) electrolyte reduction, (7) ionic diffusion, (8) dye regeneration, (9) internal voltage, (10) charge loss by recombination.

These processes determining the overall performance of dye solar cells are described in detail below.

### (1) Light absorption

Photoexcitation of the dye sensitizer takes place by absorbing a photon of an energy equal or higher than the HOMO-LUMO distance, resulting in an electronically excited state (S*). Excited electrons tend to occupy electronic states with lower energy and the electrons are injected on the $TiO_2$ conduction band, favored by the molecular anchorage on the semiconductor and the energy level of the semiconductor. This leaves the dye in its oxidized state ($S^+$) that is subsequently reduced to the ground state ($S_0$) by the redox donor species (generally $I^-$) contained in the electrolyte, see Figure 1.6.

The quantum yield of electron excitation from the molecular states $S_0$ to S* upon the absorption of one photon is close to the unity. Possible reaction channels from S* are radiative or non radiative deactivation to the ground state, electron injection into the $TiO_2$ CB (called oxidative quenching) and structural changes or degradation of the electronically excited complex. Both degradation process and deactivation to the ground state are negligible when the dye is attached to $TiO_2$ surface.[34]

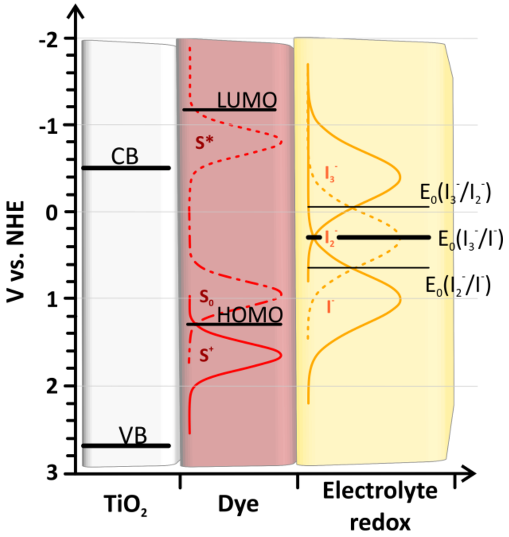

**Figure 1.6:** Energetic scheme of a DSC including the energy of dye and redox species.

### (2) Electron injection

The electron injection from the dye to the $TiO_2$ takes place during the thermal relaxation of the photoexcited molecule with a half-life around 200 ps for the N719 dye.[35] For an efficient DSC is not only important to have a fast injection, but also that the decay of the excited state is slow enough. The optimum ratio for a high efficiency DSC is around 100 times faster injection than radiative or non-radiative decay.[36] Injection kinetics are determined also by the semiconductor CB position ($E_c$). A narrower distance between the dye LUMO and $E_c$ is translated into a decrease in the probability of electron injection ($\Delta E_{inj}$) and thus a lower photocurrent.

### (3) Semiconductor electron transport

As it has been commented, under illumination, electron injection from the dye LUMO to the semiconductor conduction band occurs. Electrons injected into $TiO_2$ create an electronic density gradient in the device, as the light that crossed the sensitized electrode is absorbed. In the case of bulk semiconductor or high-doped semiconductors, injected electrons on its surface would result in a conduction band bending, creating internal electrical fields. However, in DSC, confinement character of nanostructured particles together with the intrinsic low-doping of $TiO_2$ leads to an homogeneity of the conduction band energy along the electrode.[37] Charge carriers in the nanoparticles diffuses through the semiconductor material until reaches the conductive substrate. The diode-like configuration of a DSC only permits the flow of electrons through the external circuit (except for recombination processes) generating work as the system returns to equilibrium.

In order to maintain the low-cost character of DSC devices, simple techniques of nanoparticle synthesis and processing are needed. The resulting low material purity and large ratio of surface-to-volume introduces high electronic energy disorder in the semiconductor. This is translated in a wide distribution of localized electronic states in the bandgap. In these conditions, the simplest approach to describe electron transport taking trapping into account is in terms of the classical multiple trapping (MT).[38] It includes two types of models for electronic transport: (i) diffusion of free carriers ($n_c$) through the CB and (ii) hopping of trapped electrons ($n_L$) through localized states in the bandgap.

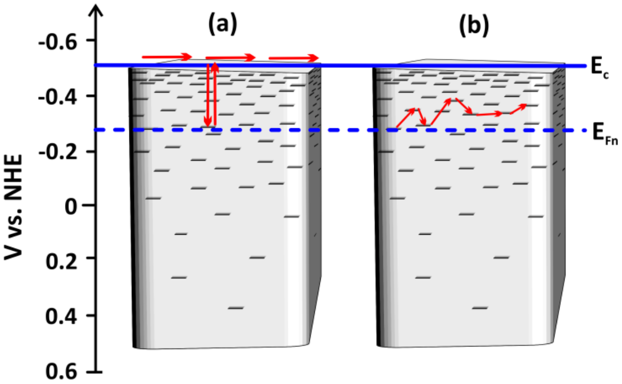

**Figure 1.7:** (a) Conduction band transport affected by trapping in a wide distribution of states in the bandgap. (b) Hopping transport in a wide distribution of states in the bandgap.

In the first case (i), injection or extraction of *n* electrons through the nanostructured electrode causes diffusion of carriers along the extended states. Only free carriers ($n_c$) localized on the lower edge of the CB at a energy $E_c$ contribute to the diffusion process. A number of carriers $n_L$ remains in a process of trapping/ detrapping from CB to the localized states, see Figure 1.7(a).

The electron diffusion coefficient at the CB, reaches its maximum value $D_0$, but it is modified by the presence of traps. A broad DOS may cause dominant effects on transport coefficients. The driving force of electron diffusion in a material is the gradient of its chemical potential. This last diffusion is represented by the chemical diffusion coefficient $D_n$,

$$D_n = \left(\frac{\partial n_c}{\partial n_L}\right) D_0 \tag{1.1}$$

The prefactor in Eq. (1.1) is the relationship of free to trapped electrons for a small variation of the Fermi level. This factor indicates a delay on the chemical diffusion response in respect to the free electrons diffusion due to the process of electron trapping.

In the case of $TiO_2$ the density of localized states ($g(E)$) follow an exponential distribution with a depth distribution $T_0$ into the bandgap. The chemical diffusion coefficient results,

$$D_n = \frac{N_c T_0}{N_L T} \exp\left[ \left(E_{Fn} - E_c\right)\left(\frac{1}{k_B T} - \frac{1}{k_B T_0}\right)\right] D_0 \qquad (1.2)$$

Where $k_B$ is the Boltzmann's constant, $T$ the temperature, $q$ the electron charge, $N_c$ electronic states in the CB and $N_L$ the total density of localized states under CB.

It is remarkable that under steady-state conditions, electron conduction is not affected by the trapping process, because the traps remain in a equilibrium. In this domain MT trapping ceases to hold, because the different kinetic phenomena occur directly through the conduction band states with no interference of the traps (which are nearly full of electrons) so $D_n$ approach $D_0$.

In the second case of electronic transport (ii), conduction is described by the theory of hopping conduction. In this case the transport is by means of carrier jumps via localized states in the bandgap, see Figure 1.7(b). The analysis of all possible transitions between sites is a complex problem, but it can be simplified for systems with an exponential DOS. When the Fermi level is below a transport energy level $E_t$, hopping systems behave similar to MT systems, where $E_t$ plays the role of a CB level. This transport plays a minor role in the global charge conductivity. [39]

### (4) – (5) Electron extraction

Charges reaching the semiconductor and TCO junction create an accumulation of electrons in the $TiO_2$, localized near the interface. As the nanostructured film is equipotential, the potential drop for the equilibration with TCO occur over a narrow region of the $TiO_2$ contacting the substrate. This corresponds to an ohmic contact between metal-semiconductor junction.[37,40] The charge transfer from the $TiO_2$ to the FTO has negligible resistance as the nanostructured film has a good electrical contact with the substrate. A metallic contact on the FTO in the external part of the device, drives the charge through the wires to the external circuit.

### (6) – (8) Redox process and ionic diffusion

The redox couple dissolved in an organic solvent is responsible of collect the charge from the counter electrode, transport the electrons to the working electrode and regenerate the dye to the ground state. Although several donor/acceptor mediators have been developed for DSC, the performance of iodide/triiodide couple remains unmatched. Moreover, the oxidized iodide products present the capability to avoid recombination with injected electrons on nanoporous $TiO_2$ thin film.

In solution, iodine anion binds with iodide to form triiodide:

$$I_2 + I^- \Leftrightarrow I_3^- \quad \left(K_1\right) \qquad (1.3)$$

The high equilibrium constant of Eq. (1.3) in most organic solvents ($pK_1$=-7.18 in acetonitrile),[41] results in a negligible concentration of free iodine. The global redox reaction occurring in the electrolyte is given by Eq.(1.4) and the redox potential of the electrolyte can be deduced by the Nernst equation Eq.(1.5).

$$I_3^- + 2e^- \Leftrightarrow 3I^- \tag{1.4}$$

$$E_{redox} = E_0^{'} + \frac{RT}{2F}\ln\left(\frac{[I_3^-]}{[I^-]^3}\right) \tag{1.5}$$

where $E'_0$ is the formal potential, $R$ the gas constant, $T$ the absolute temperature, and $F$ the Faraday constant. The standard redox potential ($E_0'$) of $I_3^-/I^-$ redox couple is reported to be +0.35 V vs. NHE, which is 0.36 V more negative than the 0.74 V vs. NHE ground state oxidation potential of the dye, see Figure 1.8.[42] In parallel, many one-electron reactions involving unstable radicals occur in the redox system, which may affect DSC performance.[43]

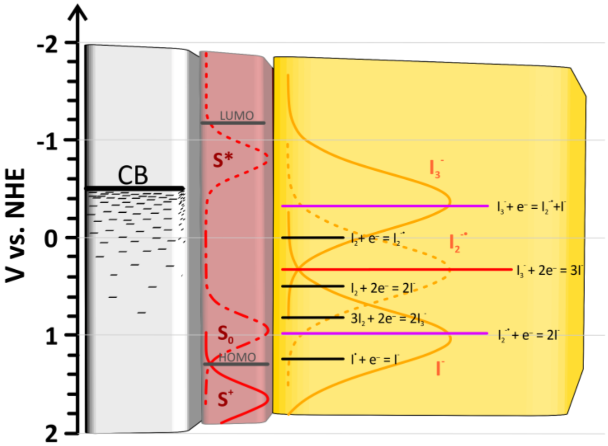

**Figure 1.8:** Redox reactions of the iodine- iodide system and their relative electrochemical potentials in acetonitrile solvent.

Previous studies proposed mechanisms where the oxidized Ru-based dye is regenerated by the reaction $2I^- \Leftrightarrow I_2^{-\bullet} + e^-$.[43,44] Even the mechanism for sensitizer reduction depends on its molecule structure, a general path for regeneration of the oxidized dye ($S^+$) can be described as follows:

$$S^+ + I^- \rightarrow (S \cdots I) \tag{1.6}$$

$$(S \cdots I) + I^- \rightarrow S_0 + I_2^{-\bullet} \tag{1.7}$$

The oxidized dye forms a complex with iodide (or eventually diiodide) under an energetically favorable reaction. A second iodide dissociates the complex leading to the ground-state dye molecule $S_0$ and giving $I_3^-$ as final product.

The transport of $I_3^-$ ions formed by oxidation of $I^-$ from the $TiO_2$ nanoparticle surface to the counter electrode interface is mainly driven by diffusion. The diffusion coefficient ($D$), distance between electrodes and concentration of the redox mediator are the main parameters affecting the ionic diffusion.[45] Low triiodide concentration, small *D* or large distance between electrodes result in photocurrent limitation of a DSC. In a common DSC device, the distance between electrodes and the iodine concentration are adequately optimized, thus not restraining the ionic diffusion. Ionic liquids (IL), for example, are viscous electrolytes with very low *D*, in comparison to acetonitrile-based electrolytes. DSCs employing IL as electrolyte have restricted the flux of redox components, being reflected in a low photocurrent.

At the counter electrode triiodide is reduced to iodide Eq. (1.4). The F-Sn oxides usually employed as cathodes in DSC are extremely poor catalysts for iodine reduction. In order to minimize efficiency losses due to the slow electron-transfer kinetics at the counter-electrode, it should be functionalized with a stable catalyst. Several materials have been investigated as counter electrodes in DSC, as carbon, graphene or PEDOT, but the high electrochemical/chemical stability of Pt has not been surpassed. Thermal decomposition of platinum-chloride on the TCO produce an interfacial catalyst that is selective for iodide/triiodide reduction in organic electrolytes.[46] Thus iodide is adsorbed dissociatively onto the Pt surface, enabling a rapid one-electron reduction.

### (9) Internal voltage

The internal voltage ($V_F$) of a DSC device is given by the difference of electrochemical potential of electrons ($E_{Fn}$) and holes ($E_{redox}$) in the materials.

$$V_F = (E_{Fn} - E_{F0}) / q \tag{1.8}$$

where *q* is the electron charge.

The redox potential of the electrolyte fixes the hole Fermi level. In the dark, electrons in the semiconductor equilibrate with the redox ($E_{F0} = E_{redox}$) due to the high concentration of charges existing in this media. The electron Fermi level ($E_{Fn}$) is given by the semiconductor CB position and its DOS.

### (10) Recombination

Electron losses by recombination in a DSC take place in an interfacial reaction between photogenerated charge and the electron-acceptor species in the electrolyte. Operation basics of a solar cell consist in a competition between two currents Eq. (1.9); output current due to extraction of the photogenerated carriers which reach its maximum value in short circuit conditions ($j_{sc}$) and recombination current ($j_{rec}$), flowing in the opposite direction to the generation.

$$j = j_{sc} - j_{rec} \tag{1.9}$$

Taking into account the concentration of electron acceptors in solution, *c*, the film thickness, *L*, the density of minority carriers (electrons), *n*, and the recombination kinetics constant $k_{rec}$, the recombination current can be expressed as:

$$j_{rec} = qLk_{rec}cn \tag{1.10}$$

Several factors influence the recombination in a DSC, being quite difficult to distinguish them with the existing DSC characterization techniques. Figure 1.9 shows the possible recombination mechanisms in a working dye solar cell. The most relevant is the charge transfer from recombination sites on the semiconductor surface. These transfer states can be classified as (i) conduction band transport states, (ii) exponential distribution of trapped states (surface states) and (iii) localized monoenergetic sub band gap states.

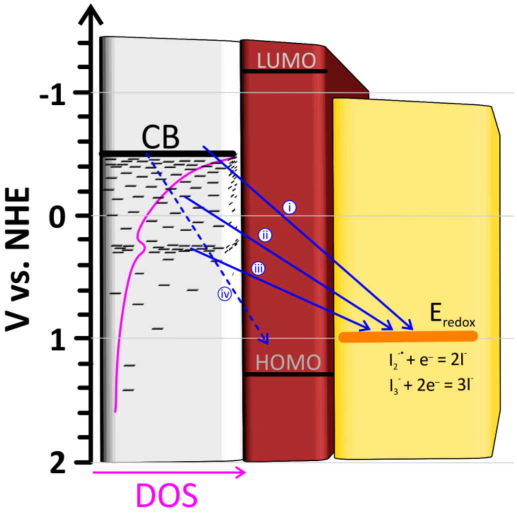

**Figure 1.9:** Possible electron recombination mechanisms in a DSC. (i) recombination from CB transport states, (ii) recombination from the exponential DOS, (iii) recombination from localized sub band gap states and (iv) recombination to the oxidized dye.

Moreover, recombination from the TCO-electrolyte interface only becomes important under certain circumstances and charge transfer from semiconductor to oxidized dye is, in general, slow enough to thought to be negligible.[47]

On the other side, the high redox ionic concentration in the electrolyte stabilizes the redox energy level in a very narrow value over all the operation conditions. Thus, only the energy levels of the semiconductor determines the rate of charge transfer. Smaller distances between semiconductor CB position and redox energy level will be translated into higher recombination rates. The global reaction for recombination is the same as the reduction of the triiodide Eq. (1.4). As previously described, multiple intermediate steps occur involving acceptor iodide radicals as $I_2^{-\bullet}$, see Figure 1.7. The recombination will be highly determined of the proximity of these acceptor species to the semiconductor nanoparticle surface.

## 1.5 Objectives

This thesis aims to show a complete view of the dye-sensitized solar cells. Starting from the optimization of device processing and it's structure, the work will show some issues concerning to DSC working conditions. By means of novel electrical characterization and data process methods, comprehensive explanations for the different processes limiting the device performance will be given.

After this general introduction, the materials employed and processing for DSC fabrication will be described in Chapter 2. The aim is to detect the potential improvements applicable to DSC from its basis, as it is the materials or processing techniques employed for its fabrication. Chapter 3 will be focused in the description of the different characterization techniques employed in this work. Next step will be the analysis of real systems. Chapter 4 will analyze the origin of $V_{oc}$ in working devices, using a quick and robust method of characterization and data analysis. The method will be employed in devices where electrolyte composition or dye molecules have been changed. Next chapter will be centered in the analysis of how the external temperature affects the performance of working DSC. By means of IS, recombination or conduction band changes will be studied. Chapter 6 will analyze novel structures for enhancing DSC performance in particular light reflectors for increasing light absorption. The diffusion resistance of the electrolyte through porous one-dimensional photonic crystals, will be studied to check the suitability of these structures for DSC. And finally, Chapter 7 focuses in the upscaling techniques for the production of series connected DSC modules. A working device will be fabricated and characterized, discussing the results.

Concluding, Chapter 8 will collect the general remarks of dye sensitized solar cells by compiling all exposed results.

## References

(1) http://www.census.gov/.

(2) http://www.unep.org/publications/ebooks/foresightreport/Portals/24175/pdfs/Foresight_Report-21_Issues_for_the_21st_Century.pdf.

(3) http://cnst.rice.edu/content.aspx?id=246.

(4) http://www.exxonmobil.com/Corporate/files/news_pub_eo.pdf.

(5) http://www.eere.energy.gov/topics/solar.html.

(6) Becquerel, A. E. Mémoire sur les effets électriques produits sous l'influence des rayons solaires. *C. R. Acad. Sci.* **1839**, *9*, 561-567.

(7) Williams, R. Becquerel Photovoltaic Effect in Binary Compounds. *The Journal of Chemical Physics* **1960**, *32*, 1505-1514.

(8) Fritts, C. E. On a New Form of Selenium Photocell. *American J. of Science* **1883**, *26*, 465.

(9) Kolomiets, B. T. *Bulletin of the USSR Academy of sciences. Physics series* **1938**, *5-6*, 695.

(10) Chapin, D. M.; Fuller, C. S.; Pearson, G. L. A New Silicon p-n Junction Photocell for Converting Solar Radiation into Electrical Power. *Journal of Applied Physics* **1954**, *25*, 676-677.

(11) Green, M. A.; Emery, K.; Hishikawa, Y.; Warta, W.; Dunlop, E. D. Solar cell efficiency tables (Version 38). *Progress in Photovoltaics: Research and Applications* **2011**, *19*, 565-572.

(12) Tang, C. W. Two-layer organic photovoltaic cell. *Applied Physics Letters* **1986**, *48*, 183-185.

(13) O' Regan, B.; Grätzel, M. A low-cost high-efficiency solar cell based on dye-sensitized colloidal TiO2 films. *Nature* **1991**, *353*, 737.

(14) http://www.nrel.gov.

(15) Tiwana, P.; Docampo, P.; Johnston, M. B.; Snaith, H. J.; Herz, L. M. Electron Mobility and Injection Dynamics in Mesoporous ZnO, SnO2, and TiO2 Films Used in Dye-Sensitized Solar Cells. *ACS Nano* **2011**, *5*, 5158-5166.

(16) Wijeratne, K.; Akilavasan, J.; Thelakkat, M.; Bandara, J. Enhancing the solar cell efficiency through pristine 1-dimentional SnO2 nanostructures: Comparison of charge transport and carrier lifetime of SnO2 particles vs. nanorods. *Electrochimica Acta* **2012**, *72*, 192-198.

(17) Li, P.; Wu, J.; Lin, J.; Huang, M.; Lan, Z.; Li, Q. Improvement of performance of dye-sensitized solar cells based on electrodeposited-platinum counter electrode. *Electrochimica Acta* **2008**, *53*, 4161-4166.

(18) Trevisan, R.; Döbbelin, M.; Boix, P. P.; Barea, E. M.; Tena-Zaera, R.; Mora-Seró, I.; Bisquert, J. PEDOT Nanotube Arrays as High Performing Counter Electrodes for Dye Sensitized Solar Cells. Study of the Interactions Among Electrolytes and Counter Electrodes. *Advanced Energy Materials* **2011**, *1*, 781-784.

(19) Wang, P.; Klein, C.; Humphry-Baker, R.; Zakeeruddin, S. M.; Grätzel, M. A High Molar Extinction Coefficient Sensitizer for Stable Dye-Sensitized Solar Cells. *Journal of the American Chemical Society* **2004**, *127*, 808-809.

(20) Barea, E. M.; Gónzalez-Pedro, V.; Ripollés-Sanchis, T.; Wu, H.-P.; Li, L.-L.; Yeh, C.-Y.; Diau, E. W.-G.; Bisquert, J. Porphyrin Dyes with High Injection and Low Recombination for Highly Efficient Mesoscopic Dye-Sensitized Solar Cells. *The Journal of Physical Chemistry C* **2011**, *115*, 10898-10902.

(21) Yan, Z.; Guang, S.; Su, X.; Xu, H. Near-Infrared Absorbing Squaraine Dyes for Solar Cells: Relationship between Architecture and Performance. *The Journal of Physical Chemistry C* **2012**, *116*, 8894-8900.

(22) Bai, Y.; Cao, Y.; Zhang, J.; Wang, M.; Li, R.; Wang, P.; Zakeeruddin, S. M.; Gratzel, M. High-performance dye-sensitized solar cells based on solvent-free electrolytes produced from eutectic melts. *Nat Mater* **2008**, *7*, 626-630.

(23) Ding, I. K.; Tétreault, N.; Brillet, J.; Hardin, B. E.; Smith, E. H.; Rosenthal, S. J.; Sauvage, F.; Grätzel, M.; McGehee, M. D. Pore-Filling of Spiro-OMeTAD in Solid-State Dye Sensitized Solar Cells: Quantification, Mechanism, and Consequences for Device Performance. *Advanced Functional Materials* **2009**, *19*, 2431-2436.

(24) Yum, J.-H.; Baranoff, E.; Kessler, F.; Moehl, T.; Ahmad, S.; Bessho, T.; Marchioro, A.; Ghadiri, E.; Moser, J.-E.; Yi, C.; Nazeeruddin, M. K.; Grätzel, M. A cobalt complex redox shuttle for dye-sensitized solar cells with high open-circuit potentials. *Nat Commun* **2012**, *3*, 631.

(25) Yella, A.; Lee, H.-W.; Tsao, H. N.; Yi, C.; Chandiran, A. K.; Nazeeruddin, M. K.; Diau, E. W.-G.; Yeh, C.-Y.; Zakeeruddin, S. M.; Grätzel, M. Porphyrin-Sensitized Solar Cells with Cobalt (II/III)–Based Redox Electrolyte Exceed 12 Percent Efficiency. *Science* **2011**, *334*, 629-634.

(26) U.S. Department od Energy, N. R. E. L. SunShot Vision study. **February 2012**, *Chapter 4*.

(27) Tobías, I.; Luque, A. Ideal efficiency of monolithic, series-connected multijunction solar cells. *Progress in Photovoltaics: Research and Applications* **2002**, *10*, 323-329.

(28) http://cleantechnica.com/2012/03/15/us-solar-facts-charts/. "2011 U.S. Solar Market Report”.

(29) Kalowekamo, J.; Baker, E. Estimating the manufacturing cost of purely organic solar cells. *Solar Energy* **2009**, *83*, 1224-1231.

(30) Mints, P. Photovoltaic Manufacturer Shipments, Capacity & Competitive Analysis. *Palo Alto, CA: Navigant Consulting Photovoltaic Service Program* **2011**, *Report NPS-Supply 6*.

(31) Jager-Waldau, A. Progress in chalcopyrite compound semiconductor research for photovoltaic applications and transfer of results into actual solar cell production. *Solar Energy Materials and Solar Cells* **2011**, *95*, 1509-1517.

(32) (EPIA), E. P. I. A. Global Market Outlook for PV until 2015. *http://www.epia.org/fileadmin/EPIA_docs/public/Global_Market_Outlook_for_Photovoltaics_until_2015.pdf* **May 2011**.

(33) Fujishima, A.; Honda, K. Electrochemical Photolysis of Water at a Semiconductor Electrode. *Nature* **1972**, *238*, 37-38.

(34) Nazeeruddin, M. K.; Kay, A.; Rodicio, I.; Humphry-Baker, R.; Mueller, E.; Liska, P.; Vlachopoulos, N.; Graetzel, M. Conversion of light to electricity by cis-X2bis(2,2'-bipyridyl-4,4'-dicarboxylate)ruthenium(II) charge-transfer sensitizers (X = Cl-, Br-, I-, CN-, and SCN-) on nanocrystalline titanium dioxide electrodes. *Journal of the American Chemical Society* **1993**, *115*, 6382-6390.

(35) Koops, S. E.; O'Regan, B. C.; Barnes, P. R. F.; Durrant, J. R. Parameters Influencing the Efficiency of Electron Injection in Dye-Sensitized Solar Cells. *Journal of the American Chemical Society* **2009**, *131*, 4808-4818.

(36) Hagfeldt, A.; Boschloo, G.; Sun, L.; Kloo, L.; Pettersson, H. Dye-Sensitized Solar Cells. *Chemical Reviews* **2010**, *110*, 6595-6663.

(37) Bisquert, J.; Garcia-Belmonte, G.; Fabregat-Santiago, F. Modelling the electric potential distribution in the dark in nanoporous semiconductor electrodes. *J Solid State Electrochem* **1999**, *3*, 337-347.

(38) Bisquert, J. Physical electrochemistry of nanostructured devices. *Physical Chemistry Chemical Physics* **2008**, *10*, 49-72.

(39) Grünewald, M.; Thomas, P. A hopping model for activated charge transport in amorphous silicon. *physica status solidi (b)* **1979**, *94*, 125-133.

(40) van de Lagemaat, J.; Park, N. G.; Frank, A. J. Influence of Electrical Potential Distribution, Charge Transport, and Recombination on the Photopotential and Photocurrent Conversion Efficiency of Dye-Sensitized Nanocrystalline TiO2 Solar Cells: A Study by Electrical Impedance and Optical Modulation Techniques. *The Journal of Physical Chemistry B* **2000**, *104*, 2044-2052.

(41) Baucke, F. G. K. B., R.; Cruse, K. The Iodide-Iodine System in Acetonitrile: Evaluation of Standard Thermodynamic Data on the Association $I^- + I_2 \rightarrow I_3^-$ from Potentiometric Measurements at 25 and 50°C. *J. Electroanal. Chem.* **1971**, *32*, 247-256.

(42) Datta, J.; Bhattacharya, A.; Kundu, K. K. Relative Standard Electrode Potentials of $I_3^-$/ $I^-$, $I_2/I_3^-$, and $I_2$/ $I^-$ Redox Couples and the Related Formation Constants of $I_3^-$ in Some Pure and Mixed Dipolar Aprotic Solvents. *Bulletin of the Chemical Society of Japan* **1988**, *61*, 1735-1742.

(43) Boschloo, G.; Hagfeldt, A. Characteristics of the Iodide/Triiodide Redox Mediator in Dye-Sensitized Solar Cells. *Accounts of Chemical Research* **2009**, *42*, 1819-1826.

(44) Rowley, J. G.; Farnum, B. H.; Ardo, S.; Meyer, G. J. Iodide Chemistry in Dye-Sensitized Solar Cells: Making and Breaking I–I Bonds for Solar Energy Conversion. *The Journal of Physical Chemistry Letters* **2010**, *1*, 3132-3140.

(45) Hauch, A.; Georg, A. Diffusion in the electrolyte and charge-transfer reaction at the platinum electrode in dye-sensitized solar cells. *Electrochimica Acta* **2001**, *46*, 3457-3466.

(46) Papageorgiou, N.; Maier, W. F.; Grätzel, M. An Iodine/Triiodide Reduction Electrocatalyst for Aqueous and Organic Media. *Journal of The Electrochemical Society* **1997**, *144*, 876-884.

(47) Cameron, P. J.; Peter, L. M. How Does Back-Reaction at the Conducting Glass Substrate Influence the Dynamic Photovoltage Response of Nanocrystalline Dye-Sensitized Solar Cells? *The Journal of Physical Chemistry B* **2005**, *109*, 7392-7398.

# Chapter 2

## Structure and optimization of DSC

## 2.1 Introduction

In the last years of research in the field of dye-sensitized solar cells, many efforts have been done to increase the overall power conversion efficiency. Some of the most successful have been focused on increasing photocurrent with new dyes. Also photovoltage has been enhanced through manipulation of both surface and lattice structure of the semiconductor. Not less important have been the studies centered in reducing internal resistances via ionic diffusion or charge transfer improvements, or even increasing stability by better encapsulation. Due to the sensibility of the internal mechanisms in a DSC, in most of cases, an increase on photocurrent is followed by a decrease on photovoltage, and vice versa. Any change in the cell constituents will alter the nature of the interfaces existing in the device. Is necessary a deep knowledge of the processes governing the operation of the cell in order to achieve the equilibrium that optimizes the DSC efficiency.

In this section all the constituents of a DSC will be described in detail, focusing in their properties and limitations. In addition, the fabrication process of DSCs used for the preparation of the samples studied in this thesis is described.

## 2.2 Materials

### 2.2.1 Substrate

The substrate of the photoelectrode needs to accomplish some basic requirements for a good performance of the solar cell:

1- Transparency, the glass and the conductive layer used should have high transmittance on the visible light, where the dye absorbs majorly.
2- Conductivity, the transparent semiconductor on the glass substrate should have enough conductivity in order to minimize internal resistances of the device.
3- Contact, the TCO must form an ohmic contact with the nanostructured semiconductor for a proper charge transfer.
4- Stability, the transparent semiconductor should not be corroded by iodine/iodide redox.
5- Low losses, it should also present a low rate of charge transfer to the electrolyte.

| Substrate | Thickness (mm) | Visible transmittance (%) | Sheet resistance (Ω/□) | Haze (%) | FTO thickness (nm) |
|---|---|---|---|---|---|
| NSG | 3.2 | ≥ 78 | 11-13 | ≤ 8 | 750 |
| TEC 15 | 2.3-3.0 | 82-84.5 | 12-14 | ≤ 0.74 | |
| TEC 8 | 2.3-3.0 | 80-81.5 | 6-9 | 12 | |

**Table 2.1:** Specific parameters of the conductive glass used in DSC fabrication.

Coated glass with a thin layer of fluorine doped tin oxide (FTO) accomplish these requirements. In this work, Nippon Sheet Glass (NSG) and Pilkington (TEC) glass substrates were employed. Table 2.1 summarizes the substrate parameters.

### 2.2.2 Sensitizer

One of the key components for high performance DSC is the light absorber. Substantial developments have been made the last decade in the engineering of novel dye structures in order to enhance the light absorption, especially in the red and near infrared regions. The pioneer was a ruthenium based dye named N3 which gave 10% efficiencies DSCs in 1993.[1] Thenceforth, a great number of amphiphilic homologues have been successfully developed reaching efficiencies over 11%, N719[2] (a tetrabutylammonium salt of N3), Z907 or black dye. The basic characteristics of these dyes are:

(i) low electrostatic charge of the dye in order to avoid repulsion between adsorbed dye units and thereby increasing the dye loading
(ii) low water-induced dye desorption in order to increase cell stability
(iii) high reversibility of the ruthenium III/II couple, enhancing dye stability[3]
(iv) grafting of the dye on the semiconductor surface, facilitated by carboxylate groups bonding the metal oxide surface, facilitates electron injection.
(v) high molar extinction coefficient (high absorption per molar unit)

In parallel to Ru dyes development, many other molecular structures have been proposed as porphyrin, phtalocyanine, organic molecules or quantum dots (see Figure 2.1), reaching efficiencies over 11%, as in the case of the porphyrin YD2.[4]

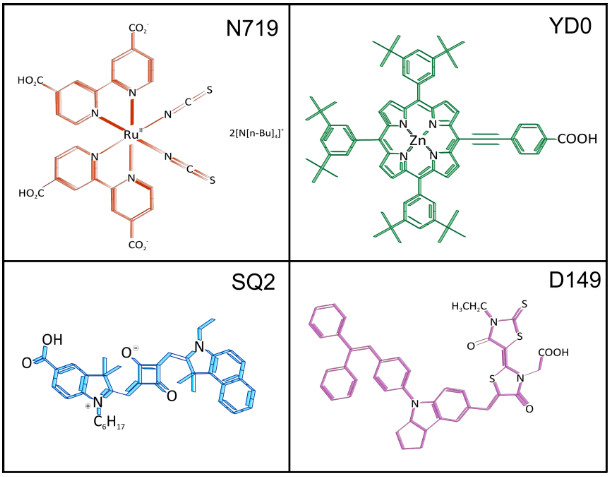
N719
YD0
SQ2
D149

**Figure 2.1:** Molecular structures of four different sensitizers for dye solar cells. The color in the image is the approximate color of the sensitized $TiO_2$ film for each dye.

To improve efficiency of DSCs, amphiphilic molecules are introduced in the dye solution in order to coadsorb on the nanoparticles during sensitization bath. Cografting of this type of molecules on the semiconductor have been reported to enhance the DSC efficiency and stability.[5,6] In particular in this work chenodeoxycholic acid has been employed as coadsorbent with Ru dyes, see Figure 2.2. The carboxylic or phosphonic group binds to the $TiO_2$ surface, while the hydrophobic end acts as a buffer between the semiconductor and the electrolyte. However, in the case of chenodeoxycholate, recombination rate is reported to increase by a factor of 5 but the net effect of this molecule is to improve $V_{oc}$ up to 40mV thanks to an upward shift of the $TiO_2$ CB.[7]

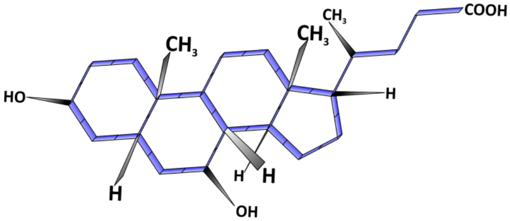

**Figure 2.2:** Molecular structure of chenodeoxycholic acid coadsorbent

Although the dye molecules adsorbed on the porous $TiO_2$ film decrease as the chenodeoxycholic acid (CDCA) concentration in the dye bath increase, there is still a global improvement of the photovoltaic performance of DSC. The performance enhancement using CDCA has been explained by three processes:[8]

(1) CDCA may fill the vacancy of the dye-adsorbed $TiO_2$ film so that the back current (from the charge recombination of the electron in mesoscopic $TiO_2$ film to the electrolyte) is reduced.

(2) It increases the Fermi level of $TiO_2$ film (shifts to more negative potential).

(3) The presence of CDCA reduces the dye aggregation, facilitating the charge separation.

### 2.2.3 Nanostructured semiconductor

A photoactive electrode is basically formed by a nanoporous semiconductor thin film deposited over a conducting glass. Some crucial properties needed in a photoelectrode are:

- Transparency to allow the dye absorbing the major part of incident light.
- High specific area to ensure the maximum of dye molecules adsorbed per unit of cell area.
- Porosity to permit good interpenetration of the electrolyte through the nanoparticles.

Up to now, the best-efficiency DSCs have been made with a 10-12 µm layer of sintered 20nm $TiO_2$ nanocrystals. Over this film, a 3-5 µm thick layer of 450nm $TiO_2$ nanocrystals has been successfully employed for back scattering of incident light thus increasing the photon absorption in the active layer. Both type of colloids are grown by hydrothermal synthesis and further processed as a printable paste.[9] All of them are based on ethyl cellulose and terpineol in order to achieve a printable texture. In this work commercial $TiO_2$ pastes from Dyesol have been employed for high performance DSC fabrication. 18NR-T has been used as transparent and active layer and WER4-0 as light scattering layer.

Alternative methods for processing $TiO_2$ paste were also explored. Thus commercial $TiO_2$ 25nm-powder (Degussa P25) was dispersed in an ethanol solution, then mixed with ethyl-cellulose and terpineol and finally concentrated in a rotavapor. The result was a low-cost printable $TiO_2$ paste leading to comparable DSC efficiencies than commercial $TiO_2$. [10]

### 2.2.4 Electrolyte

Electrolyte in a DSC consist in a redox couple dissolved in a liquid or gelificated solvent which is capable to contact the whole photoanode internal area. The electrolyte is crucial in order to regenerate the oxidized dye molecules and transporting the charge to the counter electrode. Basically, the main requirements for the electrolyte are: (i) high electrochemical and UV stability, (ii) thermal stability above 80ºC, (iii) low vapor pressure in order to avoid leakages, (iv) hydrophobicity to maintain $H_2O$ away from the photoanode, (v) high ionic diffusion coefficient.

Even is hard to find all these characteristics in a single formulation of electrolyte, the efforts undertaken last years in this field of research found several solutions for the needs of each single DSC. Acetonitrile (ACN) based electrolytes containing $I^-/I_3^-$ couple have been used for high efficiency DSC. Substituting the solvent by methoxypropionitrile (MPN) with lower volatility prevents the electrolyte leakage for high stability. Moreover, ionic liquids as alquilimidazolium are totally non volatile at the working temperatures range, but lowers ionic mobility thus decreasing efficiency.

The complex reactions of iodide/iodine pair and its high corrosivity opened the research to other redox couples as cobalt, Co(II/III),[11,12] or ferrocene ($Fc/Fc^+$)[13] with conversion efficiencies up to 12%. Finally, solid state DSC have also been developed using organic hole transporters as spiro-OMETAD. These cells do not require sealing but hardly reach efficiencies of 6% using an organic dye.[14] Recent publications report efficiencies of 10.9% employing perovskite structures as light absorbers and electron extraction.[15]

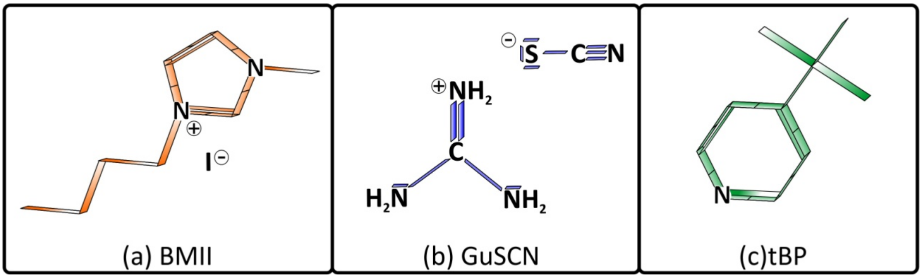

(a) BMII (b) GuSCN (c)tBP

**Figure 2.3:** Molecular structures of some of the additives commonly used in DSC electrolytes. (a) 1-butyl-3-methylimidazolium iodide, (b) guanidinium thiocyanate and (c) 4-*tert*-butylpyridine.

Some common electrolyte additives employed in DSC fabrication and it’s characteristics are:

Lithium iodide (LiI) is a very stable salt widely used in electrochemistry. It provides the necessary iodide cations for the redox couple in the electrolyte, increases charge conductivity in the electrolyte, and screens the negative charge in the semiconductor. Its positive charge produces a downward shift in the conduction that diminishes $V_{oc}$.[16] At long term, the extremely small size of $Li^+$ ions allows them to intercalate into $TiO_2$ lattice, degrading electron transport and recombination properties and displacing the UV absorption of the $TiO_2$ to the blue region of the spectra.[17] For this reason Lithium is avoided in the fabrication of DSCs designed for long lifetimes.

Ionic liquids as 1-buthyl-3-methylimidazolium iodide (BMII) (Figure 2.3(a)) have three basic advantages in DSCs electrolyte applications. BMII also provides iodide cations for the redox couple, but $BMI^+$ is a bigger cation than $Li^+$ that will not intercalate into the semiconductor structure. $BMI^+$ molecule has two amine groups which gives a base property to the electrolyte, increasing conduction band edge of the $TiO_2$. Finally, $BMI^+$ has an effect of shielding charge recombination between titanium oxide and electrolyte.[18,19]

Guanidinium thiocyanate (GuSCN) (Figure 2.3(b)) is a positively charged specie that produces a significant downwards shift of the CB. This fact increases electron injection from the dye. Conversely to expected, it improves $V_{oc}$ as the adsorption of the guanidinium cation on the $TiO_2$ surface decreases the recombination rate by a very effective surface passivation.[20,21]

4-*tert*-butylpyridine (tBP) (Figure 2.3(c)) is reported to produce a significant upwards band edge movement thus increasing $V_{oc}$. This band-edge shift is attributed to deprotonation of $TiO_2$ nanoparticles by amines, thereby charging their surface negatively.[22] Furthermore, amine groups adsorbed on the semiconductor surface coats the area not covered by the dye, blocking the recombination to the redox couple in the electrolyte.

The electrolyte solvent should be good enough for ensure a proper solution of the redox components and the additives but at the same time not cause significant dissolution of adsorbed dye. Polar organic solvents and ionic liquids are able to fulfill these requirements. Table 2.2 details the properties of the solvents employed in this work, compared with water properties.

| **Solvent** | **MP (ºC)** | **BP (ºC)** | $\varepsilon_r$ | **viscosity (cP)** | $D_{I_3^-}$ **($cm^2s^{-1}$)** |
|---|---|---|---|---|---|
| water | 0 | 100 | 80 | 0.89 | $1.1\cdot10^{-5}$ |
| acetonitrile | -44 | 82 | 36.6 | 0.34 | $1.5\cdot10^{-5}$ |
| valeronitrile | -96 | 140 | 20 | 0.71 | $1.5\cdot10^{-5}$ |
| 3-Methoxypropionitrile | -57 | 165 | 36 | 1.1 | $4\text{-}5\cdot10^{-6}$ |
| 1-methyl-3-propylimidazolium iodide | -55 | -- | -- | 880 | $1.9\cdot10^{-7}$ |

**Table 2.2:** Properties of Frequently Used Solvents for Electrolytes in Dye-Sensitized Solar Cells. MP (melting point) and BP (boiling point) at 1atm. $\varepsilon_r$ is the relative dielectric constant. Viscosity at 25ºC of the pure solvent, MPII with 0.5M $I_2$ added. $D_{I_3^-}$ is the apparent diffusion coefficient for triiodide in the electrolyte, it will depend on the final composition.[23]

Acetonitrile/valeronitrile mixture has been widely employed for high efficiency DSC. It is a low viscosity solvent but high volatile. Diffusion resistance in the electrolyte gets reduced thus decreasing the total series resistance value. This is translated in a significant increase of fill factor and efficiency of the device. On the other side, methoxypropionitrile (MPN) is commonly chosen because of its low volatility, that improves largely stability of the devices.

### 2.2.5 Counter electrode

The basic requirement for DSC counter electrodes is to present large charge transfer kinetics to the electrolyte. Usually, FTO-coated glass with deposited platinum particles are used for this purpose. Unless transparency of the cathode is not mandatory, it would increase DSC efficiency when the light arrives from both sides of the cell. A monolayer of Pt will be enough to provide catalytic effect to the conductive glass without reducing significantly the transparency. The standard procedure used in this work consist in a thermal decomposition of a wet TEC8 substrate with diluted hexacloroplatinic (IV) acid hexahydrate ($H_2PtCl_6$, Fluka) in 450ºC hot air for 30 minutes. A quicker procedure consist in Pt electrodeposition on the conductive glass. The electrochemical configuration consists in chloroplatinic acid diluted in water (1:10v), FTO glass as cathode and Pt foil as anode. An applied potential of +1.2V during 30s is enough for depositing a active Pt layer over the FTO glass, hydrogen bubbles will be originated on the Pt foil.

### 2.2.6 Advanced structures/ photonic crystals

A way for improve solar cell efficiency is introducing optical elements in the design of the device. In DSC, a back-scattering $TiO_2$ layer has been employed in order to enhance light harvesting by reflecting the unabsorbed photons back into the dyed photoelectrode.[24] However, the scatter layer eliminates the transparency of the device, one of the main attractive of this technology.

Photonic crystals (PC) are periodic nanostructures with optical properties capable of affect selectively the propagation of electromagnetic waves. In the same manner as a Bragg diffractor,[25] three dimensional inverted opals are able to reflect selected wavelengths remaining transparent for the rest.[26] From this base, PC have been chosen in DSC for the enhancement of light harvesting in specific parts of the spectrum while retaining cell transparency.[27,28] Efficiency increase up to 30% has been achieved by introducing an one-dimensional PC in a dye-solar cell. The improvement was also observed in the IPCE (incident photon-to-current conversion efficiency) of these cells. A deleterious effect appeared in the open circuit potential and fill factor of the device.[27] This fact indicates an impediment for ionic diffusion in the electrolyte due to the low porosity of the PC increasing internal series resistances.

Up to now, the porosity of nanoparticle 1DPCs has only been controlled through both the degree of aggregation and the particle size of the precursor suspensions.[29,30]

In this work the porosity of photonic crystals has been tuned by the use of a porogen in the precursor suspensions. The starting materials were suspensions of nanoparticles of $SiO_2$ and $TiO_2$. The polymer chosen to alter the porous network is polyethylene glycol (PEG) because it exhibits good film forming properties, and reduces the density of defects present in the films made by spin coating.[30]

Both np-$TiO_2$ monolayer's and np-$SiO_2$/np-$TiO_2$ stacks with 1DPC properties made of five bilayers were built by deposition of the diluted $TiO_2$ and $SiO_2$ nanoparticle suspensions by spin-coating (final speed $\omega$ = 5000 rpm; acceleration $\gamma = 9180$ rpms$^{-1}$; time 60 s), followed by heat treatment in an oven at 450ºC for 30 min to provide the films with mechanical stability. In order to achieve the desired monolayer thickness, several depositions of the same precursor suspension were carried out. The substrates used to deposit monolayer's and multilayers were silicon and glass, respectively. Both substrates were previously treated to enhance their hydrophilicity and, consequently, improve the first layer deposition. The films prepared presented high optical quality and displayed uniform color arising from the interference of the beams reflected by the different interphases. In order to build the monolayers and multilayers using the np- $SiO_2$/PEG and the np-$TiO_2$/PEG precursor suspensions we also employed the spin coating protocol described above, although in this case it was necessary to perform a thermal annealing at 300 ºC for 15 minutes in air after each deposition to eliminate the PEG from the structure and to consolidate the stacking of these layers. Without this intermediate treatment, it was not possible to create a new layer on top, since the deposited film did not adhere properly. Finally, the remaining polymer is eliminated after calcination of the whole multilayer at 450 ºC for 1 hour in air. The cross section image of an as-processed 1DPC is shown in Figure 2.4.

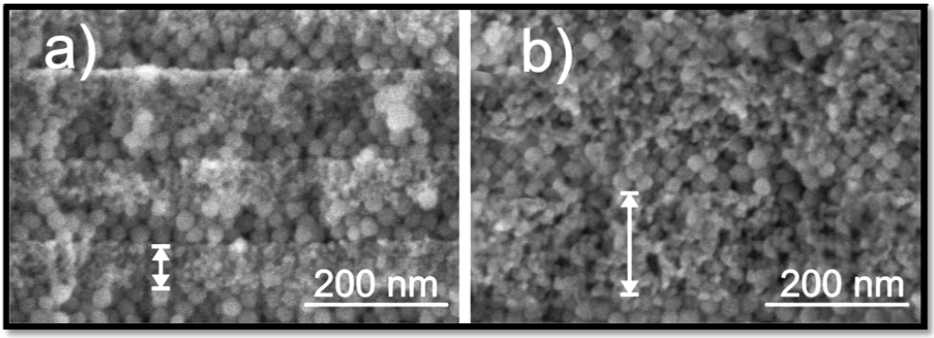

**Figure 2.4:** FESEM images of cross-sections corresponding to Bragg reflectors made of alternate layers of spherical silica particles and titania nanocrystals. The latter was mixed with PEG in weight relations of (a) 0% and (b) 75% with respect to the weight of np-TiO2 in the precursor suspension. White arrows indicate the thickness of the $TiO_2$ layer, it has to be noted the increase of thickness achieved when introducing more PEG, in (b).

## 2.3 Device fabrication

The general method to produce the working electrodes for the DSC follow this procedure: First, TEC 15 glass plates (as described in Section 2.2.1) were brushed with detergent solution and rinsed with milli-Q water, then immersed into iso-propanol and cleaned using an ultrasonic bath during 15 min, rinsed with ethanol and dried with air. After that a 150 nm compact $TiO_2$ layer was deposited by spray-pyrolisis technique with an ethanol/ acetyl acetone/ titanium (IV) isopropoxide (3:3:2 weight ratio) solution and a 450ºC hot plate. The substrates were coated by doctor blade technique with a 12 µm layer of 18-NRT and a 3 µm scatter layer of WER4-0 (section 2.2.3), then fired 30 min at 450ºC. The active area of the film was 0.25 $cm^2$. Figure 2.5 shows the cross section image of a complete $TiO_2$ film.

When cooled, films were immersed into 40mM $TiCl_4$ (aq) at 70ºC for 30 min, rinsed with milli-Q water and sintered at 570ºC for 10 min. After cooling to 40ºC, the $TiO_2$ electrodes were immersed into a 0.5mM N719 dye solution with 0.5mM chenodeoxycholic acid in a mixture of acetonitrile and *tert*-butanol 1:1 volume ratio during 16 hours.

Then, to prepare complete DSC, the working and counter electrodes (section 2.2.5) were assembled in a sandwich-type cell by pressing at 95ºC with a hot-melt film (Surlyn 25 µm thickness) as a sealant and spacer between electrodes. A drop of electrolyte solution (section 2.2.4) was put on the drilled holes, the cell was put into a small chamber where vacuum was made until most of the air inside the cell bubbled out through the electrolyte, when air came again into the chamber the electrolyte was driven into the cell. Finally the drilled holes were sealed with Surlyn and 0.1 mm thick glasses, and a tin contact was weld on the edge of FTO outside the cells.

Specific device configurations will be described in the corresponding section.

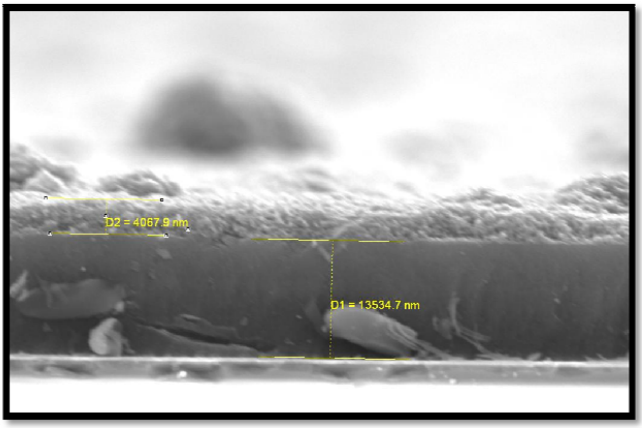

**Figure 2.5:** SEM image of nanostructured $TiO_2$ layer over an FTO glass. Transparent layer is 13.5µm thick and scatter layer is 4.1 µm thick.

## References

(1) Nazeeruddin, M. K.; Kay, A.; Rodicio, I.; Humphry-Baker, R.; Mueller, E.; Liska, P.; Vlachopoulos, N.; Graetzel, M. Conversion of light to electricity by cis-X2bis(2,2'-bipyridyl-4,4'-dicarboxylate)ruthenium(II) charge-transfer sensitizers (X = Cl-, Br-, I-, CN-, and SCN-) on nanocrystalline titanium dioxide electrodes. *Journal of the American Chemical Society* **1993**, *115*, 6382-6390.

(2) Nazeeruddin, M. K.; Kay, A.; Rodicio, I.; Humphry-Baker, R.; Müller, E.; Liska, P.; Vlachopoulos, N.; Grätzel, M. Conversion of light to electricity by cis-X 2bis(2,2′-bipyridyl-4,4′-dicarboxylate)ruthenium(II) charge-transfer sensitizers (X = Cl -, Br -, I -, CN -, and SCN -) on nanocrystalline TiO 2 electrodes. *Journal of the American Chemical Society* **1993**, *115*, 6382-6390.

(3) Klein, C.; Nazeeruddin, M. K.; Di Censo, D.; Liska, P.; Grätzel, M. Amphiphilic Ruthenium Sensitizers and Their Applications in Dye-Sensitized Solar Cells. *Inorganic Chemistry* **2004**, *43*, 4216-4226.

(4) Bessho, T.; Zakeeruddin, S. M.; Yeh, C.-Y.; Diau, E. W.-G.; Grätzel, M. Highly Efficient Mesoscopic Dye-Sensitized Solar Cells Based on Donor–Acceptor-Substituted Porphyrins. *Angewandte Chemie International Edition* **2010**, *49*, 6646-6649.

(5) Kopidakis, N.; Neale, N. R.; Frank, A. J. Effect of an Adsorbent on Recombination and Band-Edge Movement in Dye-Sensitized TiO2 Solar Cells: Evidence for Surface Passivation. *The Journal of Physical Chemistry B* **2006**, *110*, 12485-12489.

(6) Yum, J. H.; Moon, S. J.; Humphry-Baker, R.; Walter, P.; Geiger, T.; Nüesch, F.; Grätzel, M.; Nazeeruddin, M. d. K. Effect of coadsorbent on the photovoltaic performance of squaraine sensitized nanocrystalline solar cells. *Nanotechnology* **2008**, *19*, 424005.

(7) Neale, N. R.; Kopidakis, N.; van de Lagemaat, J.; Grätzel, M.; Frank, A. J. Effect of a Coadsorbent on the Performance of Dye-Sensitized TiO2 Solar Cells: Shielding versus Band-Edge Movement. *The Journal of Physical Chemistry B* **2005**, *109*, 23183-23189.

(8) Lee, K.-M.; Chen, C.-Y.; Wu, S.-J.; Chen, S.-C.; Wu, C.-G. Surface passivation: The effects of CDCA co-adsorbent and dye bath solvent on the durability of dye-sensitized solar cells. *Solar Energy Materials and Solar Cells* **2013**, *108*, 70-77.

(9) Ito, S.; Murakami, T. N.; Comte, P.; Liska, P.; Grätzel, C.; Nazeeruddin, M. K.; Grätzel, M. Fabrication of thin film dye sensitized solar cells with solar to electric power conversion efficiency over 10%. *Thin Solid Films* **2008**, *516*, 4613-4619.

(10) Ito, S.; Chen, P.; Comte, P.; Nazeeruddin, M. K.; Liska, P.; Péchy, P.; Grätzel, M. Fabrication of screen-printing pastes from TiO2 powders for dye-sensitised solar cells. *Progress in Photovoltaics: Research and Applications* **2007**, *15*, 603-612.

(11) Sapp, S. A.; Elliott, C. M.; Contado, C.; Caramori, S.; Bignozzi, C. A. Substituted Polypyridine Complexes of Cobalt(II/III) as Efficient Electron-Transfer Mediators in Dye-Sensitized Solar Cells. *Journal of the American Chemical Society* **2002**, *124*, 11215-11222.

(12) Nusbaumer, H.; Moser, J.-E.; Zakeeruddin, S. M.; Nazeeruddin, M. K.; Grätzel, M. CoII(dbbip)22+ Complex Rivals Tri-iodide/Iodide Redox Mediator in Dye-Sensitized Photovoltaic Cells. *The Journal of Physical Chemistry B* **2001**, *105*, 10461-10464.

(13) Daeneke, T.; Kwon, T.-H.; Holmes, A. B.; Duffy, N. W.; Bach, U.; Spiccia, L. High-efficiency dye-sensitized solar cells with ferrocene-based electrolytes. *Nat Chem* **2011**, *3*, 211-215.

(14) Cai, N.; Moon, S.-J.; Cevey-Ha, L.; Moehl, T.; Humphry-Baker, R.; Wang, P.; Zakeeruddin, S. M.; Grätzel, M. An Organic D-π-A Dye for Record Efficiency Solid-State Sensitized Heterojunction Solar Cells. *Nano Letters* **2011**, *11*, 1452-1456.

(15) Lee, M. M.; Teuscher, J.; Miyasaka, T.; Murakami, T. N.; Snaith, H. J. Efficient Hybrid Solar Cells Based on Meso-Superstructured Organometal Halide Perovskites. *Science* **2012**, *338*, 643-647.

(16) Pelet, S.; Moser, J.-E.; Grätzel, M. Cooperative effect and adsorbed cations and iodide on the interception of back electron transfer in the dye sensitization of nanocrystalline TiO2. *The Journal of Physical Chemistry B* **2000**, *104*, 1791-1795.

(17) Kopidakis, N.; Benkstein, K. D.; van de Lagemaat, J.; Frank, A. J. Transport-limited recombination of photocarriers in dye-sensitize nanocrystalline TiO2 solar cells. *The Journal of Physical Chemistry B* **2003**, *107*, 11307.

(18) Wang, P.; Zakeeruddin, S. M.; Humphry-Baker, R.; Grätzel, M. A Binary Ionic Liquid Electrolyte to Achieve 7% Power Conversion Efficiencies in Dye-Sensitized Solar Cells. *Chemistry of Materials* **2004**, *16*, 2694-2696.

(19) Fabregat-Santiago, F.; Bisquert, J.; Palomares, E.; Otero, L.; Kuang, D.; Zakeeruddin, S. M.; Grätzel, M. Correlation between Photovoltaic Performance and Impedance Spectroscopy of Dye-Sensitized Solar Cells Based on Ionic Liquids. *The Journal of Physical Chemistry C* **2007**, *111*, 6550-6560.

(20) Zhang, Z.; Zakeeruddin, S. M.; O'Regan, B. C.; Humphry-Baker, R.; Grätzel, M. Influence of 4-Guanidinobutyric Acid as Coadsorbent in Reducing Recombination in Dye-Sensitized Solar Cells. *The Journal of Physical Chemistry B* **2005**, *109*, 21818-21824.

(21) Zhang, C.; Huang, Y.; Huo, Z.; Chen, S.; Dai, S. Photoelectrochemical Effects of Guanidinium Thiocyanate on Dye-Sensitized Solar Cell Performance and Stability. *The Journal of Physical Chemistry C* **2009**, *113*, 21779-21783.

(22) Schlichthörl, G.; Huang, S. Y.; Sprague, J.; Frank, A. J. Band Edge Movement and Recombination Kinetics in Dye-Sensitized Nanocrystalline TiO2 Solar Cells: A Study by Intensity Modulated Photovoltage Spectroscopy. *The Journal of Physical Chemistry B* **1997**, *101*, 8141-8155.

(23) Hagfeldt, A.; Boschloo, G.; Sun, L.; Kloo, L.; Pettersson, H. Dye-Sensitized Solar Cells. *Chemical Reviews* **2010**, *110*, 6595-6663.

(24) Ferber, J.; Luther, J. Computer simulations of light scattering and absorption in dye-sensitized solar cells. *Solar Energy Materials and Solar Cells* **1998**, *54*, 265-275.

(25) Johnson, D. C.; Ballard, I.; Barnham, K. W. J.; Bishnell, D. B.; Connolly, J. P.; Lynch, M. C.; Tibbits, T. N. D.; Ekins-Daukes, N. J.; Mazzer, M.; Airey, R.; Hill, G.; Roberts, J. S. Advances in Bragg stack quantum well solar cells. *Solar Energy Materials and Solar Cells* **2005**, *87*, 169-179.

(26) Nishimura, S.; Abrams, N.; Lewis, B. A.; Halaoui, L. I.; Mallouk, T. E.; Benkstein, K. D.; van de Lagemaat, J.; Frank, A. J. Standing Wave Enhancement of Red Absorbance and Photocurrent in Dye-Sensitized Titanium Dioxide Photoelectrodes Coupled to Photonic Crystals. *Journal of the American Chemical Society* **2003**, *125*, 6306-6310.

(27) Colodrero, S.; Mihi, A.; Häggman, L.; Ocaña, M.; Boschloo, G.; Hagfeldt, A.; Míguez, H. Porous One-Dimensional Photonic Crystals Improve the Power-Conversion Efficiency of Dye-Sensitized Solar Cells. *Advanced Materials* **2009**, *21*, 764-770.

(28) Guldin, S.; Hüttner, S.; Kolle, M.; Welland, M. E.; Müller-Buschbaum, P.; Friend, R. H.; Steiner, U.; Tétreault, N. Dye-Sensitized Solar Cell Based on a Three-Dimensional Photonic Crystal. *Nano Letters* **2010**, *10*, 2303-2309.

(29) Colodrero, S.; Ocana, M.; Miguez, H. Nanoparticle-Based One-Dimensional Photonic Crystals. *Langmuir* **2008**, *24*, 4430-4434.

(30) Puzzo, D. P.; Bonifacio, L. D.; Oreopoulos, J.; Yip, C. M.; Manners, I.; Ozin, G. A. Color from colorless nanomaterials: Bragg reflectors made of nanoparticles. *Journal of Materials Chemistry* **2009**, *19*, 3500-3506.

# Chapter 3

## Measurements and electrical characterization

## 3.1 Introduction

It is unquestionable the huge research effort in last years and the improvement reached in dye solar cells efficiency due to the materials development and improvement. Even so, the parallel development of characterization techniques is essential in order to achieve more precise and quicker methods to understand the solar cell behavior. A detailed knowledge of the internal processes governing the device will launch the development of better DSCs focusing the efforts in solving the specific problem limiting the performance of the cell instead of groping for solutions.

The first step in solar cell characterization is the determination of solar cell efficiency. As explained in section 1.3 the light intensity and spectra given by a standard solar simulator is calibrated to AM1.5 (100 $mW\cdot cm^{-2}$) in order to compare the efficiency of the devices coming from different laboratories. A *j-V* curve will show many valuable characteristics, as the $V_{oc}$, related with both the energetics of the materials and the recombination rate, $j_{sc}$, related with the electron generation and injection and *FF* related with the existence and magnitude of different internal resistances. Sometimes this information result ambiguous and one must resort to specific measurement techniques for resolve the different contributions of each element in a DSC.

## 3.2 Current density - Voltage curves (*j-V*)

Current-voltage (*j-V*) curves provide a quick method for characterizing the main parameters that describe the solar cells performance. Applying a controlled voltage, the current is measured in a potentiostat, obtaining a curve similar to the one plot in Figure 3.1. Due to the internal structure of the device DSC presents diode behavior thus, under ideal conditions and considering the absence of series resistance, *j-V* curve can be modeled using the Shockley diode equation including a term of charge generation, by the following expression:

$$j = j_{sc} - j_0\left(e^{qV/mk_BT} - 1\right) \tag{3.1}$$

where $j$ is the electrical current density, $V$ is the voltage difference between the contacts, $j_{sc}$ the short circuit current density, $j_0$ the dark reverse current density, $q$ the electron charge, $k_B$ Boltzmann's constant and $T$ the absolute temperature. The coefficient $m$ is called the ideality factor that for an ideal diode $m$=1. In electrochemical systems the transfer factor $\beta = 1/m$, is more commonly used in Eq.(3.1), with $\beta<1$.

In Eq. (3.1) the total photogeneration per unit area is represented by $j_{sc}$. Short circuit current is proportional to the incident light intensity ($\phi_0$) and the properties of absorption of the radiation by the sensitizer or optical efficiency ($\eta_{opt}$). The dark reverse current ($j_d$) corresponds to the extraction of the generated carriers by the thermal surrounding radiation. The exponential represents the rate of electron recombination, related to the applied voltage

(*V*) and expressed by the Boltzmann statistics, assuming a non linear charge transfer of electrons in $TiO_2$ to electrolyte ($m>1$ or $\beta<1$).[1]

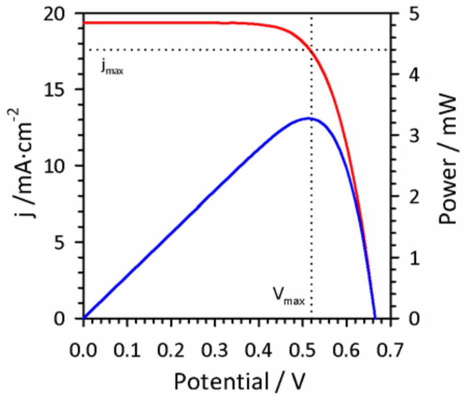

**Figure 3.1:** A typical *j*-*V* curve under illumination (red line) indicating $j_{sc}$ and $V_{oc}$. Blue line is the power curve, indicating the maximum power point ($P_{max}$) and corresponding $j_{max}$ and $V_{max}$.

Figure 3.1 shows a typical *j*-*V* curve of a high efficiency DSC. The relation between the maximum theoretical power ($V_{oc}\cdot j_{sc}$) and the real maximum power ($V_{max}\cdot j_{max}$) is represented by the fill factor (*FF*):

$$FF = \frac{V_{\max} j_{\max}}{V_{oc} j_{sc}} \tag{3.2}$$

Fill factor of a DSC reaches typical values of 0.6-0.8. The value of this parameter is strongly influenced by the presence of internal series resistances, possible leakage currents crossing the cell and also the value of $\beta$.[2,3] In silicon solar cells leakage currents are described through shunt resistance ($R_{sh}$). The closest element to $R_{sh}$ existing in DSC is the back layer recombination, $R_{bl}$, (see section 3.3). This resistance is voltage dependent and its influence is not fully understood.

Finally, the decisive parameter indicating how good is the solar cell, the efficiency ($\eta$) is the relation between the maximum output power of the device and the incident power of light ($P_{inc}$):

$$\eta = \frac{V_{\max} j_{\max}}{P_{inc}} = \frac{V_{oc} j_{sc} FF}{P_{inc}} \tag{3.3}$$

Usually $P_{inc}$ is established to AM1.5 (100 mW·cm$^{-2}$) however, is interesting the use of a wide range of illumination intensities from dark to 1 sun. This will provide information of the device response in the full range of real working conditions.

The main processes causing losses in solar cell performance are defined as the charge transfer between $TiO_2$ substrate and electrolyte ($R_{bl}$) and the voltage drop originated by series resistances in the device ($R_{series}$). Taking into account the influence of $R_{bl}$ and series resistance $R_{series}$ in the ideal equation of the diode expressed by Eq. (3.1), the phenomenological cell performance can be rewritten as:

$$j = \frac{-1}{1+{R_{series}}/{R_{bl}}}\left(j_0\left(\exp\left[\beta q\frac{V_{app}+jAR_{series}}{k_B T}\right]-1\right)-j_{sc}+\frac{V_{app}}{R_{bl}A}\right) \qquad (3.4)$$

where $V_{app}$ is the external applied voltage, and $A$ the active area of the cell.

Equation (3.4) takes into consideration the behavior of the FTO-electrolyte charge transfer as a simple resistance. This has been employed in order to simplify the equation, as the current of charge transfer in a semiconductor/electrolyte phase is governed by the Butler-Volmer relation.[4] Figure 3.2 represent the simulated *j*-*V* curves employing equation (3.4) and varying $R_{bl}$ (a), $R_{series}$ (b) and the dark current ($j_0$) in representation of $R_{rec}$ (c).

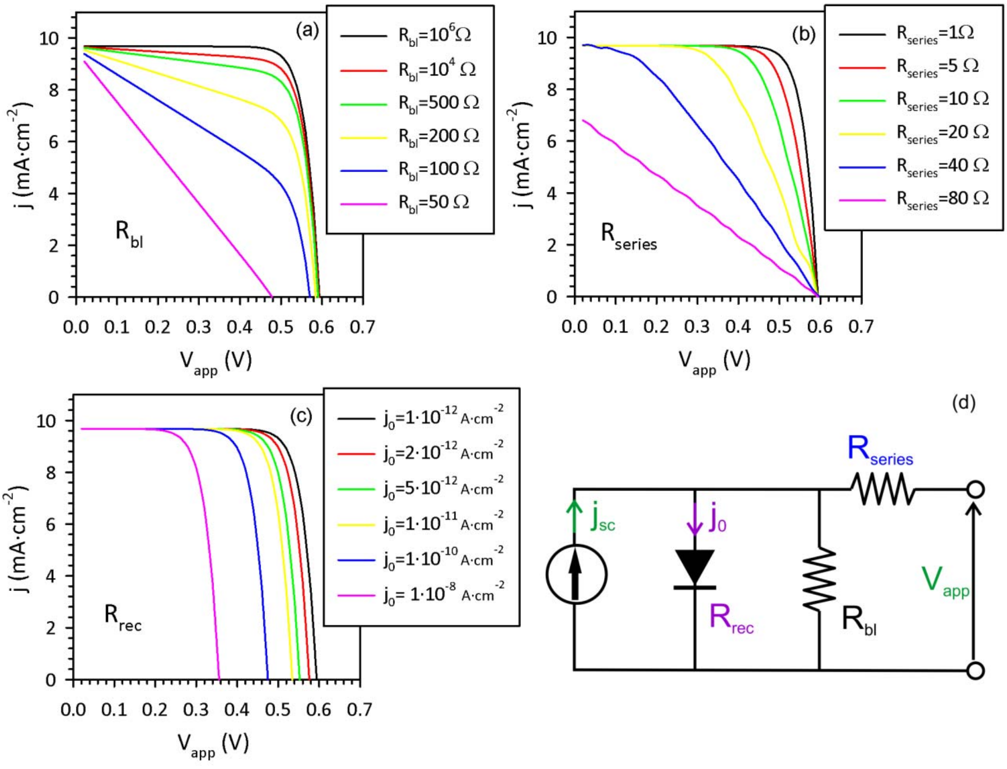

**Figure 3.2:** Effect of (a) shunt resistance, (b) series resistance and (c) $j_0$ representing recombination resistance in the shape of *j*-*V* curve. (d) Electric circuit following the standard diode model for solar cells. The parameters employed for the simulation were $T$=300K, $j_0=1\cdot10^{-12}$ mA·cm$^{-2}$, $j_{sc}$=10 mA·cm$^{-2}$, $R_{series}$=1 Ω, $R_{bl}=10^6$ Ω, $A$=1 cm$^2$, $\beta$=1.

On one hand, low shunt resistance ($R_{bl}$) means that a parallel path for electron flow exist inside the cell. This will by-pass the diode behavior affecting *j-V* curves increasing the slope at low potentials region and reducing *FF*, as we can see in Figure 3.2(a). Low $R_{bl}$ will decrease mainly the open circuit potential. On the other hand, see Figure 3.2(b), the increase of series resistance ($R_{series}$) produce a decrease of the slope of *j-V* curve in the region near $V_{oc}$, high $R_{series}$ decrease mainly the short circuit current. Finally, high electron recombination rate between the $TiO_2$ and the electrolyte species produce a decrease on $V_{oc}$, while *FF* is not significatively affected.

All along the work the devices have measured with the platinized counter electrode in negative respect to the working electrode. In this manner the resulting $V_{oc}$ has negative values but it has been plotted with positive values for better viewing.

## 3.3 Impedance Spectroscopy (IS)

Impedance spectroscopy (IS) is a characterization method which works with the system under "ideally" steady state conditions. Since the 1970s it has been largely applied in electrochemistry thanks to the possibility to separate charge transfer, transport and accumulation events occurring at the same time in several materials both solid and liquids and their interfaces.[5] This is thanks to the different characteristic times at which each process takes place. Therefore the analysis at different frequencies allows separate electrical mechanisms that *DC* techniques are not able to resolve individually. The electrochemical character of the DSC makes IS suitable for unravel their internal processes on the basis of the traditional electrochemistry models.[6,7] Several groups applied successfully IS technique to dye solar cells,[8,9] but it took several years to develop a clarified data interpretation for the porous-mixed phase structure of the DSC.[10]

IS consist in a sinusoidal small perturbation of voltage, $\hat{V}(\omega)$ around a fixed value (V) and the corresponding measurement of the *AC* electrical current, $\hat{I}(\omega)$ (or vice versa), within a range of angular frequencies ($\omega$). The small perturbation is necessary for a linear dependence between $\hat{V}(\omega)$ and $\hat{I}(\omega)$ and together with the applied stationary constraints (light intensity, temperature,...) ensures the steady state of the system. The impedance is:

$$Z(\omega)=\frac{\hat{V}(\omega)}{\hat{I}(\omega)} \tag{3.5}$$

The symbol "^" over a quantity indicates the complex amplitude of a sinusoidal (ac) small perturbation. $Z(\omega)$ is measured by scanning the frequency at values in a range of several orders of magnitude. Scanning at low frequencies as 0.01Hz consumes minutes, extending the whole measurement for hours, if this analysis is repeated for different applied bias. Long measurements have more probability of a change in steady state conditions, affecting the measured parameters. On the other side, scanning at low frequencies is often necessary, especially in non explored systems in order to identify slow processes. For this reason an equilibrium between measurement speed and precision should be found, and this is often aided by experience.

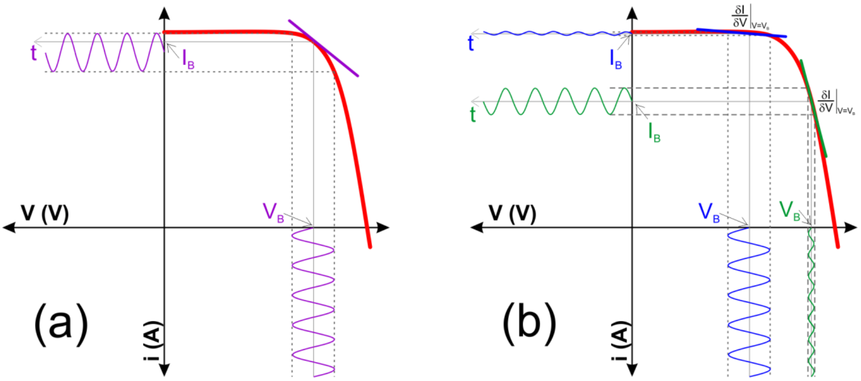

**Figure 3.3:** (a) Large amplitude voltage signal in curved areas of the *i-V* curve produce a non-linear response of the impedance. (b) Large amplitude voltage signal at low voltages of the typical *i-V* curve will produce a linear response. The exponential part of the *i-V* curve, in contrast, needs lower amplitude of the AC voltage signal to reach the linear response. This is the desired behavior for Impedance Spectroscopy measurements.

In dye solar cells, the constraints applied during IS measurements are; (i) the DC voltage, taking a range of fixed potentials where the DSC works (from 0V up to some hundred mV over $V_{oc}$). (ii) AC voltage, usually takes values of 10-20 mV, at high voltages IS is more sensitive to high perturbations (see Figure 3.3(a) and (b)) , this value should be taken carefully in order to get a linear response. (iii) Temperature and (iv) Illumination, should be constant along the IS measurement so that steady state conditions are kept.

The impedance response can be analyzed in terms of equivalent circuits. In this process, the important issue is to correlate the observed IS behavior with the physical processes occurring in the studied device. It is necessary to correlate the different circuit elements that allow the IS fitting with the physical processes taking place in the solar cell. This correlation is not straightforward and needs an intensive work to unveil it. In the case of DSCs this correlation is already known. [11-13]

To understand the circuit employed for DSC, it is necessary to describe the concept of transmission line model. In certain experimental conditions, the electrochemical impedance of a nanostructured disordered system is well described by the coupling of transport along one resistive channel and the interfacial reaction modeled as a resistor-capacitor circuit.[14]

Here, the transmission line (TL) model describes the diffusion of electrons in the $TiO_2$ together with their recombination with the holes in the electrolyte. Other resistive-capacitive elements are also included in the model, corresponding to substrate or counter-electrode interphase. The specific equivalent circuit models for fitting the impedance spectra of DSC are represented in Figure 3.4.[11,15,16]

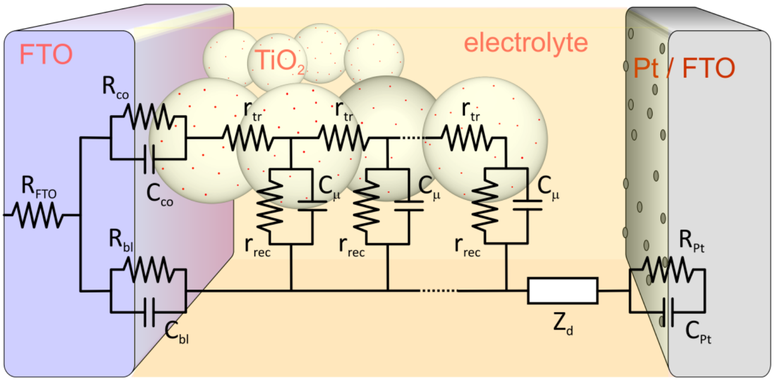

**Figure 3.4:** The general transmission-line equivalent circuit for a liquid electrolyte DSC, the element $Z_d$ accounts for diffusion of the redox species in the electrolyte. $r_{tr}$ and $r_{rec}$ are the specific resistances per unit volume.

In conclusion, the different parameters, and the physical processes that could be extracted through Impedance Spectroscopy measurements are:

- $\boldsymbol{R_{rec}}$ charge recombination resistance in the $TiO_2$/electrolyte interphase. It is obtained normalizing its specific resistance per unit volume ($r_{rec}$) through:

$$R_{rec} = \frac{r_{rec}}{v_{eff}} \tag{3.6}$$

being $v_{eff} = A \cdot L \cdot (1-p)$ the effective volume of the porous film. Where $A$ is the area, $L$ the thickness and $p$ the porosity of the $TiO_2$ film.

- $\boldsymbol{R_{tr}}$ transport resistance of electrons through $TiO_2$, which is related to the resistivity of the material, by:

$$R_{tr} = \frac{r_{tr}}{v_{eff}} \tag{3.7}$$

- $\boldsymbol{C_\mu}$ $TiO_2$ chemical capacitance.
- $\boldsymbol{R_{Pt}}$ the charge transfer resistance from $I_3^-$ to the platinized FTO counter electrode.
- $\boldsymbol{C_{Pt}}$ the interfacial (Helmholtz) capacitance at the counter electrode surface.
- $\boldsymbol{R_{bl}}$ the charge transfer resistance from $I_3^-$ to the non covered FTO in the photoanode (back-layer).
- $\boldsymbol{C_{bl}}$ the interfacial (Helmholtz) capacitance at the back layer surface.
- $\boldsymbol{R_{co}}$ and $\boldsymbol{C_{co}}$ respectively the resistance and capacitance at the FTO/$TiO_2$ interface. It is only significant when the contact is not ohmic.
- $\boldsymbol{R_{FTO}}$ is the resistance of the conducting glass and external contacts.

- ***Z*$_d$** is the Warburg element for the Nernst diffusion of the ionic species in the electrolyte. Gives the diffusion resistance $R_d$ through:

$$Z_d = R_d \frac{\tanh\left[(j\omega/\omega_d)^{1/2}\right]}{(j\omega/\omega_d)^{1/2}} \tag{3.8}$$

where $\omega$ is the angular frequency and $\omega_d$ the diffusion frequency from which diffusion coefficient may be obtained $D_{I_3^-} = \omega_d L^2$.

From these parameters, the electron lifetime in the $TiO_2$ ($\tau_n$), the diffusion coefficient of ionic species in the electrolyte ($D_n$) and electron diffusion length through $TiO_2$ ($L_n$) can be calculated by: [13]

$$\tau_n = R_{rec} C_\mu \tag{3.9}$$

$$D_n = \frac{L^2}{R_{tr} C_\mu} \tag{3.10}$$

$$L_n = \sqrt{D_n \tau_n} = L\sqrt{\frac{R_{rec}}{R_{tr}}} \tag{3.11}$$

## 3.4 Fitting to a circuit model

In order to extract the different electrical parameters from solar cell, measured IS data are fit to the proper equivalent circuit. For this purpose the ZView software package is employed which uses a non linear least square method to fit experimental data. The most common equivalent circiuts used to interprete the impedance data are described as follows.

The Nyquist plot obtained by Impedance Spectroscopy is varying along the range of potentials measured. Therefore, the circuit model in Figure 3.4 could be simplified in certain cases, reducing the number of parameters. In a first approach, $C_{co}$ and $R_{co}$ are suppressed in the model assuming an ohmic contact.[12]

At reverse bias and forward low potentials $TiO_2$ acts as an insulator (Figure 3.5(a)). Charge transfer takes place only between the back layer and the electrolyte in the working electrode. The charge transfer in the platinized counter-electrode and the FTO resistance are appreciable in the whole range of potentials.

At intermediate potentials, the whole transmission line circuit is required as $TiO_2$ contributes with its full resistance and $C_\mu$. Only electrolyte diffusion resistance remains negligible.

At high potentials, $E_{Fn}$ is close enough to the CB to yield a high electron concentration thus $TiO_2$ transport resistance becomes negligible. Here $R_{rec}$ is small enough to allow to distinguish the third arc corresponding to $R_d$.

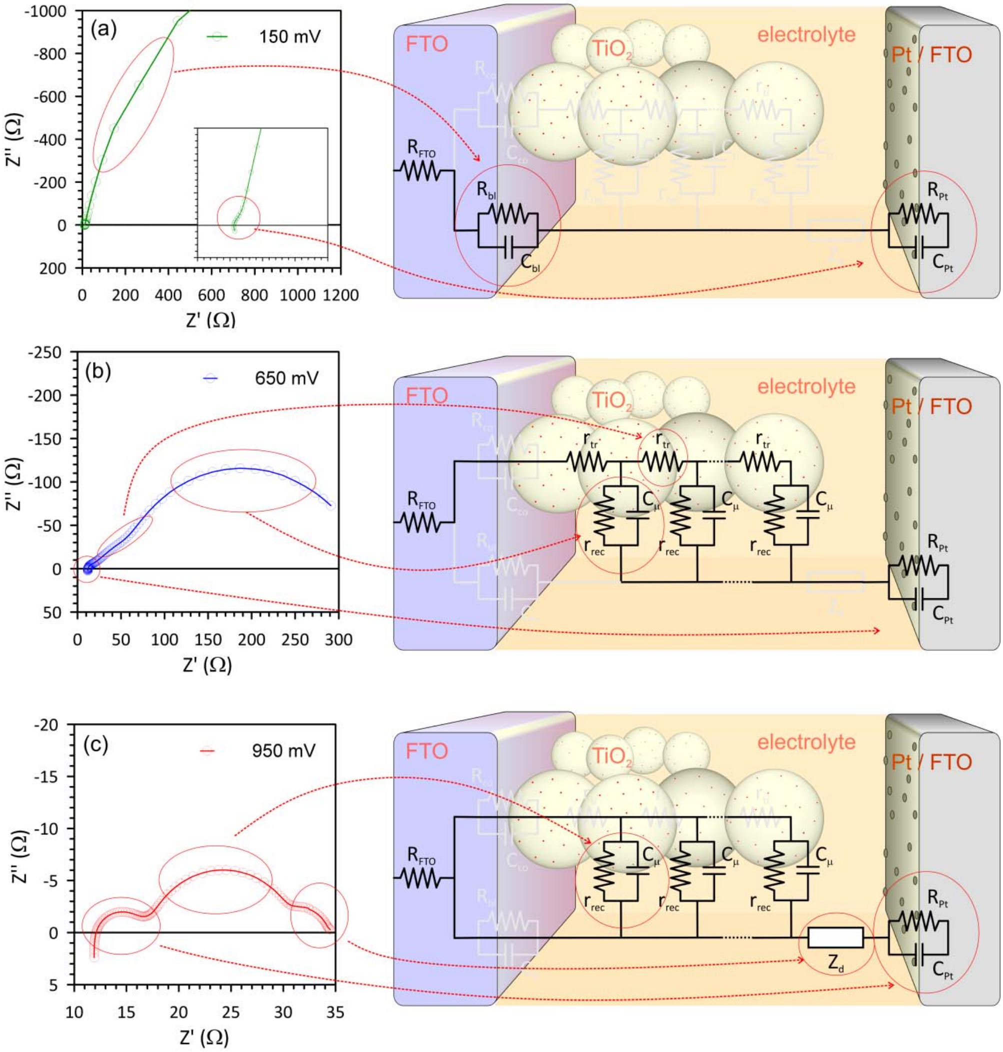

**Figure 3.5:** Experimental Nyquist plots of impedance spectra and their correspondent simplified equivalent circuit models. (a) Low potentials, (b) intermediate potentials and (c) high potentials.

It has to be pointed out that, in some cases, the characteristic frequency of the diffusion element presents a value very similar to that from the recombination arc. In such cases, the equivalent circuit for the fitting should connect the *Zd* element in series to the $R_{rec}$ and both elements in parallel to $C_{\mu}$. Otherwise, obtained $C_{\mu}$ would have lower values than the real ones, what may yield to confusion with a saturation of the chemical capacitance at high potentials, attributed to the Helmholtz capacitance of the electrolyte.

## 3.5 Voltage drop correction at $R_{series}$

Results of recombination resistance ($R_{rec}$) and chemical capacitance ($C_\mu$) obtained from the fitting of the Nyquist plots of the impedance spectra are represented after substracting the effect of the series resistances,

$$V_F = V_{app} - V_{series} \tag{3.12}$$

where $V_F$ is the voltage drop in the sensitized electrode, $V_{app}$ is the applied potential during the measurement and $V_{series}$ is the potential drop at the total series resistance.

$$V_{series} = \int_{j_{SC}}^{j} R_{series}\, dj \tag{3.13}$$

Main contributions to $R_{series}$ are given by [17]

$$R_{series} = R_{FTO} + R_{Pt} + R_d \tag{3.14}$$

The resulting corrected potential ($V_F$) corresponds to the real voltage difference in the photoanode. In further analysis of impedance data along this work the corrected voltage of the devices will be calculated as follows:

$$V_F = V_{app} + \frac{j}{j_{sc} - j} \int_{j_{SC}}^{j} R_{series}\, dj \tag{3.15}$$

## 3.6 Incident photon-to-current conversion efficiency (IPCE)

The incident photon-to-current conversion efficiency (IPCE) or external quantum efficiency (EQE) determines the ratio of generated carriers ($N_{electron}$) in the solar cell in relation to the number of incident photons ($N_{photons}$) as a function of wavelength.[18]

$$IPCE = \frac{N_{electron}}{N_{photon}} \tag{3.16}$$

from the general definition of electrical current, the number of generated electrons can be expressed as:

$$j_{gen} = N_{electron} \frac{q}{t} \tag{3.17}$$

the total number of photons can also be deduced from the energy (E) of incident light power:

$$P_{inc} = \frac{E}{t} = N_{photon} \frac{h\nu}{t} = N_{photon} \frac{h}{t} \frac{c}{\lambda} \tag{3.18}$$

where *h* is Planck's constant and the electromagnetic frequency *v* is expressed in terms of light speed (*c*) divided per the incident wavelength (*λ*). Combining equations (3.17) and (3.18) in (3.16), we obtain:

$$IPCE = \frac{j_{gen}}{P_{inc}} \frac{hc}{q} \frac{1}{\lambda} \tag{3.19}$$

We can then determine the photocurrent of the test device at any given incident photon flux *ϕ(λ)* by:

$$j_{sc} = \int q \, IPCE(\lambda) \, \phi(\lambda) \, d\lambda \tag{3.20}$$

For high performance DSC, the spectral response (IPCE) should match the spectral distribution of sunlight. In Figure 3.6, red curve represents a red dye (N719) that matches the solar spectra in the visible better than the dye YD20 does, N719-sensitized DSC gives higher photocurrent than YD20 DSC.

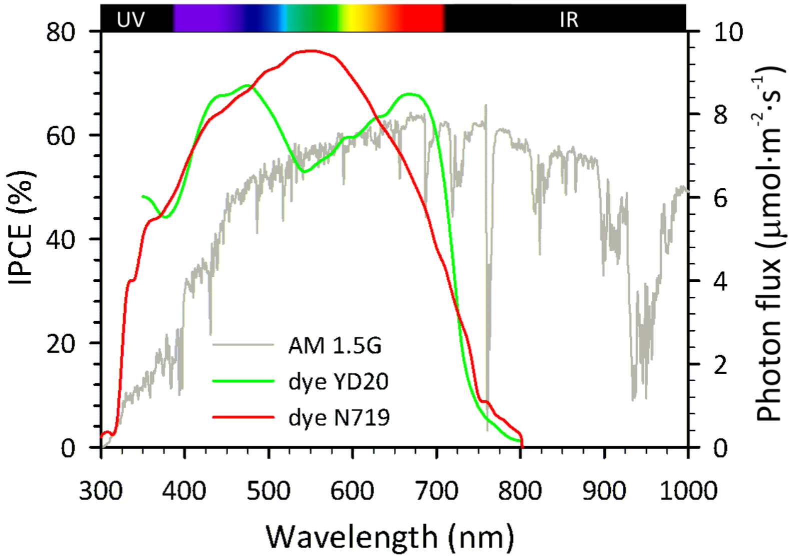

**Figure 3.6:** Incident photon to current conversion efficiency representation for a red-colored Ruthenium dye and green-colored porphyrin dye. The solar photon flux is represented at the back as a grey line.

## References

(1) Bisquert, J.; Fabregat-Santiago, F. Impedance spectroscopy: A general introduction and application to dye-sensitized solar cells In *Dye-sensitized Solar Cells*; Kalyanasundaram, K., Ed.; EPFL Press
CRC Press: Lausanne
Boca Raton, 2010.

(2) Prince, M. B. Silicon Solar Energy Converters. *Journal of Applied Physics* **1955**, *26*, 534-540.

(3) Simon M. Sze, K. K. N. *Physics of Semiconductor Devices* New York, 1981.

(4) Memming, R. Semiconductor Electrochemistry; Wiley-VCH: Weinheim, 2002; pp 155.

(5) Tomkiewicz, M. Impedance spectroscopy of rectifying semiconductor-electrolyte interfaces. *Electrochimica Acta* **1990**, *35*, 1631-1635.

(6) Kelly, J. J.; Memming, R. The Influence of Surface Recombination and Trapping on the Cathodic Photocurrent at p-Type III-V Electrodes. *Journal of The Electrochemical Society* **1982**, *129*, 730-738.

(7) Vanmaekelbergh, D. Direct and surface state mediated electron transfer at semiconductor/electrolyte junctions—II. A comparison of the interfacial admittance. *Electrochimica Acta* **1997**, *42*, 1135-1141.

(8) Zaban, A.; Meier, A.; Gregg, B. A. Electric Potential Distribution and Short-Range Screening in Nanoporous TiO2 Electrodes. *The Journal of Physical Chemistry B* **1997**, *101*, 7985-7990.

(9) van de Lagemaat, J.; Park, N. G.; Frank, A. J. Influence of Electrical Potential Distribution, Charge Transport, and Recombination on the Photopotential and Photocurrent Conversion Efficiency of Dye-Sensitized Nanocrystalline TiO2 Solar Cells: A Study by Electrical Impedance and Optical Modulation Techniques. *The Journal of Physical Chemistry B* **2000**, *104*, 2044-2052.

(10) Albery, W. J.; Elliott, C. M.; Mount, A. R. A transmission line model for modified electrodes and thin layer cells. *Journal of Electroanalytical Chemistry and Interfacial Electrochemistry* **1990**, *288*, 15-34.

(11) Fabregat-Santiago, F.; Bisquert, J.; Garcia-Belmonte, G.; Boschloo, G.; Hagfeldt, A. Influence of electrolyte in transport and recombination in dye-sensitized solar cells studied by impedance spectroscopy. *Solar Energy Materials and Solar Cells* **2005**, *87*, 117-131.

(12) Fabregat-Santiago, F.; Bisquert, J.; Palomares, E.; Otero, L.; Kuang, D.; Zakeeruddin, S. M.; Grätzel, M. Correlation between Photovoltaic Performance and Impedance Spectroscopy of Dye-Sensitized Solar Cells Based on Ionic Liquids. *The Journal of Physical Chemistry C* **2007**, *111*, 6550-6560.

(13) Fabregat-Santiago, F.; Garcia-Belmonte, G.; Mora-Sero, I.; Bisquert, J. Characterization of nanostructured hybrid and organic solar cells by impedance spectroscopy. *Physical Chemistry Chemical Physics* **2011**, *13*, 9083-9118.

(14) Bisquert, J.; Garcia-Belmonte, G.; Fabregat-Santiago, F.; Ferriols, N. S.; Bogdanoff, P.; Pereira, E. C. Doubling Exponent Models for the Analysis of Porous Film Electrodes by Impedance. Relaxation of TiO2 Nanoporous in Aqueous Solution. *The Journal of Physical Chemistry B* **2000**, *104*, 2287-2298.

(15) Wang, Q.; Ito, S.; Grätzel, M.; Fabregat-Santiago, F.; Mora-Seró, I.; Bisquert, J.; Bessho, T.; Imai, H. Characteristics of High Efficiency Dye-Sensitized Solar Cells†. *The Journal of Physical Chemistry B* **2006**, *110*, 25210-25221.

(16) Fabregat-Santiago, F.; Garcia-Belmonte, G.; Bisquert, J.; Zaban, A.; Salvador, P. Decoupling of Transport, Charge Storage, and Interfacial Charge Transfer in the Nanocrystalline TiO2/Electrolyte System by Impedance Methods. *The Journal of Physical Chemistry B* **2001**, *106*, 334-339.

(17) Fabregat-Santiago, F.; Bisquert, J.; Palomares, E.; Otero, L.; Kuang, D.; Zakeeruddin, S. M.; Grätzel, M. Correlation between Photovoltaic Performance and Impedance Spectroscopy of Dye-Sensitized Solar Cells Based on Ionic Liquids. *J. Phys. Chem. C* **2007**, *111*, 6550-6560.

(18) Kamat, P. V. http://www.nd.edu/~pkamat/pdf/ipce.pdf.

# Chapter 4

## Origin of open circuit voltage in DSC

The results on this chapter are published in:

- Raga, S. R.; Barea, E. M.; Fabregat-Santiago, F. Analysis of the Origin of Open Circuit Voltage in Dye Solar Cells. *The Journal of Physical Chemistry Letters* **2012**, *3*, 1629-1634.
- Ripolles-Sanchis, T.; Guo, B.-C.; Wu, H.-P.; Pan, T.-Y.; Lee, H.-W.; Raga, S. R.; Fabregat-Santiago, F.; Bisquert, J.; Yeh, C.-Y.; Diau, E. W.-G. Design and characterization of alkoxy-wrapped push-pull porphyrins for dye-sensitized solar cells. *Chem. Commun.* **2012**, *48*, 4368-4370.

## 4.1 Introduction

As seen in section 3.2, the parameters governing the efficiency in a DSC are the photocurrent, photovoltage and fill factor. Nowadays, the only way to improve $j_{sc}$ is developing new dyes absorbing in the IR region or with optical collectors/ concentrators situated externally to the device. *FF* has been also maximized by reducing the $R_{series}$. Therefore the major part of possible improvements for enhancing device performances come through the $V_{oc}$ enhancement.

The open circuit voltage ($V_{oc}$) in a dye solar cell is given by the energetic difference between the Fermi level of electrons ($E_{Fn}$) and the Fermi level of holes ($E_{Fp}$), which coincides with the redox energy level ($E_{redox}$) of the electrolyte, see Figure 4.1. In dark and equilibrium conditions, the Fermi level of electrons (now $E_{F0}$) also matches with the redox $E_{redox}$ so in DSC we may define $E_{F0} = E_{redox} = E_{Fp}$ and the potential in the film $V_F = (E_{Fn} - E_{F0})/q$.

The maximum $V_{oc}$ value is theoretically limited by the gap of the dye molecule, which is around 1.60 eV for common sensitizers.[1,2] The actual value of photovoltage in DSC lie around 0.7V and rarely exceeds 0.9V. Primary voltage losses are originated in one side due to energy mismatches between the $E_{redox}$ and HOMO level of the dye and in the other side by the lower energy level of $TiO_2$ CB ($E_c$) in respect to the LUMO of the dye. In addition, the density of localized states (DOS) under the CB together with the electron recombination flux in the semiconductor originates further lowering in the $E_{Fn}$ value. The maximum attainable voltage is then reduced to: [3,4]

$$V_{oc} = \left(E_{Fn} - E_{redox}\right)/q \qquad (4.1)$$

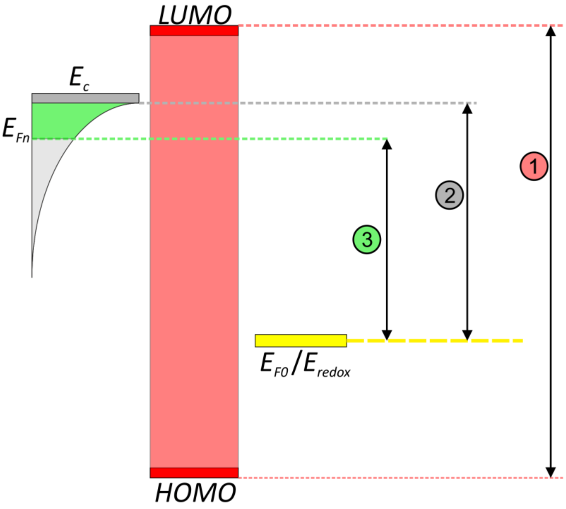

**Figure 4.1:** Energetic levels of the TiO2, dye molecules and redox of the electrolyte. The numbers indicate the different possible $V_{oc}$ attainable in a DSC. (1) Theoretical maximum $V_{oc}$, given by the gap of the absorber, (2) Maximum possible $V_{oc}$ attainable is conditioned by the position of the bottom of the $TiO_2$ nanocrystal CB. (3) real $V_{oc}$ depends on both the recombination rate and the DOS distribution.

In contrast, energetic level mismatches are fundamental to ensure electron or hole injection from the dye to the electron/hole acceptors in order to separate the photogenerated charge. The downwards shift of $E_c$ in the semiconductor leads to an enhancement of the electron injection efficiency from the dye to the $TiO_2$. The higher the distance between LUMO level of the excited dye and the CB of $TiO_2$ the more favorable the charge transfer. [5-7]

The purpose of this chapter is to analyze the origin open circuit voltage of the DSC by means of impedance spectroscopy technique, evaluating separately the effect of recombination losses and $E_c$ position. Starting from a theoretical model it will be corroborated by measuring samples with different electrolytes and controlled properties. Finally extend the application of this technique to the analysis of devices where the molecular structure of the dye is varied.

## 4.2 Theory background

### Recombination resistance

Charge recombination is a parameter directly related with photovoltage as given by the equation[8]

$$R_{rec} = \left( \frac{\partial j_{rec}}{\partial V_F} \right)^{-1} \tag{4.2}$$

where $j_{rec}$ is the current for charge losses produced by recombination. In many cases, it has been found that

$$R_{rec} \approx R_0 \exp\left[ -\beta q V_F / k_B T \right] \tag{4.3}$$

with $R_0$ a parameter that determines the activation of recombination given by[8,9]

$$R_0 = \frac{\sqrt{\pi \lambda k_B T}}{q^2 L \alpha k_r c_{ox} N_s} \exp\left[ \alpha \frac{E_C - E_{redox}}{k_B T} + \frac{\lambda}{4 k_B T} \right] \tag{4.4}$$

$\alpha$ a parameter describing the distribution of surface states from where the recombination takes place, $c_{ox}$, the concentration of acceptor species (here $I_3^-$) in the electrolyte, $\lambda$ the reorganization energy of acceptor species, $N_s$ the total number of states contributing to the recombination and $k_r$ a time constant accounting for recombination rate. $R_0$ can be extracted from the linear regression of Eq. (4.2) with experimental data. This fact together with Eq. (4.1) from section 3 yields to:[8,10]

$$j = j_{sc} + j_0 - \frac{k_B T}{\beta q} \frac{1}{R_{rec}} \tag{4.5}$$

being $j_0 = k_B T / \beta q R_0$ a constant equivalent to reverse bias dark current in p-n junction diodes and solar cells. Eq. (4.5) together with Eq. (4.3) at open circuit conditions ($j = 0$) yield to

$$V_{oc} = \frac{k_B T}{\beta q} \ln \frac{\beta q R_0 j_{SC}}{k_B T} \tag{4.6}$$

This expression is very similar to others generally used in the literature but using direct experimental parameters obtained from IS.[9]

**CB dependence**

A quick look to Eq. (4.6) allows concluding that, if analyzing samples with similar $\beta$ the changes in the value of $j_{sc}$ only may produce small modifications in $V_{oc}$, the main element determining the differences in $V_{oc}$ is the prefactor, $R_0$, of the recombination resistance.

To complete this analysis it is needed to know the origin of the observed differences in $R_{rec}$. Eq. (4.4) shows the dependence of $R_0$ (and then $V_{oc}$) in both the energy difference $E_c - E_{redox}$ and the rate $k_r$, at which the electrons in $TiO_2$ are lost. Quantification of the contribution of each of these effects to the voltage is feasible with data obtained from impedance spectroscopy: First it is needed to have an estimation of the position of the conduction band, or at least of the CB shift ($\Delta E_c$). Then, using the definition of the voltage at the equivalent conduction band position[8]

$$V_{ecb} = V_F - \Delta E_c / q, \tag{4.7}$$

it is possible to compare all the samples at a voltage in which the $TiO_2$ contains the same electron concentration. Comparison of recombination resistance at $V_{ecb}$ provides direct information of the contribution to the photovoltage of the differences in recombination rate

**Chemical capacitance**

The chemical capacitance, $C_\mu$, provides quantitative information about the position of the conduction band. As [11]

$$C_\mu = C_0 \exp\left[\frac{\alpha q}{k_B T} V_F\right], \tag{4.8}$$

with

$$C_0 = L(1-p)\alpha \frac{q^2 N_t}{k_B T} \exp\left[(E_{redox} - E_c)\frac{\alpha}{k_B T}\right], \tag{4.9}$$

where $N_t$ is the total number of trap states below the conduction band of the $TiO_2$, and $p$ the porosity of the film. $N_t$ is an intrinsic property of $TiO_2$ that may be affected by the synthesis method of the nanoparticles, the electrolyte composition or the adsorbed molecules. At this stage we can only use estimations from previous papers, $N_t = 2.5\cdot10^{19}$ cm$^{-3}$,[12] and we assume minimal variations of this value. Shifts in the capacitance data obtained from IS are equivalent to shifts in $E_c$, whenever the samples contain the same semiconductor material. Here the analysis of experimental $C_\mu$ and Eq. (4.9) was used to calculate the $\Delta E_c$.

## 4.3 Electrolyte additives

The use of different additives such anionic and cationic molecules dissolved in the electrolyte allows to modify conduction band position or rate of charge transfer in a controlled manner as their interaction with the semiconductor surface produces well known effects.

Thus, the position of the conduction band edge ($E_c$) is affected by protonation or deprotonation of the nanoparticles, producing an increase or decrease of the $V_{oc}$.[13-15] On the other side, specific additives as big molecules may cover the surface of $TiO_2$ uncoated by dye thus reducing the recombination of electrons with $I_3^-$ in the electrolyte.[15]

In this work, four different electrolytes have been tested with different compositions of additives and solvents. The effect of each component is described in Section 2.2.4 and the composition of all electrolytes is indicated in Table 4.1.

| Name | BMII | $I_2$ | GuSCN | LiI | tBP | Solvent |
|---|---|---|---|---|---|---|
| **A** | 0.6 M | 0.03 M | 0.1 M |  | 0.5 M | A/V (85:15) |
| **B** |  | 0.05 M |  | 0.5 M | 0.5 M | MPN |
| **C** |  | 0.05 M |  | 0.5 M |  | MPN |
| **D** | 0.6 M | 0.03 M | 0.1 M |  | 0.5 M | MPN |

**Table 4.1:** Composition of electrolytes employed in the fabrication of DSCs. The solvents denominations are MPN for methoxypropionitrile, and A/V for a mixture of acetonitrile and valeronitrile 85:15 in volume.

The solar cell parameters obtained for DSC with four different electrolytes under 1sun illumination intensity are depicted in Table 4.2 and *j*-*V* curves of these cells are presented in Figure 4.2.

| Name | $V_{oc}$ (V) | $J_{sc}$ (mA/cm$^2$) | FF | η (%) |
|---|---|---|---|---|
| **Cell A** | 0.716 | 12.92 | 0.67 | 6.19 |
| **Cell B** | 0.650 | 16.91 | 0.53 | 5.95 |
| **Cell C** | 0.462 | 18.30 | 0.44 | 3.70 |
| **Cell D** | 0.758 | 11.00 | 0.63 | 5.22 |

**Table 4.2:** Photovoltaic performance of the DSCs containing different electrolyte composition.

Dye solar cells prepared with electrolytes A and D present similar open circuit voltage. These electrolytes only differ on the solvent, while use the same additives and concentrations. This fact suggests that the nature of both solvents has little effect on the photovoltage. For cells B and C the $V_{oc}$ is much lower. These cells contain lithium iodide in the electrolyte and neither contain ionic liquid nor GuSCN. Cell C presents a more pronounced decrease, this sample does not contain 4-*tert*-butylpyridine. On the other side, cells B and C provide higher photocurrent than cells A and D.

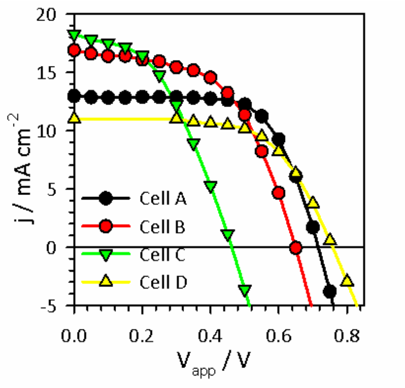

**Figure 4.2:** *j-V* curves of the DSCs with different electrolytes as described in Table 4.1 (lines) and obtained from IS measurements (symbols). The open circuit voltages differ significantly with the additives contained in the electrolyte.

In this first view of *j-V* curves results, the origin of the photovoltage variation found is not conclusive, as the additives of the electrolytes are expected to affect both the CB energy level and recombination rates.

Results of recombination resistance ($R_{rec}$) and chemical capacitance ($C_\mu$) obtained from the fitting of the Nyquist plots of the impedance spectra are plotted in Figure 4.3. These values are represented after subtracting the effect of the series resistance on the voltage (see section 3.3).

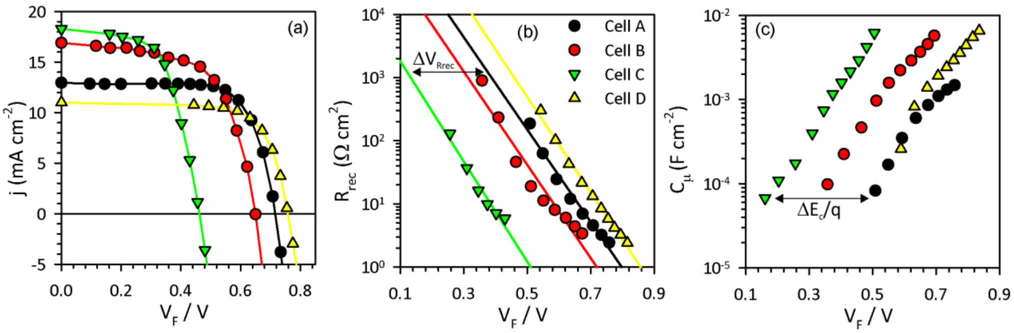

**Figure 4.3:** *j-V*$_F$ curves (a) and impedance results of the cells with different electrolytes. (b) Recombination resistance between the semiconductor and the acceptor species in the electrolyte. (c) Chemical capacitance of the $TiO_2$. Voltage drop due to internal series resistance has been corrected in all plots. $\Delta V_{rec}$ and $\Delta E_c/q$ between samples A and C are represented in panels a and b, respectively.

The first clear result observed in Figure 4.3(b) is the strong correlation between $V_{oc}$ and $R_{rec}$. Using cell A as a reference, the voltage differences found in the $V_{oc}$ of the samples analyzed match very well with the shift in $R_{rec}$ ($\Delta V_{Rrec}$ ) observed in Figure 4.3(b). This indicates that $R_{rec}$ is the parameter that dominates photovoltage, despite the differences in $j_{sc}$.

$\beta$ and $R_0$ parameters in Eq. (4.2) are calculated from the linear regression of the $R_{rec}$ plots in Figure 4.3(b). Once the photocurrent is known, Eq. (4.5) allows calculating $V_{oc}$ exclusively from recombination parameters. As may be seen in Table 4.3, calculation of photovoltage using Eq. (4.5) with the values of $R_0$ and $\beta$ fit well (within 10mV error) with the values obtained from the *j*-*V* curve.

| Parameters | Cell A | Cell B | Cell C | Cell D |
|---|---|---|---|---|
| **Average $R_{series}$ (Ω)** | 15.1 | 15.8 | 22.3 | 27.3 |
| **$R_0$ (Ω cm$^2$)** | $6.82 \cdot 10^5$ | $2.05 \cdot 10^5$ | $1.13 \cdot 10^4$ | $2.87 \cdot 10^6$ |
| **$\beta$** | 0.439 | 0.443 | 0.477 | 0.452 |
| **$\alpha$** | 0.282 | 0.308 | 0.349 | 0.259 |
| **Calculated $V_{oc}$ (V)** | 0.712 | 0.651 | 0.454 | 0.768 |
| **Experimental $V_{oc}$ (V)** | 0.716 | 0.650 | 0.462 | 0.758 |
| **$E_c$-$E_{redox}$ (eV)** | 0.976 | 0.801 | 0.618 | 0.936 |
| **$\Delta E_c/q$ vs. ref (mV)** | Ref. | -180 | -330 | -50 |
| **$\Delta V_k$ (mV)** | Ref. | +114 | +78 | +96 |
| **$\Delta V_{Rrec}$ (mV)** | Ref. | -66 | -252 | +44 |

**Table 4.3:** Photovoltaic parameters obtained from IS analysis: $R_{series}$ represents the series resistance of the cell; $R_0$ is the recombination prefactor parameter from Eq. (4.3); $\beta$ is the charge transfer coefficient for recombination of electrons; *calculated* $V_{oc}$ is the open circuit voltage obtained from Eq. (4.5) at T=305 K; $\alpha$ is the exponential electron trap distribution parameter; $E_c$-$E_{redox}$ the value estimated from Eq. (4.8), $p$ = 0.5 and $L$ = 7 µm; $\Delta E_c/q$ *vs. ref* is the shift in the conduction band of $TiO_2$. A negative value imply a downwards shift of the conduction band. It is the energy shift needed to compare all the cells at the same conduction band level obtained after displacing the capacitances in Figure 4.3(b); $\Delta V_k$ is the voltage difference in $R_{rec}$ due to the differences in recombination rates; $\Delta V_{Rrec}$ is the sum of $\Delta E_c$ *vs. ref.* and $\Delta V_k$.

The data in Table 4.3 and Figure 4.3(c) show the different displacement of the CB towards lower energies for samples B, C and D respect the sample A. The small difference found for samples A and D indicates that the change in solvent has a minor role in changing the CB. In addition, according to expectations, for sample B the use of LiI instead of BMII and GuSCN results in a large downwards shift in CB which is even greater for sample with electrolyte C in which tBP is not present. Even so, real difference in $R_{rec}$ are still not discernible in Figure 4.3(b).

When plotting at the equivalent conduction band position, Figure 4.4(a) and (b), $V_{oc}$ and $R_{rec}$ displacements match well. As this representation of $R_{rec}$ is free from the effect of CB shifts, this plot allows computing the effect of the differences in recombination rate on the $V_{oc}$ of the different cells taking into account only the values at potentials near $V_{oc}$, see $\Delta V_k$ in Table 4.3. In other words, it is possible to calculate the rate constant contribution to the photovoltage, despite the fact that absolute values of $k_r$ could not be estimated and the value of $N_s$ is not known (Eq. (4.4)). The values obtained for $\Delta V_k$ fit well with the expected effect of the electrolytes in the properties of the cells as described in the following analysis.[10,12-14]

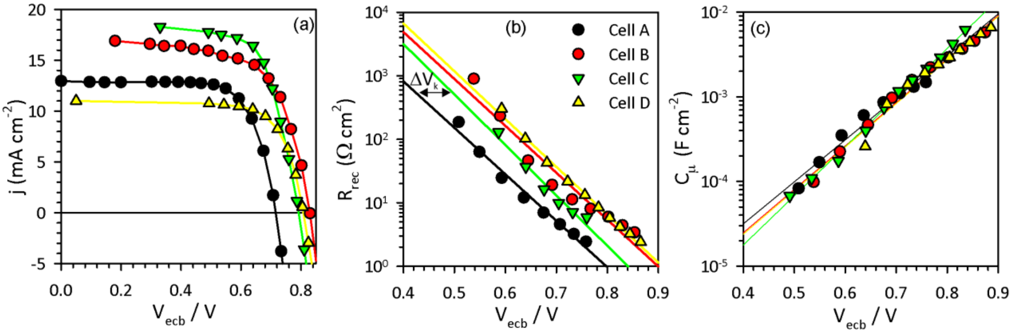

**Figure 4.4:** Values of *j-V* curves (a), recombination resistance (b) and chemical capacitance (c) represented at the equivalent CB position taking *Cell A* as a reference.

After comparing the samples with the same solvent in Figure 4.4(a), it is found that Cell C presents the lower internal $R_{rec}$ (and lower $\Delta V_k$) of the three. The fact that this electrolyte has no surface blocking additives confirm this result, yielding to a larger $k_r$ and smaller $R_0$. In the case of the sample with electrolyte B, the addition of tBP displaces the $V_{oc}$ 18 mV upward. The extra addition of BMII and GuSCN in electrolyte D adds another 20 mV to the photovoltage with respect to sample B.

Focusing into samples A and D with the same additives but different solvents it is observed that cell A presents a higher internal recombination ($k_r$) that diminishes the displaced $V_{oc}$ in 96 mV with regard to cell D. This result suggests that the passivation of the surface of $TiO_2$ with GuSCN and tBP is more efficient in the MPN-based electrolyte.

Finally, small contributions from the $j_{sc}$ may fulfill the small differences between $\Delta V_{Rrec}$ and the real $V_{oc}$ shifts from Figure 4.2, as indicates Eq. (4.5). For a given $R_{rec}$, the larger photocurrent pushes upwards the *j-V* curve yielding to an increase in $V_{oc}$ even the shifts are of only a few mV.[16]

## 4.4 Application: dye structures

Over the last years, lot of research for the DSC improvement has been focused in the development of novel sensitizers. Commonly, these variations consist in small variations of the main structure as the substitution of functional groups. These changes focuses in the enhancement of light harvesting and to improve the molecule anchoring on $TiO_2$ surface. However, parallel effects on the recombination rate of the cell may be observed. In this section the IS method developed above will be employed in the analysis of DSC with three different porphyrin dyes with unknown effect on $V_{oc}$.

In the present study, three porphyrin sensitizers were designed based on the structure of YD2-o-C8, the dye employed in DSC with 12.3% record (see Figure 4.5).[17] The modifications were focused in an extended $\pi$-conjugation in order to enhance the light-harvesting ability. Basically all of them have the same *ortho*-substituted porphyrin core with two phenylethynyl (PE) groups acting as a $\pi$-bridge in the *meso*-position of the ring. YD20 and YD22 dyes have the acceptor group (ethynylbenzoic acid) the same as that of YD2-o-C8 but with different donor groups: YD20 has a triphenylamino group with two methoxyl substitutes and YD22 has a phenylamino group with two n-butyl chains. On the other hand, YD20 and YD21 dyes have the same donor group but the cyanoacrylic acid was used as an anchoring group in YD21.

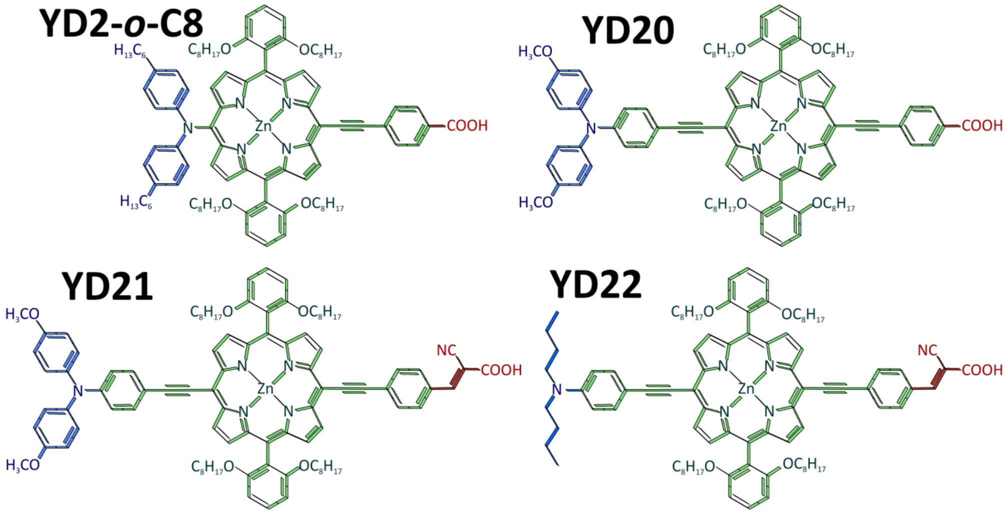

**Figure 4.5:** Molecular structures for YD2-*o*-C8 and the derivatives YD20-YD22 porphyrin dyes. The different functional groups are colored. The donor group (blue) is attached to the porphyrin core with two PE groups (green) acting as a π-bridge. The acceptor group (red) is the responsible of the chemical adsorption on the $TiO_2$.

*j-V* curves of DSC with three different dyes under 1sun illumination intensity are presented in Figure 4.6. Table 4.4 shows the photovoltaic parameters and the amounts of dye loading.

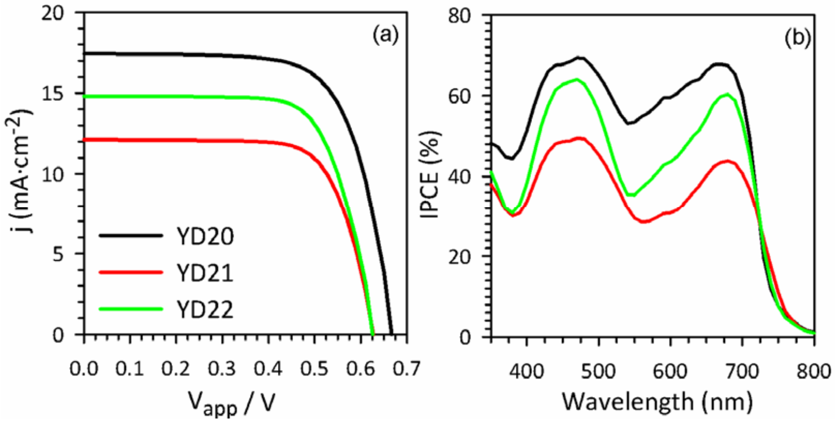

**Figure 4.6:** (a) j-V characteristics of DSC devices prepared with the porphyrin dyes with an active layer of 0.16 $cm^2$, (b) the corresponding action spectra for the efficiency of incident photon-to-current conversion efficiency (IPCE).

| | Dye loading (nmol/cm$^2$) | $V_{oc}$ (V) | $J_{sc}$ (mA/cm$^2$) | *FF* | $\eta$ (%) |
|---|---|---|---|---|---|
| **YD20** | 161 | 0.676 | 17.43 | 0.69 | 8.1 |
| **YD21** | 132 | 0.631 | 12.05 | 0.72 | 5.5 |
| **YD22** | 134 | 0.634 | 14.87 | 0.70 | 6.6 |

**Table 4.4:** Photovoltaic performance of porphyrin-based DSC.

The photocurrent obtained in *j-V* curves matches with the IPCE measurement (Figure 4.6(b)). In turn, dye YD20 present the highest $j_{sc}$, in agreement with the higher amount of loaded dye. However, YD21 presents a larger decrease in photocurrent despite the amount of dye loading in the cell is the same as for YD22. In contrast, the $V_{oc}$ is almost the same for DSC with dyes YD21 and YD22 and lower than that of YD20.

From the fitting of the impedance spectra for the three DSC, $R_{rec}$ and $C_\mu$ have been obtained, represented in Figure 4.7. All parameters obtained from the analysis of the IS data are detailed in Table 4.5.

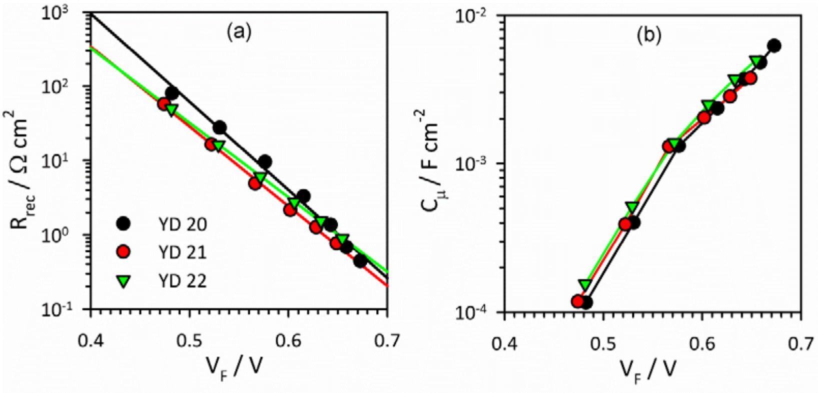

**Figure 4.7:** Impedance results of the cells with different porphyrin dyes. (a) Recombination resistance between the semiconductor and the acceptor species in the electrolyte. (b) Chemical capacitance of the $TiO_2$.

In a first view of Figure 4.7 it is observed a less significant dependence of recombination rate and CB position by varying the dye structure in a DSC rather than the electrolyte composition. Even the small shifts observed in these plots it would be possible to distinguish slight differences between dyes. From Figure 4.7(b), the relative position of the conduction band edge of $TiO_2$ ($\Delta E_c/q$) may be estimated in the same manner it was performed in the previous section. Through these calculations, it was estimated an $E_c$ displacement for YD21 of +4 mV and YD22 -10 mV with respect to YD20, indicating that all the $TiO_2$ conduction bands remain almost unchanged for the three dyes.

| Parameters | YD20 | YD21 | YD22 |
|---|---|---|---|
| **Average $R_{series}$ (Ω)** | 14.5 | 15.7 | 16.8 |
| **$R_0$ (Ω cm$^2$)** | $3.3\cdot10^8$ | $4.2\cdot10^7$ | $2.1\cdot10^7$ |
| $\beta$ | 0.713 | 0.645 | 0.603 |
| $\alpha$ | 0.534 | 0.518 | 0.524 |

| Parameters | YD20 | YD21 | YD22 |
|---|---|---|---|
| **Calculated $V_{oc}$ (V)** | 0.691 | 0.662 | 0.684 |
| **Experimental $V_{oc}$ (V)** | 0.676 | 0.631 | 0.634 |
| **$E_c$-$E_{redox}$ (eV)** | 0.790 | 0.789 | 0.781 |
| **$\Delta E_c/q$ vs. ref (mV)** | Ref. | +4 | -10 |
| **$\Delta V_k$ (mV)** | Ref. | -33 | -9 |
| **$\Delta V_{Rrec}$ (mV)** | Ref. | -29 | -19 |

**Table 4.5:** Photovoltaic parameters obtained from IS analysis for the DSC containing different dyes. These parameters have been calculated in the same manner than those from Table 4.3, here $L$= 15 µm. $\Delta V_k$ is the voltage difference in $R_{rec}$ due to the differences in recombination rates; $\Delta V_{Rrec}$ is the sum of $\Delta E_c$ *vs. ref.* and $\Delta V_k$.

To understand the origin of the small differences in the $V_{oc}$ found for the three different dyes it is needed to analyze the behavior of the recombination resistance in Figure 4.7(a). The results here match very well with the analysis in section 4.3: as it can be seen in Figure 4.7(a), YD20 has the larger recombination resistance and $V_{oc}$, whereas YD21 and YD22 have similar values of $R_{rec}$ showing almost the same $V_{oc}$. In addition, the small differences found for the position of the conduction band edge ($E_c$) may also help to fine tune the roles of the linker in these Zn–porphyrin dyes. Taking as a reference YD20, $E_c$ was leveled for all samples.

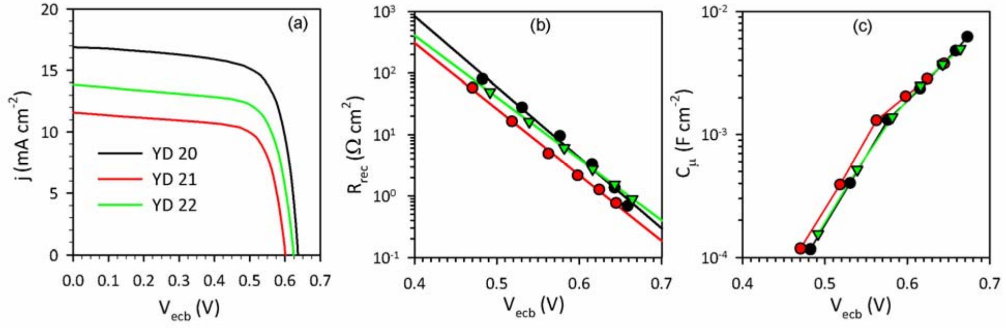

**Figure 4.8:** Values of *j-V* curves extracted from IS data (a), recombination resistance (b) and chemical capacitance (c) represented at the equivalent CB position taking *YD20* as a reference.

In Figure 4.8(b), the recombination resistance of the YD21 device is smaller compared to that of the YD20 and YD22 devices. In other words, charge recombination is a major problem for the poor performance of the YD21 device. These results allow us to make a conclusion: compared to the YD20 device, the smaller $V_{oc}$ of YD22 was due to a small shift in conduction band but the smaller $V_{oc}$ of YD21 was due to a significant charge recombination, see $\Delta V_k$ in Table 4.5. From the structural viewpoint, the use of cyanoacrylic acid as an acceptor and an anchoring group in YD21 might provide more free space (less amount of dye-loading) for the charge recombination than the use of the rigid ethynylbenzoic acid in YD20 and YD22. Moreover, YD21 might be tilted on the surface of $TiO_2$ for the charge recombination to occur more easily.

## 4.5 Conclusions

It has been shown that photovoltage in solar cells can be exclusively described in terms of short circuit photocurrent and recombination resistance. The method proposed here for the analysis of the data allowed evaluating the influence of conduction band shifts, recombination rate changes and short circuit photocurrent in the photovoltage.

The procedure has been subsequently applied in the analysis of other DSC where the dye structure effects was tested. Successfully, lower $V_{oc}$ was found to be caused by an increase of recombination for the dye YD21 may be due to higher area of non covered $TiO_2$ surface.

# References

(1) Grätzel, M. Recent Advances in Sensitized Mesoscopic Solar Cells. *Accounts of Chemical Research* **2009**, *42*, 1788-1798.

(2) Bisquert, J. Dilemmas of Dye-Sensitized Solar Cells. *ChemPhysChem* **2011**, *12*, 1633-1636.

(3) Boschloo, G.; Hagfeldt, A. Characteristics of the Iodide/Triiodide Redox Mediator in Dye-Sensitized Solar Cells. *Accounts of Chemical Research* **2009**, *42*, 1819-1826.

(4) Barea, E. M.; Ortiz, J.; Paya, F. J.; Fernandez-Lazaro, F.; Fabregat-Santiago, F.; Sastre-Santos, A.; Bisquert, J. Energetic factors governing injection, regeneration and recombination in dye solar cells with phthalocyanine sensitizers. *Energy & Environmental Science* **2010**, *3*, 1985-1994.

(5) Liu, Y.; Hagfeldt, A.; Xiao, X.-R.; Lindquist, S.-E. Investigation of influence of redox species on the interfacial energetics of a dye sensitized nanoporous $TiO_2$ solar cell. *Solar Energy Materials and Solar Cells* **1998**, *55*, 267-281.

(6) van de Lagemaat, J.; Park, N.-G.; Frank, A. J. Influence of Electrical Potential Distribution, Charge Transport, and Recombination on the Photopotential and Photocurrent Conversion Efficiency of Dye-Sensitized Nanocrystalline TiO2 Solar Cells: A Study by Electrical Impedance and Optical Modulation Techniques. *The Journal of Physical Chemistry B* **2000**, *104*, 2044-2052.

(7) Fabregat-Santiago, F.; Bisquert, J.; Garcia-Belmonte, G.; Boschloo, G.; Hagfeldt, A. Impedance spectroscopy study of the influence of electrolyte conditions in parameters of transport and recombination in dye-sensitized solar cells. *Solar Energy Materials and Solar Cells* **2005**, *87*, 117-131.

(8) Fabregat-Santiago, F.; Garcia-Belmonte, G.; Mora-Sero, I.; Bisquert, J. Characterization of nanostructured hybrid and organic solar cells by impedance spectroscopy. *Physical Chemistry Chemical Physics* **2011**, *13*, 9083–9118.

(9) Bisquert, J.; Fabregat-Santiago, F. Impedance spectroscopy: A general introduction and application to dye-sensitized solar cells In *Dye-sensitized Solar Cells*; Kalyanasundaram, K., Ed.; EPFL Press

CRC Press: Lausanne

Boca Raton, 2010.

(10) Sze, S. M. *Physics of Semiconductor Devices*, 2nd ed.; John Wiley and Sons: New York, 1981.

(11) Bisquert, J. Chemical capacitance of nanostructured semiconductors: its origin and significance for heterogeneous solar cells. *Physical Chemistry Chemical Physics* **2003**, *5*, 5360.

(12) Fabregat-Santiago, F.; Mora-Seró, I.; Garcia-Belmonte, G.; Bisquert, J. Cyclic Voltammetry Studies of Nanoporous Semiconductors. Capacitive and Reactive Properties of Nanocrystalline $TiO_2$ Electrodes in Aqueous Electrolyte. *The Journal of Physical Chemistry B* **2002**, *107*, 758-768.

(13) Haque, S. A.; Palomares, E.; Cho, B. M.; Green, A. N. M.; Hirata, N.; Klug, D. R.; Durrant, J. R. Charge Separation versus Recombination in Dye-Sensitized Nanocrystalline Solar Cells: the Minimization of Kinetic Redundancy. *Journal of the American Chemical Society* **2005**, *127*, 3456-3462.

(14) Zhang, Z.; Zakeeruddin, S. M.; O'Regan, B. C.; Humphry-Baker, R.; Grätzel, M. Influence of 4-Guanidinobutyric Acid as Coadsorbent in Reducing Recombination in Dye-Sensitized Solar Cells. *The Journal of Physical Chemistry B* **2005**, *109*, 21818-21824.

(15) Kopidakis, N.; Neale, N. R.; Frank, A. J. Effect of an Adsorbent on Recombination and Band-Edge Movement in Dye-Sensitized TiO2 Solar Cells: Evidence for Surface Passivation. *The Journal of Physical Chemistry B* **2006**, *110*, 12485-12489.

(16) Barea, E. M.; Zafer, C.; Gultekin, B.; Aydin, B.; Koyuncu, S.; Icli, S.; Fabregat-Santiago, F.; Bisquert, J. Quantification of the Effects of Recombination and Injection in the Performance of Dye-Sensitized Solar Cells Based on N-Substituted Carbazole Dyes. *The Journal of Physical Chemistry C* **2010**, *114*, 19840-19848.

(17) Yella, A.; Lee, H.-W.; Tsao, H. N.; Yi, C.; Chandiran, A. K.; Nazeeruddin, M. K.; Diau, E. W.-G.; Yeh, C.-Y.; Zakeeruddin, S. M.; Grätzel, M. Porphyrin-Sensitized Solar Cells with Cobalt (II/III)–Based Redox Electrolyte Exceed 12 Percent Efficiency. *Science* **2011**, *334*, 629-634.

# Chapter 5

## Temperature effects in DSC

The results on this chapter are published in:

- Sonia R. Raga, Francisco Fabregat-Santiago. Temperature effects in dye-sensitized solar cells. *Physical Chemistry Chemical Physics* **2013**, *15*, 2328-2336.

# 5.1 Introduction

Dye sensitized solar cells have been introduced as a low-cost technology for complementing the existing photovoltaic devices. Unless their efficiency is relatively lower than other devices in standard conditions (see Section 1.1), DSC present several advantages in real operating conditions:

By one side, their efficiency under diffuse light or under a wide range of incident angles remains high, making this technology suitable for indoor applications, cloudy places and high light incidence angle installations, as facades.[1-4] This is thanks to the high internal area of the nanoporous film and high scattering ability of the $TiO_2$ nanoparticles.

On the other side, DSC does not present a dramatical efficiency drop at high temperatures, in comparison to Si or CdTe solar cells.[5] In contrast, in a wide range of temperatures, from -20ºC to 80ºC, a maximum in device performance is found close to the normal operation cell temperature (NOCT) around 50ºC.[3] The origin of this behavior is due to the combination of many factors, as the variation of internal resistances or energetic shifts, affecting the final efficiency.

This section will analyze in detail all the parameters affecting directly the DSC performance in a range of temperatures from -7ºC to 70ºC by the study of IS measurements in order to provide be a clear picture of the role of temperature in DSC performance.

# 5.2 Stability test

Dye solar cells are known to vary their efficiency with aging. Several previous studies demonstrated the performance enhancement in the first days after cell fabrication. This apparent increase in efficiency has been attributed to a better electrolyte penetration into $TiO_2$ pores, a redistribution of electrolyte additives on the $TiO_2$ nanoparticles thus shifting the $TiO_2$ CB and even the activation of the Pt-coated counter-electrode.[6-8] After that, the performance may remain almost constant for good devices with time if stored under dark conditions, or it may decrease progressively when undergoing light soaking and warming test cycles. In this work we focus in the study of temperature effects in DSC, for this reason a stability test has been performed in order to minimize the effects of cell aging on the results obtained.

The DSC in this work were fabricated following the standard procedure detailed in Section 2.3. N719 was employed as sensitizer, and the electrolyte was MPN-based, containing BMII 0.6M, $I_2$ 0.03M, GuSCN 0.1M and tBP 0.5M. Five cells were prepared for statistical significance, and a 500h stability test was performed. Parameters shown in Figure 5.1 were extracted from *j-V* curves obtained under 1 sun AM1.5G illumination conditions. Between measurements the devices were stored in dark at room temperature. The performance evolution with time for all samples is shown in Figure 5.1. The most stable cell was chosen for the study of impedance.

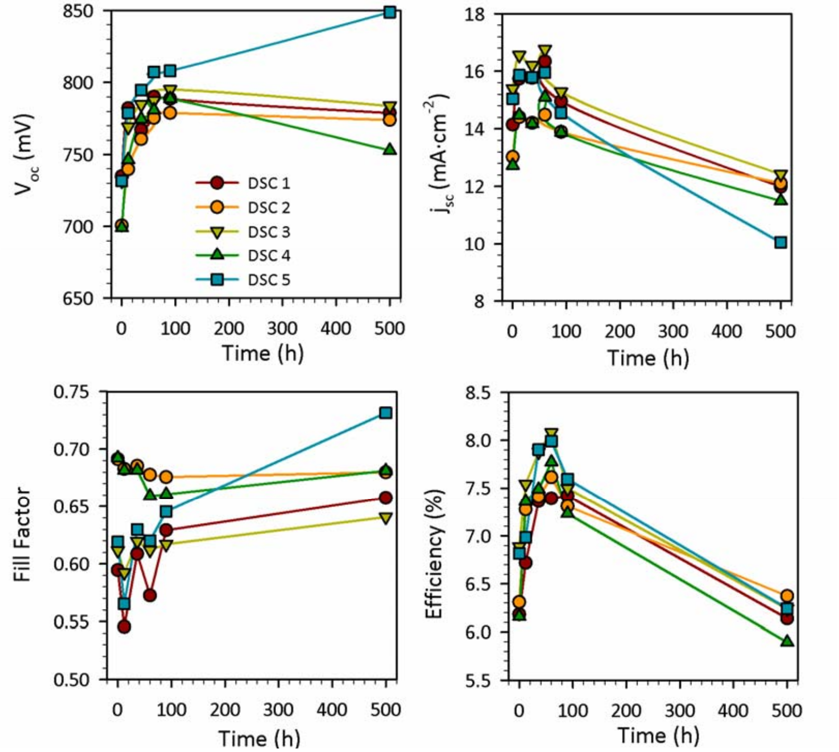

**Figure 5.1:** Evolution of the performance parameters for 5 dye solar cells with time. Maximum in efficiency is reached after 4 days from cell assembly, then $J_{sc}$ and $V_{oc}$ decrease until it reaches a nearly constant value where the cell stabilizes with a smooth decay after 21 days. Performance parameters were obtained under 1 sun illumination provided by a solar simulator.

## 5.3 Device performance at different temperatures

One of the basic application of solar cells is integrating them in outdoor constructions. In this conditions, the environmental temperature may vary depending on the latitude from several degrees Celsius below 0 in winter season in northern countries up to 40-50ºC in summer and near the tropics. Under full sunlight irradiance, the temperature in the surface of a photovoltaic device may rise up to 60ºC.[9] In most of the existing photovoltaic technologies it has been reported a decrease of device performance with rising temperatures.[10] Thus, is interesting to understand the influence of the external temperature in DSC performance applying these devices in large-scale outdoor facilities?, as roofing or solar fields. Thereby, we studied the effect of the external temperature in the performance of a DSC, in a range from -7ºC to 70ºC.

Figure 5.2 shows the effect of temperature on the *J-V* curves of a DSC taken both in the dark and under LED illumination equivalent to 1 sun. The correspondent solar cell parameters are detailed in Table 5.1. In Figure 5.2(a), it may be observed that the rise in temperature produces an onset of photocurrent at lower potentials and thus under illumination (Figure 5.2(b)) this shift is translated into a decrease of open circuit voltage.

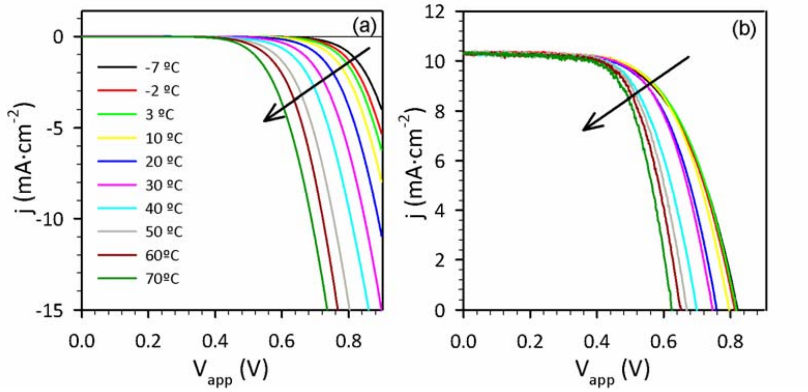

**Figure 5.2:** *J-V* curves at different temperatures obtained after IS measurements in dark (a) and illumination (b) conditions. Arrows indicate the direction of temperature increase.

In Figure 5.2 and Table 5.1 it is clearly seen that the main parameters affecting the efficiency are *FF* and $V_{oc}$ values. To describe the origin of changes in *FF* and $V_{oc}$ the procedure described in previous sections has been followed. Therefore, it has been found that while the main contributions to *FF* variations were associated to series or back layer resistances, for the $V_{oc}$ the main factor reducing its final value was ascribed to the changes in CB position with some extra contribution from the accelerated recombination kinetics at temperatures exceeding 50ºC.

| *T* (ºC) | $J_{sc}$ (mA·cm$^{-2}$) | $V_{oc}$ (V) | *Fill Factor* | *η* (%) | $R_{series}$ (Ω·cm$^2$) |
|---|---|---|---|---|---|
| **-7** | 10.3 | 0.82 | 0.60 | 5.10 | 9.9 |
| **-2** | 10.3 | 0.81 | 0.61 | 5.14 | 8.6 |
| **3** | 10.3 | 0.82 | 0.61 | 5.19 | 8.5 |
| **10** | 10.3 | 0.80 | 0.63 | 5.16 | 6.8 |
| **20** | 10.3 | 0.76 | 0.63 | 4.95 | 6.5 |
| **30** | 10.3 | 0.75 | 0.64 | 4.95 | 5.8 |
| **40** | 10.3 | 0.72 | 0.64 | 4.74 | 5.9 |
| **50** | 10.3 | 0.67 | 0.65 | 4.49 | 5.5 |
| **60** | 10.3 | 0.65 | 0.66 | 4.44 | 5.3 |
| **70** | 10.3 | 0.62 | 0.67 | 4.31 | 5.2 |

**Table 5.1:** Characteristic parameters determining the efficiency of DSC and total series resistance calculated with equation 3.14.

The first step followed was to determine the origin of *FF* improvement when increasing temperature by the breakdown of the total series resistances through the study of IS data. Then, the $V_{oc}$ will be analyzed in a similar manner than in Chapter 4, associating the changes of the different parameters to the rising temperatures.

## 5.4 Series resistance analysis

We focus first on the different contributions to $R_{series}$ and its dependence on temperature. Equation (3.14) in section 3.5 indicates the main contributions to $R_{series}$ (see Table 5.1): the charge transfer resistance at the platinized counter electrode ($R_{Pt}$), diffusion resistance of ions in the electrolyte ($R_d$) and the resistance of the conducting glass plus contacts and wires ($R_{FTO}$).[11]

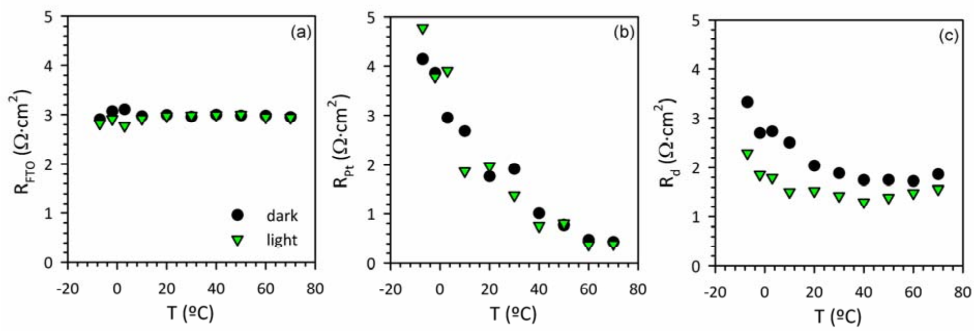

**Figure 5.3**: Temperature dependence of the different contributions to the series resistance of the DSC. (a) Resistance of the FTO conducting glass plus contacts and wires; (b) Resistance of the platinized counter electrode; (c) Diffusion resistance.

Figure 5.3 shows the average values of the different contributions to $R_{series}$. As shown in Figure 5.4(b) and (c), $R_{Pt}$ and $R_d$ are also voltage-dependent, therefore we have used the mean as representative value for all temperatures. In the experimental section of this chapter, the conditions for obtaining these values are indicated. At high temperatures, the main contributor to $R_{series}$ is $R_{FTO}$ which presents a nearly constant value for all the temperatures both in the dark and under illumination, Figure 5.3(a). This result is confirmed by measurements of plain FTO in which the same trend, a very slightly increase of $R_{FTO}$ with rising temperature is observed, see Figure 5.4(a). At low temperatures, as may be seen in Figure 5.3(b) and (c), charge transfer at the counter electrode and diffusion resistance in the electrolyte presented comparable contributions to $R_{series}$.

Figure 5.3(b) shows that $R_{Pt}$ in dark and under illumination present the same values both rising as the temperature diminishes. This result indicates that the counter is in thermal equilibrium with the cooling plate over which it is located. Note that for allowing the better illumination possible, the counter electrode side of the DSC is in contact with the refrigerating Peltier element. The reduction in $R_{Pt}$, with rising temperatures is due to the acceleration of charge transfer kinetics with the redox regeneration.

Diffusion resistance of the electrolyte shown in Figure 5.3(c) presents variations both, with illumination conditions and external temperature of the cell. At high temperatures a decrease in the electrolyte resistance is expected under illumination as the increased concentration of $I_3^-$ due to the regeneration of the dye increases the conductivity in the solution. However this change is not enough to explain the large differences found for $R_d$ at low external temperatures. In the dark, the increase of $R_d$ indicates an increment on the viscosity of the electrolyte when temperature diminishes.[12] Under illumination, part of the electrolyte is in contact and thermal equilibrium with the $TiO_2$ film and very likely at higher temperature than the side in contact with the counter electrode. A gradient of temperature will be then built in the electrolyte between these two electrodes, constrained to 15 µm. In these conditions electrical measurements provide a value of $R_d$ associated with the average viscosity of the electrolyte.

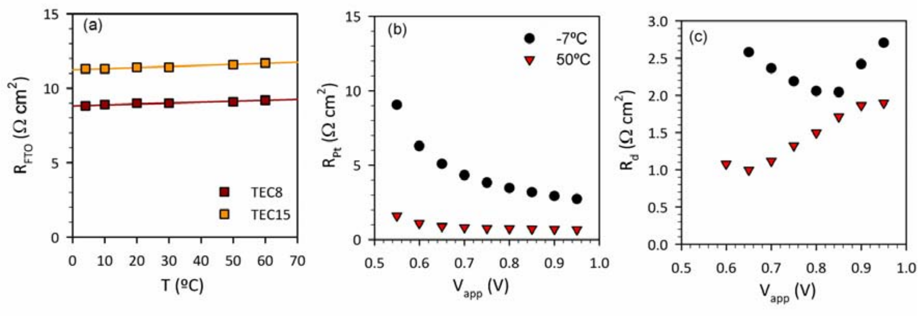

**Figure 5.4:** (a) Changes the resistance of two 1 cm$^2$ FTO samples with temperature. As for our samples their change is minimal with a slight increase with rising temperatures. Changes with applied potential are lower than 5%. The effect of potential is relevant both for counter electrode resistance (b) and diffusion resistance (c). At low temperatures these resistances take larger values than at high temperatures. The minimum in $R_d$ in (c) occurs near $V_{oc}$ when the current is crossing the cell is zero. Note that the overlap between recombination and diffusion arc shown in Figure 5.12 produces increasing errors (> 20%) in the values of $R_d$ at the lower potentials, see experimental section.

In summary, total series resistance decreases with rising temperatures due to the changes in $R_{Pt}$ and $R_d$, while $R_{FTO}$ remains nearly constant. The first two resistances dominate at low temperatures while the last one provides the main $R_{series}$ contribution at high temperature.

## 5.5 Capacitance analysis

The value of $R_{series}$ in each cell is important for an accurate analysis of the parameters associated with $TiO_2$. As described in section 3.5, $R_{series}$ is needed to correct $V_{app}$ and obtain reliable values of the internal voltage drop in the film, Further analysis in this section will be based on $V_F$.

We focus first on the effect of temperature on the chemical capacitance of the $TiO_2$. Measurements of $C_\mu$ in dark and illumination, Figure 5.5(a) and (b), show very similar slopes at high potentials, following Eqs. (4.8) and (4.9).

In Figure 5.5(a) and (b), $C_\mu$ values are clearly shifted towards lower potentials for increasing temperatures. In previous works, it has been shown that chemical capacitance is independent of temperature.[13,14] However, if nanoparticles are small enough, the series contribution of Helmholtz capacitance may produce visible effects on the total capacitance of the film.[15,16] Here we find that $C_\mu$ values are clearly shifted towards lower potentials for increasing temperatures.

Although the trend of this displacement agrees with changes in the Helmholtz capacitance with temperature, the relatively large displacement of the chemical capacitance and the constant slope vs. the potential are not compatible with an explanation based on Helmholtz contribution. [29]

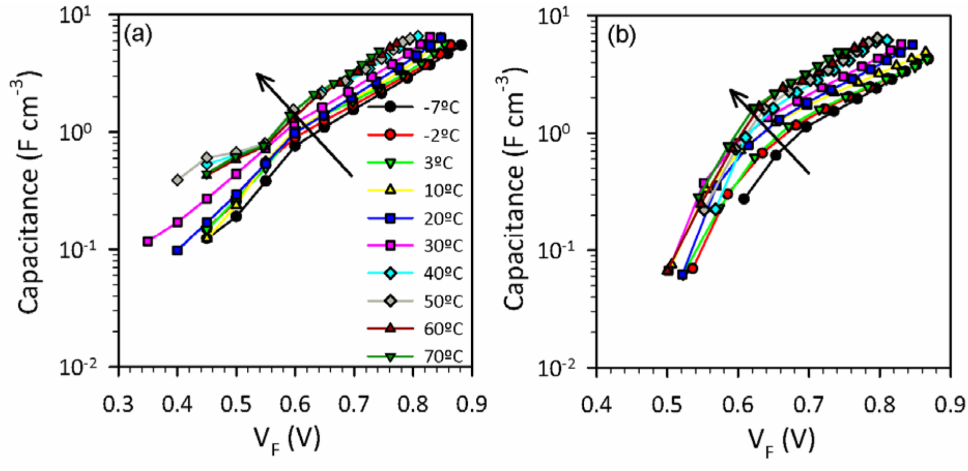

**Figure 5.5:** Values of $TiO_2$ capacitances: (a) in dark and (b) under illumination conditions.

Other possible origin of the shift in $C_\mu$ could be on changes in the $E_{redox}$ ($E_{F0}$) due to temperature. Nernst equation has been used to calculate the change in $E_{redox}$ yielding to a change lower than 10 mV in the full range of temperatures. Assuming that neither the distribution nor the total amount of trap states changed with temperature, we may attribute the shift observed in $C_\mu$ to a displacement in the energy of the conduction band.[17]

Equation (4.9) was used to estimate $E_c$ position for each temperature. Figure 5.6 shows the reduction on $E_c$ level during measurements which, within the experimental error, was nearly the same both for dark and light measurements, taken sequentially.

Movement of the position of the $E_c$ during aging of cells is a phenomenon well known by experimentalists in the field. It depends on time and also on measurement conditions, what produces a variety of behaviors: sometimes $E_c$ rises with time,[18] commonly in fresh samples, and in other occasions it drops.[19] In our case, the cells were pre-aged during 500 h, as explained in section 5.1, before the IS measurements to increase stability and reproducibility of data. Repeated measurement at 20ºC after completing the measurements of the temperature series yielded to similar $E_c$ value obtained at this temperature during the series measurement (see Figure 5.5). The origin of this particular behavior of $E_c$ found for our samples is not yet clear. One possibility could be reversible adsorption/desorption of electrolyte additives, dye or even environmental contamination (i.e. $H^+$ from $H_2O$) at the surface of the $TiO_2$. Other changes in the band gap may be associated to temperature, as it has been reported for other semiconductors, the bandgap diminishes with increasing temperatures.[20]

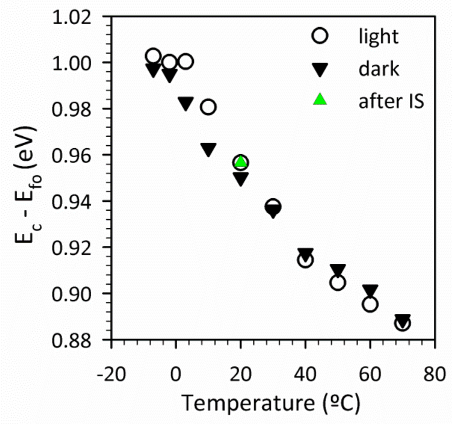

**Figure 5.6:** Values of conduction band position during the measurements. Green triangle represents CB position after all IS measurements, at 20ºC and under dark conditions.

To analyze separately the effects of the variations of $E_c$ in the performance of the DSC from other contributions, the voltage needs to be corrected from the conduction band shift at the different temperatures,[20] so we used $\Delta E_c(T)=E_c(T)-E_c(-7ºC)$ with -7ºC (dark) as the reference temperature for comparison, see Table 5.2.

| T (ºC) | -7 | -2 | 3 | 10 | 20 | 30 | 40 | 50 | 60 | 70 |
|---|---|---|---|---|---|---|---|---|---|---|
| $\Delta E_c/q$ (mV) dark | Ref. | 2 | 14 | 34 | 47 | 61 | 80 | 87 | 96 | 109 |
| $\Delta E_c/q$ (mV) light | -5 | -3 | -3 | 17 | 40 | 60 | 83 | 95 | 102 | 110 |

**Table 5.2:** Voltage shift carried out to $V_F$ to obtain $V_{ecb}$ calculated by the difference between $(E_c-E_{F0})$ at a certain *T* and $(E_c-E_{F0})$ at -7ºC for both dark and illumination conditions.

After representing all *j-V* curves at the same level of CB (Figure 5.7) other contributions can be analyzed independently from $E_c$ position. In the dark, Figure 5.7(a), the onset in photocurrent occurs at lower voltages with increasing temperature however, under illumination, Figure 5.7(b), $V_{oc}$ takes the same values for all curves up to 40ºC (see Table 5.3). Only the measurements above 50ºC present a noticeable decrease in $V_{oc}$. This result indicates that in the dark a rise of the temperature of the sample produces an increase in recombination, while for illuminated samples up to 40ºC this effect is not occurring. Therefore, the changes in $V_{oc}$ up to 40ºC are only produced by $E_c$ shifts and not due to temperature changes.

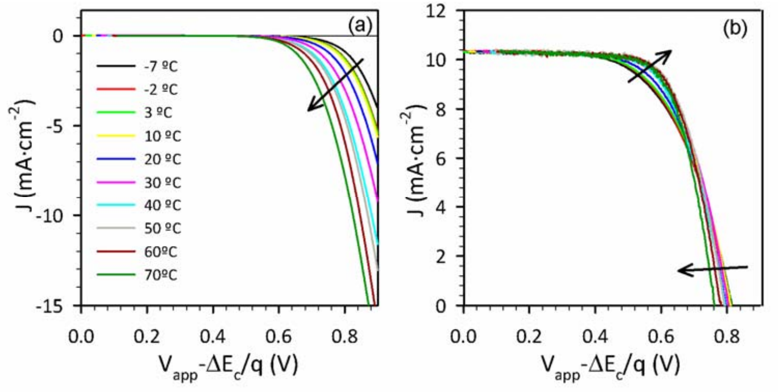

**Figure 5.7:** *j-V* curves from Figure 5.2 after shifting the applied potential by the difference in the conduction band energy respect to the measurements taken at 50ºC. (a) In the dark and (b) under illumination, all the curves for temperatures below 40ºC overlap very well within a ±5mV $V_{oc}$ interval error.

| *T* (ºC) | $J_{sc}$ (mA·cm$^{-2}$) | $V_{oc}$ (V) | *Fill Factor* | *η* (%) |
|---|---|---|---|---|
| -7 | 10.3 | 0.82 | 0.60 | 5.10 |
| -2 | 10.3 | 0.82 | 0.61 | 5.19 |
| 3 | 10.3 | 0.82 | 0.62 | 5.22 |
| 10 | 10.3 | 0.82 | 0.64 | 5.40 |
| 20 | 10.3 | 0.81 | 0.65 | 5.42 |
| 30 | 10.3 | 0.82 | 0.66 | 5.61 |
| 40 | 10.3 | 0.80 | 0.67 | 5.59 |
| 50 | 10.3 | 0.79 | 0.69 | 5.64 |
| 60 | 10.3 | 0.76 | 0.70 | 5.48 |
| 70 | 10.3 | 0.73 | 0.71 | 5.33 |

**Table 5.3:** Characteristic parameters determining the efficiency of DSC in Figure 5.7(b).

A detailed analysis of the recombination resistances evolution with temperature is necessary for understanding the behavior of $V_{oc}$ after $E_c$ correction.

## 5.6 Recombination analysis

We focus now on the study of the recombination resistance. As explained in Chapter 4, once the short circuit photocurrent is fixed, $V_{oc}$ is determined by recombination kinetics that may be analyzed through the recombination resistance.[11,21,22]

According to Eq. (4.5) and Eq. (4.6) from section 4.2, the larger $R_{rec}$ obtained in the dark ($J_{sc}$ = 0, $V_{oc}$ = 0), the smaller current density at a given potential. Under illumination this condition for $R_{rec}$ yields to a larger photopotential. Thus the analysis of $R_{rec}$ will be used in the description of the *J-V* curves obtained in this work.

Figure 5.8(a) and (b), show the variation of recombination resistance vs. the corrected potential at the different temperatures measured both in the dark and under illumination. $R_{rec}$ follows the Eq. (4.3) in section 4.2.

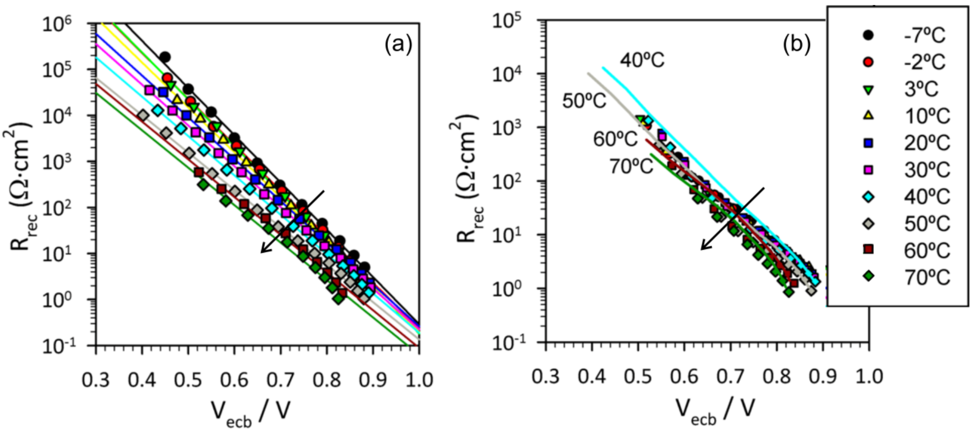

**Figure 5.8:** Values of $TiO_2$ recombination resistances versus the equivalent conduction band potential in dark (a) and under illumination (b). Lines in (b) represent $R_{rec}$ in dark conditions for 40ºC to 70ºC. Black arrows indicate the increase of temperature.

The decrease of recombination resistance with increasing temperature shown in Figure 5.8(a) and (b), is associated to a decrease in $R_0$ and it is responsible for the onset of current losses occurring at lower potentials, as the application of Eq. (4.5) describe.[11] The behavior of $R_{rec}$ in the dark is the expected one, attributed to a higher reaction kinetics of electrolyte acceptor species on the semiconductor surface due to the rising temperature.[13] However, under illumination all the values of $R_{rec}$ taken for temperatures equal and lower than 40ºC converge, see Figure 5.8(b), and they have very close values to those of $R_{rec}$ in the dark at 40ºC, plotted as a blue line in this figure. This result is in agreement with the *j-V* shapes obtained in Figure 5.7.

The phenomena observed in $R_{rec}$ under illumination may have two origins:

(i) The real temperature of the $TiO_2$ layer was increased to a value close to 40ºC for all the measurements done up to this temperature. This would imply that the heat accumulated into the active film due to the light absorption cannot be efficiently evacuated, neither through the 2.3 cm thick FTO glass substrate nor through the electrolyte side (Figure 5.9). Note that despite the use of LED to illuminate the samples effects such as thermalization of charges and energy losses due to recombination and transport (Joule effect) still occur and would be responsible for the heating of the $TiO_2$ film.

(ii) A second possibility could be that the increased concentration of acceptor species in the electrolyte (i.e. $I_3^-$) close to the $TiO_2$ surface after dye regeneration would increase the recombination to levels close to those occurring at 40ºC in the dark. For higher temperatures, faster recombination kinetics may dominate the process over the $I_3^-$ concentration in the same manner than in dark measurements.

The precision in this study is not enough to separate which of the two phenomena is dominating. The shift in conduction band suggest the second phenomena dominates but a local increase of film temperature cannot be fully discarded.

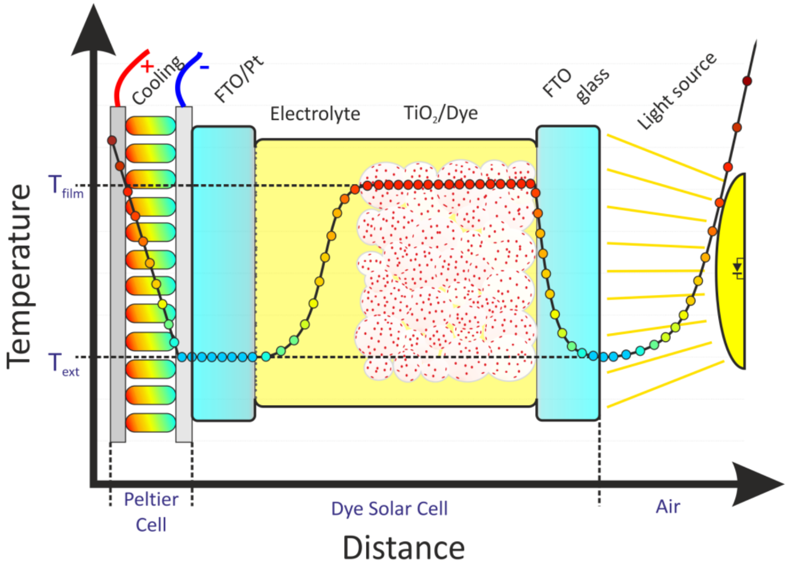

**Figure 5.9:** Scheme of the temperature distribution in an illuminated dye solar cell in contact with a cold substrate (Peltier Cell).

## 5.7 Comparison between PV technologies

The result of the combination of the behavior of recombination and series resistances produces the characteristic shape of DSC the efficiency temperature curve shown in Figure 5.10. Our data, taken from $J$-$V_{app}$ curves after $\Delta E_c$ correction, see Figure 5.7(b) and Table 5.3, have been normalized to be able of comparing the results with data published from Sony for a 9.3% efficient DSC 17 $cm^2$ module.[3] The good match found suggest the same mechanisms dominating the behavior of both cell and module.

Therefore at low temperatures while recombination in the $TiO_2$ film is constant, the decrease of the counter and diffusion contributions to the total series resistance of the DSC with increasing temperatures improves $FF$. Between 20 and 40ºC both $R_{rec}$ and $R_{series}$ present little changes and so does efficiency. Above 40ºC the decrease in recombination resistance and thus the $V_{oc}$, produce a reduction in the efficiency that may not be compensated by further increases in $FF$. For these temperatures, see Figure 5.2, $R_{series}$ is dominated by the nearly constant $R_{FTO}$, while $R_d$ stabilizes and $R_{Pt}$ present only a small reduction.

As mentioned above, the fact that the maximum efficiency in a DSC is obtained at a temperature close to the normal operating cell temperature (NOCT), is an aspect to take into account when comparing DSCs with other technologies. Therefore, taking 47 ºC as NOCT, the efficiency of a CdTe module drops from a nominal value of 11 % to a practical value of 10.4 %. A polycrystalline silicon (pc-Si) module with nominal efficiency of 13.7% presents, at this NOCT a real efficiency of 12.3 %, see Figure 5.10.

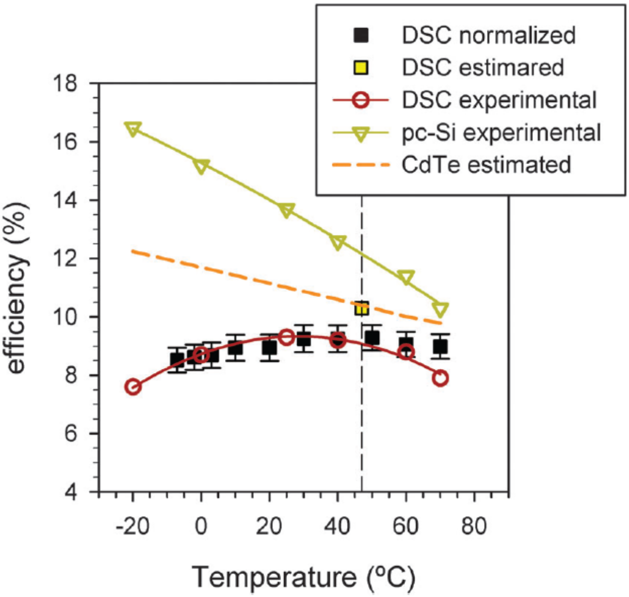

**Figure 5.10:** Comparison of energy conversion efficiencies for different photovoltaic technologies and temperatures. Black squares represent the efficiency obtained from *J-V* curves in Figure 5.7(b) and Table 5.3 normalized to match the published data of a 9.3% efficient 17 cm$^2$ DSC module (red void circles).[3] Yellow square represents the estimation obtained for the record 9.9% efficient module taking into consideration the extra energy collected by DSCs in real outdoor conditions. pc-Si experimental (green triangles) stands for data from a commercial polycrystalline silicon solar module and CdTe estimated (orange dash line) is the simulation of a 11% module with temperature coefficient -0.25 % K$^{-1}$. The dotted line marks NOCT temperature, where performance comparison approaches real operation conditions.

Record DSC modules reaching 9.9 % efficiency are not so far from the values obtained for these standard and commercial panels.[23] Furthermore, the ability of DSC to capture low incidence angle and diffuse light results in both an extension of energy production hours in static installations and a higher efficiency in cloudy days.[1,4] Energy production increases of 10% in sunny days and 20% in cloudy days have been reported for DSC with respect to pc-Si modules for outdoor installations with the same nominal power.[1,4] Part of this rise in energy output is due to the lower real efficiency of pc-Si at NOCT, as mentioned above. If the larger energy production per Watt Peak installed were translated into an increase in the “effective” efficiency of DSC, and a rough 5 % increase is considered, the comparable performance of the DSC would rise to 10.3 % for a nominal 9.9 % module, yellow square in Figure 5.10, the same level than CdTe panels simulated in Figure 5.7.

## 5.8 Conclusions

We have observed that out of conduction band shifts, electron loss by recombination in $TiO_2$ is the same for external temperatures ranging between -7 and 40ºC. This effect may be due to the combined effect of a rise in the temperature of active film and the increase in the acceptor species in the electrolyte close to the $TiO_2$ surface after dye regeneration under high light intensity. The constant recombination resistance pattern in this range of temperatures determines the constant $V_{oc}$ attained for data compared at the same position of conduction band. The decrease in total series resistance with rising temperatures produces an increase in *FF* and thus in efficiency up to this high temperature. Above 40ºC recombination accelerates producing a decay in $V_{oc}$. As further reduction in series resistance is limited, efficiency decreases above 40ºC are observed. Finally we remarked that for a correct comparison of efficiencies between solar technologies the values at operating temperatures should be used rather than the nominal ones. This yields a narrower and more realistic gap between the different technologies compared, than under nominal conditions.

## 5.9 Experimental

The analysis of series resistances obtained from IS measurements, in section 5.4 are crucial for the interpretation of the temperature effects in DSC performance. However, some assumptions have been done in the fitting procedure before obtaining the values for $R_{FTO}$, $R_{Pt}$ and $R_d$ employed in the work.

In the case of FTO resistance shown in Figure 5.11 it may be observed a decrease of resistance with the increased applied potential. The variation is more pronounced for higher temperatures. The data employed in Figure 5.3(a) is a mean value of the resistances at all potentials.

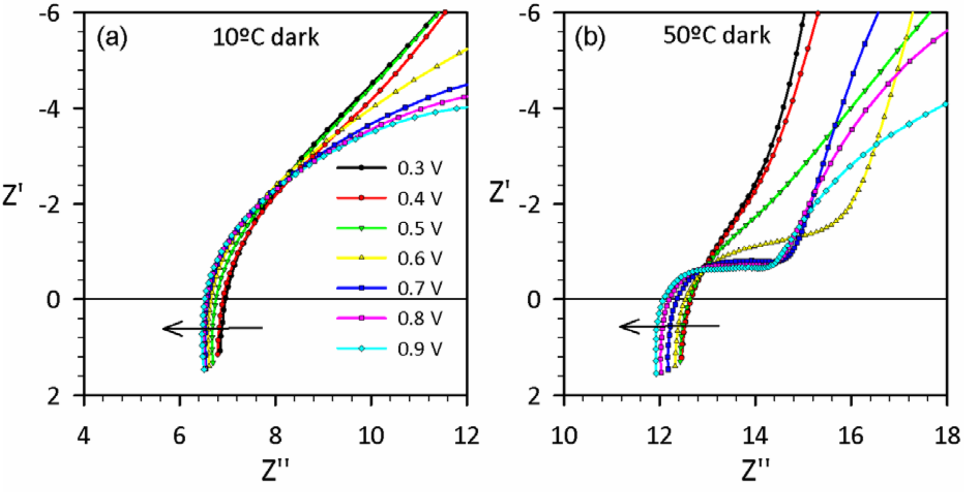

**Figure 5.11:** Evolution of impedance spectra with potential at different temperatures. The values and changes of $R_{FTO}$ and $R_{Pt}$ may be observed at both 10ºC (a) and 50º (b) in dark conditions. The decrease in resistance with the applied potential is about 0.5Ω with an external temperature of 10ºC, and about 0.7Ω for 50ºC.

The arc corresponding to charge transfer resistance at the counter electrode is also appearing in Figure 5.11. It may be observed the large variation both with the applied potential and temperature, as shown in Figures 3(b) and 4(b). For potentials below 0.55V, this arc is overlapped by the transmission line or the recombination contribution. For this reason the value of $R_{pt}$ obtained here presents relatively large errors. The absolute $R_{Pt}$ value taken at each temperature shown in Figure 5.3(b) corresponds to the mean value of the resistance in the potential range from 0.6 to 0.95V.

Finally, the diffusion contribution plotted in Figure 5.12 shows how $R_d$ decreases when increasing the applied potential. Due to the large increase in recombination resistance at lower potentials, overlapping the diffusion arc, it was only possible to fit $R_d$ at potentials higher than 0.7 V. Moreover, in certain potential region, the characteristic times of the recombination and diffusion processes are found to be very close and therefore, the arcs associated to these processes overlap partially as may be seen in Figure 5.12. In these cases, the approach made in the circuit of Figure 3.4 is not accurate enough to obtain good parameters. To solve this a Randles equivalent circuit with the Warburg element in series with $R_{rec}$ and in parallel with the chemical capacitance of the $TiO_2$ is used. This change in the circuit model minimized the errors obtained from the fitting at these potentials.

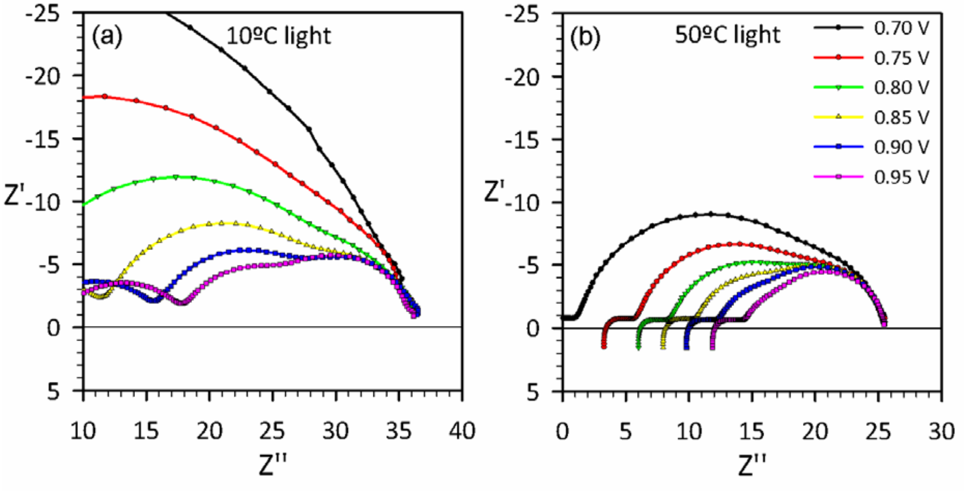

**Figure 5.12:** Nyquist plot showing the arc corresponding to the diffusion of ionic species in the electrolyte at 10ºC (a) and 50ºC (b). All the spectra have been shifted to for a better comparison at the different potentials. Note that diffusion and recombination are partially overlapped. This is attributed to the use of methoxypropionitrile as solvent.

# References

(1) Toyoda, T.; Sano, T.; Nakajima, J.; Doi, S.; Fukumotoa, S.; Ito, A.; Tohyamaa, T.; Yoshida, M.; Kanagawa, T.; Motohiro, T.; Shiga, T.; Higuchi, K.; Tanaka, H.; Takeda, Y.; Fukano, T.; Katoh, N.; Takeichi, A.; Takechi, K.; Shiozawa, M. Outdoor performance of large scale DSC modules. *Journal of Photochemistry and Photobiology A: Chemistry* **2004**, *164*, 203-207.

(2) Kalyanasundaram, K. Dye-sensitized Solar Cells. In *Dye-sensitized Solar Cells*; Kalyanasundaram, K., Ed.; CRC Press: Boca Raton, 2010.

(3) Nozawa, T. Organic Solar Cells Now Produced in Volume. *Nikkei Electronics Asia* **2008**, *July*, http://techon.nikkeibp.co.jp/article/HONSHI/20080625/20153868/.

(4) Brooks, K.; Murray, P.; Au, F.; Duong, H.; Harikisun, R.; Desilvestro, H. Status of Industrialization of Dye Solar Cells for BIPV Applications. In *3rd Nordic PV Conference* Tallinn, Estonia, 2009; Vol. http://www.irc.ee/pvconference/?page=participants.

(5) Mohring, H.-D.; Stellbogen, D. “Annual Energy Harvest of PV Systems – Advantages and Drawbacks of Different PV Technologies.”; 23rd European Photovoltaic Solar Energy Conference, 1-5 September 2008, , 2008, Valencia, Spain.

(6) Wang, Z.-S.; Cui, Y.; Dan-oh, Y.; Kasada, C.; Shinpo, A.; Hara, K. Molecular Design of Coumarin Dyes for Stable and Efficient Organic Dye-Sensitized Solar Cells. *The Journal of Physical Chemistry C* **2008**, *112*, 17011-17017.

(7) Hara, K.; Wang, Z.-S.; Cui, Y.; Furube, A.; Koumura, N. Long-term stability of organic-dye-sensitized solar cells based on an alkyl-functionalized carbazole dye. *Energy & Environmental Science* **2009**, *2*, 1109-1114.

(8) Zhang, Z.; Ito, S.; Moser, J.-E.; Zakeeruddin, S. M.; Grätzel, M. Influence of Iodide Concentration on the Efficiency and Stability of Dye-Sensitized Solar Cell Containing Non-Volatile Electrolyte. *ChemPhysChem* **2009**, *10*, 1834-1838.

(9) http://www.wpi.edu/Pubs/E-project/Available/E-project-042408-181823/unrestricted/PPTReport.pdf. page 17.

(10) Singh, P.; Ravindra, N. M. Temperature dependence of solar cell performance—an analysis. *Solar Energy Materials and Solar Cells* **2012**, *101*, 36-45.

(11) Fabregat-Santiago, F.; Garcia-Belmonte, G.; Mora-Sero, I.; Bisquert, J. Characterization of nanostructured hybrid and organic solar cells by impedance spectroscopy. *Physical Chemistry Chemical Physics* **2011**, *13*, 9083–9118.

(12) Fabregat-Santiago, F.; Bisquert, J.; Palomares, E.; Otero, L.; Kuang, D.; Zakeeruddin, S. M.; Grätzel, M. Correlation between Photovoltaic Performance and Impedance Spectroscopy of Dye-Sensitized Solar Cells Based on Ionic Liquids. *The Journal of Physical Chemistry C* **2007**, *111*, 6550-6560.

(13) Wang, Q.; Ito, S.; Grätzel, M.; Fabregat-Santiago, F.; Mora-Seró, I.; Bisquert, J.; Bessho, T.; Imai, H. Characteristics of High Efficiency Dye-sensitized Solar Cells. *The Journal of Physical Chemistry B* **2006**, *110*, 19406-19411.

(14) Cao, Y.; Bai, Y.; Yu, Q.; Cheng, Y.; Liu, S.; Shi, D.; Gao, F.; Wang, P. Dye-Sensitized Solar Cells with a High Absorptivity Ruthenium Sensitizer Featuring a 2-(Hexylthio)thiophene Conjugated Bipyridine. *The Journal of Physical Chemistry C* **2009**, *113*, 6290-6297.

(15) Abayev, I.; Zaban, A.; Kytin, V. G.; Danilin, A. A.; Garcia-Belmonte, G.; Bisquert, J. Properties of the electronic density of states in TiO2 nanoparticles surrounded with aqueous electrolyte. *Journal of Solid State Electrochemistry* **2007**, *11*, 647-653.

(16) Movilla, J. L.; Garcia-Belmonte, G.; Bisquert, J.; Planelles, J. Calculation of the electronic density of states induced by impurities in TiO2 quantum dots. *Physical Review B* **2005**, *72*, 153313.

(17) O'Regan, B.; Durrant, J. R. Calculation of Activation Energies for Transport and Recombination in Mesoporous TiO2/Dye/Electrolyte Films-Taking into Account Surface Charge Shifts with Temperature. *The Journal of Physical Chemistry B* **2006**, *110*, 8544-8547.

(18) Feng, L.; James Robert, J.; Nripan, M.; Qing, W. Evolution of Charge Collection / Separation Efficiencies in Dye-Sensitized Solar Cells Upon Aging: A Case Study. *Journal of the Electrochemical Society* **2011**, *158*, B1158-B1163.

(19) Listorti, A.; Creager, C.; Sommeling, P.; Kroon, J.; Palomares, E.; Fornelli, A.; Breen, B.; Barnes, P. R. F.; Durrant, J. R.; Law, C.; O'Regan, B. The mechanism behind the beneficial effect of light soaking on injection efficiency and photocurrent in dye sensitized solar cells. *Energy & Environmental Science* **2011**, *4*, 3494-3501.

(20) O'Donnell, K. P.; Chen, X. Temperature dependence of semiconductor band gaps. *Applied Physics Letters* **1991**, *58*, 2924-2926.

(21) Barea, E. M.; Ortiz, J.; Payá, F. J.; Fernández-Lázaro, F.; Fabregat-Santiago, F.; Sastre-Santos, A.; Bisquert, J. Energetic factors governing injection, regeneration and recombination in dye solar cells with phthalocyanine sensitizers. *Energy & Environmental Science* **2010**, *3*, 1985–1994.

(22) Barea, E. M.; Zafer, C.; Gultekin, B.; Aydin, B.; Koyuncu, S.; Icli, S.; Santiago, F. F.; Bisquert, J. Quantification of the Effects of Recombination and Injection in the Performance of Dye-Sensitized Solar Cells Based on N-Substituted Carbazole Dyes. *The Journal of Physical Chemistry C* **2010**, *114*, 19840-19848.

(23) Morooka, M.; Ogura, R.; Orihashi, M.; Takenaka, M. Development of dye-sensitized solar cells for practical applications. *Electrochemistry* **2009**, *77*, 960–965.

# Chapter 6

## Photonic crystal application for DSC

The results on this chapter are published in:

- Lopez-Lopez, C.; Colodrero, S.; Raga, S. R.; Lindstrom, H.; Fabregat-Santiago, F.; Bisquert, J.; Miguez, H. Enhanced diffusion through porous nanoparticle optical multilayers. *Journal of Materials Chemistry* **2012**, *22*, 1751-1757.

## 6.1 Introduction

In the state of the art of the DSCs few improvements could be done as the theoretical maximum efficiency attainable for DSC (around 14-20%) is almost reached by the best efficiency cell in lab scale (12%). Due to the sensibility of the charge-transport and recombination dynamics in a DSC, changing the cell materials or interphase usually cause a balance between the increase of photocurrent with a detrimental effect on photovoltage, or viceversa.[1] One way to improve DSC efficiency without altering the active materials and thus the kinetic balance, is to increase the light-harvesting efficiency of the device. Concentrators have been already successfully employed to increase CIGS and a-Si solar cells efficiencies focusing in the increase of the incident light to the device.[2] Another technique consist in reflecting back to the device the non absorbed photons by means of scattering particles or coherent mirrors. $TiO_2$ particles of 400-500 nm diameter have been widely employed as scatter layers, but at the expense of the device transparency. Photonic crystals (PC), however, present an enhanced property; they are able to keep the transparency of the device while reflecting the useful part of the spectra back to the sensitized nanoparticles. In this manner, one of the main attractive of DSC technology is retained.

In 2003 it was reported for the first time the potential application of photonic crystals to enhance light harvesting in a DSC.[3] After that, several works were focused in the integration of photonic structures on the DSC photoelectrode, with great success in efficiency enhancement.[4-7] Significant increase in the short circuit photocurrent and efficiency was reached in DSC integrating different PC structures between the active layer and the counter electrode, mainly inverted opal and nanoparticle structures, see Figure 6.1.

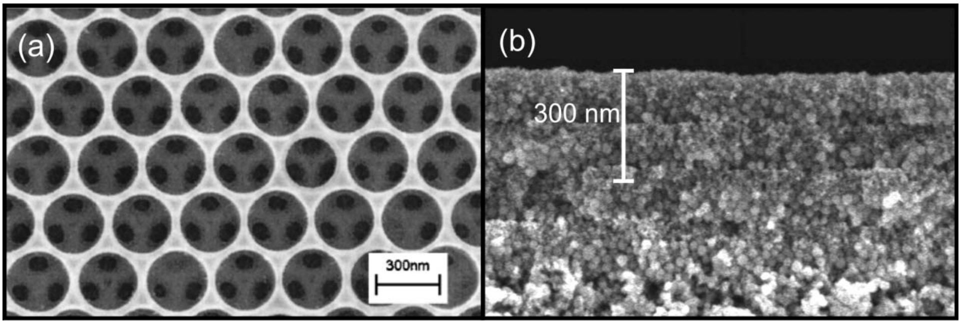

**Figure 6.1:** Examples of two photonic crystal structures: (a) $TiO_2$ inverted opal structure, fabricated by burning organic spheres embedded in a $TiO_2$ matrix. (b) $TiO_2$ and $SiO_2$ nanoparticle structure, fabricated by burning $TiO_2$ and $SiO_2$ nanoparticles in an organic matrix.

The light harvesting was increased up to a 40% in the case of inverted opal $TiO_2$ (acting as active layer too), or 18% for uni-dimensional photonic crystals (1DPC) prepared from colloidal $TiO_2$ and $SiO_2$ suspensions (see Figure 6.2). [8-10] Nevertheless, thick inverse opals (5–10 µm thick) have a deleterious effect on electrolyte diffusion through the cell, which results in a significant reduction in both the open-circuit photovoltage and the photocurrent in real operation conditions. Even though nanoparticle-based 1DPC have good optical properties with only a half micron thickness and are capable to significantly enhance $j_{sc}$, their integration in DSC also decreases photovoltage and fill factor of the device, indicating poor diffusion of ionic species in the electrolyte through the pores, causing a lowering in *FF* and $V_{oc}$, as demonstrated in Figure 6.2.

In this section we will analyze the effect in electrolyte diffusion resistance of newly designed 1DPC photonic crystals with increased porosities.

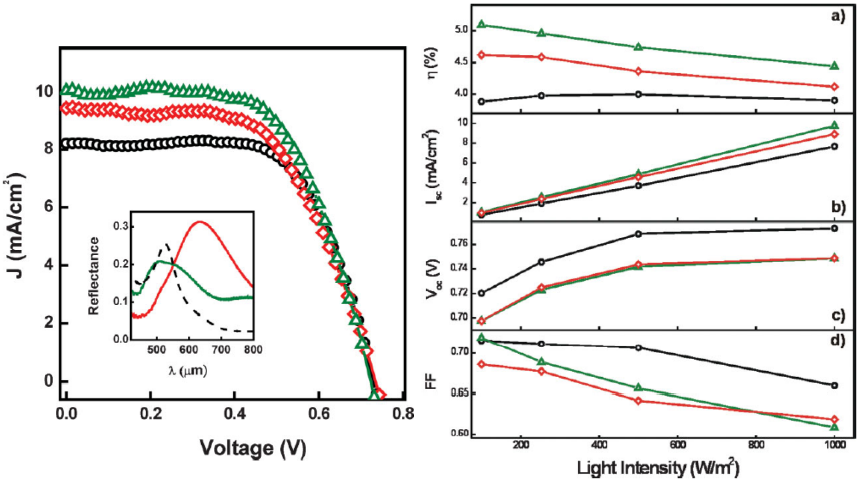

**Figure 6.2:** (LEFT) *J-V* characteristics of a 7.5mm thick dye-sensitized nc-$TiO_2$ electrode coupled to different 1D PCs under one-sun illumination. The lattice parameters are 120±10nm (green), and 160±10nm (red). The *J-V* curve for a reference cell with the same nc-$TiO_2$ electrode is also plotted (black). The inset shows the corresponding specular reflectance spectra of the PC-based solar cell (absolute units) together with the absorption spectrum of the ruthenium dye (arbitrary units). (RIGHT) a) Efficiency $\eta$, b) short-circuit current $I_{sc}$, c) open-circuit voltage $V_{oc}$, and d) fill factor, FF, of the samples plotted in the *j-V* curve, under illumination at different light intensities. (Figures extracted from Adv. Mater. 2009, 21, 764–770)[9]

## 6.2 Photonic crystals

As introduced in section 2.2.6 photonic crystals consist in one-dimensional periodic nanostructures of alternated materials with different dielectric constants. These structures can reflect selectively photons with desired wavelengths, thus being suitable for photovoltaic applications. The electrochemical character of the DSCs requires an interconnected porous media through where ions move. For these reason porous one-dimensional photonic crystals (1DPCs) have been studied for DSC application. Between the different possible techniques to create porous 1DPCs,[11-13] the most versatile is the deposition of nanoparticle suspensions by spin or dip coating.[14] Higher dielectric contrast it is found for multilayers built by alternate deposition of amorphous $SiO_2$ and nanocrystalline $TiO_2$.[15] However, the small pore size of these layers was not overcome since the use of a polymeric porogen (polyethylene glycol, PEG), mixed with the precursor suspensions. The polymer was used for the deposition of the $TiO_2$ and

$SiO_2$ layers and then eliminated to generate a more open interconnected void network. This allowed the control of both the degree of porosity and the pore size distribution of $TiO_2$ (np-$TiO_2$) and $SiO_2$ nanoparticle (np-$SiO_2$) layers integrated in 1DPCs. In this section it will be demonstrated the improved mass transport through the as-prepared nanoparticle 1DPCs through the diffusion analysis made by IS.

The studied photonic crystals in this work consist in 8 alternated layers of $TiO_2$/$SiO_2$ spin-coated films, the fabrication procedure is detailed in section 2.2.6. Different weight concentrations of PEG have been added to the $TiO_2$ and $SiO_2$ precursors in order to modify the porosity of the 1DPC. Table 6.1 describes the characteristics of the as prepared 1DPC.

| Sample | PEG in $SiO_2$ (%) | PEG in $TiO_2$ (%) | Porosity (%) | Thickness (nm) |
|---|---|---|---|---|
| **$TiO_2$-0** | 0 | 0 | 45.5 | 600 |
| **$TiO_2$-25** | 0 | 25 | 49.5 | 520 |
| **$TiO_2$-50** | 0 | 50 | 50.5 | 400 |
| **$TiO_2$-75** | 0 | 75 | 52 | 440 |
| **$SiO_2$** | 50 | 50 | 53.5 | 510 |

**Table 6.1:** Characteristics of the multilayer photonic crystals prepared. The porosity is the average of the porosity of both materials indicated.

## 6.2.1 Light properties

Table 6.1 demonstrates that the porosity increases when PEG is added to the precursor suspensions. In this basis 1DPCs were built in order to prove that these new highly porous layers can also be integrated in a stack that presents photonic crystal properties.

The values of the effective refractive index of each layer within the periodic stack were estimated and detailed in Table 6.2. It can be noticed that the porosity of the np-$TiO_2$ layers remains practically unaltered after being integrated in the Bragg reflector when compared to that measured for monolayer.

| Material | PEG (%) | $n_{eff}$ monolayer | $n_{eff}$ in multilayer |
|---|---|---|---|
| **$TiO_2$** | 0 | 1.70 | 1.69 |
| | 25 | 1.58 | 1.59 |
| | 50 | 1.55 | 1.54 |
| | 75 | 1.49 | 1.49 |
| **$SiO_2$** | 0 | 1.25 | 1.27 |
| | 50 | 1.22 | 1.22 |

**Table 6.2:** Refractive index ($n_{eff}$) of the different nanoparticle monolayer and multilayers, estimated from the analysis of the optical reflectance.

The specular reflectance spectra of these samples are displayed in Figure 6.3. The comparison between the different spectra reveals that the presence of larger pores has a low effect in the final performance of the multilayers as Bragg reflectors.

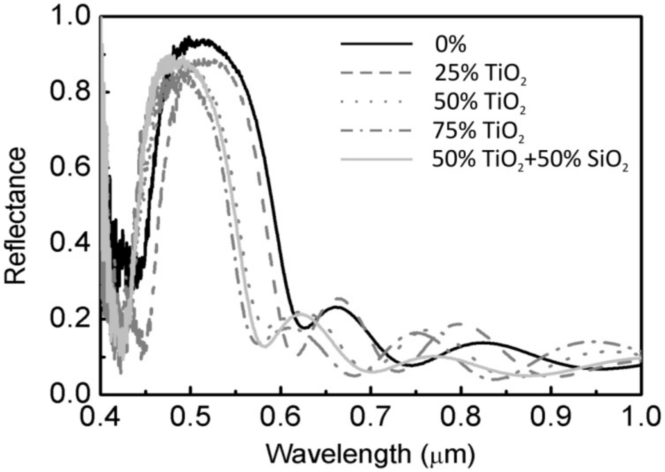

**Figure 6.3:** Specular reflectance spectra of 1DPCs in which different weight ratios of PEG were added to the precursor suspensions.

In all cases, the number of layers deposited is similar (N= 10) and primary maxima present intensities above 80%. Slightly higher peaks are achieved for 1DPCs in which the pores are finer. The reason for this effect is the lower refractive index contrast existing between the layers of np-$TiO_2$ and np-$SiO_2$ in those multilayers showing enhanced porosity, which diminishes the scattering strength of the lattice. Also, a clear narrowing of the peak spectral width is observed as the porosity increases. The generation of a more open pore network yields both lower average refractive index, as it can be estimated from the data shown in Table 6.2, and thus may lead to spectrally thinner Bragg reflections.

## 6.2.2 Diffusion through nanopores

### Experimental

IS analysis was performed using cells containing a solution 0.13M of iodine in 1-butyl-3-methylimidazonium iodide. Each cell was composed of two platinized FTO electrodes, one of them with a np-$SiO_2$/np-$TiO_2$ multilayer deposited over the Pt-coated glass. An area of 1 x 1 $cm^2$ was drawn over conductive glass leaving a 2 mm wide strip in one of the sides to evacuate the charge and make the contacts. FTO out of this area was removed via etching with Zn powder and diluted HCl. Then the electrodes were electroplatinized by submerging them into a diluted chloroplatinic acid aqueous solution using a Pt sheet as a counter electrode and applying a potential of 1.5 V during 1 minute. Dark FTO electrodes were obtained meaning that a high concentration of Pt was deposited over the surface. With the catalyst treatment, the electrode $SnO_2$ substrates are made extremely active with respect to the iodide/triiodide reaction and could well have exchange currents around 200 mA/$cm^2$.[16]

The cells were mounted after drop casting the electrolyte in one of the electrodes and fixing the second by pressing it strongly with a clamp. Pressing electrodes together with a clamp ensures to reach a distance between electrodes equal to the photonic crystal thickness. The removal of external FTO avoids both short circuiting of the cells and direct diffusion of iodide between uncovered FTO layers, minimizing edge effects. The conductive strips of the opposed electrodes were oriented in contrary faces also to prevent short circuits. The iodine concentration used in the electrolyte is lower than that found in literature because the short distance between electrodes makes it more difficult to reach the current saturation regime.[17] Furthermore, a pure ionic liquid was necessary in this experiment to both avoid evaporation during measurements and to be able of appreciating the differences in diffusion due to porosity. Figure 6.4 shows the electrochemical configuration of the 1DPC-electrolyte sandwich.

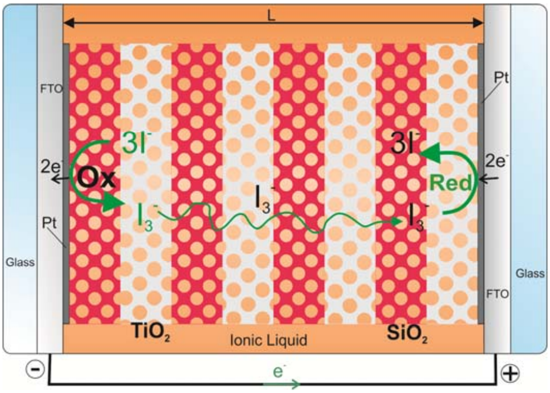

**Figure 6.4:** Scheme of the sandwich cells measured in this study.

## Results and discussion

In order to assess the effect of the modified pore network of 1DPCs on mass transport, curves of current density vs. potential (*j–V* curves) and impedance spectroscopy (IS) measurements were performed.

First, a *j-V* curve between 0 and 1.5 V was made to measure the limiting currents reached for each 1DPC. As shown in Figure 6.5(a), the increase of the layer porosity and pore size with the addition of PEG produces a rise both in the slope at low potentials and in the value of the limiting current ($j_{lim}$) plateau (Figure 6.5(b)) of the *j-V* curves. These results prove the enhancement of mass transport of an electrolyte embedded in 1DPC as a result of the control of porosity.

$j_{lim}$ allows to calculate the diffusion coefficient by means of the expression given in the literature,[18]

$$D = \frac{L\, j_{\lim}}{2nF\, c(I_3^-)\, p} \tag{6.1}$$

where *n*=2 is the number of electrons involved in the electrochemical reduction of triiodide at the electrode, *F* is Faraday's constant, $c(I_3^-)$ is the concentration per volume unit of $I_3^-$, assumed uniform along the whole cell and *p* the porosity, necessary in the equation as the electrolyte diffuses in the channels free of solid. Results of diffusion coefficient calculated with Eq.(6.1) for all the photonic crystals give an average value of $D = (2.0 \pm 0.3)\cdot 10^{-8}$ cm$^2$ s$^{-1}$. These results will be further analyzed with IS values in Figure 6.7.

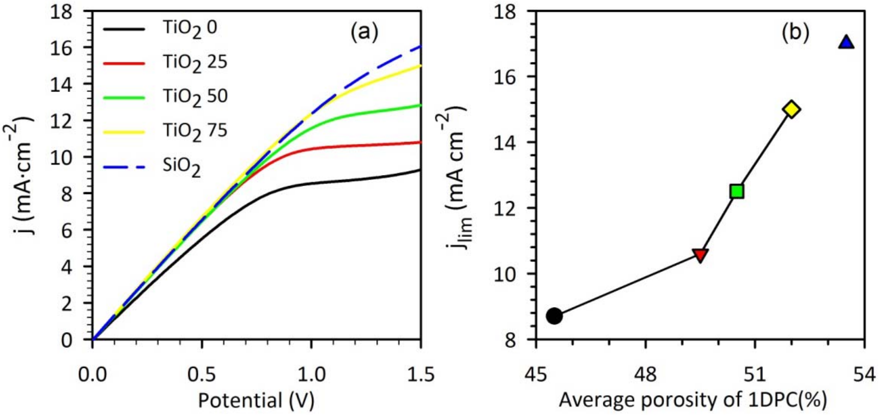

**Figure 6.5:** (a) *j–V* curves for the 1DPCs prepared from precursor suspensions containing different amounts of PEG in the np-$TiO_2$ layer. (b) limit current obtained by extrapolating the values of the plateau on *j–V* curves *versus* average porosity of the multilayer.

For a more detailed analysis of these results, each sample was measured by galvanostatic impedance spectroscopy at four different currents between 0 mA and the limiting current obtained in j-V curves. The Nyquist plots (Figure 6.6(a)) obtained from 1DPCs were fitted to the Randles circuit model detailed in Figure 6.6(b).

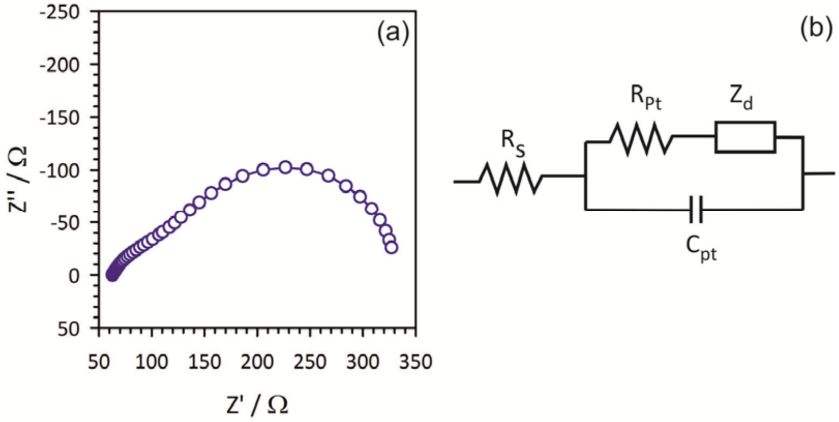

**Figure 6.6:** Randles circuit used to fit experimental data $R_s$ represents the resistance of the FTO and the contacts, $R_{Pt}$ and $C_{Pt}$ are the charge-transfer resistance and double-layer capacitance at the counter electrode (platinized FTO glass) and $Z_d$ is the Warburg element showing the Nernst diffusion of $I_3^-$ in electrolyte.

It allows analyzing separately the physical processes of carrier transport and charge transfer that take place in our device. Here $R_s$ corresponds to the sum of the resistances associated to FTO, contacts and wires, $R_{Pt}$ and $C_{Pt}$ are the charge-transfer resistance and double-layer capacitance from the platinized electrodes, respectively, and $Z_d$ is the diffusion impedance, which represents the resistance to mass transfer through the porous structure. Through the expression of $Z_d$ given by Eq. (3.8) we obtain $R_d$, which is the resistance associated to diffusion of triiodide ions in the electrolyte and is the parameter that will be more affected by variations of the pore network in the multilayers.

From the diffusion frequency and film thickness, *L*, the diffusion coefficient may be obtained using

$$D = \omega_d L^2 \tag{6.2}$$

that yielded values comprised between 1.5 and $2.5 \cdot 10^{-8}$ $cm^2s^{-1}$ (see Figure 6.7), in good agreement with data obtained from $j_{lim}$ calculations.[18]

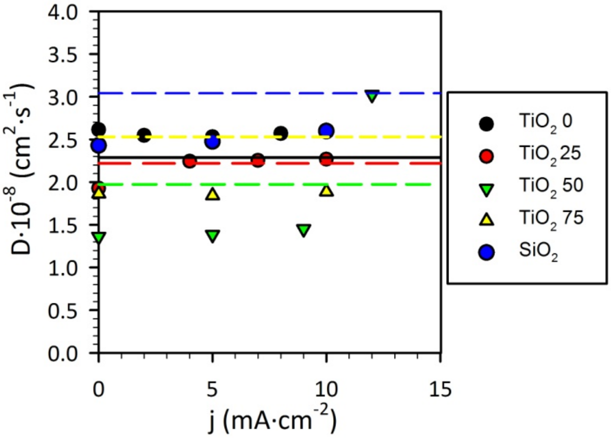

**Figure 6.7:** Dashed lines represent diffusion coefficient calculated from $j_{lim}$ (Eq. 6.1) and dots represent *D* values obtained from IS data (Equation 3).

The values of diffusion coefficient are one order of magnitude lower than those obtained in the free electrolyte (0.2M $I_2$) or even for 10 μm-thick nanostructured $TiO_2$ layer (0.03M $I_2$),[17,19] indicating certain difficulties in the transport of $I_3^-$ through the 1DPC. We associate these low values of *D* with the increased tortuosity and constrictivity introduced by the 1DPC relative to the free electrolyte. The significant error introduced by estimating film thickness and porosity in the calculations make diffusion coefficient between samples not appropriated to compare.

In practical terms, the diffusion resistance is the most relevant parameter of $Z_d$ since its value determines, together with $R_s$ and $R_{Pt}$, the total series resistance of the device. Thus it may influence its performance, mainly through the loss of fill factor, but eventually also by a drop in short circuit current.[20,21] We thus focus our study on $R_d$ in what follows.

Figure 6.8(a) displays $R_d$ as obtained from the analysis of the impedance spectra measured at several current densities, *j*, of the photonic crystals possessing different pore networks. In all cases, $R_d$ increases as the current does, reaching rather large values when $j_{lim}$ is approached. It can be readily seen from Figure 6.8(a) that samples with higher porosity present lower diffusion resistance, reaching values similar to those commonly found in optimized devices for $R_s$ (1-5 Ω cm$^2$) and $R_{Pt}$ (1- 3 Ω cm$^2$).[21,22]

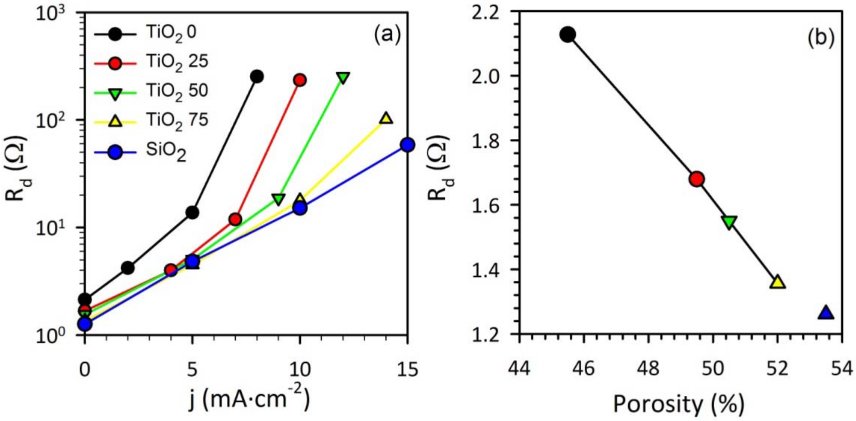

**Figure 6.8:** (a) Diffusion resistance ($R_d$) versus current density ($j$) as extracted from the impedance spectroscopy analysis. (b) Diffusion resistance obtained at j=0 mA·cm$^{-2}$ versus average porosity of the 1DPC prepared using different PEG : np-TiO$_2$ weight ratios.

Figure 6.8(b) clearly shows the dependence of $R_d$ measured at 0 mA versus the average porosity within the multilayer structure. Again a clear decay of $R_d$ as porosity is increased can be observed while, consequently, the opposite trend is observed for $j_{lim}$, as shown in Figure 6.5(b). It should also be noticed that this enhanced mass transport must be caused by the combined effect of both larger porosity and average pore size. However, these two effects cannot be analyzed separately: each time porosity is increased (see Table 6.1), the bottlenecks, responsible for the hindering of diffusion, are also enlarged thus also contributing to a better flow of species through the multilayer.

Impedance spectroscopy analysis confirms that multilayers built using mixtures of nanoparticles and PEG always present larger effective sections for the diffusion of $I_3^-$ species, which results in lower diffusion resistances. This result, combined with the use of optimized electrolytes, allows beating the limitations to efficiency introduced by the addition of the 1DPC extra layers in photoelectrochemical devices such as dye sensitized solar cells.[23]

## 6.3 Characterization techniques

Specific characterization techniques will be described as follows:

**Porosity and thickness**

The porous mesostructure of the $TiO_2$ and $SiO_2$ films was assessed by Specular Reflectance Porosimetry (SRP). This technique allows to obtain the effective refractive index of each one of the films and, by using the Bruggeman equation, analyze the evolution of both the overall porosity and the pore size distribution as the concentration of PEG in the precursor liquid varies.[24]

The thickness was determined from cross-section images acquired with a field-emission scanning electron microscope (FESEM, Hitachi S-4800 operating at 2 kV).

**Reflectance spectra**

Analysis of the specular reflectance spectra obtained at normal incidence was performed by simulating and fitting the optical response measured at the different solvent partial pressures. To do so, we employed a code written in MatLab based on the transfer matrix method and that has been thoroughly described before.[25] Reflectance spectra were attained using a Fourier transform spectrophotometer (Bruker IFS-66 FTIR) attached to a microscope and operating in reflection mode with a 4x objective with 0.1 of numerical aperture (light cone angle ±5.7º).

## 6.4 Conclusions

Uni-dimensional photonic crystals have been introduced as a method for enhance light harvesting in DSC without any modification of the active materials of these devices. It has been reported a 18% increase in DSC photocurrent by integrating nanoparticulate-1DPC as light reflector. However, insertion of an additional layer between the active $TiO_2$ layer and the counter electrode may increase series resistance (diffusion resistance) of the device, thus reducing the fill factor. Here we presented a method to enhance the mass transport through nanoparticle multilayers displaying one-dimensional photonic crystal properties. The concentration of polymer in the precursor suspensions is varied in order to tune the final porosity of the layers. Five stacks of these highly porous layers have been prepared and characterized by cyclic voltammetry and impedance spectroscopy measurements. All the devices display intense Bragg reflections as well as improved mass transport. Diffusion resistance ($R_d$) has been obtained for an electrolyte embedded in the structure from impedance spectroscopy measurements. It resulted in a linear dependence between porosity and $R_d$. These materials presenting combined optical and transport properties will give rise to improved performance when integrated into photo-electrochemical devices.

# References

(1) Haque, S. A.; Palomares, E.; Cho, B. M.; Green, A. N. M.; Hirata, N.; Klug, D. R.; Durrant, J. R. Charge Separation versus Recombination in Dye-Sensitized Nanocrystalline Solar Cells: the Minimization of Kinetic Redundancy. *Journal of the American Chemical Society* **2005**, *127*, 3456-3462.

(2) van Sark, W. Luminescent solar concentrators - A low cost photovoltaics alternative. *Renew. Energy* **2013**, *49*, 207-210.

(3) Nishimura, S.; Abrams, N.; Lewis, B. A.; Halaoui, L. I.; Mallouk, T. E.; Benkstein, K. D.; van de Lagemaat, J.; Frank, A. J. Standing Wave Enhancement of Red Absorbance and Photocurrent in Dye-Sensitized Titanium Dioxide Photoelectrodes Coupled to Photonic Crystals. *Journal of the American Chemical Society* **2003**, *125*, 6306-6310.

(4) Tetreault, N.; Gratzel, M. Novel nanostructures for next generation dye-sensitized solar cells. *Energy & Environmental Science* **2012**, *5*, 8506-8516.

(5) Han, S.-H.; Lee, S.; Shin, H.; Suk Jung, H. A Quasi-Inverse Opal Layer Based on Highly Crystalline TiO2 Nanoparticles: A New Light-Scattering Layer in Dye-Sensitized Solar Cells. *Advanced Energy Materials* **2011**, *1*, 546-550.

(6) Barber, G. D.; Hoertz, P. G.; Lee, S.-H. A.; Abrams, N. M.; Mikulca, J.; Mallouk, T. E.; Liska, P.; Zakeeruddin, S. M.; Grätzel, M.; Ho-Baillie, A.; Green, M. A. Utilization of Direct and Diffuse Sunlight in a Dye-Sensitized Solar Cell — Silicon Photovoltaic Hybrid Concentrator System. *The Journal of Physical Chemistry Letters* **2011**, *2*, 581-585.

(7) Colodrero, S.; Mihi, A.; Anta, J. A.; Ocaña, M.; Míguez, H. n. Experimental Demonstration of the Mechanism of Light Harvesting Enhancement in Photonic-Crystal-Based Dye-Sensitized Solar Cells. *The Journal of Physical Chemistry C* **2009**, *113*, 1150-1154.

(8) Lee, S.-H. A.; Abrams, N. M.; Hoertz, P. G.; Barber, G. D.; Halaoui, L. I.; Mallouk, T. E. Coupling of Titania Inverse Opals to Nanocrystalline Titania Layers in Dye-Sensitized Solar Cells†. *The Journal of Physical Chemistry B* **2008**, *112*, 14415-14421.

(9) Colodrero, S.; Mihi, A.; Häggman, L.; Ocaña, M.; Boschloo, G.; Hagfeldt, A.; Míguez, H. Porous One-Dimensional Photonic Crystals Improve the Power-Conversion Efficiency of Dye-Sensitized Solar Cells. *Advanced Materials* **2009**, *21*, 764-770.

(10) Jin, M.; Kim, S. S.; Yoon, M.; Li, Z.; Lee, Y. Y.; Kim, J. M. Mesoporous Inverse Opal TiO2 Film as Light Scattering Layer for Dye-Sensitized Solar Cell. *Journal of Nanoscience and Nanotechnology* **2012**, *12*, 815-821.

(11) Fuertes, M. C.; López-Alcaraz, F. J.; Marchi, M. C.; Troiani, H. E.; Luca, V.; Míguez, H.; Soler-Illia, G. J. A. A. Photonic Crystals from Ordered Mesoporous Thin-Film Functional Building Blocks. *Advanced Functional Materials* **2007**, *17*, 1247-1254.

(12) de Oliveira, P. W.; Becker-Willinger, C.; Jilavi, M. H. Sol–Gel Derived Nanocomposites for Optical Applications. *Advanced Engineering Materials* **2010**, *12*, 349-361.

(13) Schubert, M. F.; Xi, J. Q.; Kim, J. K.; Schubert, E. F. Distributed Bragg reflector consisting of high- and low-refractive-index thin film layers made of the same material. *Applied Physics Letters* **2007**, *90*, 141115-141113.

(14) Colodrero, S.; Ocana, M.; Miguez, H. Nanoparticle-Based One-Dimensional Photonic Crystals. *Langmuir* **2008**, *24*, 4430-4434.

(15) Puzzo, D. P.; Bonifacio, L. D.; Oreopoulos, J.; Yip, C. M.; Manners, I.; Ozin, G. A. Color from colorless nanomaterials: Bragg reflectors made of nanoparticles. *Journal of Materials Chemistry* **2009**, *19*, 3500-3506.

(16) Papageorgiou, N.; Maier, W. F.; Grätzel, M. An Iodine/Triiodide Reduction Electrocatalyst for Aqueous and Organic Media. *Journal of The Electrochemical Society* **1997**, *144*, 876-884.

(17) Fabregat-Santiago, F.; Bisquert, J.; Palomares, E.; Otero, L.; Kuang, D.; Zakeeruddin, S. M.; Grätzel, M. Correlation between Photovoltaic Performance and Impedance Spectroscopy of Dye-Sensitized Solar Cells Based on Ionic Liquids. *The Journal of Physical Chemistry C* **2007**, *111*, 6550-6560.

(18) Hauch, A.; Georg, A. Diffusion in the electrolyte and charge-transfer reaction at the platinum electrode in dye-sensitized solar cells. *Electrochimica Acta* **2001**, *46*, 3457-3466.

(19) Papageorgiou, N.; Barbé, C.; Grätzel, M. Morphology and Adsorbate Dependence of Ionic Transport in Dye Sensitized Mesoporous TiO2 Films. *The Journal of Physical Chemistry B* **1998**, *102*, 4156-4164.

(20) Fabregat-Santiago, F.; Bisquert, J.; Garcia-Belmonte, G.; Boschloo, G.; Hagfeldt, A. Influence of electrolyte in transport and recombination in dye-sensitized solar cells studied by impedance spectroscopy. *Solar Energy Materials and Solar Cells* **2005**, *87*, 117-131.

(21) Fabregat-Santiago, F.; Garcia-Belmonte, G.; Mora-Sero, I.; Bisquert, J. Characterization of nanostructured hybrid and organic solar cells by impedance spectroscopy. *Physical Chemistry Chemical Physics* **2011**, *13*, 9083-9118.

(22) Liu, J.; Li, R.; Si, X.; Zhou, D.; Shi, Y.; Wang, Y.; Jing, X.; Wang, P. Oligothiophene dye-sensitized solar cells. *Energy & Environmental Science* **2010**, *3*, 1924-1928.

(23) Colodrero, S.; Forneli, A.; López-López, C.; Pellejà, L.; Míguez, H.; Palomares, E. Efficient Transparent Thin Dye Solar Cells Based on Highly Porous 1D Photonic Crystals. *Advanced Functional Materials* **2012**, *22*, 1303-1310.

(24) Colodrero, S.; Ocaña, M.; González-Elipe, A. R.; Míguez, H. Response of Nanoparticle-Based One-Dimensional Photonic Crystals to Ambient Vapor Pressure. *Langmuir* **2008**, *24*, 9135-9139.

(25) Lozano, G.; Colodrero, S.; Caulier, O.; Calvo, M. E.; Míguez, H. n. Theoretical Analysis of the Performance of One-Dimensional Photonic Crystal-Based Dye-Sensitized Solar Cells. *The Journal of Physical Chemistry C* **2010**, *114*, 3681-3687.

# Chapter 7

## Upscaling techniques for DSC

## 7.1 Introduction

Dye sensitized solar cells were born and developed with the purpose of creating a technology for obtaining a cheap energy from a renewable source. Up to now, most of the research efforts have been focused in improving the efficiency and understanding its operating processes. All these studies were based on small area devices, smaller than 1cm$^2$, with a maximum peak power of approximately 11mW. In the reality this is not applicable to any purpose, unless the output power is increased by connecting several devices in series. Nowadays, the step from the lab-scale to the industrialization is a challenge for DSC. Many drawbacks have risen from the first attempt of upscaling them: The increase of series resistances, sealing problems or stability are some of the problems that should be overcome for obtaining commercial DSC devices. As an example, currently, world record-calibrated efficiencies of 11.0% and 11.4% on active area are reported for small-scale DSC (1 and 0.23 cm$^2$ respectively) and 9.9% for a small DSC module (17 cm$^2$).[1] The maximum efficiency reported in a publication, however, is around 12.3% efficiency, but it has not been reproduced and measured in any reference test center as the National Renewable Energy Laboratory (NREL) or similar.[1]

Many companies have succeeded in the fabrication of DSC modules for commercial purpose, applicable to feed small appliances, and new projects for roofing and integration to constructions are emerging. For example, G24i is commercializing cell phone chargers made of DSC integrated in backpacks,[2] or the union of Dyesol and Tata steel companies are developing building integrated DSC, printed directly over steel roof.[3] In short, the most important topics that are essential for a reliable and cheap production technology leading to a successful market introduction are:

- large area deposition of uniform $TiO_2$ layers;
- development of methods for dye staining and electrolyte filling;
- internal electrical interconnection of individual cells;
- hermetic sealing of modules;
- long-term stability;
- evaluation of process steps in terms of costs;
- coverage of market demand

Because of the direct relevance to the manufacturing of commercial products, little work is found in publications about these issues, being difficult to find specific information on processing methods or sealing materials, for example.

In this section, an overview of the main challenges for large scale production will be reviewed and two prototype DSC modules will be fabricated, measured and discussed. Other application for upscaled DSC, as ornamental working devices will be also reviewed.

## 7.2 Upscaling DSC into series connected modules

The first DSC module reported was fabricated in 1995, it consisted in a 100x100mm parallel DSC grid with conductive charge collectors, externally connected in series.[4] Initially, the challenge of this kind of modules was to avoid metal corrosion of the collection grid by iodide electrolyte, and the existing polymer or ceramic glazes were not able to avoid electrolyte leakage. As a consequence, the research on DSC modules was suspended from 1997 to 2001, until new isolation technique for the metal grid was found through a glass frit.[4,5] It lead to modules up to 6% efficiency with an active area of 40x60cm$^2$.[6,7] After that, different module designs were also investigated and much higher efficiencies have been reached. Up to now, three different configuration are the most promising for fabricating DSC modules: the W-type, the Z-type and monolithic.[8,9] Moreover, computational simulations have also been performed in order to find an optimal geometry for each structure.[10] However, all designs present its own advantages and drawbacks. In all of them stability is most important issue and a matter of finding the way to obtaining an hermetic sealing. An overview of these different module configurations follows.

### 7.2.1 Z-Series interconnect

This structure consist in two opposing electrodes with a conductive layer as a contact between cells. This layer may also act as a barrier for electrolyte between cells (see Figure 7.1). If it consists in a corrodible metal (Ag, Cu, Au, Ni,...) it must be isolated from the electrolyte with an inert media as polymer or glass frit. Other option may be the combination of a metal and a non corrosive electrolyte but, up to now, the corrosive iodide redox system is the one providing the best performance.

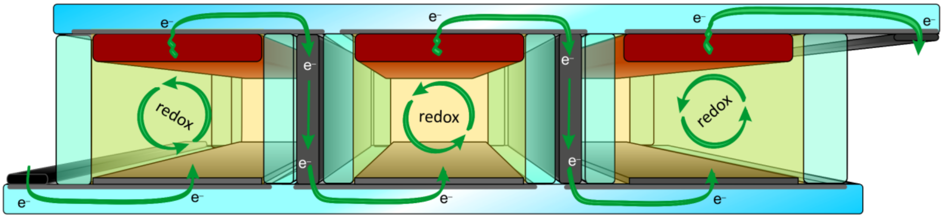

**Figure 7.1:** Z-type series connected DSC module.

The advantage of this type of modules is their high voltage output, the relatively small internal resistance losses and also the facility for treating separately the working and counter electrodes (WE and CE). The high conductivity of the metallic collectors reduces the series resistances that may be high for semiconductor collectors as FTO, provided that the distance between the active area and the metal is short enough. Treating separately the working and counter electrodes ensures that surface treatments as $TiCl_4$ coating and dye staining of the $TiO_2$ do not interfere with the platinized counter-electrode. Thus, a layer of $TiO_2$ from the $TiCl_4$ treatment in the counter electrode may increase substantially the resistance for the electrolyte regeneration. On the other side, a direct contact between Pt particles and dye solution may degrade the molecules decreasing the light harvesting efficiency of the cells. The lifetime of the solution may be also reduced, being unable to recycle it in other modules and thus increasing the cost of mass production.

The main disadvantage of the Z-module, as already commented, is the possibility of the metallic charge collector to be corroded by the iodine in the electrolyte that at long term would increase the resistance at the interconnect lowering the *FF*. The first issue was overcomed by the development of low-temperature glass frits. They consist in ceramic mixtures that sinterize at temperatures below 550ºC. The low temperature melting is very important in order to avoid the phase transition of $TiO_2$ from anatase to rutile, occurring in the range of 550 - 1000°C. Rutile is reported to decrease around 30% the photocurrent of the devices related to the lesser amount of adsorbed dye on the nanoparticles.[11]

The efficiency of these kind of modules is highly dependent on the geometry and size of the device. Up to now, it is difficult to compare between the performance of the cells prepared in different laboratories. Usually the record-efficiency devices are attained for small area-DSC, and thus the effective output power is not applicable to any purpose. And viceversa, mass-scale products with acceptable power output are based on wide area devices, that may be constrained to ornamental applications. In October 2011 it was reported the first fully up-scaled fabrication of 6000 $cm^2$ dye solar module prototypes at Fraunhofer institute. The output power of these large-area modules are relatively high 6.50W ($\eta \approx 2.3\%$), that is enough to charge most of small electrical appliances. However, the corresponding 100 $cm^2$ module fabricated by the same process, presented higher efficiency ($\eta \approx 4.4\%$) at expenses of lower power output of 0.33W.[12]

### 7.2.2 W-series interconnect

In this structure the interconnects between neighboring cells are achieved by sharing the TCO substrate of one working electrode with the next counter electrode (see Figure 7.2). The bias sense in neighboring units is alternated along the module, so a proper sealing is still needed in order to avoid electrolyte flow between cells.

Some advantages of W-modules are the smaller interdistance between cells and the simplicity of the materials employed. The open area between module units can be smaller compared to that of Z modules because of the absence of vertical metallic interconnects. This allows a high ratio of active area in the device while maintaining a relative high FF. The sharing of FTO substrate from one working electrode to the next counter-electrode avoids the employment of a metallic grid and thus the corrosion problem disappears.

In contrast, the disadvantages between other series-connection designs are the detrimental current mismatch effect and the treatment of the counter and working electrode in the same substrate, as commented before. The current mismatch is originated by different illumination intensity in the half of the cells, having the electrolyte and Pt counter electrode which absorbs around a 25% of the light. This requires a design of bigger area in the cells having the $TiO_2$ in the backwards in order to compensate the reduced incident light. However, this assumption may only be valid under one illumination intensity (*i.e.* 1sun), and the mismatch may be unavoidable with changing illumination conditions due to variations in absorption and recombination characteristics of the active area.

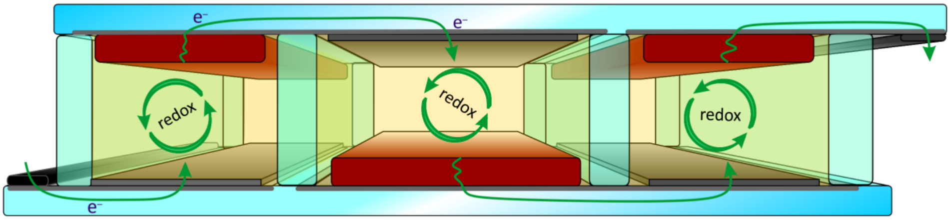

**Figure 7.2:** W-type series connected DSC module.

Because of the lower performance from the counter-electrode side illumination, this design provides about 80% of the performance of a similar Z-module. Other factors described above (e.g. treating together both electrodes) may reduce performance by a further 10%.[4,13] In 2009, Han et al obtained module efficiencies of 8.2% and 8.4% for active areas of 25.45cm$^2$ and 26.47cm$^2$ respectively.[14,15] The ease of processing of this kind of module allows the hand-made production of working devices in laboratory scale, in a relatively short time. This is interesting in terms to accelerate the optimization of the modules by varying thicknesses, active areas or sealing methods and thus is the structure chosen for the performance analysis below.

### 7.2.3 Monolithic series interconnection

This concept was firstly introduced by Kay et al. as an alternative to the one using two substrates.[16] It consists in a multilayer overlay of different functional materials over a single TCO substrate, connected in series by a conductive counter-electrode layer in contact with the neighbor cell (see Figure 7.3).

The main advantage is the ease for volume production as all the elements are sequentially printed, so the thickness is efficiently controlled by printing conditions. The cost of the module is reduced in comparison with the previous structures, as one of the TCO substrate is eliminated, what represents about a 25% of the materials cost.

However, this kind of structure presents some disadvantages originated by the employment of non optimized materials that basically increase up to 2.5 times the series resistances in comparison to common DSC.[17] Moreover, the staining of the $TiO_2$ implicates that the whole device should be dipped into the dye bath, at expenses of solution polluting and unnecessary adsorption on $ZrO_2$ and C nanoparticles. The adherence between layers and the opacity is also a drawback in this design.

The first layer over FTO consist in the nanostructured $TiO_2$, it is the same active layer than the other DSC module designs. Over the $TiO_2$, a porous insulator layer is necessary for avoiding short circuit with the counter electrode. Commonly, $ZrO_2$ nanoparticles are employed for this purpose, this layer has three main functions.[17-19] The basic function is to avoid direct contact between $TiO_2$ and carbon nanoparticles that may result in a short circuit. This layer should be porous enough to allow a good diffusion of the ionic species in the electrolyte. However, the resulting diffusion resistance is several times greater in these cells than the common DSC having a gap between electrodes. The third function is the back reflection of light, acting as a scatter layer and increasing the light harvesting of the active later. The third layer is based in carbon nanoparticles and graphite, and creates a porous and conductive media where the regeneration of triiodide takes place. The carbon nanoparticles are covered by platinum particles for catalyzing the reaction. This layer has higher resistivity than the common FTO substrate used as counter-electrode, together with the added diffusion resistance results in a huge increase of the series-resistance of the cell. In order to create a series connection, this layer is printed over the working electrode substrate of the neighboring cell, see Figure 7.3.

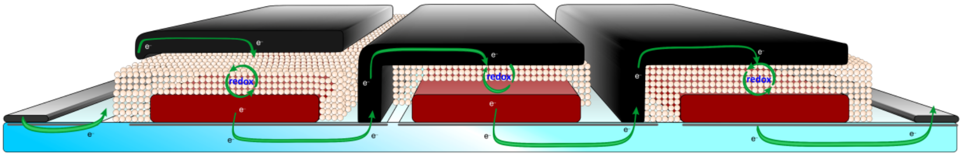

**Figure 7.3:** Monolithic series connected DSC module.

Highest efficiencies obtained with stable monolithic module configuration barely reached 2.57% efficiency with a $P_{max}$ of 156.9 mW for 61 $cm^2$-sized devices.[18] Record efficiencies of 5.6% (for 21 $cm^2$) and 5.8% (for 55 $cm^2$) has been achieved at expenses of poor stability since no encapsulation was used between cells.[16] As shown in Solaronix, a non-published result obtained 5.7% efficiency in a monolithic module of 34 cells, with a total active area of 595 $cm^2$ the stability was not studied.

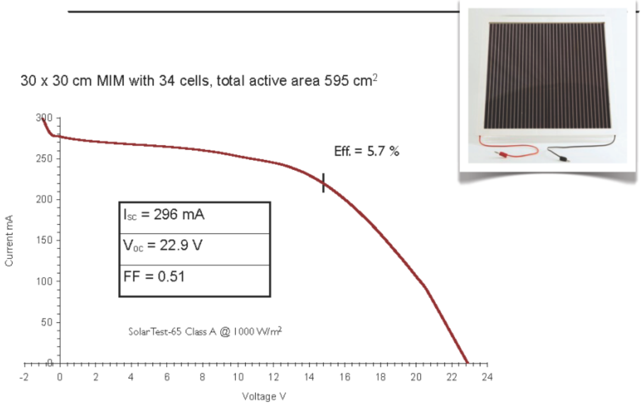

**Figure 7.4:** *J-V* curve of the large area monolithic module of 5.7% efficiency fabricated in Solaronix. Figure published with permission from Solaronix.

Recently, Takeda, Kato and Toyoda proposed an alternative method for retaining the transparency of monolithic modules, by substituting the carbon counter-electrode with FTO nanoparticles covered with Pt particles, with a maximum power output of 210mW in a 90.25 $cm^2$ module.[20]

Further improvements must be done in this technology in order to minimize the series resistances, as it is the most promising method to the mass production of photovoltaic panels. The improvements should come basically from an increase of conductivity of the counter-electrode layer and reduce the thickness and increase the porosity of the separator inert layer.

## 7.3 Device preparation

In this work, the W-module DSC has been chosen for describe its fabrication and characterization procedures. The reason of this election is the similarity of the materials employed with the laboratory test DSCs what enables the use of experimental know how, with no need of further materials developments, and eases the assembling procedure.

As explained above, in a W-type DSC module, the FTO substrate connects the working and counter electrode of neighboring units. In order to drive the electrons to the right path, FTO needs to be isolated in a certain configuration, as shown in Figure 7.2, to define isolated sections in the electrode. The simplest method, firstly reported on 1976 for ITO substrates, is via acidic etching.[21] In this process, the desired pattern is delimited with a scotch tape or similar, in order to avoid wetting of the surrounding FTO. A thin layer of Zn powder is spread on the uncovered FTO and wetted with diluted HCl. Immediately, Zn reacts energetically with the HCl producing active (nascent) hydrogen ($H^o$) which reduces $SnO_2$ at the exposed FTO surface to metallic Sn, see Figure 7.4. Metallic tin flakes are seen to rise to the surface of the bath, and some of the Sn is also reported to dissolve with the $H^+$ in the solution to produce more $H^o$ in the same manner as Zn, aiding the continuation of the etching.[22] $H_2$(g) is also released during this process.

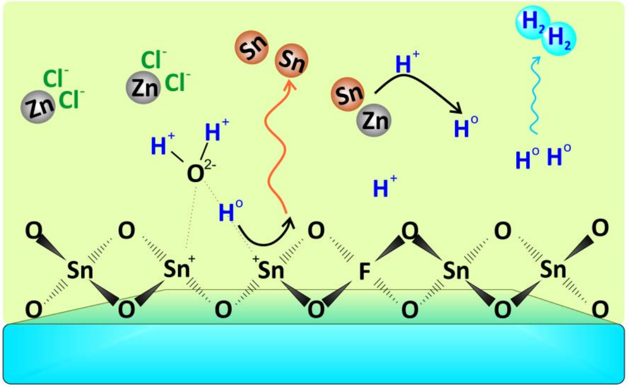

**Figure 7.5:** Scheme of the mechanism for FTO etching on a glass substrate, employing Zn powder and HCl solution. Zn reacts with $H^+$ forming $H^o$, it reacts with shallow $SnO_2$ and releases metallic Sn. The reaction continues until all FTO has reacted or $H^+$ is exhausted.

The reaction is finally stopped with an excess of water and the glass is cleaned with the standard procedure described in section 2.3. Other methods for etching an FTO pattern are laser scribing or plasma etching, these are much more precise methods but at expenses of high energy consumption, increasing the final cost of the DSC module. In practical terms the laser-scribing is more efficient for mass production.

The next step is the deposition of the nanostructured $TiO_2$ layer using the screen-printing method. In one half of the module, six 6x95 mm bars are printed over the FTO substrate, while over the other FTO substrate five 7x95 mm $TiO_2$ films are screen printed. The width difference in the $TiO_2$ is for compensating the current loss due to light shadowing by the electrolyte, as explained above. The thickness of the $TiO_2$ layers is 7 µm and they may be sinterized in advance to form a solid phase that won't be damaged in the next printing steps.

For the counter-electrodes, a cellulose-based paste containing chloroplatinic acid in terpineol is screen-printed between the $TiO_2$ layers, in the opposite configuration (i.e. the FTO substrate containing six 6x95 mm $TiO_2$ bars is printed with five 7x95 mm Pt bars, centered and separated 2 mm from each other, and viceversa). Other possibility is to humidify with a brush the desired FTO area with diluted chloroplatinic acid. This produces a inhomogeneous layer darker than the printed one. The Pt layer should never be in contact with the FTO-$TiO_2$ electrode as it may increase recombination between FTO and electrolyte in the working electrode, producing the loss of (a great) part of the photogenerated charge.

After Pt layers are properly burnt at 450ºC, each half of the module is stained separately in a dye bath. The platinized counter electrode should be previously covered with auto adhesive film in order to minimize direct contact with the dye solution.

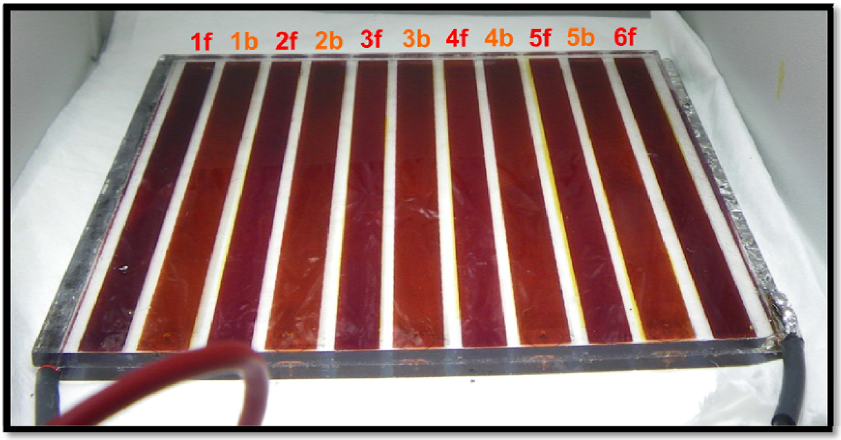

**Figure 7.6:** Picture of the complete DSC W-module illuminated by white LED lamp, close to 1sun intensity. The individual front cells (6x95mm), from left to right are named from 1f to 6f. In the same manner the back cells (7x95mm) are named from left to right 1b to 5b.

Once the dye is completely adsorbed on $TiO_2$ nanoparticles, the assembling and the electrolyte injection should be done in few minutes in order to minimize the contact with air humidity. All photoanodes must be perfectly aligned with the correspondent counter electrodes maximizing the active area of the individual cells. It is desirable to minimize the light exposure and heat supply during sealing to maintain the properties of the light harvester.

Otherwise, the sealing may be performed under inert atmosphere. Electrolyte is injected in a similar manner than for test cells, described in Section 2.3.

Three different modules have been fabricated, one of them handmade using methods as acid etching of FTO, brush-painted Pt and employing $TiO_2$ prepared with P25 commercial nanoparticles (see Section 2.2.3). The second one has been prepared in the company SOLARONIX, with an automatized process, employing industrial methods for etching, deposition, calcination and sealing, and also commercial $TiO_2$ and Pt pastes. The electrolytes employed for the fabrication of both devices are similar with the only difference of a higher concentration of tBP in the handmade module. The third one is a monolithic DSC fabricated in the company SOLARONIX, employing an automatized process and the commercial products fabricated in the same company.

## 7.4 *j-V* module characterization

Figure 7.6 shows the *j-V* curve and the *P-V* curve of the as prepared W-modules at 100mW·cm$^{-2}$ illumination intensity. Photovoltaic parameters extracted from Figure 7.6 are detailed in Table 7.3. The active area of both modules is 67cm$^2$.

The main differences between both modules are the highest $V_{oc}$ and lower photocurrent of the handmade one. This indicates, on the one side, an increase of the $TiO_2$ CB edge due to higher concentration of tBP in the electrolyte, as discussed in Chapter 4. On the other side, the P25-based $TiO_2$ paste may contain aggregates, reducing the specific surface and thus the dye loading resulting into a decreased photocurrent. From the curve slope near $V_{oc}$ we can deduce that, qualitatively, the total series resistance of the automatized module is smaller than the handmade one. Lastly, in Figure 7.7 we observe an "stair shape" in the *i-V* curve with a large drop in photocurrent from short circuit to about 1.5V.

| Sample | $V_{oc}$ (V) | $i_{sc}$ (mA) | $P_{max}$ (mW) | $V_{pp}$ (V) | $i_{pp}$ (mA) | *FF* | $\eta$ (%) |
|---|---|---|---|---|---|---|---|
| **Handmade** | 8.40 | 35.5 | 132 | 6.41 | 20.7 | 0.45 | 1.98 |
| **Automatized** | 7.24 | 58.8 | 175 | 5.77 | 30.4 | 0.41 | 2.61 |

**Table 7.1:** Photovoltaic parameters of the W-type module. $P_{max}$ is the power value at the maximum peak, $V_{pp}$ and $i_{pp}$ the corresponding voltage and current at the peak power. Only efficiency is normalized to the active area of the module (67 cm$^2$). Taking into account that the $V_{oc}$ of all 11 units is similar, in the Handmade module it may have a value of 0.764V and 0.658V for the Automatized one.

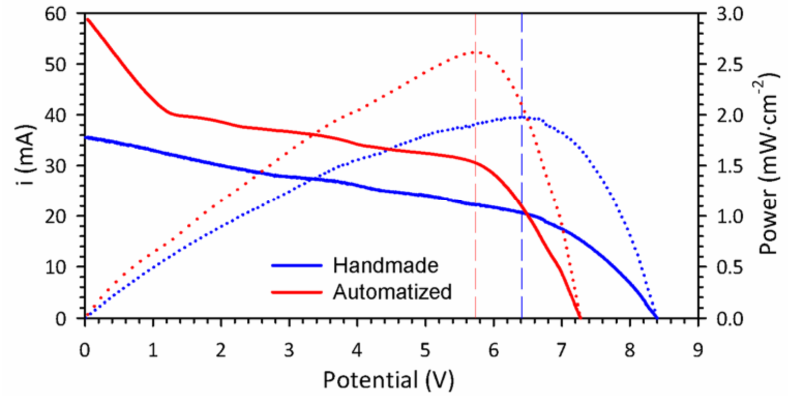

**Figure 7.7:** *i-V* curves for the *Handmade* (blue line) and *Automatized* (red line) DSC W-modules having an area of 67 cm$^2$. The corresponding *P-V* curves are represented with the same colors and dotted lines. The vertical dashed lines indicate the voltage at peak power ($V_{pp}$).

In Section 3.2, *j-V* curves have been described by means of Eq. (3.4), including charge generation, recombination, voltage drop at series resistances and charge loss due to shunt resistances. As observed in the simulations of Figure 3.2 (a) and (b), an increase of the slope at low potentials indicate a decrease of charge transfer resistance between the uncovered FTO in the working electrode and the electrolyte ($R_{bl}$). Assuming the possibility that a very low $R_{bl}$ occurs in the automatized module, this could cause the current drop at low potentials. However, this explanation is not enough to explain the *plateau* at almost constant current for the potential interval of 1.5-6V. As the module consists in two different geometries of units it is expected that many of the parameters affecting the *j-V* shape will vary from every second cell. Among all the existing variables, the most affected by the W-module configuration are:

- Photogeneration ($j_{sc}$): differences due to the different area and illumination of some of the units.
- Series resistance ($R_{series}$): wider units may have higher FTO resistance. The front illumination of the electrolyte has unknown effects in the diffusion or the reaction of the ionic species. Temperature differences between different illuminated units studied in Chapter 5 may also vary these resistances.
- Recombination resistance ($R_{rec}$): Differences in photogeneration may also result in a different concentration of triiodide species near $TiO_2$ nanoparticles, affecting the recombination rate.
- Shunt resistance ($R_{bl}$): the conjoint treatment of the counter and working electrodes, in particular the Pt deposition and calcination, may pollute part of the uncovered FTO in the working electrode, decreasing the value of $R_{bl}$.

At any rate, the largest difference between the front and back cells of the module is supposed to come from the mismatch in photogenerated current. In further analysis we will assume a similar value for the rest of the variables detailed above for all the module units. A simple experiment has been carried out in order to evaluate the changes in the *i-V* curve with progressive shading of the individual DSC units, this is developed in next section.

## 7.5 Shading test

In order to ascertain the individual contribution of every module unit to the final *i-V* curve shape, they were shadowed with semi transparent tape, reducing the 25% of incident light. In a first check, the front cells were shadowed, one by one, measuring the *i-V* curve (see Table 7.2 and Figure 7.8). The same procedure was performed with the back cells (see Table 7.3 and Figure 7.9). It has to be pointed out that these measurements were performed after 20 days of cell stabilization, the efficiency then slightly decreased from the first measurement, detailed in Table 7.3.

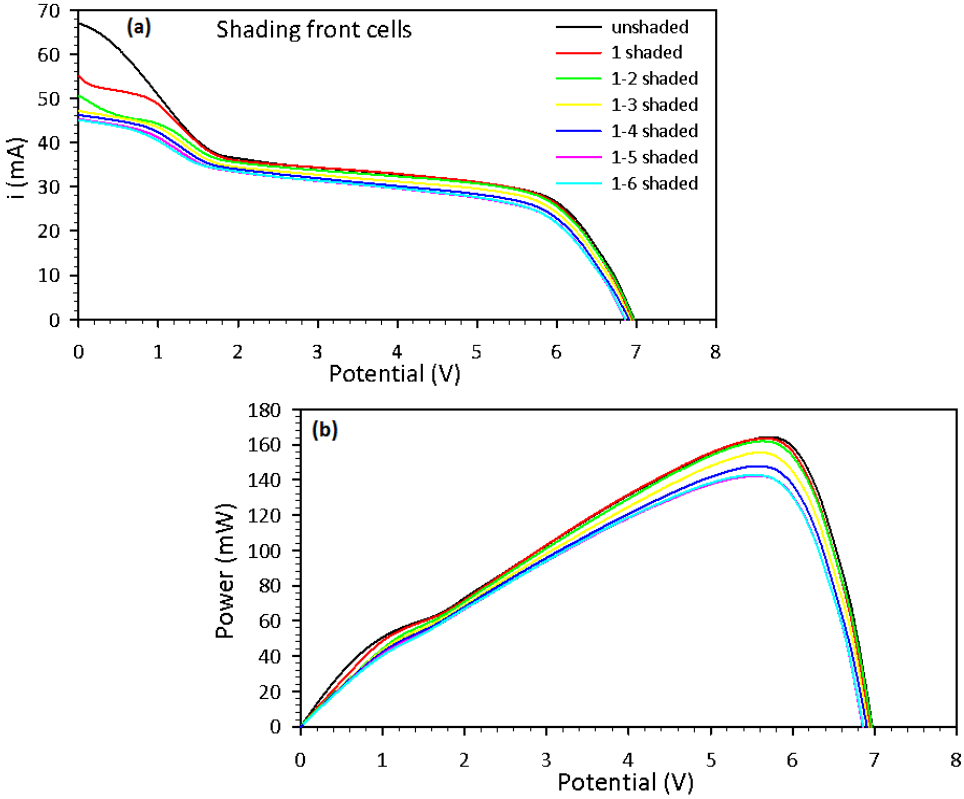

**Figure 7.8:** Current- voltage (a) and Power-voltage (b) curves for the DSC W-module shading the 25% of the incident light on the front cells with semi-transparent tape.

| Sample | $V_{oc}$ (V) | $i_{sc}$ (mA) | *FF* | $\eta$ (%) |
|---|---|---|---|---|
| **Unshaded** | 6.99 | 67.51 | 0.35 | 2.45 |
| **1f** | 6.99 | 56.59 | 0.41 | 2.44 |
| **1-2f** | 6.99 | 51.18 | 0.45 | 2.42 |
| **1-3f** | 6.99 | 47.40 | 0.47 | 2.32 |
| **1-4f** | 6.99 | 46.45 | 0.46 | 2.21 |
| **1-5f** | 6.89 | 45.20 | 0.46 | 2.12 |
| **1-6f** | 6.89 | 45.00 | 0.46 | 2.13 |

**Table 7.2:** Photovoltaic parameters of the shaded DSC modules from Figure 7.12.

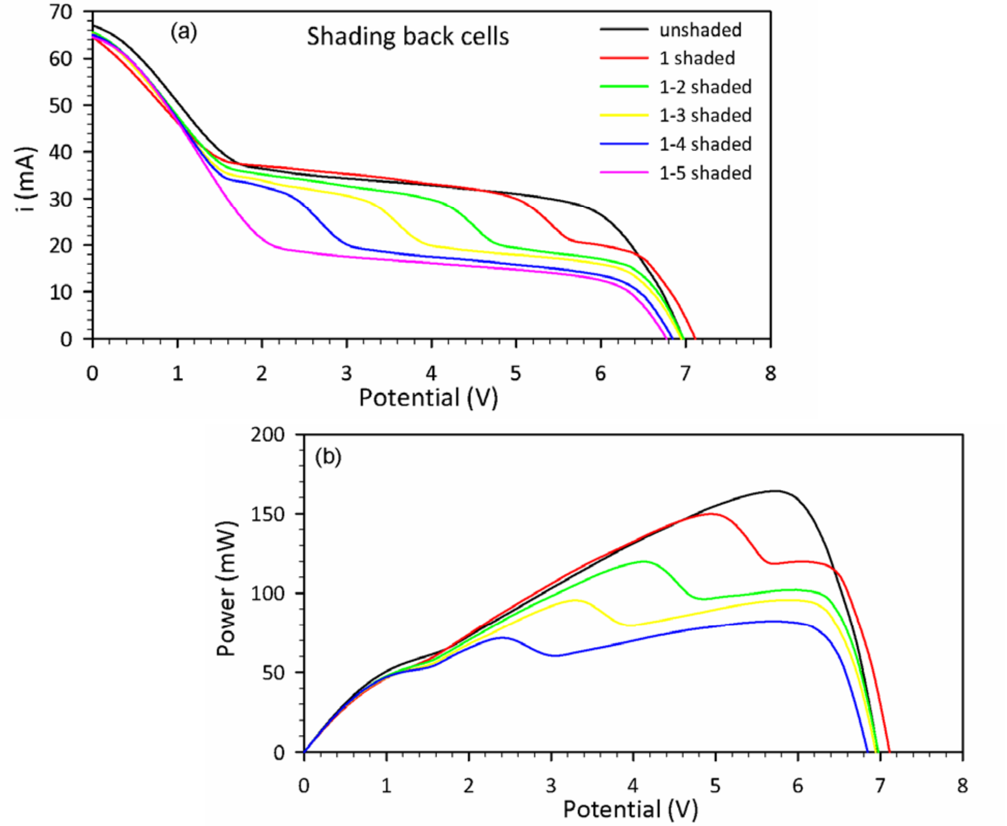

**Figure 7.9:** Current- voltage (a) and Power-voltage (b) curves for the DSC W-module shading the 25% of the incident light on the back cells with semi-transparent tape.

| Sample | $V_{oc}$ (V) | $i_{sc}$ (mA) | *FF* | $\eta$ (%) |
|---|---|---|---|---|
| **Unshaded** | 6.99 | 67.5 | 0.35 | 2.45 |
| **1b** | 7.17 | 65.5 | 0.32 | 2.23 |
| **1-2b** | 6.99 | 66.2 | 0.26 | 1.79 |
| **1-3b** | 6.99 | 65.9 | 0.21 | 1.43 |
| **1-4b** | 6.81 | 65.5 | 0.18 | 1.23 |
| **1-5b** | 6.81 | 65.0 | 0.17 | 1.14 |

**Table 7.3:** Photovoltaic parameters of the shaded DSC modules from Figure 7.13. The overall performance decreases more than a half when shading 5 cells. The parameter that is mostly affected by the shadowing here is the fill factor, while $i_{sc}$ and $V_{oc}$ remain almost constant.

Figure 7.8(a) shows the current drop at low potentials when shading one of the front units. When shading two units there is a short circuit current drop. However, no observable variations in the *i-V* curve appear at potentials higher than 1.5V. After the third or further units are shaded, the $i_{sc}$ stabilizes at 46mA, decreasing also the overall current along the *i-V* curve. $V_{oc}$ is maintained constant and the *FF* increased significatively with the shading, due to the smaller mismatch in the illumination of front and back cells. It can be noticed that the overall performance is not decreasing significatively when shading 6 cells. This indicates that the back cells already limit the performance of the module, remarking the importance of solving the problem of photogeneration mismatch.

Attention is focused now on the effect of shading the back cells over the DSC: in Figure 7.9(a) we can observe the almost constant $i_{sc}$ after this shading. Here, a third plateau appears, increasing its length around 0.9-1V for each additional shaded cell. In Figure 7.9(b) and Table 7.5 is clearly seen the huge reduction in *FF*, while $V_{oc}$ and $i_{sc}$ are maintained almost constant. The efficiency decrease is governed by this reduction in *FF*.

## 7.6 Results and discussion

It is widely known that in a series connected circuit, the overall current of the system is limited by the weakest of all the units and the total $V_{oc}$ is the sum of the voltage of every unit. In addition, if the elements connected in series are diodes, the current flow is only possible in one direction. Ideal solar cells presents diode behavior thus the series connection of these devices also results in the current limitation by the less efficient unit in the module. If the breakdown voltage is surpassed, the current may flow. This has been already observed in series connected Si or thin film solar cells, where the complete shading of a single unit drops the output power to zero.[23,24] If the reverse voltage that suffers the shaded unit surpasses its breakdown voltage it results in a damaged device, invalidating the whole solar panel.

With this assumption we analyze the $i_{sc}$ obtained in Figure 7.7. A single DSC unit sized 0.6x9.5 cm$^2$ with this $i_{sc}$ provides a $j_{sc}$ of 10.5 mA·cm$^{-2}$. That value is very close to the current density of a 7µm-thick $TiO_2$ film under 1sun illumination conditions (see Table 5.1 in Chapter 5). As the thickness of the $TiO_2$ layer in the module is also 7 µm, we can say that the current density obtained corresponds to a fully illuminated unit. This leads us to think that the back-illuminated samples, receiving less than 1sun intensity, are not limiting the photocurrent of a complete DSC w-module. This suggests that, in a DSC, other paths exist for evacuating the current excess originated at the more efficient units.

Thus it may be interpreted the flow of electrons in a DSC module at different applied voltages. In order to simplify the analysis a two cells-series connected module is assumed. Figure 7.10 shows the energetic levels of a DSC W-module consisting of the two units (named 1 and 2). In this system is stated that cell 2 is under 1sun illumination and cell 1 is receiving 40% less illumination intensity and thus less photocurrent. Series resistances are considered negligible in this model.

In the first case, Figure 7.10(a) the module is left at open circuit. In this situation the contribution to the total open circuit voltage of the module is the sum of the $V_{oc}$ of all units, in this case 0.7V. Due to the particular characteristics of DSCs, the $V_{oc}$ of Cell 1 is similar to the $V_{oc}$ of Cell 2 despite its lower illumination. In DSC is known that low illumination intensities are enough to create an electron injection rate that elevates $E_{Fn}$ over $E_{F0}$ to values near $V_{oc}$. Note that the series connection equilibrates the redox potential of Cell 1 with the electron Fermi level of Cell 2.

In the second case, Figure 7.10(b), the module is short-circuited. As discussed above, the short circuit current of the whole module at 1 sun matched the expected short circuit current of a single unit at the same illumination intensity. Thus, it is deduced that the photocurrent obtained in that case is coming from Cell 2, receiving higher illumination. In this case, Cell 2 is working with certain bias lower than $V_{oc}$ though. However the photocurrent given by the module is close to $j_{sc}$ of Cell 2. As seen in section 3.2, a photocurrent near $j_{sc}$ is maintained at relative high potentials if the fill factor of that cell is good enough. The electrons injected by $TiO_2$ of Cell2 to the FTO at the working electrode are conducted to the counter electrode interface of Cell 1. The injection of the photocurrent from Cell 2 to Cell 1 forces the internal voltage of Cell 1 to be negative with respect to previous cell. The condition of short circuit yields to that the two cells present the same absolute value of their internal potentials.

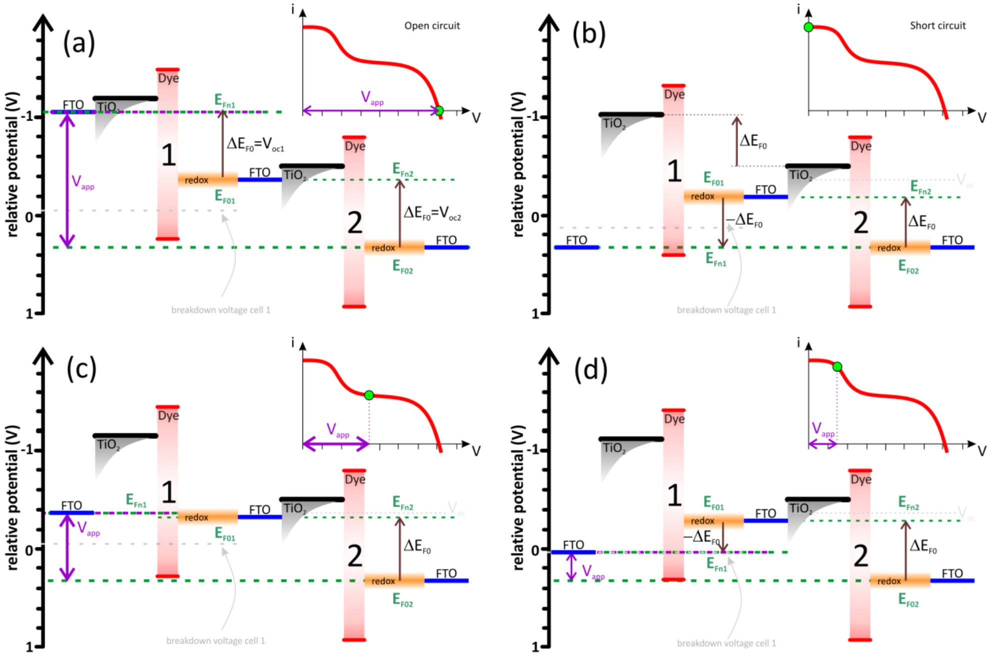

**Figure 7.10:** Energetic scheme representing the energy levels of all components in two DSC connected in series. The y-axis representing the potential is related to cell 2, the energy values for Cell 1 are relative to the position of $E_{Fn2}$. The FTO situated in the middle is shared in both Cell 1 counter-electrode and Cell 2 working electrode. $E_{Fn}$ level at $V_{oc}$ for both cells is represented as a grey line in schemes (b), (c) and (d).

Figures 10(a) and 10(b) correspond to the intermediate potentials. For understanding these cases the breakdown voltage concept for DSC has to be introduced. When measuring at forward bias, the onset of photocurrent occurs at about 0.7 V. In these conditions the electrons flow from the FTO of the working electrode to the $TiO_2$, then transferred to the electrolyte and finally injected to the counter electrode. At reverse bias, the electrons at the counter-electrode are transferred to the electrolyte and then they are directly injected to the uncovered FTO of the working-electrode. At reverse potentials the $TiO_2$ behaves as an insulator, thus is not possible to inject the charge directly from the electrolyte. Figure 7.11 shows the voltammetries of a complete DSC at forward (positive) and reverse (negative) voltages. It is observed that the onset in photocurrent in both senses is not symmetric regarding to zero bias.

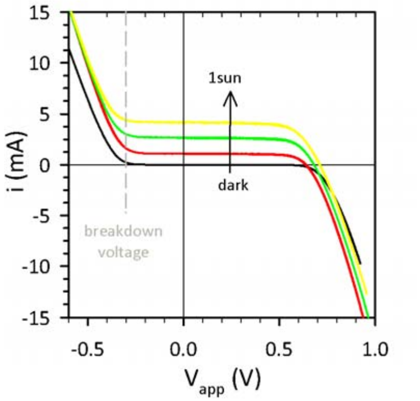

**Figure 7.11:** Voltammetric curves at forward and reverse potentials of a DSC taken in the dark (black line), at 1000W·cm$^2$ (yellow line) and two intermediate illumination intensities (red and green line).

Previous works demonstrated that the charge transfer in the FTO/electrolyte fits well with the Butler-Volmer relation.

$$i = i'_0\left(\exp\left(\frac{\beta' q}{kT}V_F\right) - \exp\left(\frac{-(1-\beta')q}{kT}V_F\right)\right) \tag{7.1}$$

where $i'_0$ is the exchange current and $\beta'$ the transfer factor that for metals takes the value of 0.5. For FTO, it has been found that $\beta' \approx 0.25$-$0.3$.[25] The first term in Eq. 7.1 represents the forward current, note that the charge transfer model is similar to the one employed for recombination in $TiO_2$, see Eq. (3.1).

From Figure 7.11 we have to point out that the onset of photocurrent takes place at -0.3V. This indicates that the electron injection at reverse bias is not possible unless $E_{Fn}$ is situated more than 0.3V below $E_{F0}$ (or $E_{redox}$).

At this point we proceed to analyze Figure 7.10(c), where the applied bias on the module is 0.7 V. Cell 2 is biased at a voltage slightly lower than open circuit, the photocurrent given by this cell is enough to drive the electrons to Cell 1 and thus regenerate its oxidized dye molecules efficiently. In Cell 1, $E_{Fn1}$ is situated some milivolts over $E_{F01}$, thus the given photocurrent is near $j_{sc1}$. If the applied voltage decreases few milivolts, $E_{Fn}$ in both cells diminish. In these conditions photocurrent in Cell 2 increases to a value that equals the $j_{sc}$ Cell 1 is able to provide. In this condition $E_{Fn1}$ approaches the breakdown voltage very quickly.

In Figure 7.10(d), the current injected from Cell2, which is larger than $j_{sc1}$, is able to cross through the complete cell. For this to happen, $E_{Fn1}$ level need to surpass the breakdown voltage thus part of the cross the electrolyte to be transferred directly to the FTO of the working electrode bypassing the $TiO_2$. This is reflected in the increase in photocurrent at the lower voltages of the *i-V* curves shown in Figs. 8 and 9. The output current is limited to the $j_{sc}$ of Cell 2, as seen in Figure 7.10(d). This property protects the individual cells from over currents without the need of using extra diodes.

With this basis, the DC equivalent circuit in a DSC may be rewritten in a different way than for the common solar cells, see Figure 7.12.[26]

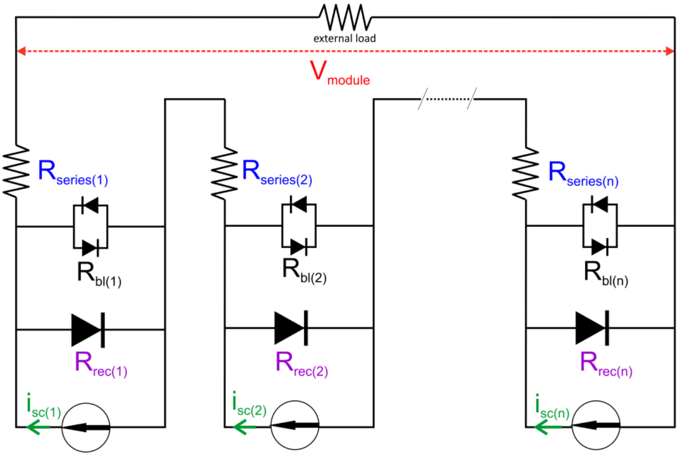

**Figure 7.12:** Equivalent circuit for *n* series connected DSC. $i_{sc(n)}$ is the photocurrent, $R_{rec(n)}$ the recombination resistance, $R_{bl(n)}$ the charge transfer resistance between FTO and electrolyte described with a Butler-Volmer equation and $R_{series(n)}$ is the total series resistance, all related to the unit cell *(n)*.

The shunt resistance appearing in Eq.(3.4) may be changed by a double diode behaving as the Butler-Volmer indicated in Eq. (7.1) that accounts for the FTO contribution.[25] In order to simplify the expression, series resistances have not been taken into account, the current in one DSC is thus:

$$i = i_0\left(\exp\left[\frac{\beta q}{k_B T}V_F\right]-1\right)-i_{sc}+i'_0\left(\exp\left(\frac{\beta' q}{kT}V_F\right)-\exp\left(\frac{-(1-\beta')q}{kT}V_F\right)\right) \qquad (7.2)$$

where the positive elements are the current flowing in forward (current loss) and the negative flowing in reverse (current extraction).

For the module with *n* series connected DSCs, and taking into account that the redox energy level of Cell*(n-1)* matches the electron Fermi level of Cell*(n)*, as shown in Figure 7.10, thus the potential may be written as:

$$-qV_{F(n)} = (E_{Fn(n)} - E_{F0(n)}) = (E_{Fn(n)} - E_{Fn(n+1)}) = (E_{F0(n-1)} - E_{F0(n)}) \qquad (7.3)$$

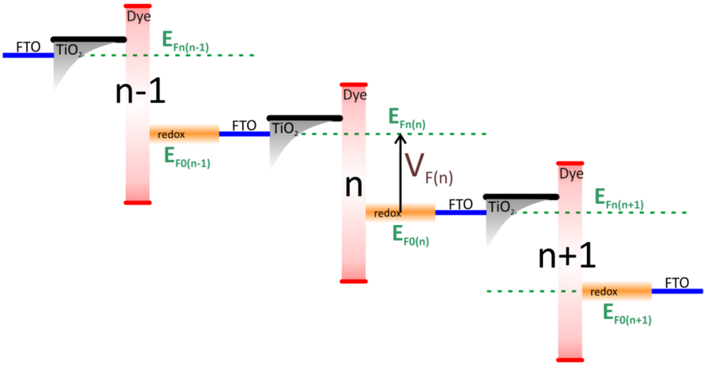

**Figure 7.13:** Energy levels in a module regarding to the unit *(n)*.

Taking into account Eq. (7.2) and (7.3), the current in a series connected DSC module with n units is:

$$i = i_{0(n)}\left[\exp\left(\frac{\beta_{(n)}q}{k_B T}V_{F(n)}\right)-1\right]-i_{sc(n)}+ \\ +i'_{0(n)}\left[-\exp\left(\frac{\beta'_{(n)}q}{kT}V_{F(n)}\right)+\exp\left(-\frac{\left(1-\beta'_{(n)}\right)q}{kT}V_{F(n)}\right)\right] \tag{7.4}$$

and

$$V_{F(total)}=\sum_{(n)}V_{F(n)} \tag{7.5}$$

where all the variables may have different values for each unit.

In real cells we have to consider de presence of the series resistance contribution of each individual cell producing a voltage loss within the module. From Eq. (3.15), a good approach to estimate the external potential of the module would be:

$$V_{app}=V_{F(total)}+\frac{i}{i-i_{sc}}\int_{i_{SC}}^{i}\sum_{(n)}\left[R_{series(n)}\right]di \tag{7.6}$$

### Behavior in other Configurations

The current bypass effect observed and interpreted for W-modules may also be observed in other DSC module configurations. In the case of monolithic solar cells, Figure 7.14, the current mismatch appearing in Figure 7.7 is not observed. In this case, all working electrodes are printed in the same substrate thus receiving the same light intensity. The *FF* here takes similar values than the obtained for the W-modules in Table 7.1, however, this low value is caused by the high series resistances instead of the current mismatch. As explained above, the electrolyte diffusion and the low conductivity of the counter electrode increase several times $R_{series}$.

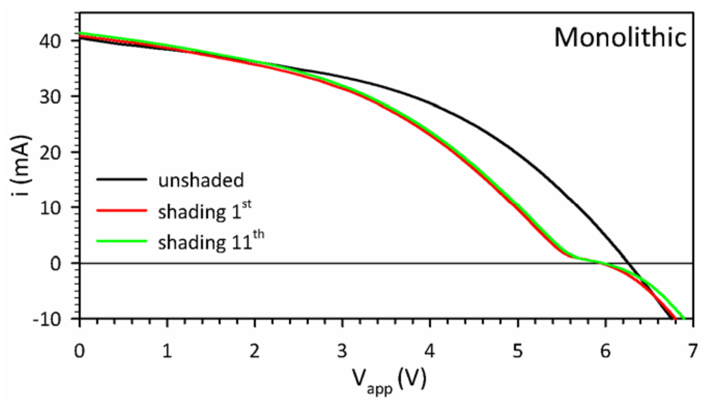

**Figure 7.14:** Current- voltage curve for the DSC monolithic module unshaded (black line) and shading one of the units with blue tape (red and green lines).

| Sample | $V_{oc}$ (V) | $i_{sc}$ (mA) | FF | η (%) |
|---|---|---|---|---|
| **Monolithic** | 6.26 | 40.65 | 0.45 | 1.92 |
| **Shading 1st** | 5.94 | 40.88 | 0.40 | 1.62 |
| **Shading 11th** | 5.94 | 41.44 | 0.40 | 1.65 |

**Table 7.4:** Photovoltaic parameters of the DSC module *i-V* curves from Figure 7.13. The individual $V_{oc}$ of every unit is around 0.6 V. This low $V_{oc}$ in respect to the automatized W-module (with the same electrolyte) is attributed to higher recombination.

In this case the counter electrode is completely opaque, thus when shading with the scotch tape, the unit is not receiving diffuse light from the surroundings and the current drops to very low values. If we observe in Figure 7.14 the "plateau" analogue to these of Figure 7.7, the length is less than 0.6V. This may be due, on the one hand, because of the deposition of carbon or Pt particles on the FTO, reducing its $R_{bl}$. On the other hand, these particles can also be adhered on the $TiO_2$ or reduced the dye loading, this may increase $R_{rec}$, in agreement with the lower in Voc obtained. The reduction in dye loading or pollution of dye molecules may also explain the low photocurrent obtained, about 7.4 mA·cm$^{-2}$.

## 7.7 Ornamental applications

One of the most attractive of the DSC seen in many photovoltaic tradeshows is the possibility of print designs acting as the active layer of the device. Taking profit of the multiple possibilities of printing methods, one can tune the opacities or even the color of a DSC. By printing different number of $TiO_2$ layers over the substrate, the thickness can be tuned, resulting in diverse tonalities of the adsorbed dye. A DSC with a printed logo as the one showed in Figure 7.15 can be employed as creative objects for office, as an example.

**Figure 7.15:** 10x10 cm$^2$ DSC with the logo of Universitat Jaume I with $i_{sc}$≈160mA and $V_{oc}$≈0.7V.

## 7.8 Conclusions

The upscaling of the laboratory-scale dye solar cells has been studied. The main advantages and drawbacks of three different DSC module structures have been described. Two 11-units W-module and one monolithic module have been constructed and characterized through *i*-*V* curves. In the case of the W-module it has been found a critical limitation in the performance of the whole device caused by the photocurrent mismatch between cells. However, compared with Si or thin film technologies, the effect of shadowing part of the DSC doesn't result in a dramatical decrease of the efficiency. On one hand, the $V_{oc}$ is maintained practically constant. At low illumination intensities, the dye molecules are still able to collect the diffuse light and inject enough electrons to the $TiO_2$ to achieve a rise of the $E_{Fn}$ in the system to an almost constant value. Thanks to these properties, the open circuit voltage may remain almost constant for a wide range of incident light. DSC efficiencies surpass those of classic semiconductor solar cells in cloudy days and under the illumination conditions such sunset and sunrise. Briefly, the open circuit voltage is not the limiting parameter for the overall performance of the DSC module.

On the other hand, although the major part of the module is shadowed, the short circuit current of the module is given by the more efficient of the units. The cell units transports the excess of current coming from the neighboring cells through ionic diffusion in the electrolyte. As reported, in previous studies based on Si or thin film solar cells, the shading of a series connected module present a real problem, limiting the applications of the solar cells to open areas. The partial shading generates a dramatic current drop limited by the shaded cells. The large reverse bias across the shaded cell produce an enormous power dissipation in a small area. Finally, it result in local overheating, or "hot-spots", which in turn leads to destructive effects, such as cell or glass cracking, melting of solder or degradation of the solar cell. This problem was overcame using bypass diodes in an external circuit of the solar cell module.[27,28] The bypass can only be applied on a set of series connected cells (between 12 and 36 cells), otherwise the circuit would be more complex and not viable to produce in commercial applications.[27]

In this manner, DSC modules present an advantage respect to other solar panels; an integrated circuit for evacuating the excess of charge on every shadowed unit. This advantage simplifies the processing of complete modules for outdoor applications, avoiding the step of the integration of external circuits including bypass diodes.

# References

(1) Green, M. A.; Emery, K.; Hishikawa, Y.; Warta, W.; Dunlop, E. D. Solar cell efficiency tables (version 40). *Progress in Photovoltaics: Research and Applications* **2012**, *20*, 606-614.

(2) http://www.g24i.com/pages,outdoor-power-solutions,87.html.

(3) http://www.dyesol.com/index.php?page=Dyesol+Commercialisation+of+DSC.

(4) Tulloch, G. E. Light and energy—dye solar cells for the 21st century. *Journal of Photochemistry and Photobiology A: Chemistry* **2004**, *164*, 209-219.

(5) Sastrawan, R.; Beier, J.; Belledin, U.; Hemming, S.; Hinsch, A.; Kern, R.; Vetter, C.; Petrat, F. M.; Prodi-Schwab, A.; Lechner, P.; Hoffmann, W. A glass frit-sealed dye solar cell module with integrated series connections. *Solar Energy Materials and Solar Cells* **2006**, *90*, 1680-1691.

(6) Dai, S.; Wang, K.; Weng, J.; Sui, Y.; Huang, Y.; Xiao, S.; Chen, S.; Hu, L.; Kong, F.; Pan, X.; Shi, C.; Guo, L. Design of DSC panel with efficiency more than 6%. *Solar Energy Materials and Solar Cells* **2005**, *85*, 447-455.

(7) Späth, M.; Sommeling, P. M.; van Roosmalen, J. A. M.; Smit, H. J. P.; van der Burg, N. P. G.; Mahieu, D. R.; Bakker, N. J.; Kroon, J. M. Reproducible manufacturing of dye-sensitized solar cells on a semi-automated baseline. *Progress in Photovoltaics: Research and Applications* **2003**, *11*, 207-220.

(8) Hanke, K. P. Upscaling of the Dye Sensitized Solar Cell*. *Zeitschrift für Physikalische Chemie* **1999**, *212*, 1-9.

(9) Hashmi, G.; Miettunen, K.; Peltola, T.; Halme, J.; Asghar, I.; Aitola, K.; Toivola, M.; Lund, P. Review of materials and manufacturing options for large area flexible dye solar cells. *Renewable and Sustainable Energy Reviews* **2011**, *15*, 3717-3732.

(10) Zhang, Y.-D.; Huang, X.-M.; Gao, K.-Y.; Yang, Y.-Y.; Luo, Y.-H.; Li, D.-M.; Meng, Q.-B. How to design dye-sensitized solar cell modules. *Solar Energy Materials and Solar Cells* **2011**, *95*, 2564-2569.

(11) Park, N. G.; van de Lagemaat, J.; Frank, A. J. Comparison of Dye-Sensitized Rutile- and Anatase-Based TiO2 Solar Cells. *The Journal of Physical Chemistry B* **2000**, *104*, 8989-8994.

(12) Hinsch, A.; Veurman, W.; Brandt, H.; Loayza Aguirre, R.; Bialecka, K.; Flarup Jensen, K. Worldwide first fully up-scaled fabrication of 60 × 100 cm2 dye solar module prototypes. *Progress in Photovoltaics: Research and Applications* **2012**, *20*, 698-710.

(13) Giordano, F.; Petrolati, E.; Brown, T. M.; Reale, A.; Di Carlo, A. Series-Connection Designs for Dye Solar Cell Modules. *Electron Devices, IEEE Transactions on* **2011**, *58*, 2759-2764.

(14) Han, L.; Fukui, A.; Chiba, Y.; Islam, A.; Komiya, R.; Fuke, N.; Koide, N.; Yamanaka, R.; Shimizu, M. Integrated dye-sensitized solar cell module with conversion efficiency of 8.2%. *Applied Physics Letters* **2009**, *94*, 013305-013303.

(15) Fukui, A.; Fuke, N.; Komiya, R.; Koide, N.; Yamanaka, R.; Katayama, H.; Han, L. Dye-Sensitized Photovoltaic Module with Conversion Efficiency of 8.4%. *Appl. Phys. Express* **2009**, *2*, 82202.

(16) Kay, A.; Grätzel, M. Low cost photovoltaic modules based on dye sensitized nanocrystalline titanium dioxide and carbon powder. *Solar Energy Materials and Solar Cells* **1996**, *44*, 99-117.

(17) Ito, S. T., Kaoru Fabrication of Monolithic Dye-Sensitized Solar Cell Using Ionic Liquid Electrolyte. *International Journal of Photoenergy* **2012**, *2012*, 6.

(18) Rong, Y.; Li, X.; Ku, Z.; Liu, G.; Wang, H.; Xu, M.; Liu, L.; Hu, M.; Xiang, P.; Zhou, Z.; Shu, T.; Han, H. Monolithic all-solid-state dye-sensitized solar module based on mesoscopic carbon counter electrodes. *Solar Energy Materials and Solar Cells* **2012**, *105*, 148-152.

(19) Pettersson, H.; Gruszecki, T. Long-term stability of low-power dye-sensitised solar cells prepared by industrial methods. *Solar Energy Materials and Solar Cells* **2001**, *70*, 203-212.

(20) Takeda, Y.; Kato, N.; Toyoda, T. Advances in monolithic series-interconnected solar-cell development. *Solar & Alternative Energy* **2009**, 3.

(21) Bradshaw, G.; Hughes, A. J. Etching methods for indium oxide/tin oxide films. *Thin Solid Films* **1976**, *33*, L5-L8.

(22) McLean, D.; Feldman, B. Method for etching; Feldman Technology Corporation, Watsonville, Calif.: USA, 1999.

(23) http://www.reuk.co.uk/Effects-of-Shading-on-Solar-Panels.htm.

(24) Quaschning, V.; Hanitsch, R. Numerical simulation of current-voltage characteristics of photovoltaic systems with shaded solar cells. *Solar Energy* **1996**, *56*, 513-520.

(25) Fabregat-Santiago, F.; Bisquert, J.; Garcia-Belmonte, G.; Boschloo, G.; Hagfeldt, A. Influence of electrolyte in transport and recombination in dye-sensitized solar cells studied by impedance spectroscopy. *Solar Energy Materials and Solar Cells* **2005**, *87*, 117-131.

(26) Bishop, J. W. Computer simulation of the effects of electrical mismatches in photovoltaic cell interconnection circuits. *Solar Cells* **1988**, *25*, 73-89.

(27) Silvestre, S.; Boronat, A.; Chouder, A. Study of bypass diodes configuration on PV modules. *Applied Energy* **2009**, *86*, 1632-1640.

(28) http://www.eurems.com/links-topics/technical-info/bypass-diodes.

# Chapter 8

## Conclusions

## 8.1 Conclusions

Here we summarize the main results and conclusions reported in this thesis. The dye-sensitized solar cells have been introduced in chapter 1 as a photovoltaic technology that can develop in a real contribution to solve the energetic problem. Chapter 2 reviews the materials employed in the fabrication of DSC, detailing the possible effects in the final performance of the device. All along the work we have demonstrated that the impedance spectroscopy represented a great tool for the analysis of the electrical behavior of DSC. This characterization technique has been described in detail in chapter 3.

The analysis of the origin of the open circuit potential in DSC, one of the fundamental parameters for solar cell performance, is the focus of attention in chapter 4. $V_{oc}$ was tuned by varying the additives in the electrolyte composition or the dye structure. It is shown how the photovoltage in solar cells can be exclusively described in terms of short circuit photocurrent and recombination resistance. The analysis method for the data obtained from IS, allowed the evaluation of the influence of conduction band shifts, recombination rate changes and short circuit photocurrent in the $V_{oc}$. This method can be straightforward applied for other photovoltaic devices.

The purpose of chapter 5 was the temperature effects in DSC. This is a parameter, many times forgotten in the laboratory research, but fundamental to describe real solar cell properties. In this study it is found an increase in FF induced by a overall decrease of the series resistances with rising temperatures up to 40º. The variation in $V_{oc}$ has been attributed to different recombination kinetics along the temperature range. At external temperatures ranging between -7 and 40ºC where $V_{oc}$ presents similar values, it is observed the same kinetic rate for $TiO_2$ electron recombination. As this is only occurring under illumination, the causes may have two origins. First, a rise in the temperature of active film may be caused by radiative heating from the light source. Second, an increase in the acceptor species in the electrolyte close to the $TiO_2$ surface after dye regeneration occurring under illumination. Above 40ºC recombination kinetics accelerates producing a decay in $V_{oc}$. The overall effect of both series and recombination resistances is a variation in DSC efficiency with a maximum on 40ºC. In this sense, it is important to highlight that at this common temperature for cell operation, the efficiency of DSC is closer to other technologies than under nominal conditions.

Other important issues for DSC have been also analyzed along this thesis. Chapter 6 studies the electrical properties of Uni-dimensional photonic crystals (1-DPC) which have been introduced in the literature as a method for enhance light harvesting in DSC. However, the insertion of an additional layer will induce higher diffusion resistance in the DSC. In this chapter, a method for enhancing the mass transport through nanoparticle multilayers displaying 1-DPC properties is provided. The concentration of polymer in the precursor suspensions is varied in order to tune the final porosity of the layers. Diffusion resistance ($R_d$) has been obtained for an electrolyte embedded in the structure from impedance spectroscopy measurements. It resulted in a linear dependence between porosity and $R_d$ with values as low as 1.3Ω for layers with 53% of porosity.

Finally, in chapter 7, most common techniques for upscaling DSC are reviewed. This represents the first step for the industrialization of these devices. When characterizing a W-module by *i*-*V* curves it is found a “stair shape” in the plots. This is found to be caused by a photocurrent mismatch between the module units. Contrary to the common result obtained in series connected Si solar cells, a shaded unit only limits partially the $i_{sc}$ of the module. Furthermore, it is found that the uncovered FTO at the working electrode acts as an integrated “bypass” diode in DSC. This protects shadowed cells from over currents at reverse polarizations. This is a great advantage for these devices as simplifies the process of complete module fabrication for outdoor applications. The step of the integration of external circuits with bypass diodes employed in Si solar cells is avoided in DSC.

In summary, this thesis contributes to understand several specific points for the application of the DSC as suitable solar cell technology: from the $V_{oc}$ formation fundamentals to the final module characterization, passing through the study of alternative scattering layers and the effect of temperature. This study would help in the optimization of DSC devices and its further application as active energy production technology.

# APPENDIX I

## LIST OF ABBREVIATIONS

| **Abbreviation** | **Description** |
|---|---|
| A | cell active area |
| ACN | acetonitrile |
| AM1.5G | air mass 1.5 global |
| a-Si | amorphous Silicon |
| BMII | 1-buthyl-3-methylimidazolium iodide |
| BP | boiling point |
| $C$ | capacitance |
| $C_{co}$ | capacitance at the FTO/$TiO_2$ interface |
| CB | conduction band |
| CIGS | Copper Indium Gallium Selenide |
| $C_\mu$ | chemical capacitance |
| $c_o$ | light speed |
| $c_{ox}$ | concentration of acceptor species |
| c-Si | crystalline Silicon |
| DI | deionized |
| $D$ | ionic diffusion coefficient |
| $D_n$ | electron diffusion coefficient |
| $D_{I_3^-}$ | ionic diffusion of $I_3^-$ |
| DOS | density of states |
| DSC | dye solar cell |
| $E_c$ | conduction band energy level |
| $E_{Fn}$ | electron Fermi level |
| $E_{F0}$, $E_{redox}$, $E_{Fp}$ | hole Fermi level |

| | |
|---|---|
| $E_g$ | band gap energy |
| $E'_0$ | standard redox potential |
| $E_t$ | transport level energy in $TiO_2$ |
| EQE | external quantum efficiency |
| $F$ | Faraday's constant |
| $f$ | frequency |
| FF | fill factor |
| FTO | fluorine-doped tin oxide |
| GuSCN | guanidinium thiocyanate |
| $h$ | Planck's constant |
| HOMO | highest occupied molecular orbital |
| $i$ | current |
| $i_{pp}$ | current at the peak power |
| $\hat{I}$ | small current perturbation |
| IL | ionic liquid |
| IPCE | incident photon to current efficiency |
| IR | infrared |
| IS | impedance spectroscopy |
| $j_0$ | reverse dark current density |
| $j_{lim}$ | diffusion-limited current density |
| $j_{max}$ | current at the maximum power point |
| $j_{rec}$ | recombination current density |
| $j_{sc}$ | short circuit current density |
| $j$-$V$ | current density- voltage |
| $k_B$ | Boltzmann's constant |
| $k_r$ | internal recombination |

| | |
|---|---|
| $k_{rec}$ | recombination kinetics constant |
| $L$ | film thickness |
| LED | light emitting diodes |
| LiI | lithium iodide |
| $L_n$ | electron diffusion length |
| LUMO | lowest unoccupied molecular orbital |
| $m$ | ideality factor for a diode |
| MP | melting point |
| MPN | methoxypropionitrile |
| NHE | normal hydrogen electrode |
| $n_c$ | number of free carriers |
| $n_{eff}$ | refractive index |
| $n_L$ | number of trapped electrons |
| NOCT | normal operation cell temperature |
| $N_c$ | total number of electronic states |
| $N_{electron}$ | number of generated carriers in a DSC |
| $N_L$ | total electron trap density |
| $N_{photon}$ | number of incident photons in a DSC |
| $N_s$ | total number of states |
| $N_t$ | total number of trap states below the CB |
| np | nano particle |
| OSC | organic solar cell |
| $p$ | porosity of the nanostructured film |
| PE | phenylethynyl |
| PEG | polyethylene glycol |
| pc-Si | polycrystalline Silicon |

| | |
|---|---|
| PC | photonic crystals |
| $P_{inc}$ | incident power of light |
| PV | photovoltaic |
| $q$ | electron charge |
| $R$ | gas constant |
| $R_{bl}$ | back layer resistance |
| $R_{co}$ | resistance at the FTO/$TiO_2$ interface |
| $R_d$ | diffusion resistance |
| $R_{FTO}$ | FTO resistance |
| $R_{Pt}$ | platinized counter-electrode resistance |
| $R_{rec}$ | recombination resistance |
| $R_{series}$ | series resistance |
| $R_{sh}$ | shunt resistance |
| $R_{tr}$ | transport resistance |
| SEM | scanning electron microscope |
| $T$ | absolute temperature |
| $T_0$ | coefficient for the depth of the DOS |
| $t$ | time |
| tBP | 4-*tert*-butylpiridine |
| TCO | transparent conductive oxide |
| UV | ultraviolet |
| $V$, $V_{app}$ | external applied voltage |
| $V_{ecb}$ | equivalent conduction band voltage |
| $v_{eff}$ | effective volume of the film |
| $V_F$ | corrected potential |
| $\Delta V_k$ | voltage shift due to recombination rates |

| | |
|---|---|
| $V_{max}$, $V_{pp}$ | voltage at the maximum power point |
| $V_{oc}$ | open circuit voltage |
| $\Delta V_{Rrec}$ | voltage shift due to $R_{rec}$ |
| $\hat{V}$ | small voltage perturbation |
| $Z$ | complex impedance |
| $Z'$ | real impedance |
| $Z''$ | imaginary impedance |
| $Z_d$ | diffusion impedance |
| 1DPC | one-dimensional photonic crystals |
| $\alpha$ | electron trap distribution parameter |
| $\beta$ | recombination parameter |
| $\phi$ | incident photon flux |
| $\theta$ | angle of incidence of sunlight |
| $\eta$ | power conversion efficiency |
| $\eta_{opt}$ | optical efficiency |
| $\lambda$ | wavelength |
| $\nu$ | electromagnetic frequency |
| $\sigma$ | conductivity |
| $\tau_n$ | electron lifetime |
| $\omega$ | angular frequency |
| $\omega_d$ | characteristic diffusion frequency |

# APPENDIX II

## ACKNOWLEDGEMENTS

I wish to thank, in the first place, Dr. Francisco Fabregat Santiago for his encouragement and guidance during my phD from the very beginning. He helped me to develop my research skills and build my knowledge base in physics. I also thank Dr. Iván Mora Serò for his enthusiasm and his very inspirational discussions. He has been a great support in every step of this work. They both have made me enjoy science.

I really acknowledge Prof. Juan Bisquert, leader of the growing group “Grup de Dispositius Fotovoltaics and Optoelectronics” in the Universitat Jaume I. He has given me the opportunity to be part of his team during this three years, where I have had the chance to develop my knowledge and make good relationships with researchers from all around the world.

I thank Dr. Toby Meyer for giving me the opportunity to visit his company Solaronix where I learnt a lot about DSC and modules. I also thank David, Fredéric and all the people in the company for helping me every day during my stay there. Merci! I also thank Dr. Thomas Moehl for his kind support in my visit at EPFL. Danke!

Of course, I express my gratitude to all my colleagues and members of the group, whose fruitful discussions helped a lot in my work. I also thank all the doctors, students, visitors, administrative and technical staff for the insuperable moments we had both in the laboratory and in the bars.

Finally, I want to acknowledge all my family and friends for their patience and support in these years. Gràcies!

# APPENDIX III

## PUBLICATIONS AND CONFERENCES

### Publications related with this thesis:

**“Analysis of the Origin of Open Circuit Voltage in Dye Solar Cells”**
Raga, S. R.; Barea, E. M.; Fabregat-Santiago, F.
*The Journal of Physical Chemistry Letters* **2012**, *3*, 1629-1634.
**DOI:** 10.1021/jz3005464

**“Design and characterization of alkoxy-wrapped push-pull porphyrins for dye-sensitized solar cells”**
Ripolles-Sanchis, T.; Guo, B.-C.; Wu, H.-P.; Pan, T.-Y.; Lee, H.-W.; Raga, S. R.; Fabregat-Santiago, F.; Bisquert, J.; Yeh, C.-Y.; Diau, E. W.-G.
*Chem. Commun.* **2012**, *48*, 4368-4370.
**DOI:** 10.1039/C2CC31111A

**“Temperature effects in dye-sensitized solar cells”**
Sonia R. Raga, Francisco Fabregat-Santiago.
*Physical Chemistry Chemical Physics* **2013**, *15*, 2328-2336.
**DOI:**10.1039/C2CP43220J

**“Enhanced diffusion through porous nanoparticle optical multilayers”**
Lopez-Lopez, C.; Colodrero, S.; Raga, S. R.; Lindstrom, H.; Fabregat-Santiago, F.; Bisquert, J.; Miguez, H.
*Journal of Materials Chemistry* **2012**, *22*, 1751-1757
**DOI:** 10.1039/C1JM15202E

### Other publications:

**“$SiO_2$ Aerogel Templated, Porous $TiO_2$ Photoanodes for Enhanced Performance in Dye-Sensitized Solar Cells Containing a Ni(III)/(IV) Bis(dicarbollide) Shuttle”**
Tina C. Li, Francisco Fabregat-Santiago, Omar K. Farha, Alexander M. Spokoyny, Sonia R. Raga, Juan Bisquert, Chad A. Mirkin, Tobin J. Marks, and Joseph T. Hupp
*Journal of Physical Chemistry C* **2011,** 115, 11257–11264
**DOI:** 10.1021/jp112139h

**“How Charge-Neutrality Level of Interface States Controls Energy Level Alignment in Cathode Contacts of Organic Bulk-Heterojunction Solar Cells”**
Antonio Guerrero, Luís Fernando Quintino Pereira Marchesi, Pablo P. Boix, Sonia Ruiz-Raga, Teresa Ripollés-Sanchis, Germà Garcia-Belmonte, and Juan Bisquert
*ACS Nano* **2012**, 6 (4), 3453–3460
**DOI:** 10.1021/nn300486a

**“Molecular Electronic Coupling Controls Charge Recombination Kinetics in Organic Solar Cells of Low Bandgap Diketopyrrolopyrrole, Carbazole and Thiophene Polymers”**
Ripolles-Sanchis, Teresa; R.Raga, Sonia; Guerrero, Antonio; Welker, Matthias; Turbiez, Mathieu; Bisquert, Juan; Garcia-Belmonte, Germà
Journal of Physical Chemistry C, **2013**, Accepted

## Conference assistance:

National School of Molecular Materials. Peñafiel (Spain). February **2010**

European Science Foundation grant, hosted by Prof. Michael Graetzel. Research visit in EPFL working on Solid State Dye Solar Cells. Lausanne (Switzerland). April **2010**

HOPV 10 (Hybrid and Organic Photovoltaics) congress. Assissi (Italy). May **2010**

ISOPHOS (International School on Organic Photovoltaics). Oral presentation entitled “*Preparation and Characterization of Dye Solar Cells*”. Ventotene (Italy). September **2010**

ESMOLNA (European School on Molecular Nanoscience). Oral presentation entitled “Impedance Characterization for Dye-Sensitized Solar Cells” Madrid (Spain). October **2010**

HOPV 11 (Hybrid and Organic Photovoltaics) congress. Valencia (Spain). May **2011**

ISUenergy (International Summer University on Energy). Falera (Switzerland). August **2011**

Zing Conferences: Electrochemistry . Lanzarote (Spain). February **2012**

HOPV 12 (Hybrid and Organic Photovoltaics) congress. Presentation of a poster entitled “*Temperature effects on Dye-Sensitized Solar Cells*”. Uppsala (Sweden). May **2012**

THE JOURNAL OF PHYSICAL CHEMISTRY Letters
Letter
pubs.acs.org/JPCL

# Analysis of the Origin of Open Circuit Voltage in Dye Solar Cells

Sonia R. Raga,* Eva M. Barea, and Francisco Fabregat-Santiago*

Photovoltaics and Optoelectronic Devices Group, Departament de Física, Universitat Jaume I, 12071 Castelló, Spain

**ABSTRACT:** Changes in the composition of the electrolyte are known to affect the parameters that determine the performance of dye solar cells. This paper describes a robust method for the analysis of the photovoltage in dye solar cells. The method focuses on the study of recombination resistance and chemical capacitance of $TiO_2$ obtained from impedance spectroscopy. Four dye solar cells with electrolytes producing known effects on photovoltage behavior have been studied. Effects of conduction band shifts and changes in recombination rate in the photovoltage have been evaluated quantitatively.

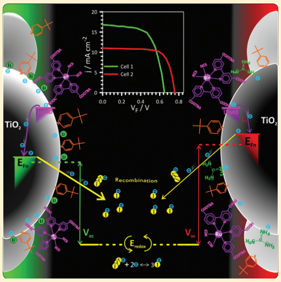

**SECTION:** Energy Conversion and Storage; Energy and Charge Transport

Dye-sensitized solar cells (DSCs) have attracted significant attention as alternatives to conventional solid-state photovoltaic devices during past decades.[1] This technology is suggested to be produced at a lower cost than silicon-based solar cells thanks to the easy manufacturing procedures and low temperatures used in its fabrication. DSC performance has reached power conversion efficiencies exceeding 12%.[2,3]

The operation of DSCs may be summarized as follows: Under illumination, a dye attached to a nanostructured semiconductor (generally $TiO_2$) absorbs a photon. This photon excites one electron from the highest occupied molecular orbital (HOMO) level into the lowest unoccupied molecular orbital (LUMO). The electron is injected from the LUMO of the dye to the conduction band (CB). Simultaneously, the oxidized dye is regenerated by a redox couple present in an electrolyte surrounding the semiconductor. Once the charges are separated between the semiconductor and electrolyte media, they can diffuse toward the contacts where they are collected.

The parameters determining DSCs solar to power conversion are the short circuit current density ($j_{sc}$), the open circuit photovoltage ($V_{oc}$) and the fill factor (FF). $j_{sc}$ is given by the light harvesting efficiency of the dye, its capacity to inject electrons into the $TiO_2$ CB, and the ability of the semiconductor to transport them to the collecting electrode. $V_{oc}$ is given by the difference of the Fermi level of electrons in the $TiO_2$ and the redox potential of the electrolyte, $V_{oc} = (E_{Fn} - E_{redox})/q$.[4] Finally, FF provides the reduction of the real power with respect to the product $j_{sc} \times V_{oc}$. FF is controlled mainly by total series resistance of the DSC, although it also has some contribution from recombination resistance.[5,6]

At the current stage of DSC development, the photocurrent is only limited by the absorption spectra of the dye, as most top class laboratories are able to collect nearly 100% of photogenerated electrons. Contributions of series resistance have been also reduced to a minimum through the right design of cell geometries and choice of materials. These improvements together with the use of small area samples provide large and reproducible FFs. In this scenario, the decisive parameter to enhance the performance of DSC is the open circuit photovoltage.

The maximum theoretical $V_{oc}$ attainable by a solar cell is limited by the gap of the absorber. In the case of DSC, the effective gap of the dyes attached to $TiO_2$ lies around 1.60 eV.[7,8] However, best cells rarely reach $V_{oc}$ values larger than half of this value. The main losses reducing photovoltage from its theoretical limit are the energy mismatches between $E_{redox}$ and HOMO levels and between the $E_c$ of the semiconductor and the LUMO of the dye, which reduce the maximum attainable voltage to $(E_c - E_{redox})/q$, and the electron recombination in the semiconductor film that determines the final $E_{Fn}$ position.[9,10]

The purpose of this work is to deepen the understanding of the relationship between recombination losses and $V_{oc}$. With this aim, impedance spectroscopy (IS) was used to accurately evaluate the effects of changes in electrolyte composition over charge recombination in $TiO_2$. A new procedure to analyze the origin of $V_{oc}$ is proposed. This procedure allows separating the effects of $TiO_2$ CB shifts and recombination rate variations in photovoltage.[10,11]

To fulfill this objective, the $V_{oc}$ was tuned by adding electrolyte additives such as LiI, 4-*tert*-butylpyridine (tBP), 1-butyl-3-methylimidazolium iodide (BMII), and guanidinium thiocyanate (GuSCN), whose effect on the photovoltage is

**Received:** May 2, 2012
**Accepted:** June 1, 2012
**Published:** June 1, 2012

dx.doi.org/10.1021/jz3005464 | *J. Phys. Chem. Lett.* 2012, 3, 1629−1634

well-known. The electrolyte composition is shown in Table 1, and a description of the role of each of these additives follows.

### Table 1. Composition of Electrolytes Employed in the Fabrication of DSCs[a]

| electrolyte/DSC name | BMII | $I_2$ | GuSCN | LiI | tBP | solvent |
|---|---|---|---|---|---|---|
| A | 0.6 M | 0.03 M | 0.1 M | | 0.5 M | A/V (85:15) |
| B | | 0.05 M | | 0.5 M | 0.5 M | MPN |
| C | | 0.05 M | | 0.5 M | | MPN |
| D | 0.6 M | 0.03 M | 0.1 M | | 0.5 M | MPN |

[a] Abbreviations of the additives are as follows: BMII for 1-butyl-3-methylimidazolium iodide, GuSCN for guanidinium thiocyanate, LiI for Lithium Iodide, tBP for 4-*tert*-butylpyridine. The solvent denominations are MPN for methoxypropionitrile, and A/V for a mixture of acetonitrile and valeronitrile 85:15 in volume.

Lithium iodide is a very stable salt widely used in electrochemistry. It provides the necessary iodide anions for the redox couple in the electrolyte and the lithium cations needed to screen the negative charge in the semiconductor, and increases charge conductivity in the electrolyte. The presence of positive ions at the $TiO_2$ surface is known to produce a downward shift in the CB of the semiconductor, with respect to a situation in which they are not present. Previous works have reported that, the smaller the size of the cation and the larger the shift in CB, the higher the photocurrent and the lower the $V_{oc}$.[12,22] At long-term, the extremely small size of $Li^+$ allows it to intercalate into a $TiO_2$ lattice, degrading electron transport and recombination properties.[13] For these reasons, although convenient in this study, lithium is avoided in the fabrication of DSCs designed for long lifetimes.

tBP (Figure 1a) is reported to produce a significant upward band edge movement, thus increasing $V_{oc}$. This band-edge shift is attributed to deprotonation of $TiO_2$ nanoparticles by amines that, together with a displacement of cations from the surface, reduces the positive charge allocated right on the semiconductor.[14] By contrast, tBP adsorbed on the semiconductor surface coats the area not covered by the dye. This fact blocks the recombination to the redox couple in the electrolyte.

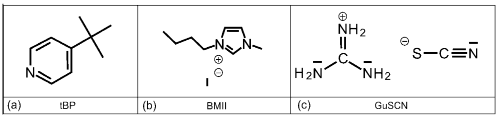

Figure 1. Molecular structures of some of the additives commonly used in DSC electrolytes: (a) tBP, (b) BMII, and (c) GuSCN. Dash on the amine group (c) stands for the nonbonding electron pair on the nitrogen atom.

Ionic liquids such as 1-butyl-3-methylimidazolium iodide (BMII) (Figure 1b) present some advantages in DSC electrolyte applications. The $BMI^+$ molecule is a bigger cation than $Li^+$ and has two amine groups in its structure. Consequently, the CB in $TiO_2$ remains at a higher energy than when using lithium, and the cation is not able oto intercalate into the semiconductor structure. Furthermore, $BMI^+$ appears to be very effective at shielding the semiconductor surface from charge recombination toward the electrolyte.[5,15]

Cations from GuSCN in Figure 1c are reported to shift downward at the $TiO_2$ CB around 100 mV.[17] This fact increases electron injection efficiency from the dye, enhancing photocurrent. In contrast to what is expected, GuSCN also improves $V_{oc}$, as the adsorption of the guanidinium cation on the $TiO_2$ surface produces a very effective surface passivation layer, yielding a notable decrease in recombination rate.[16,17]

In this study we also analyzed the effect of two different solvents: an acetonitrile/valeronitrile mixture and methoxypropionitrile. Acetonitrile/valeronitrile is widely used for high efficiency DSCs. The low viscosity of this solvent reduces diffusion resistance in the electrolyte, a requisite to obtain good fill factor and efficiency of the device.[5] Methoxypropionitrile is commonly chosen, as its low volatility improves long-term stability of the devices.

*j*−*V* curves of DSC made with the four different electrolytes of Table 1 taken under 1 sun illumination intensity are presented in Figure 2. The photovoltaic parameters obtained from these curves are shown in Table 2.

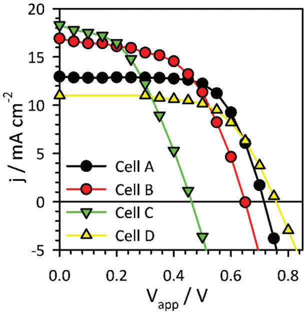

Figure 2. *j*−*V* curves of the DSCs with different electrolytes as described in the text (lines) and obtained from IS measurements (symbols). The open circuit voltages differ significantly with the additives contained in the electrolyte.

### Table 2. Photovoltaic Performance Parameters of DSCs Analyzed[a]

| | area ($cm^2$) | $V_{oc}$ (V) | $J_{sc}$ ($mA/cm^2$) | FF | $\eta$ (%) |
|---|---|---|---|---|---|
| cell A | 0.25 | 0.716 | 12.92 | 0.67 | 6.19 |
| cell B | 0.28 | 0.650 | 16.91 | 0.53 | 5.95 |
| cell C | 0.25 | 0.462 | 18.30 | 0.44 | 3.70 |
| cell D | 0.25 | 0.758 | 11.00 | 0.63 | 5.22 |

[a] The name of the cells refers to the name of the electrolyte they contain given in Table 1.

Dye solar cells prepared with electrolytes A and D present similar open circuit voltage. These electrolytes only differ on the solvent, while they contain the same additives and concentrations. This result suggests that the nature of both solvents has little effect on the photovoltage. For cells B and C, the $V_{oc}$ is much lower. These cells contain lithium iodide in the electrolyte, and neither contain ionic liquid nor GuSCN. This decrease is more pronounced for cell C, which does not contain tBP. On the other hand, cells B and C provide higher photocurrent than cells A and D.

In this first view of *j*−*V* curve results, the origin of the photovoltage variation found is not conclusive, as the additives

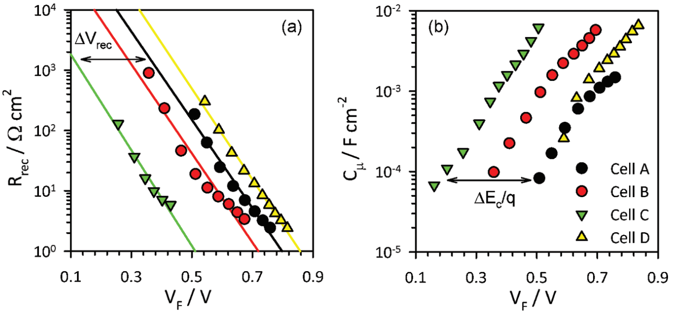

**Figure 3.** Impedance results of the cells with different electrolytes. (a) Recombination resistance between the semiconductor and the acceptor species in the electrolyte. (b) Chemical capacitance of the TiO$_2$. Voltage drop due to internal series resistance has been corrected in all plots. $\Delta V_{rec}$ and $\Delta E_c/q$ beween samples A and C are represented in panels a and b, respectively.

of the electrolytes are expected to affect both the CB energy level and recombination rates.

For a fine evaluation of the influence of the different additives used on the electrical response of the DSCs, we may use IS data. IS is a common technique that provides information about charge transport, accumulation, and loses in films and devices. Details about the interpretation of the parameters obtained through IS data in connection to the performance of DSCs are provided in recent papers.[11,18] Here we will focus in the analysis of the changes in recombination resistance ($R_{rec}$) and chemical capacitance ($C_\mu$) and their relationship with the photovoltage. Results of $R_{rec}$ and $C_\mu$ obtained from the fitting of the Nyquist plots of the impedance spectra are shown in Figure 3. These values have been represented after subtracting the effect of the series resistance on the voltage,

$$V_F = V_{app} - V_{series} \tag{1}$$

where $V_F$ is the corrected voltage, $V_{app}$ is the applied voltage during the measurement, and $V_{series} = [j/(j_{sc} - j)]\int_{j_{sc}}^{j} R_{series}\, dj$ is the voltage drop at the total series resistance.[5] Main contributions to $R_{series}$ are given by the contacts, the conducting glass, charge transfer at the Pt counter-electrode, and electrolyte diffusion resistances.

The first clear result observed in Figure 3a is the strong correlation between $V_{oc}$ and $R_{rec}$: Using cell A as a reference, the voltage differences found in the $V_{oc}$ of the samples analyzed match very well with the voltage shift in $R_{rec}$ ($\Delta V_{R_{rec}}$) observed in Figure 3a (see Table 3). This indicates that $R_{rec}$ is the parameter that dominates photovoltage, despite the differences in $j_{sc}$.

This behavior has its origin in the relationship between the resistance, the current, and the voltage given by[18]

$$R_{rec} = \left(\frac{\partial j_{rec}}{\partial V_F}\right)^{-1} \approx R_0 \exp\left[-\beta\frac{qV_F}{k_BT}\right] \tag{2}$$

where $j_{rec}$ is the current for charge losses produced by recombination ($j = j_{sc} - j_{rec}$), $\beta$ is a coefficient given by the nonlinear charge transfer ($\beta < 1$) of electrons in TiO$_2$ to electrolyte, $q$ is the electron charge, $k_B$ is Boltzmann's constant, $T$ is the temperature, and $R_0$ is a parameter that determines the activation of recombination given by[18,19]

### Table 3. Photovoltaic Parameters Obtained from IS Analysis[a]

| parameters | Cell A | Cell B | Cell C | Cell D |
|---|---|---|---|---|
| average $R_{series}$ (Ω) | 15.1 | 15.8 | 22.3 | 27.3 |
| $R_0$ (Ω cm$^2$) | $6.82 \times 10^5$ | $2.05 \times 10^5$ | $1.13 \times 10^4$ | $2.87 \times 10^6$ |
| $\beta$ | 0.439 | 0.443 | 0.477 | 0.452 |
| $\alpha$ | 0.282 | 0.308 | 0.349 | 0.259 |
| calculated $V_{oc}$ (V) | 0.712 | 0.651 | 0.454 | 0.768 |
| $E_c - E_{redox}$ (eV) | 0.976 | 0.801 | 0.618 | 0.936 |
| $\Delta E_c/q$ vs ref (mV) | ref. | −180 | −330 | −50 |
| $\Delta V_k$ (mV) | ref. | +114 | +78 | +96 |
| $\Delta V_{R_{rec}}$ (mV) | ref. | −66 | −252 | +44 |

[a] $R_{series}$ is the series resistance of the cell; $R_0$ is the recombination prefactor parameter from eq 3; $\beta$ is the charge transfer coefficient for recombination of electrons; $\alpha$ is the exponential electron trap distribution parameter; calculated $V_{oc}$ is the open circuit voltage obtained from eq 6 at $T = 305$ K; $E_c - E_{redox}$ is the value estimated from eq 9, taking $N_t = 2.5 \times 10^{19}$ cm$^{-3}$; $\Delta E_c$ vs ref is the energy shift needed to compare all the cells at the same CB level obtained after displacing the capacitances in Figure 3b; $\Delta V_k$ is the voltage difference in $R_{rec}$ due to the differences in recombination rates; $\Delta V_{R_{rec}}$ is the sum of $\Delta E_c/q$ and $\Delta V_k$.

$$R_0 = \frac{\sqrt{\pi\lambda k_BT}}{q^2 L\alpha k_r c_{ox} N_s}\exp\left[\alpha\frac{E_c - E_{redox}}{k_BT} + \frac{\lambda}{4k_BT}\right] \tag{3}$$

with $L$ being the film thickness, $c_{ox}$ the concentration of acceptor species (here $I_3^-$) in the electrolyte, $\lambda$ the reorganization energy of the acceptor species, $N_s$ the total number of surface states contributing to the recombination, $\alpha$ a parameter related to the electron trap distribution below the CB, and $k_r$ the rate constant accounting for recombination kinetics.

In general, as may be observed in Figure 3a, $R_{rec}$ approaches quite well the single exponential behavior given in eq 2. This fact together with the general approach for the $j$−$V$ curve in DSC[18,20]

$$j = j_{sc} - j_0(\exp[\beta qV_F/k_BT] - 1) \tag{4}$$

yields

$$j = j_{sc} + j_0 - \frac{k_B T}{\beta q}\frac{1}{R_{rec}} \tag{5}$$

where $j_0 = k_BT/\beta qR_0$ is a constant equivalent to reverse bias dark current in p−n junction diodes and solar cells. Equation 5 together with eq 2 yields, at open circuit conditions ($j = 0$),

$$V_{oc} = \frac{k_B T}{\beta q} \ln \frac{\beta q R_0 j_{sc}}{k_B T} \tag{6}$$

As may be seen in Table 3, calculation of open circuit photovoltage using eq 6 with the values of $R_0$ and $\beta$ extracted from Figure 3a fit well (within 10 mV error) with the values obtained from the $j$−$V$ curve in Table 2. Therefore, once the photocurrent is known, eq 6 allows calculating $V_{oc}$ exclusively from recombination parameters. Note that this expression is very close to others generally used in the literature but using direct experimental parameters obtained from IS.[9]

A quick look to eq 6 and Tables 2 and 3 suggests that, as $\beta$ is similar in all the samples, and the changes in the value of $j_{sc}$ only may produce small modifications in the logarithm calculation, the main element determining the differences in $V_{oc}$ is the prefactor $R_0$ of the recombination resistance. This assumption agrees well with the results commented above.

To complete this analysis, the origin of the observed differences in $R_{rec}$ was investigated. Equation 3 shows the dependence of $R_0$ (and then $V_{oc}$) on both the energy difference $E_c - E_{redox}$ and the rate $k_r$ at which the electrons in $TiO_2$ are lost. Quantification of the contribution of each of these effects to the voltage is feasible with data obtained from IS. First, it is needed to have an estimation of the position of the CB, or at least of its shift ($\Delta E_c$) with respect to a reference (cell A in our case). Then, using the definition of the voltage at the equivalent CB position,[18]

$$V_{ecb} = V_F - \Delta E_c/q \tag{7}$$

it will be possible to compare all the samples at a voltage in which the $TiO_2$ contains the same electron concentration.

The chemical capacitance, $C_\mu$, represented in Figure 3b, provides quantitative information about the position of the CB as[21]

$$C_\mu = C_0 \exp[\alpha q V_F/k_B T] \tag{8}$$

with

$$C_0 = L(1-p)\alpha \frac{q^2 N_t}{k_B T} \exp[\alpha(E_{redox} - E_c)/k_B T] \tag{9}$$

being a constant, $N_t$ the total number of trap states below the CB, and $p$ the porosity of the film. Provided that all the films have the same geometrical dimensions and assuming that the additives do not change the number of traps in the $TiO_2$, shifts in the capacitance of Figure 3b are equivalent to shifts in $E_c$. This procedure was used to calculate the $\Delta E_c$ shown in Table 3, which, within experimental error, matches quite well with the changes in $E_c - E_{redox}$ obtained from eq 9. In Figure 4 one can see the collapse of the capacitance of all the samples in the representation at $V_{ecb}$.

The data in Table 3 and Figure 3b show the different displacement of the CB toward lower energies for samples B, C, and D with respect to sample A. The small difference found for samples A and D indicates that the change in solvent has a minor role in changing the CB. By contrast, and according to expectations, for sample B, the use of LiI instead of BMII and GuSCN results in a large downward shift in CB, which is even greater for the sample with electrolyte C in which tBP is not present.

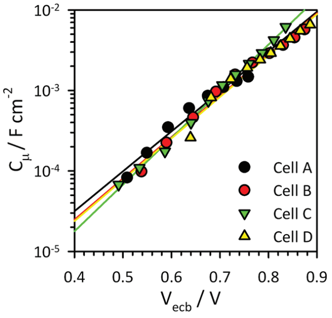

**Figure 4.** Chemical capacitance represented at the same energy level of the CB, taking cell A as a reference.

The values of $\Delta E_c/q$ and $\Delta V_{oc}$ do not match; otherwise when $j$−$V$ curves were compared at $V_{ecb}$ as in Figure 5a, the displaced $V_{oc}$ would match for all the samples. This result suggests that changes in the rate transfer due to the variations in electrolyte composition produce relevant effects in the photopotential. The relative value of this contribution, labeled $\Delta V_k$ in Table 3, may be obtained measuring the voltage difference between $R_{rec}$ of the different samples in Figure 5b. As this representation of $R_{rec}$ is free from the effect of CB shifts, $\Delta V_k$ computes the voltage contribution of recombination kinetics to the $V_{oc}$ for the different cells. Therefore it is possible to calculate the contribution to the photovoltage due to changes in the rate constant, despite the fact that absolute values of $k_r$ could not be estimated as the value of $N_s$ is not known.

It was found that $\Delta V_k$ takes values very close to the differences in the displaced $V_{oc}$ of Figure 5(a). As may be seen from Table 3, the sum of $\Delta V_k$ and $\Delta E_c/q$ represents the main contributions to photovoltage.

The values obtained for $\Delta V_k$ fit well with the expected effect of the electrolytes in the properties of the cells.[14−17] Thus when comparing the samples with the same solvent at $V_{ecb}$, it is found that cell C presents the lower $R_{rec}$ (and lower $\Delta V_k$) of the three. This agrees with the fact that this electrolyte has no surface blocking additives that would yield a larger $k_r$ and smaller $R_0$. In the case of the sample with electrolyte B, the addition of tBP displaces the $V_{oc}$ 18 mV upward. The extra addition of BMII and GuSCN in electrolyte D adds another 20 mV to the photovoltage with respect to sample B.

Focusing on samples A and D with the same additives but different solvents, it is observed that cell A presents a higher internal recombination that diminishes the displaced $V_{oc}$ in 96 mV with regard to cell D. This result suggests that the passivation of the surface of $TiO_2$ with GuSCN and tBP is more efficient in the MPN-based electrolyte.

Finally, a small contribution to the $V_{oc}$ has its origin in the differences of photocurrent obtained for the different cells. Thus, for a given $R_{rec}$, the larger photocurrent pushes the $j$−$V$ curve upward, yielding an increase in $V_{oc}$.[11] However, and as indicated above, in general, photocurrent contribution to photovoltage is small, as it is governed by eq 6.

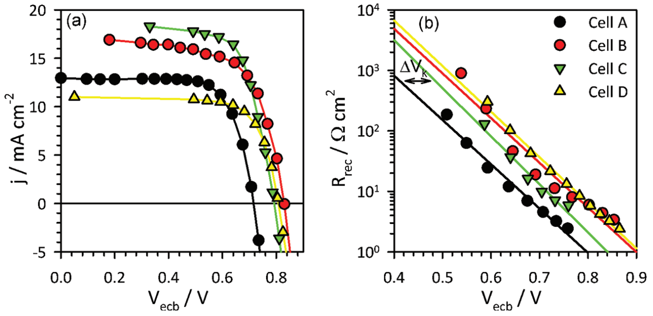

**Figure 5.** Values of $j-V$ curves (a) and recombination resistance (b) represented at the equivalent CB position taking cell A as a reference. In panel b, the potential shift $\Delta V_k$ between cells A and C is plotted.

The explanation of the differences between the photocurrent of the different samples fits well with the one done in previous works: The downward shift of $E_c$ in the semiconductor leads to an enhancement of the electron injection efficiency from the dye to the $TiO_2$. The higher the distance between the LUMO level of the excited dye and the CB of $TiO_2$, the more favorable the charge transfer.[22−24] A maximum is found when all the light harvested by the dye is collected.

In summary, it has been shown that photovoltage in solar cells can be exclusively described in terms of short circuit photocurrent and recombination resistance. The method proposed here for the analysis of the data allowed evaluating the influence of CB shifts, recombination rate changes, and short circuit photocurrent in the photovoltage. In the cases presented here, changes in both CB and rate constants for recombination dominated the $V_{oc}$. Potentially, the procedure may be applied in the analysis of other solar cell technologies.

## ■ EXPERIMENTAL SECTION

*DSC Preparation.* Working electrodes for the DSC were prepared on a 15 Ω/□ FTO glass previously cleaned. A 150 nm compact $TiO_2$ layer was deposited by spray-pyrolisis technique with a solution of ethanol/acetil acetone/titanium(IV) isopropoxide (3:3:2 weight ratio) and a 450 °C hot plate. The substrates were coated by doctor blade technique with a 7 μm layer of 20 nm $TiO_2$ nanoparticles and a 3 μm scatter layer of 450 nm $TiO_2$ nanoparticles (respectively 18-NRT and WER0-4 from Dyesol), and calcined at 450 °C for 30 min. After sintering, films were immersed into 40 mM $TiCl_4$ (aq) at 70 °C for 30 min, rinsed with Milli-Q water, and sintered at 570 °C for 10 min. After cooling down to 40 °C, the $TiO_2$ electrodes were immersed overnight into a 0.5 mM dye solution containing Ditetrabutylammonium cis-bis(isothiocyanato) bis(2,2′-bipyridyl-4,4′-dicarboxylato) ruthenium(II) (N719) in a mixture of acetonitrile and *tert*-butanol 1:1 volume ratio.

As counter electrodes, 8 Ω/□ FTO-coated glasses were drilled with a 1 mm diameter drill tip and cleaned. Over this electrode, a drop of chloroplatinic acid solution from Sigma Aldrich was spread, and the resulting glass was fired in a 450 °C air flow.

The working and counter electrodes were assembled in a sandwich-type cell by pressing at 95 °C with a hot-melt film (Surlyn 25 μm thickness) as a sealant and spacer between electrodes. A drop of electrolyte solution was put through the drilled holes and sealed with Surlyn and 0.1 mm thick glasses. Finally, a tin contact was weld on the edge of FTO outside the cells.

The compositions of the four different electrolytes employed in this work are detailed in Table 1. The assembled solar cells were named as the type of electrolyte they contain.

*Solar Cell Characterization.* Acquisition of the IS measurements were carried out with a FRA-equipped PGSTAT-30 from Autolab. The amplitude of the AC signal was 25 mV at low applied voltages and 10 mV at high forward bias. The frequency range scanned values between 400 kHz and 0.1 Hz at the different $V_{app}$. Illumination was provided by a 1000 W class-A solar simulator from Newport, filtered at AM1.5 G and with the light intensity adjusted with an NREL-calibrated Si solar cell with a KG-5 filter to 1 sun (100 mW/cm$^2$). All measurements were carried out with an opaque mask 0.5 mm per side bigger than the active area.

## ■ AUTHOR INFORMATION

### Corresponding Author

*E-mail: fran.fabregat@fca.uji.es.

### Notes

The authors declare no competing financial interest.

## ■ ACKNOWLEDGMENTS

The authors want to thank Prof. Juan Bisquert for fruitful discussions. This work is supported by the "Institute of Nanotechnologies for Clean Energies" funded by the Generalitat Valenciana under project ISIC/2012/008, Ministerio de Economia y Competitividad of Spain under Projects Consolider HOPE CSD2007-00007 and MAT2010-19827 and Generalitat Valenciana under Project PROMETEO/2009/058. S.R.R. acknowledges financial support from the Bancaixa foundation under Project Innova 11I272.

## ■ REFERENCES

(1) O' Regan, B.; Grätzel, M. A Low-Cost High-Efficiency Solar Cell Based on Dye-Sensitized Colloidal $TiO_2$ Films. *Nature* **1991**, *353*, 737.

(2) Yu, Q.; Wang, Y.; Yi, Z.; Zu, N.; Zhang, J.; Zhang, M.; Wang, P. High-Efficiency Dye-Sensitized Solar Cells: The Influence of Lithium Ions on Exciton Dissociation, Charge Recombination, and Surface States. *ACS Nano* **2010**, *4*, 6032−6038.

(3) Yella, A.; Lee, H.-W.; Tsao, H. N.; Yi, C.; Chandiran, A. K.; Nazeeruddin, M. K.; Diau, E. W.-G.; Yeh, C.-Y.; Zakeeruddin, S. M.; Grätzel, M. Porphyrin-Sensitized Solar Cells with Cobalt (II/III)

Based Redox Electrolyte Exceed 12% Efficiency. *Science* **2011**, *334*, 629−634.

(4) Wang, Q.; Ito, S.; Grätzel, M.; Fabregat-Santiago, F.; Mora-Seró, I.; Bisquert, J.; Bessho, T.; Imai, H. Characteristics of High Efficiency Dye-Sensitized Solar Cells. *J. Phys. Chem. B* **2006**, *110*, 19406−19411.

(5) Fabregat-Santiago, F.; Bisquert, J.; Palomares, E.; Otero, L.; Kuang, D.; Zakeeruddin, S. M.; Grätzel, M. Correlation between Photovoltaic Performance and Impedance Spectroscopy of Dye-Sensitized Solar Cells Based on Ionic Liquids. *J. Phys. Chem. C* **2007**, *111*, 6550−6560.

(6) Chiba, Y.; Islam, A.; Watanabe, Y.; Komiya, R.; Koide, N.; Han, L. Dye-Sensitized Solar Cells with Conversion Efficiency of 11.1. *Jpn. J. Appl. Phys.* **2006**, *45*, L638−L640.

(7) Grätzel, M. Recent Advances in Sensitized Mesoscopic Solar Cells. *Acc. Chem. Res.* **2009**, *42*, 1788−1798.

(8) Bisquert, J. Dilemmas of Dye-Sensitized Solar Cells. *ChemPhysChem* **2011**, *12*, 1633−1636.

(9) Boschloo, G.; Hagfeldt, A. Characteristics of the Iodide/Triiodide Redox Mediator in Dye-Sensitized Solar Cells. *Acc. Chem. Res.* **2009**, *42*, 1819−1826.

(10) Barea, E. M.; Ortiz, J.; Payá, F. J.; Fernández-Lázaro, F.; Fabregat-Santiago, F.; Sastre-Santos, A.; Bisquert, J. Energetic Factors Governing Injection, Regeneration and Recombination in Dye Solar Cells with Phthalocyanine Sensitizers. *Energy Environ. Sci.* **2010**, *3*, 1985−1994.

(11) Barea, E. M.; Zafer, C.; Gultekin, B.; Aydin, B.; Koyuncu, S.; Icli, S.; Fabregat-Santiago, F.; Bisquert, J. Quantification of the Effects of Recombination and Injection in the Performance of Dye-Sensitized Solar Cells Based on N-Substituted Carbazole Dyes. *J. Phys. Chem. C* **2010**, *114*, 19840−19848.

(12) Pelet, S.; Moser, J.-E.; Grätzel, M. Cooperative Effect and Adsorbed Cations and Iodide on the Interception of Back Electron Transfer in the Dye Sensitization of Nanocrystalline $TiO_2$. *J. Phys. Chem. B* **2000**, *104*, 1791−1795.

(13) Kopidakis, N.; Benkstein, K. D.; van de Lagemaat, J.; Frank, A. J. Transport-Limited Recombination of Photocarriers in Dye-Sensitize Nanocrystalline $TiO_2$ Solar Cells. *J. Phys. Chem. B* **2003**, *107*, 11307.

(14) Schlichthörl, G.; Huang, S. Y.; Sprague, J.; Frank, A. J. Band Edge Movement and Recombination Kinetics in Dye-Sensitized Nanocrystalline $TiO_2$ Solar Cells: A Study by Intensity Modulated Photovoltage Spectroscopy. *J. Phys. Chem. B* **1997**, *101*, 8141−8155.

(15) Wang, P.; Zakeeruddin, S. M.; Humphry-Baker, R.; Grätzel, M. A Binary Ionic Liquid Electrolyte to Achieve 7% Power Conversion Efficiencies in Dye-Sensitized Solar Cells. *Chem. Mater.* **2004**, *16*, 2694−2696.

(16) Zhang, Z.; Zakeeruddin, S. M.; O'Regan, B. C.; Humphry-Baker, R.; Grätzel, M. Influence of 4-Guanidinobutyric Acid as Coadsorbent in Reducing Recombination in Dye-Sensitized Solar Cells. *J. Phys. Chem. B* **2005**, *109*, 21818−21824.

(17) Kopidakis, N.; Neale, N. R.; Frank, A. J. Effect of an Adsorbent on Recombination and Band-Edge Movement in Dye-Sensitized $TiO_2$ Solar Cells: Evidence for Surface Passivation. *J. Phys. Chem. B* **2006**, *110*, 12485−12489.

(18) Fabregat-Santiago, F.; Garcia-Belmonte, G.; Mora-Sero, I.; Bisquert, J. Characterization of Nanostructured Hybrid and Organic Solar Cells by Impedance Spectroscopy. *Phys. Chem. Chem. Phys.* **2011**, *13*, 9083−9118.

(19) Bisquert, J.; Fabregat-Santiago, F. Impedance Spectroscopy: A General Introduction and Application to Dye-Sensitized Solar Cells. In *Dye-Sensitized Solar Cells*; Kalyanasundaram, K., Ed.; EPFL Press and CRC Press: Lausanne, Switzerland and Boca Raton, FL, 2010.

(20) Sze, S. M. *Physics of Semiconductor Devices*, 2nd ed.; John Wiley and Sons: New York, 1981.

(21) Bisquert, J. Chemical Capacitance of Nanostructured Semiconductors: Its Origin and Significance for Heterogeneous Solar Cells. *Phys. Chem. Chem. Phys.* **2003**, *5*, 5360.

(22) Liu, Y.; Hagfeldt, A.; Xiao, X.-R.; Lindquist, S.-E. Investigation of Influence of Redox Species on the Interfacial Energetics of a Dye Sensitized Nanoporous $TiO_2$ Solar Cell. *Sol. Energy Mater. Sol. Cells* **1998**, *55*, 267−281.

(23) van de Lagemaat, J.; Park, N.-G.; Frank, A. J. Influence of Electrical Potential Distribution, Charge Transport, and Recombination on the Photopotential and Photocurrent Conversion Efficiency of Dye-Sensitized Nanocrystalline $TiO_2$ Solar Cells: A Study by Electrical Impedance and Optical Modulation Techniques. *J. Phys. Chem. B* **2000**, *104*, 2044−2052.

(24) Fabregat-Santiago, F.; Bisquert, J.; Garcia-Belmonte, G.; Boschloo, G.; Hagfeldt, A. Impedance Spectroscopy Study of the Influence of Electrolyte Conditions in Parameters of Transport and Recombination in Dye-Sensitized Solar Cells. *Sol. Energy Mater. Sol. Cells* **2005**, *87*, 117−131.

ChemComm

View Online / Journal Homepage
Dynamic Article Links

Cite this: DOI: 10.1039/c2cc31111a

www.rsc.org/chemcomm

COMMUNICATION

# Design and characterization of alkoxy-wrapped push–pull porphyrins for dye-sensitized solar cells†‡

Teresa Ripolles-Sanchis,[a] Bo-Cheng Guo,[b] Hui-Ping Wu,[c] Tsung-Yu Pan,[c] Hsuan-Wei Lee,[b] Sonia R. Raga,[a] Francisco Fabregat-Santiago,[a] Juan Bisquert,*[a] Chen-Yu Yeh*[b] and Eric Wei-Guang Diau*[c]

*Received 15th February 2012, Accepted 9th March 2012*
**DOI: 10.1039/c2cc31111a**

**Three alkoxy-wrapped push–pull porphyrins were designed and synthesized for dye-sensitized solar cell (DSSC) applications. Spectral, electrochemical, photovoltaic and electrochemical impedance spectroscopy properties of these porphyrin sensitizers were well investigated to provide evidence for the molecular design.**

Porphyrins are promising candidates as highly efficient sensitizers for dye-sensitized solar cells (DSSC) because of their superior light-harvesting ability in the visible region.[1–3] Recent advances on the development of a porphyrin sensitizer (**YD2-*o*-C8**) with co-sensitization of an organic dye (**Y123**) using a cobalt-based electrolyte attained a power conversion efficiency of 12.3%,[4] which is superior to those developed based on Ru complexes[5] and becomes a new milestone in this area. The key structural feature on molecular design of a highly efficient porphyrin sensitizer is to bear with long alkoxyl chains in the *ortho*-positions of the *meso*-phenyls so as to effectively envelope the porphyrin ring to reduce the degree of dye aggregation for a higher electron injection yield and to form a blocking layer for a better charge collection yield.[6] In the present study, we further design three porphyrin sensitizers (**YD20–YD22**, Chart 1) based on the structure of **YD2-*o*-C8** but with extended π-conjugation in order to enhance the light-harvesting ability. Basically all of them have the same *ortho*-substituted porphyrin core with two phenylethynyl (PE) groups acting as a π-bridge in the *meso*-position of the ring. **YD20** and **YD22** dyes have the acceptor group (ethynylbenzoic acid) the same as that of **YD2-*o*-C8** but with different donor groups: **YD20** has a triphenylamino group with two methoxyl substitutes and **YD22** has a phenylamino group with two *n*-butyl chains. On the other hand, **YD20** and **YD21** dyes have the same donor group but the cyanoacrylic acid was used as an anchoring group in **YD21**. This approach mimics the molecular design of an organic dye[7] having the acrylonitrile group with strong electron-pulling power to act as an efficient acceptor for the porphyrin dye.

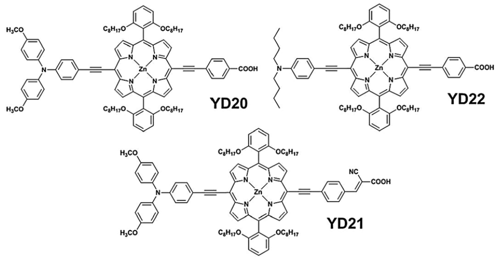

**Chart 1** Molecular structures for **YD20–YD22** porphyrin dyes.

The details for the syntheses, optical and electrochemical characterizations of **YD20–YD22** are given in ESI.‡ These porphyrin dyes were fabricated into DSSC devices for photovoltaic and electrochemical impedance spectroscopy (EIS) characterizations. Fig. 1a and b show the *J*–*V* curves and the corresponding Incident Photon to Current Conversion Efficiency (IPCE) action spectra for the **YD20–YD22** devices, respectively; the obtained photovoltaic parameters and the amounts of dye-loading are summarized in Table 1. The results indicate that the short-circuit current densities ($J_{SC}$) exhibit a trend **YD20** > **YD22** > **YD21** and the open-circuit voltages ($V_{OC}$) display a trend **YD20** > **YD22** ~ **YD21**; the overall power conversion efficiencies ($\eta$) show the same order as $J_{SC}$, which is consistent with the variations of the IPCE action spectra showing the same order. As a result, **YD20** has the highest $J_{SC}$ (17.43 mA cm$^{-2}$) and $V_{OC}$ (676 mV), which yields the greatest $\eta$ (8.1%) among the three porphyrins under investigation. Even though the cyanoacrylic substitute makes **YD21** a slight red shift in the absorption spectrum (Fig. S1, ESI‡), the floppy feature of the C=C double bond might tilt the molecules adsorbed on $TiO_2$ film to significantly decrease its IPCE values and the corresponding current density. However, **YD20** and **YD22** have the same anchoring group and very similar

---

[a] *Photovoltaics and Optoelectronic Devices Group, Departament de Física, Universitat Jaume I, 12071 Castelló, Spain. E-mail: bisquert@fca.uji.es; Tel: +34-964-38-7540*
[b] *Department of Chemistry and Center of Nanoscience & Nanotechnology, National Chung Hsing University, Taichung 402, Taiwan. E-mail: cyyeh@dragon.nchu.edu.tw; Fax: +886-4-22862547; Tel: +886-4-22852264*
[c] *Department of Applied Chemistry and Institute of Molecular Science, National Chiao Tung University, Hsinchu 30010, Taiwan. E-mail: diau@mail.nctu.edu.tw; Fax: +886-3-5723764; Tel: +886-3-5131524*

† This article is part of the ChemComm "Porphyrins and Phthalocyanines" web themed issue.

‡ Electronic supplementary information (ESI) available. See DOI: 10.1039/c2cc31111a

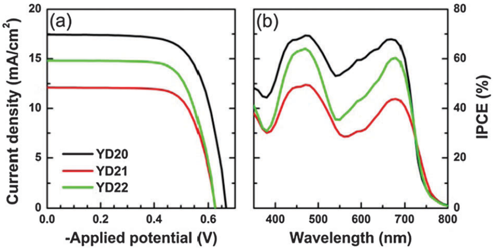

**Fig. 1** (a) Current *vs.* voltage characteristics of DSSC devices prepared with YD20 (black), YD21 (red), and YD22 (green) under illumination of simulated AM 1.5 full sunlight (100 W cm$^{-2}$) with an active layer of 0.16 cm$^2$ and (b) the corresponding action spectra for the efficiency of incident photon-to-current conversion (IPCE).

**Table 1** Photovoltaic parameters of porphyrin-based dye-sensitized solar cells (active layer 0.16 cm$^2$) under 100 mW cm$^{-2}$ light illumination (AM 1.5 G) for **YD20–YD22**

| Dye | Dye loading/ nmol cm$^{-2}$ | $J_{SC}$/ mA cm$^{-2}$ | $V_{OC}$/ mV | FF | $\eta$ (%) |
|---|---|---|---|---|---|
| **YD20** | 161 | 17.43 | 676 | 0.686 | 8.1 |
| **YD21** | 132 | 12.05 | 631 | 0.721 | 5.5 |
| **YD22** | 134 | 14.87 | 634 | 0.700 | 6.6 |

absorption spectra (Fig. S1, ESI‡), therefore, the differences in IPCE and photocurrent are related to the effect of the donor groups. Note that the decrease in the IPCE occurs at a nearly constant level for all the wavelengths of the spectra for **YD21** compared to **YD20**. Thus, the loss of electrons is independent of the energy of the absorbed photons. Transport and injection losses may be considered for the decrease in IPCE, which is discussed in the following.

Dye loading measurements yielded 161, 132, and 134 nmol cm$^{-2}$ for **YD20**, **YD21** and **YD22**, respectively. The changes in $J_{SC}$ between the dyes with the same anchoring group, **YD20** and **YD22**, may be understood in terms of the different amounts of loaded sensitizer. Further explanation is needed for sample **YD21** as the decrease in $J_{SC}$ is larger despite the amount of dye loading in the cell is the same as for **YD22**.

Electrochemical Impedance Spectroscopy was used to complete the analysis of injection and to gain insight into the transport and charge losses characteristics of the DSSC with the different dyes.[8] From the fitting of impedance spectra of the DSSC at different applied potentials under 1 sun illumination, we obtained the chemical capacitance ($C_\mu$), transport resistance in the TiO$_2$ ($R_{tr}$), recombination resistance ($R_{rec}$), as a function of the Fermi level voltage ($V_F$) shown in Fig. 2a, b, and c, respectively. Other contributions to the total resistance of the cell such as diffusion, counter electrode and FTO resistances were grouped as series resistance ($R_s$). The effect of $R_s$ in the applied potential ($V_{app}$) was removed to obtain the $V_F$ that may be calculated through $V_F = V_{app} - jR_s$. From the plot of $C_\mu$ *vs.* $-V_F$ shown in Fig. 2a, the position of the conduction band edge of TiO$_2$ ($E_c$) may be estimated as reported elsewhere.[9] Through these calculations, we estimated that for **YD20** $E_c \approx -0.48$ V *vs.* NHE, while for **YD21** $E_c$ was displaced +4 mV and **YD22** −10 mV. Data from transport resistance shown in Fig. 2b also provide very small displacements in $E_c$, corroborating that all the TiO$_2$ conduction bands remain almost unchanged for the three dyes as obtained from the capacitance data.

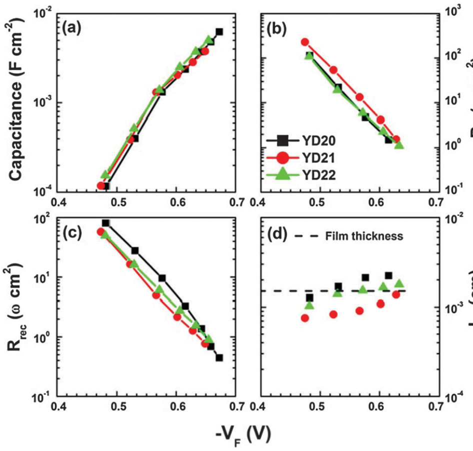

**Fig. 2** (a) Capacitance, (b) transport resistance, (c) recombination resistance, and (d) diffusion length of **YD20–YD22** dyes in DSSC plotted with respect to the Fermi level voltage ($-V_F$) with removing the effect of series resistance.

To understand the origin of the small differences in the $V_{OC}$ found for the three different dyes it is needed to analyze the behavior of the recombination resistance in Fig. 2c. In previous studies,[8,10] when comparing the recombination resistance of different samples it has been found that the higher the value of $R_{rec}$, the larger the $V_{OC}$, while only very large changes in photocurrent produce small variations in $V_{OC}$. The results here match very well with this analysis: as it can be seen in Fig. 2c, **YD20** has the larger recombination resistance and $V_{OC}$, whereas **YD21** and **YD22** have similar values of $R_{rec}$ showing almost the same $V_{OC}$.

Data from $R_{rec}$ and $R_{tr}$ may be used to calculate the diffusion length ($L_n$) in TiO$_2$ film shown in Fig. 2d as[8]

$$L_n = L\sqrt{R_{rec}/R_{tr}} \tag{1}$$

where $L$ is the film thickness (15 μm) represented as a dashed curve in Fig. 2d. The $L_n$ values exhibit a systematic trend with the order **YD20** > **YD22** > **YD21** with those of **YD20** and **YD22** reaching values greater than their film thickness whereas those of **YD21** being significantly smaller than the film thickness. This implies that the **YD21** device suffers from a poorer collection efficiency of injected electrons what produces the extra decrease in $J_{SC}$ found for this sample.

The small differences found for the position of the conduction band edge ($E_c$) may also help to fine tune the roles of the linker in these Zn–porphyrin dyes. If the Fermi level potential is shifted the amounts found for the displacement of $E_c$, it is possible to compare the recombination resistance of the DSSC at the potential level with the same number of injected electrons. To do this we define the potential at the equivalent conduction band position[8]

$$V_{ecb} = V_F - \Delta E_c/e \tag{2}$$

where $e$ is the electron charge and $\Delta E_c = E_c - E_{c,ref}$, for which $E_{c,ref}$ is the position of the conduction band of **YD20**. Based on

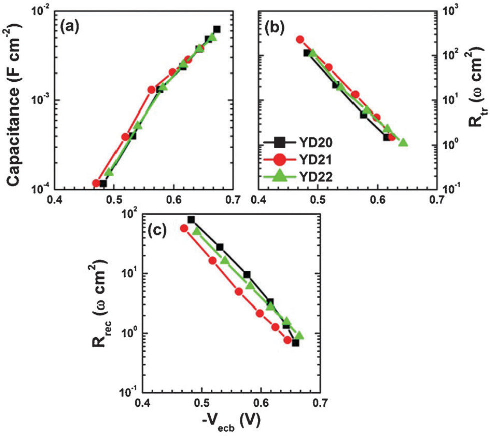

**Fig. 3** (a) Capacitance, (b) transport resistance, and (c) recombination resistance of **YD20–YD22** dyes in DSSC plotted with respect to the equivalent common conduction band voltage ($-V_{ecb}$).

these conditions, we transfer Fig. 2a–c into Fig. 3a–c, which show $C_\mu$ (a), $R_{tr}$ (b), and $R_{rec}$ (c) as a function of $-V_{ecb}$. While the chemical capacitance (Fig. 3a) and the transport resistance (Fig. 3b) of the three dyes match quite well, the recombination resistance (Fig. 3c) of the **YD21** device is much smaller compared to that of the **YD20** and **YD22** devices. In other words, charge recombination is a major problem for the poor performance of the **YD21** device. These results allow us to make a conclusion: compared to the **YD20** device, the smaller $V_{OC}$ of **YD22** was due to a small shift in conduction band but the smaller $V_{OC}$ of **YD21** was due to a significant charge recombination. From the structural viewpoint, the use of cyanoacrylic acid as an acceptor and an anchoring group in **YD21** might provide more free space (less amount of dye-loading) for the charge recombination than the use of the rigid ethynylbenzoic acid in **YD20** and **YD22**. Moreover, **YD21** might be tilted on the surface of $TiO_2$ for the charge recombination to occur more easily.

In conclusion, although the concept for molecular design with the cyanoacrylic acid acceptor has been widely applied in highly efficient organic dyes,[7] such an approach does not work well for the porphyrin sensitizers as demonstrated herein. The greater performance in the **YD20** device than the other two devices is attributed to its rigid structural feature for a larger amount of dye-loading, which combined with the higher recombination resistance and diffusion length yields to larger $J_{SC}$ and $V_{OC}$. Modification of the porphyrin structure with extended π-conjugation for better light harvesting is feasible to boost up the device performance in the near future.

This work was partially supported by National Science Council of Taiwan and Ministry of Education of Taiwan, under the ATU program. JB acknowledges support by projects from Ministerio de Ciencia e Innovación (MICINN) of Spain (Consolider HOPE CSD2007-00007, MAT2010-19827), and Generalitat Valenciana (PROMETEO/2009/058). SRR thanks financial support from Bancaixa foundation under project Innova 11I272. CYY and EWGD acknowledge support by projects from National Science Council of Taiwan and Ministry of Education of Taiwan, under the ATU program.

## Notes and references

1 (*a*) H. Imahori, T. Umeyama and S. Ito, *Acc. Chem. Res.*, 2009, **42**, 1809–1818; (*b*) M. V. Martínez-Díaz, G. de la Torre and T. Torres, *Chem. Commun.*, 2010, **46**, 7090–7108; (*c*) X.-F. Wang and H. Tamiaki, *Energy Environ. Sci.*, 2010, **3**, 94–106.
2 (*a*) C.-W. Lee, H.-P. Lu, C.-M. Lan, Y.-L. Huang, Y.-R. Liang, W.-N. Yen, Y.-C. Liu, Y.-S. Lin, E. W.-G. Diau and C.-Y. Yeh, *Chem.–Eur. J.*, 2009, **15**, 1403–1412; (*b*) H.-P. Lu, C.-L. Mai, C.-Y. Tsia, S.-J. Hsu, C.-P. Hsieh, C.-L. Chiu, C.-Y. Yeh and E. W.-G. Diau, *Phys. Chem. Chem. Phys.*, 2009, **11**, 10270–10274; (*c*) H.-P. Lu, C.-Y. Tsai, W.-N. Yen, C.-P. Hsieh, C.-W. Lee, C.-Y. Yeh and E. W.-G. Diau, *J. Phys. Chem. C*, 2009, **113**, 20990–20997; (*d*) C.-P. Hsieh, H.-P. Lu, C.-L. Chiu, C.-W. Lee, S.-H. Chuang, C.-L. Mai, W.-N. Yen, S.-J. Hsu, E. W.-G. Diau and C.-Y. Yeh, *J. Mater. Chem.*, 2010, **20**, 1127–1134; (*e*) T. Bessho, S. M. Zakeeruddin, C.-Y. Yeh, E. W.-G. Diau and M. Grätzel, *Angew. Chem., Int. Ed.*, 2010, **49**, 6646–6649.
3 (*a*) C.-Y. Lin, C.-F. Lo, L. Luo, H.-P. Lu, C.-S. Hung and E. W.-G. Diau, *J. Phys. Chem. C*, 2009, **113**, 755–764; (*b*) C.-Y. Lin, Y.-C. Wang, S.-J. Hsu, C.-F. Lo and E. W.-G. Diau, *J. Phys. Chem. C*, 2010, **114**, 687–693; (*c*) C.-F. Lo, S.-J. Hsu, C.-L. Wang, Y.-H. Cheng, H.-P. Lu, E. W.-G. Diau and C.-Y. Lin, *J. Phys. Chem. C*, 2010, **114**, 12018–12023; (*d*) C.-L. Wang, Y.-C. Chang, C.-M. Lan, C.-F. Lo, E. W.-G. Diau and C.-Y. Lin, *Energy Environ. Sci.*, 2011, **4**, 1788–1795.
4 A. Yella, H.-W. Lee, H. N. Tsao, C. Yi, A. K. Chandiran, M. K. Nazeeruddin, E. W.-G. Diau, C.-Y. Yeh, S. M. Zakeeruddin and M. Grätzel, *Science*, 2011, **334**, 629–634.
5 (*a*) C.-Y. Chen, M. Wang, J.-Y. Li, N. Pootrakulchote, L. Alibabaei, C. Ngoc-le, J.-D. Decoppet, J.-H. Tsai, C. Grätzel, C.-G. Wu, S. M. Zakeeruddin and M. Grätzel, *ACS Nano*, 2009, **3**, 3103–3109; (*b*) Y. Cao, Y. Bai, Q. Yu, Y. Cheng, S. Liu, D. Shi, F. Gao and P. Wang, *J. Phys. Chem. C*, 2009, **113**, 6290–6297; (*c*) Q. Yu, Y. Wang, Z. Yi, N. Zu, J. Zhang, M. Zhang and P. Wang, *ACS Nano*, 2010, **4**, 6032–6038.
6 (*a*) Y.-C. Chang, C.-L. Wang, T.-Y. Pan, S.-H. Hong, C.-M. Lan, H.-H. Kuo, C.-F. Lo, H.-Y. Hsu, C.-Y. Lin and E. W.-G. Diau, *Chem. Commun.*, 2011, **47**, 8910–8912; (*b*) C.-L. Wang, C.-M. Lan, S.-H. Hong, Y.-F. Wang, T.-Y. Pan, C.-W. Chang, H.-H. Kuo, M.-Y. Kuo, E. W.-G. Diau and C.-Y. Lin, *Energy Environ. Sci.*, 2012, DOI: 10.1039/C2EE03308A, Advance Article.
7 (*a*) G. Zhang, H. Bala, Y. Cheng, D. Shi, X. Lv, Q. Yu and P. Wang, *Chem. Commun.*, 2009, 2198–2200; (*b*) Z. Ning and H. Tian, *Chem. Commun.*, 2009, 5483–5495; (*c*) Z. Ning, Y. Fu and H. Tian, *Energy Environ. Sci.*, 2010, **3**, 1170–1181.
8 F. Fabregat-Santiago, G. Garcia-Belmonte, I. Mora-Sero and J. Bisquert, *Phys. Chem. Chem. Phys.*, 2011, **13**, 9083–9118.
9 E. M. Barea, J. Ortiz, F. J. Payá, F. Fernández-Lázaro, F. Fabregat-Santiago, A. Sastre-Santos and J. Bisquert, *Energy Environ. Sci.*, 2010, **3**, 1985–1994.
10 (*a*) E. M. Barea, C. Zafer, B. Gultekin, B. Aydin, S. Koyuncu, S. Icli, F. F. Santiago and J. Bisquert, *J. Phys. Chem. C*, 2010, **114**, 19840–19848; (*b*) E. M. Barea, V. González-Pedro, T. Ripollés-Sanchis, H.-P. Wu, L.-L. Li, C.-Y. Yeh, E. W.-G. Diau and J. Bisquert, *J. Phys. Chem. C*, 2011, **115**, 10898–10902.

PCCP

RSC Publishing

PAPER

View Article Online
View Journal

# Temperature effects in dye-sensitized solar cells†

Cite this: DOI: 10.1039/c2cp43220j

Sonia R. Raga and Francisco Fabregat-Santiago*

Received 13th September 2012,
Accepted 10th December 2012

DOI: 10.1039/c2cp43220j

www.rsc.org/pccp

In the standard solar cell technologies such as crystalline silicon and cadmium telluride, increments of temperature in the cell produce large variations in the energy conversion efficiency, which decreases at a constant rate. In dye solar cells the efficiency remains roughly constant with a maximum at around 30–40 °C and further decays above this temperature. In this work, the origin of this characteristic behavior is explained. Data show that under illumination recombination kinetics in the active layer of the cell is the same between −7 and 40 °C. Consequently, the efficiency of the cell remained virtually constant, with only small differences in the fill factor associated with changes in the series resistance. A further increase in temperature up to 70 °C produces an increase in recombination kinetics yielding lower photopotential and device performance. Finally, it is emphasized that at the normal operating temperatures of solar cells, the gap among the conversion efficiency of different technologies is much smaller than generally acknowledged.

## Introduction

Dye sensitized solar cells (DSCs) are a promising alternative to silicon or thin film solar cells due to the low cost materials and simplicity in their fabrication process. These characteristics make DSC technology a candidate for large scale production of cheap energy.[1,2] The highest efficiencies reached with DSCs, 11–12%,[3–6] have been obtained using $TiO_2$ nanostructures for collecting the electrons, a redox electrolyte based on $I^-/I_3^-$ for transporting the holes and a ruthenium dye attached to the semiconductor nanoparticles for absorbing the radiation and separating the charges into the different charge carrier media.[7,8] A recent publication has also reported 12% efficiency with porphyrin dyes and cobalt based redox electrolyte.[9]

Some of the beneficial characteristics of DSCs are that they maintain a high efficiency under diffuse or low light incident angle and that their performance presents little changes at environmental temperatures ranging between −20 and 80 °C.[10–13] Power conversion efficiency drops for rising temperatures in the case of the most extended technologies, at rates around $-0.45\%\ K^{-1}$ in mono- and polycrystalline silicon cells and of $-0.25\%\ K^{-1}$ for cadmium telluride.[14] In normal operation, cell temperatures (NOCT) rise to about 45–50 °C and consequently, their efficiency drops from nominal values approximately 10% for Si and 5% for CdTe. Dye solar cells instead present a maximum in the energy conversion efficiency close to NOCT.[12] This is a key aspect in the discussion of best performing solar cell technologies: as DSCs for 17 $cm^2$ modules have reached 9.9% efficiency,[15] the increase in efficiency at NOCT together with the decrease in the other technologies reduces the efficiency gap under the real operating conditions to a short distance.

From a more fundamental view, the progress in the field of DSCs has been very exciting in the last few years from both points of view, the enhancement of the device performance and the development of the models needed to understand the origin of the behavior of DSCs. Very relevant contributions have been focused on describing the mechanisms that control parameters such as the short circuit photocurrent, $J_{sc}$, open circuit photopotential, $V_{oc}$, and fill factor, FF, that determine the performance of the solar device.[16–19]

In general, charge collection is well resolved in DSCs, with efficiencies close to 100% in good cells. Photovoltage, however, presents large variations affected by charge recombination between $TiO_2$, dye or electrolyte composition and also by the energetic position of the $TiO_2$ conduction band in relation to the redox energy level in the electrolyte.[20–22] Recombination of charge plays a major role in the photopotential attained by the DSC[17,22] and it is determined by different mechanisms that involve variations in acceptor species: Miyashita *et al.*[23] proposed that there is a locally increased concentration of $I_3^-$ near the dye under illumination and Boschloo and Hagfeldt[16] remarked the generation of other acceptor species as $I_2^{-\bullet}$. On another hand O'Regan and Durrant[24] suggested that recombination increases

---

Photovoltaic and Optoelectronic Devices Group, Departament de Física, Universitat Jaume I, 12071 Castelló, Spain. E-mail: fran.fabregat@fca.uji.es; Fax: +34-964-729218; Tel: +34-964-387537

† Electronic supplementary information (ESI) available: Measures of performance of DSC for 500 h lifetime tests, Nyquist plots showing series resistances, values of conduction band shifts, plots of capacitance values *vs.* $V_{ecb}$, comparison of capacitance in the dark and under illumination, comments on transport resistance and performance data of DSC after shifting the applied potential the displacement in the conduction band edge ($\Delta E_c$). See DOI: 10.1039/c2cp43220j

due to a binding between dye molecules and iodine, an effect that does not exclude the previously mentioned ones. Moreover, recombination of charge increases when the $TiO_2$ conduction band position decreases.[25,26]

In this paper we used previously developed models to report the effect of temperature on DSCs. To simplify the analysis, we focused the study on the FF and $V_{oc}$ while keeping the short circuit photocurrent constant. Current density *vs.* potential (*J–V*) curves and impedance spectroscopy (IS) measurements were taken both in the dark and under illumination in a temperature range between −7 °C and 70 °C. A detailed analysis of the origin of the characteristic behavior of the parameters governing the performance of the solar cells is provided and an explanation for the changes in the energy conversion efficiency with the temperature is given.

## Experimental

### Dye-sensitized solar cell preparation

Working electrodes for the DSC were prepared on 2.3 mm thickness and 15 $\Omega\ \square^{-1}$ FTO glass plates. First, glasses were brushed with detergent solution and rinsed with Milli-Q water, then immersed into iso-propanol and cleaned using an ultrasonic bath for 15 min, then rinsed with ethanol and dried with air. After that a 150 nm compact $TiO_2$ layer was deposited by the spray-pyrolysis technique with an ethanol/acetyl acetone/titanium(IV) isopropoxide (3 : 3 : 2 weight ratio) solution and a 450 °C hot plate. The substrates were coated by the doctor blade technique with a 7 μm layer of 20 nm size $TiO_2$ nanoparticles and a 3 μm scatter layer of 450 nm size $TiO_2$ nanoparticles (respectively 18-NRT and WER4-0 from Dyesol), then fired 30 min at 450 °C. The active area of the film was 0.25 $cm^2$. When cooled, films were immersed into 40 mM $TiCl_4$ (aq) at 70 °C for 30 min, rinsed with Milli-Q water and sintered at 570 °C for 10 min. After cooling to 40 °C, the $TiO_2$ electrodes were immersed into a N719 dye solution (0.5 mM in a mixture of acetonitrile and *tert*-butanol, 1 : 1 volume ratio) for 16 hours.

As counter electrodes, 8 $\Omega\ \square^{-1}$ FTO coated glasses were drilled with a 1 mm diameter drill tip and cleaned with the same procedure as mentioned above. The counter electrodes were prepared with a drop of chloroplatinic acid solution from Sigma Aldrich on the FTO and then fired in a 450 °C air flow.

The working and counter electrodes were assembled in a sandwich-type cell by pressing at 95 °C with a hot-melt film (Surlyn 25 μm thickness) as a sealant and spacer between electrodes. A drop of electrolyte solution (0.60 M 1-butyl-3-methylimidazolium iodide, 0.03 M $I_2$, 0.10 M guanidinium thiocyanate, and 0.50 M 4-*tert*-butylpyridine in methoxypropionitrile) was placed on the drilled holes, then the cell was placed into a small chamber where vacuum was applied until most of the air inside the cell bubbled out through the electrolyte, when air came again into the chamber the electrolyte was driven into the cell. Finally the drilled holes were sealed with Surlyn and 0.1 mm thick glasses, and a tin contact was welded on the edge of FTO outside the cells. Five cells were prepared for statistical significance and a 500 h stability test was performed. Average performance data under 1 sun AM1.5G illumination at room temperature are provided in Fig. S1 of ESI.† The average performance evolution with time is shown in Fig. S2 (ESI†). The most stable cells were chosen for the study of impedance.

### Solar cell characterization

*J–V* curves were taken using a Keithley 2612 System Source Meter. Impedance measurements were carried out using a FRA-equipped PGSTAT-30 from Metrohm-Autolab, applying a 25 mV AC signal at low potentials and a 10 mV AC signal at high potentials, we could minimize the noise while keeping linearity in the response of the DSC. The frequency of the measurements was scanned between 400 kHz and 0.1 Hz at forward applied bias that ranged from 0.3 V to 0.9 V. Below 0.3 V the large impedance found corresponds to FTO and impedance data are not needed for the interpretation of DSC behavior.

At environmental temperature, for fresh samples and during the ageing experiments shown in ESI,† illumination was provided by a solar simulator filtered at AM1.5G and light intensity adjusted with an NREL-calibrated Si solar cell with a KG-5 filter to 1 sun intensity (100 mW $cm^{-2}$). A white-light LED lamp was used to obtain *J–V* curves and impedance spectroscopy measurements in temperature controlled experiments. The power of the LED lamp was adjusted (with variations $< 2\%$) to obtain the same photocurrent as that provided with the 1 sun AM1.5G solar simulator at environmental temperature. Proceeding this way is important for several reasons: analysis of data at the same current makes it much clear to state the gross effects of temperature in the solar cell; the absence of IR light in the LED lamp ensures a minimum influence of the power source in the temperature of the device; finally, temperature variations have little effects in short circuit current. Together with the fact that the small changes in illumination intensity to keep the current constant produce tiny variations in $V_{oc}$ and FF, this ensures that changes in efficiency are minimal. However, as the light spectrum is not matching AM1.5G standard and the illumination power is not exactly the same in all the measurements, we used the term apparent efficiency instead of efficiency to describe DSC performance.

The temperature was controlled using a Peltier cell monitored by a computer, in the range of temperatures from −7 °C to 70 °C. Note that for allowing the better illumination possible, the counter electrode side of the DSC is in contact with the refrigerating Peltier element.

## Results and discussion

Fig. 1 shows the effect of temperature on the *J–V* curves of a DSC taken both in the dark and under LED illumination equivalent to 1 sun. In Fig. 1(a), it may be observed that the rise in temperature produces an onset of photocurrent at lower potentials and thus under illumination (Fig. 1(b)) this shift is translated into a decrease in open circuit voltage.

For a better understanding of the origin of this behavior, we have examined the physical processes occurring in DSCs by means of IS, carried out at each of the measured temperatures. Characteristic Nyquist plots are shown in Fig. S3 and S4 of ESI.†

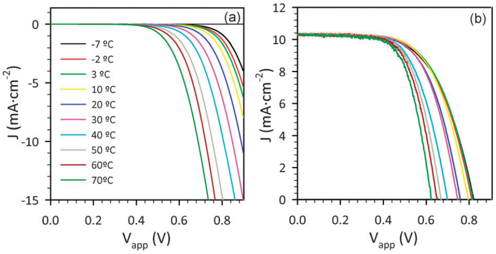

**Fig. 1** *J–V* curves at different temperatures obtained after IS measurements in the dark (a) and under illumination (b) conditions.

The analysis of impedance spectra has been made by employing the equivalent circuits previously reported for DSCs.[25] This allows studying separately parameters, such as the chemical capacitance ($C_\mu$) and the recombination ($R_{rec}$) and transport resistances ($R_{tr}$), that describe the processes of accumulation, loss and transport of the charge in the $TiO_2$ and the different contributions to total series resistance given by

$$R_{series} = R_{FTO} + R_{Pt} + R_d \tag{1}$$

with $R_{FTO}$ the resistance of the conducting glass plus contacts and wires, $R_{Pt}$ the charge transfer resistance at the platinized counter electrode and $R_d$ the diffusion resistance originated by the transport of holes in the electrolyte.

We focus first on the effect of temperature over $R_{series}$. Fig. 2 shows the average values of the different contributions to $R_{series}$. At high temperatures, the main contributor to $R_{series}$ is $R_{FTO}$ which presents a nearly constant value for all the temperatures both in the dark and under illumination, Fig. 2(a). This result is confirmed by measurements of plain FTO in which the same trend, a very slight increase in $R_{FTO}$ with rising temperature, is observed, see Fig. 3(a). Note that while cell design may reduce $R_{FTO}$, once it is established, temperature has little effect on it.

At low temperatures, as may be seen in Fig. 2(b) and (c), charge transfer at the counter electrode and diffusion resistance in the electrolyte showed comparable or even larger values than $R_{FTO}$. In Fig. 2(b) it may be observed that $R_{Pt}$ in the dark and under illumination presents the same values, which rise as the temperature diminishes. This result indicates that the counter electrode is in thermal equilibrium with the cooling plate over which it is located. The reduction in $R_{Pt}$, with rising temperatures, is attributed to the acceleration of charge transfer kinetics with the redox regeneration.

Diffusion resistance of the electrolyte shown in Fig. 2(c) presents both variations under illumination conditions and external temperature of the cell. At high temperatures decrease in the electrolyte resistance is expected under illumination as the increased concentration of $I_3^-$ due to the regeneration of the dye increases the conductivity in the solution. However this change seems not enough to explain the large differences found for $R_d$ at low external temperatures. In the dark, the increase in $R_d$ indicates an increment in the viscosity of the electrolyte when temperature diminishes.[27] Under illumination, part of the electrolyte is in contact and in thermal equilibrium with the $TiO_2$ film which could present a higher temperature than that of the counter electrode. Therefore, a gradient of temperature will be built in the electrolyte between these two electrodes. This gradient could be remarkable as the distances between the hot active electrode and the cold counter electrode are constrained to 15 μm. Under these conditions electrical measurements provide a value of $R_d$ associated with the average viscosity of the electrolyte.

In summary, total series resistance decreases with rising temperatures due to the changes in $R_{Pt}$ and $R_d$, while $R_{FTO}$ remains nearly constant. The first two resistances dominate at low temperatures while the last one provides the main $R_{series}$ contribution at high temperature.

For an accurate analysis of the parameters associated with $TiO_2$, applied potential needs to be corrected from the potential drop at $R_{series}$ at each temperature. As may be observed in Fig. 3(b) and (c), $R_{Pt}$ and $R_d$ change also with potential, therefore to obtain the potential drop at the $TiO_2$ film, $V_F = (E_{Fn} - E_{F0})/q$, it is needed to proceed through the integral[17,29]

$$V_F = V_{app} + \frac{J}{J_{sc} - J}\int_{J_{sc}}^{J} R_{series}\,dJ \tag{2}$$

Fig. 4 shows the chemical capacitance of the $TiO_2$. Measurements of $C_\mu$ in the dark and under illumination, Fig. 4(a) and (b), show very similar slopes at high potentials, following the expression[28]

$$C_\mu = C_0 \exp\left[\frac{q}{k_B T_0} V_F\right] \tag{3}$$

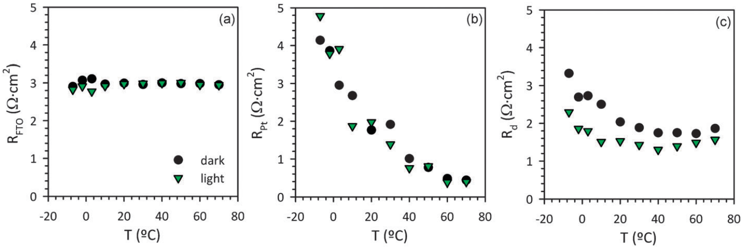

**Fig. 2** Temperature dependence of the different contributions to the series resistance of the DSC. (a) Resistance of the FTO conducting glass plus contacts and wires; (b) resistance of the platinized counter electrode; and (c) diffusion resistance.

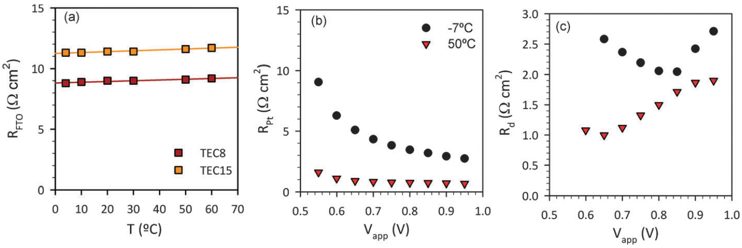

**Fig. 3** (a) Changes in the resistance of two 1 cm$^2$ FTO samples with temperature. As for our samples their change is minimal with a slight increase with rising temperatures. Changes with applied potential are lower than 5%. The effect of potential is relevant both for counter electrode resistance (b) and diffusion resistance (c). At low temperatures these resistances take larger values than at high temperatures. The minimum in $R_d$ in (c) occurs near $V_{oc}$ where current crossing the cell is zero. Note that the overlap between recombination and diffusion arc shown in Fig. S3 and S4 (ESI†) produces increasing errors (>20%) in the values of $R_d$ at the lower potentials.

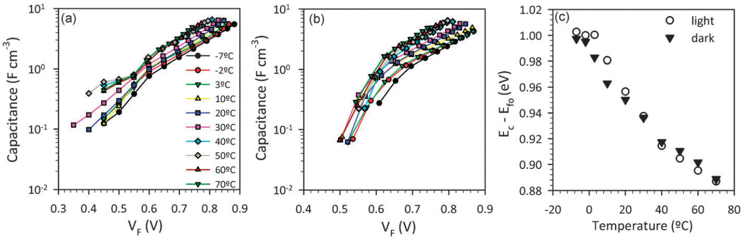

**Fig. 4** Values of TiO$_2$ capacitances: (a) in the dark and (b) under illumination conditions. (c) Values of conduction band position during the measurements.

where $T$ is the film temperature, $q$ the electron charge, $k_B$ the Boltzmann constant, $T_0$ a parameter with temperature units determining the depth of the trap distribution tail under conduction band, and $C_0$ a parameter given by

$$C_0 = \frac{(1-p)Lq^2N_L}{k_BT_0}\exp\left[\frac{q}{k_BT_0}(E_{F0}-E_c)\right] \qquad (4)$$

where $p$ is the porosity of the TiO$_2$ layer, $L$ the thickness, $N_L$ the total electron trap density,[30,31] $E_{F0} - E_c$ is the difference between the dark (equilibrium) Fermi level and conduction band position of TiO$_2$.

In previous studies, it has been shown that chemical capacitance is independent of temperature.[4,32] However, if nanoparticles are small enough, the series contribution of Helmholtz capacitance may produce visible effects on the total capacitance of the film.[33,34] Here we find that $C_\mu$ values are clearly shifted towards lower potentials for increasing temperatures. Although this displacement would agree with changes in the Helmholtz capacitance with temperature, the relatively large displacement of the capacitance and the constant slope *vs.* the potential are not compatible with an explanation based on Helmholtz contribution.[29]

Other possible origin of the shift in $C_\mu$ could be on changes in the $E_{redox}$ ($E_{F0}$) due to temperature. The Nernst equation has been used to calculate the change in $E_{redox}$ yielding a change lower than 10 mV in the full range of temperatures. Assuming that neither the distribution nor the total amount of trap states changed with temperature, we may attribute the shift observed in $C_\mu$ to a displacement in the energy of the conduction band.[35]

Eqn (4) was used to estimate the $E_c$ position for each temperature using $N_L = 2.5 \times 10^{19}$ cm$^{-3}$. Fig. 4(c) shows the reduction in the $E_c$ level during measurements which, within the experimental error, was nearly the same both in the dark and under illumination conditions. Transport resistance was also used to test changes in $E_c$ yielding the same conclusions, see ESI† for more details.

Movement of the position of the $E_c$ during aging of cells is a phenomenon well known by experimentalists in the field. It depends on time and also on measurement conditions, which produces a variety of behaviors: sometimes $E_c$ rises with time,[36] commonly in fresh samples, in other occasions it drops.[37] In our case, the cells were pre-aged for 500 h (see Fig. S1 in ESI†) before the IS measurements to increase stability and reproducibility of data. Repeated measurements at 20 °C after completing the measurement of the temperature series yielded the same $E_c$ value obtained for TiO$_2$ at this temperature during the series measurement. This result suggests reversibility in TiO$_2$ $E_c$ movement with temperature that, as far as we know, is reported for the first time. The origin of this behavior of $E_c$ with temperature found for our samples is not yet clear. One possibility could be reversible adsorption/desorption of electrolyte additives, dye or even environmental contamination (*i.e.* H$^+$ from H$_2$O) at the surface of the TiO$_2$. Other possibility could be narrowing of band gap of TiO$_2$ with temperature. Future work should be devoted to clarify this aspect.

To analyze separately the effects of the variations in $E_c$ in the performance of the DSC from other contributions, the voltage needs to be corrected from the conduction band shift at the

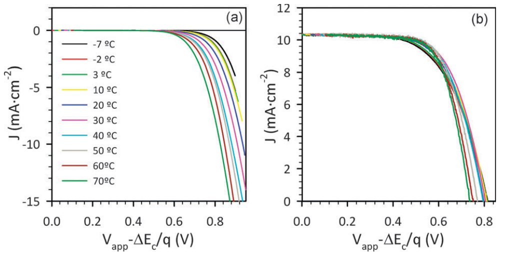

**Fig. 5** *J–V* curves from Fig. 1 after shifting the applied potential by the difference in the conduction band energy with respect to the measurements taken at 50 °C. (a) In the dark and (b) under illumination.

different temperatures,[20] so we used $\Delta E_c(T) = E_c(T) - E_c(-7\ ^\circ\mathrm{C})$ with −7 °C (dark) as the reference temperature for comparison. Data are summarized in Table S1 of ESI.†

Fig. 5 shows the modified *J–V* curves obtained after addition of $\Delta E_c$ to the voltage. In the dark, Fig. 5(a), the onset in photocurrent occurs at lower voltages with increasing temperature however, under illumination, Fig. 5(b), $V_{oc}$ takes the same values for all curves up to 40 °C. Only the measurements above 50 °C present a noticeable decrease in $V_{oc}$. This result indicates that in the dark a rise in the temperature of the sample produces an increase in recombination rate, while for illuminated samples up to 40 °C this effect does not occur. Therefore, the changes in $V_{oc}$ up to 40 °C are only produced by $E_c$ shifts and not due to changes in charge transfer rate associated with temperature.

To explain this result we focus now on the analysis of the recombination resistance. As published before, once the short circuit photocurrent is fixed, $V_{oc}$ and the ideal $J$–$V_F$ curve (the *J–V* with $R_{series} = 0$) are determined by recombination kinetics that may be analyzed through the recombination resistance.[17,38,39] As

$$R_{rec} = \left(\frac{dJ}{dV_F}\right)^{-1}, \tag{5}$$

the photopotential is determined by

$$V_{oc} = V_0 + \int_{J_{sc}}^{0} R_{rec} dJ \tag{6}$$

and the current density at the different $V_F$ by

$$J = J_{sc} - \int_{V_0}^{V_F} \frac{dV_F}{R_{rec}} \tag{7}$$

with $V_0$ the potential drop in series resistance of the cell under short circuit conditions.

According to eqn (6) and (7) the larger $R_{rec}$ produces a smaller current density for a given potential for measurements taken in the dark ($J_{sc} = 0$ and $V_0 = 0$), while under illumination it yields a larger photopotential. Therefore the study of $R_{rec}$ helps in the understanding of the obtained *J–V* curves.

Fig. 6(a) and (b) show the variation in recombination resistance *vs.* the corrected potential at the different temperatures measured both in the dark and under illumination. $R_{rec}$ roughly follows

$$R_{rec} = R_0 \exp\left[-\frac{\beta q}{k_B T} V_F\right] \tag{8}$$

with $\beta$ a coefficient associated with the non-linearity of the charge transfer process and equivalent to the non-ideality factor ($m = 1/\beta$) of the diode equation used for standard semiconductor solar cells, and $R_0$ the pre-exponential parameter.

This result agrees well with a recombination process occurring through extended surface states in an energy tail distributed below the CB which, following the probabilistic model of Marcus[40], after some simplifications yields eqn (8) with[32]

$$R_0 = \frac{T_0\sqrt{\pi\lambda k T}}{q^2 L k_0 c_{ox} N_s T} \exp\left[\frac{E_c - E_{redox}}{k_B T_0} + \frac{\lambda}{4 k_B T}\right] \tag{9}$$

where $\lambda$ is the reorganization energy, $L$ the film thickness, $c_{ox}$ the concentration of acceptor species in the electrolyte, $N_s$ the density of states near the $TiO_2$ surface and $k_0$ a time constant for tunneling, also named rate constant. Other contributions from recombination through localized surface states below the conduction band may also occur, which would modify eqn (8).[32]

The decrease in recombination resistance with increasing temperature shown in Fig. 6(a) and (b) is associated with a decrease in $R_0$ and is responsible for the onset of current loss that occurs at lower potentials, as the application of eqn (7) describes.[17] This fact explains the result of dark *J–V* curves shown in Fig. 1(a), and the decrease in the open circuit potential shown in Fig. 1(b) and Table 1.

Eqn (9) shows the dependence of $R_0$ on temperature, the concentration of acceptor species in the electrolyte and $E_c$. Therefore, the decrease in recombination resistance when increasing temperature shown in Fig. 6(a) and (b) should be also affected by the shift in $E_c$. If the definition of the common equivalent conduction band potential,[17,38,39]

$$V_{ecb} = V_F - \Delta E_c/q \tag{10}$$

is used, the representation of the recombination resistance *vs.* $V_{ecb}$ provided in Fig. 6(c) and (d) allows the analysis of the data independently of $E_c$ changes.

Thus under dark conditions, as can be seen in Fig. 6(c), $R_{rec}$ decreases when temperature increases. This is the expected behavior attributed to an accelerated reaction kinetics of electrolyte acceptor species on the semiconductor surface due to the rising temperature.[32]

However, under illumination all the values of $R_{rec}$ taken for temperatures equal and lower than 40 °C converge, see Fig. 6(d), and they have very close values to those of $R_{rec}$ in the dark at 40 °C, see blue line in Fig. 6(d).

This phenomenon may have two origins: on the one hand and despite the cooling provided, the real temperature of the $TiO_2$ layer was increased to a value close to 40 °C for all the measurements done up to this temperature. This would imply that the heat accumulated into the active film due to the light

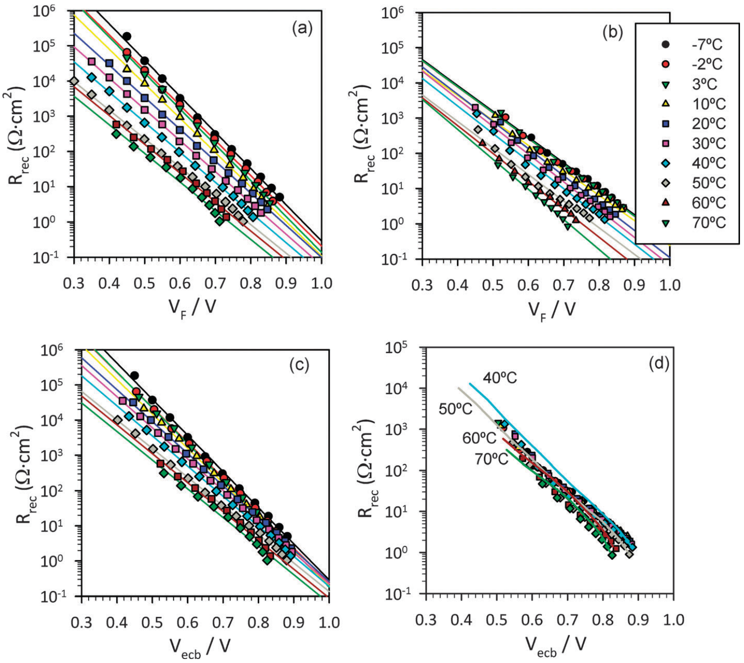

**Fig. 6** Values of $TiO_2$ recombination resistances *versus* corrected potential in the dark (a) and under illumination conditions (b) and *versus* the equivalent conduction band potential in the dark (c) and under illumination (d). Lines in (d) represent $R_{rec}$ under dark conditions for 40 °C (light blue), 50 °C (grey), 60 °C (brown) and 70 °C (dark green).

**Table 1** Characteristic parameters determining the efficiency of DSCs and average series resistance in the range of temperatures indicated

| $T$ (°C) | $J_{sc}$ (mA cm$^{-2}$) | $V_{oc}$ (V) | Fill factor | $\eta_{app}$ (%) | $R_{series}$ ($\Omega$ cm$^2$) |
|---|---|---|---|---|---|
| −7 | 10.3 | 0.82 | 0.60 | 5.10 | 9.9 |
| −2 | 10.3 | 0.81 | 0.61 | 5.14 | 8.6 |
| 3 | 10.3 | 0.82 | 0.61 | 5.19 | 8.5 |
| 10 | 10.3 | 0.80 | 0.63 | 5.16 | 6.8 |
| 20 | 10.3 | 0.76 | 0.63 | 4.95 | 6.5 |
| 30 | 10.3 | 0.75 | 0.64 | 4.95 | 5.8 |
| 40 | 10.3 | 0.72 | 0.64 | 4.74 | 5.9 |
| 50 | 10.3 | 0.67 | 0.65 | 4.49 | 5.5 |
| 60 | 10.3 | 0.65 | 0.66 | 4.44 | 5.3 |
| 70 | 10.3 | 0.62 | 0.67 | 4.31 | 5.2 |

absorption from a high intensity irradiation source cannot be efficiently evacuated neither through the 2.3 mm thick FTO glass substrate nor through the electrolyte side. Note that despite the use of LED to illuminate the samples effects such as thermalization of charges and energy loss due to recombination and transport (Joule effect) still occur and would be responsible for the heating of the $TiO_2$ film.

A second possibility could be that the increased concentration of acceptor species in the electrolyte (*i.e.* $I_3^-$) close to the $TiO_2$ surface after dye regeneration would increase the recombination to levels close to those occurring at 40 °C in the dark.

In our case, the precision obtained for transport resistance data, see ESI,† is not enough to discriminate which of the two phenomena is dominating. The shift in the conduction band with rising temperatures shown in Fig. 4(c) suggests that the second phenomenon dominates, but a local increase in film temperature cannot be fully discarded.

As shown in Fig. 6(d), for the measurements taken above 50 °C under illumination, $R_{rec}$ is smaller than at 40 °C, in a similar manner than for dark measurements, which may be attributed to a faster recombination kinetics attained at these higher temperatures. The effect of this reduction in $R_{rec}$ is that for temperatures larger than 50 °C, the photopotential decreases with respect to the other temperatures as shown in Fig. 5(b).

In Fig. 6(d) it is possible to observe small differences between $R_{rec}$ in the dark and under illumination. This implies that recombination in the illuminated sample is a more complex process than the single mechanism provided by eqn (8). Other contributions to recombination processes may be related to variations in acceptor species in the electrolyte. A more detailed study about this aspect and how it modifies eqn (8) is out of the scope of this paper and will be analyzed in a separate piece of work.

The result of the combination of the behavior of recombination and series resistances produces the characteristic shape of DSCs, the efficiency temperature curve is shown in Fig. 7. Our data, taken from $J$–$V_{app}$ curves after $\Delta E_c$ correction (see Fig. 5(b) and Table S2 in ESI†), have been normalized to be able to

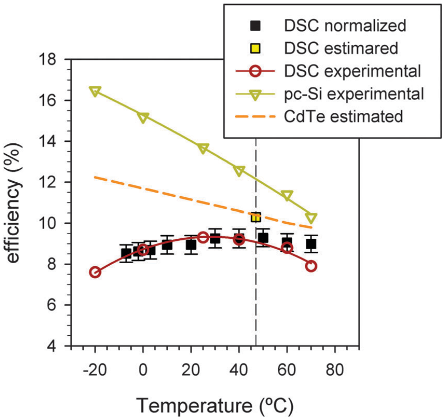

**Fig. 7** Comparison of energy conversion efficiencies for different photovoltaic technologies and temperatures. Black squares represent the apparent efficiency obtained from *J–V* curves in Fig. 5(b) normalized to match the published data of a 9.3% efficient DSC module (red void circles). Error bars are included to represent the mismatch with standard AM1.5G illumination conditions. Yellow square represents the estimation obtained for the record 9.9% efficient module taking into consideration extra energy collected by DSCs under real outdoor conditions. pc-Si experimental (green triangles) stands for data from a commercial polycrystalline silicon solar module and CdTe estimated (orange dashed line) is the simulation of a 11% module with a temperature coefficient of −0.25% $K^{-1}$. The dotted line represents the NOCT temperature, where performance comparison approaches real operation conditions.

compare the results with data published from Sony for a 9.3% efficient DSC 17 $cm^2$ module.[12] The good match found suggests similar mechanisms dominating the behavior of both cell and module.

Therefore at low temperatures while recombination rate in the $TiO_2$ film is constant, the decrease in the counter and diffusion contributions to the total series resistance of the DSC with increasing temperatures improves FF. Between 20 and 40 °C both $R_{rec}$ and $R_{series}$ present little changes and so does efficiency. Above 40 °C the decrease in recombination resistance and thus the $V_{oc}$ produces a reduction in the efficiency that may not be compensated by further increases in FF. For these temperatures, see Fig. 2, $R_{series}$ is dominated by the nearly constant $R_{FTO}$, while $R_d$ stabilizes and $R_{Pt}$ presents only a small reduction.

As mentioned above, the fact that the maximum efficiency in a DSC is obtained at a temperature close to the normal operating cell temperature (NOCT) is an aspect to take into account when comparing DSCs with other technologies. Therefore, considering 47 °C as NOCT, the efficiency of a CdTe module drops from a nominal value of 11% to a practical value of 10.4% while a polycrystalline silicon (pc-Si) module with a nominal efficiency of 13.7% presents, at this NOCT, a real efficiency of 12.3%, see Fig. 7.

Record DSC modules reaching 9.9% efficiency are not so far from the values obtained for these standard and commercial panels.[15] Furthermore, the ability of DSCs to capture low incidence angle and diffuse light results in both an extension of effective energy production hours and a higher performance in cloudy days.[10,13] Energy production increases of 10% in sunny days and 20% in cloudy days have been reported for DSCs with respect to pc-Si modules for outdoor static installations with the same nominal power.[10,13] Part of this rise in energy output is due to the lower real efficiency of pc-Si at NOCT, as just mentioned. Therefore, considering a rough 5% as the "effective" performance increase in the DSC per watt peak installed with respect to conventional technologies, the comparable efficiency of the DSC would rise to 10.3% for a nominal 9.9% module, see yellow square in Fig. 7. This is at the same level than CdTe panels at NOCT.

## Conclusions

We have observed that out of conduction band shifts, electron loss by recombination in $TiO_2$ is the same for external temperatures ranging between −7 and 40 °C. This effect may be due to the combined effect of a rise in the temperature of active film and the increase in the acceptor species in the electrolyte close to the $TiO_2$ surface after dye regeneration under high light intensity. The constant recombination resistance pattern in this range of temperatures determines the constant $V_{oc}$ attained for data compared at the same position of conduction band. The decrease in total series resistance with rising temperatures produces an increase in FF and thus in efficiency up to this high temperature. Above 40 °C recombination accelerates producing a decay in $V_{oc}$. As further reduction in series resistance is limited, efficiency decreases above 40 °C are observed.

Finally we remarked that for a correct comparison of efficiencies between solar technologies the values at operating temperatures should be used rather than the nominal ones. This yields a narrower and more realistic gap between the different technologies than under nominal conditions.

## Acknowledgements

Financial support from Ministerio de Cíencia e Innovación under project HOPE CSD2007-00007 and Generalitat Valenciana under Project PROMETEO/2009/058 are acknowledged. Serveis Centrals d'Instrumentació Científica from Universitat Jaume I are acknowledged for the profilometry measurements. SRR thanks Pablo P. Boix for helping in lab setup.

## References

1 M. Grätzel, Dye-sensitized solar cells, *J. Photochem. Photobiol., C*, 2003, **4**, 145–153.
2 V. Marin, E. Holder, M. M. Wienk, E. Tekin and D. Kozodaev, Schubert, U. S. Ink-Jet Printing of Electron Donor/Acceptor Blends: Towards Bulk Heterojunction Solar Cells, *Macromol. Rapid Commun.*, 2005, **26**, 319–324.
3 Y. Chiba, A. Islam, Y. Watanabe, R. Komiya, N. Koide and L. Han, Dye-Sensitized Solar Cells with Conversion Efficiency of 11.1, *Jpn. J. Appl. Phys.*, 2006, **45**, L638–L640.

4 Y. Cao, Y. Bai, Q. Yu, Y. Cheng, S. Liu, D. Shi, F. Gao and P. Wang, Dye-Sensitized Solar Cells with a High Absorptivity Ruthenium Sensitizer Featuring a 2-(Hexylthio)thiophene Conjugated Bipyridine, *J. Phys. Chem. C*, 2009, **113**, 6290–6297.

5 Q. Yu, Y. Wang, Z. Yi, N. Zu, J. Zhang, M. Zhang and P. Wang, High-Efficiency Dye-Sensitized Solar Cells: The Influence of Lithium Ions on Exciton Dissociation, Charge Recombination, and Surface States, *ACS Nano*, 2010, **4**, 6032–6038.

6 M. Grätzel, *Hybrid and Organic Photovoltaic Conference, HOPV'11*, 2011, Valencia, Spain.

7 B. C. O'Regan and M. Grätzel, A low-cost high-efficiency solar cell based on dye-sensitized colloidal $TiO_2$ films, *Nature*, 1991, **353**, 737.

8 M. K. Nazeeruddin, A. Kay, I. Rodicio, R. Humphry-Baker, E. Müller, P. Liska, N. Vlachopoulos and M. Grätzel, Conversion of light to electricity by *cis*-X 2bis(2,2′-bipyridyl-4,4′-dicarboxylate)ruthenium(II) charge-transfer sensitizers ($X = Cl^-$, $Br^-$, $I^-$, $CN^-$, and $SCN^-$) on nanocrystalline $TiO_2$ electrodes, *J. Am. Chem. Soc.*, 1993, **115**, 6382–6390.

9 A. Yella, H.-W. Lee, H. N. Tsao, C. Yi, A. K. Chandiran, M. K. Nazeeruddin, E. W.-G. Diau, C.-Y. Yeh, S. M. Zakeeruddin and M. Grätzel, Porphyrin-Sensitized Solar Cells with Cobalt(II/III) Based Redox Electrolyte Exceed 12 Percent Efficiency, *Science*, 2011, **334**, 629–634.

10 T. Toyoda, T. Sano, J. Nakajima, S. Doi, S. Fukumotoa, A. Ito, T. Tohyamaa, M. Yoshida, T. Kanagawa, T. Motohiro, T. Shiga, K. Higuchi, H. Tanaka, Y. Takeda, T. Fukano, N. Katoh, A. Takeichi, K. Takechi and M. Shiozawa, Outdoor performance of large scale DSC modules, *J. Photochem. Photobiol., A*, 2004, **164**, 203–207.

11 K. Kalyanasundaram, Dye-sensitized Solar Cells, in *Dye-sensitized Solar Cells*, ed. K. Kalyanasundaram, CRC Press, Boca Raton, 2010.

12 T. Nozawa, Organic Solar Cells Now Produced in Volume. *Nikkei Electronics Asia* 2008, *July*, http://techon.nikkeibp.co.jp/article/HONSHI/20080625/20153868/.

13 K. Brooks, P. Murray, F. Au, H. Duong, R. Harikisun, H. Desilvestro, Status of Industrialization of Dye Solar Cells for BIPV Applications. In 3rd Nordic PV Conference Tallinn, Estonia, 2009, Vol. http://www.irc.ee/pvconference/?page=participants.

14 H.-D. Mohring, D. Stellbogen, ''Annual Energy Harvest of PV Systems – Advantages and Drawbacks of Different PV Technologies.'', 23rd European Photovoltaic Solar Energy Conference, 1–5 September 2008, 2008, Valencia, Spain.

15 M. Morooka, R. Ogura, M. Orihashi and M. Takenaka, Development of dye-sensitized solar cells for practical applications, *Electrochemistry*, 2009, **77**, 960–965.

16 G. Boschloo and A. Hagfeldt, Characteristics of the Iodide/Triiodide Redox Mediator in Dye-Sensitized Solar Cells, *Acc. Chem. Res.*, 2009, **42**, 1819–1826.

17 F. Fabregat-Santiago, G. Garcia-Belmonte, I. Mora-Sero and J. Bisquert, Characterization of nanostructured hybrid and organic solar cells by impedance spectroscopy, *Phys. Chem. Chem. Phys.*, 2011, **13**, 9083–9118.

18 J. R. Jennings, Y. R. Liu and Q. Wang, Efficiency Limitations in Dye-Sensitized Solar Cells Caused by Inefficient Sensitizer Regeneration, *J. Phys. Chem. C*, 2011, **115**, 15109–15120.

19 J. Bisquert and F. Fabregat-Santiago, Impedance spectroscopy: A general introduction and application to dye-sensitized solar cells, in *Dye-sensitized Solar Cells*, ed. K. Kalyanasundaram, EPFL Press, CRC Press, Lausanne, Boca Raton, 2010.

20 Z. Zhang, P. Chen, T. N. Murakami, S. M. Zakeeruddin and M. Gratzel, The 2,2,6,6-tetramethyl-1-piperidinyloxy radical: An efficient, iodine-free redox mediator for dye-sensitized solar cells, *Adv. Funct. Mater.*, 2008, **18**, 341–346.

21 T. Daeneke, T.-H. Kwon, A. B. Holmes, N. W. Duffy, U. Bach and L. Spiccia, High-efficiency dye-sensitized solar cells with ferrocene-based electrolytes, *Nat. Chem.*, 2011, **3**, 211–215.

22 S. R. Raga, E. M. Barea and F. Fabregat-Santiago, Analysis of the Origin of Open Circuit Voltage in Dye Solar Cells, *J. Phys. Chem. Lett.*, 2012, **3**, 1629–1634.

23 M. Miyashita, K. Sunahara, T. Nishikawa, Y. Uemura, N. Koumura, K. Hara, A. Mori, T. Abe, E. Suzuki and S. Mori, Interfacial Electron-Transfer Kinetics in Metal-Free Organic Dye-Sensitized Solar Cells: Combined Effects of Molecular Structure of Dyes and Electrolytes, *J. Am. Chem. Soc.*, 2008, **130**, 17874–17881.

24 B. C. O'Regan and J. R. Durrant, Kinetic and Energetic Paradigms for Dye-Sensitized Solar Cells: Moving from the Ideal to the Real, *Acc. Chem. Res.*, 2009, **42**, 1799–1808.

25 F. Fabregat-Santiago, J. Bisquert, G. Garcia-Belmonte, G. Boschloo and A. Hagfeldt, Impedance spectroscopy study of the influence of electrolyte conditions in parameters of transport and recombination in dye-sensitized solar cells, *Sol. Energy Mater. Sol. Cells*, 2005, **87**, 117–131.

26 Y. Liu, A. Hagfeldt, X.-R. Xiao and S.-E. Lindquist, Investigation of influence of redox species on the interfacial energetics of a dye sensitized nanoporous $TiO_2$ solar cell, *Sol. Energy Mater. Sol. Cells*, 1998, **55**, 267–281.

27 F. Fabregat-Santiago, J. Bisquert, E. Palomares, L. Otero, D. Kuang, S. M. Zakeeruddin and M. Grätzel, Correlation between Photovoltaic Performance and Impedance Spectroscopy of Dye-Sensitized Solar Cells Based on Ionic Liquids, *J. Phys. Chem. C*, 2007, **111**, 6550–6560.

28 J. Bisquert, Chemical capacitance of nanostructured semiconductors: its origin and significance for heterogeneous solar cells, *Phys. Chem. Chem. Phys.*, 2003, **5**, 5360.

29 J. Bisquert, F. Fabregat-Santiago, I. Mora-Seró, G. Garcia-Belmonte and S. Giménez, Electron Lifetime in Dye-Sensitized Solar Cells: Theory and Interpretation of Measurements, *J. Phys. Chem. C*, 2009, **113**, 17278–17290.

30 G. Boschloo and D. Fitzmaurice, Spectroelectrochemical Investigation of Surface States in Nanostructured $TiO_2$ Electrodes, *J. Phys. Chem. B*, 1999, **103**, 2228–2231.

31 F. Fabregat-Santiago, I. Mora-Seró, G. Garcia-Belmonte and J. Bisquert, Cyclic voltammetry studies of nanoporous semiconductor electrodes. Models and application to nanocrystalline $TiO_2$ in aqueous electrolyte, *J. Phys. Chem. B*, 2003, **107**, 758–769.

32 Q. Wang, S. Ito, M. Grätzel, F. Fabregat-Santiago, I. Mora-Seró, J. Bisquert, T. Bessho and H. Imai, Characteristics of High Efficiency Dye-sensitized Solar Cells, *J. Phys. Chem. B*, 2006, **110**, 19406–19411.

33 I. Abayev, A. Zaban, V. G. Kytin, A. A. Danilin, G. Garcia-Belmonte and J. Bisquert, Properties of the electronic density of states in $TiO_2$ nanoparticles surrounded with aqueous electrolyte, *J. Solid State Electrochem.*, 2007, **11**, 647–653.

34 J. L. Movilla, G. Garcia-Belmonte, J. Bisquert and J. Planelles, Calculation of the electronic density of states induced by impurities in $TiO_2$ quantum dots, *Phys. Rev. B: Condens. Matter Mater. Phys.*, 2005, **72**, 153313.

35 B. O'Regan and J. R. Durrant, Calculation of Activation Energies for Transport and Recombination in Mesoporous $TiO_2$/Dye/Electrolyte Films-Taking into Account Surface Charge Shifts with Temperature, *J. Phys. Chem. B*, 2006, **110**, 8544–8547.

36 L. Feng, J. James Robert, M. Nripan and W. Qing, Evolution of Charge Collection/Separation Efficiencies in Dye-Sensitized Solar Cells Upon Aging: A Case Study, *J. Electrochem. Soc.*, 2011, **158**, B1158–B1163.

37 A. Listorti, C. Creager, P. Sommeling, J. Kroon, E. Palomares, A. Fornelli, B. Breen, P. R. F. Barnes, J. R. Durrant, C. Law and B. O'Regan, The mechanism behind the beneficial effect of light soaking on injection efficiency and photocurrent in dye sensitized solar cells, *Energy Environ. Sci.*, 2011, **4**, 3494–3501.

38 E. M. Barea, J. Ortiz, F. J. Payá, F. Fernández-Lázaro, F. Fabregat-Santiago, A. Sastre-Santos and J. Bisquert, Energetic factors governing injection, regeneration and recombination in dye solar cells with phthalocyanine sensitizers, *Energy Environ. Sci.*, 2010, **3**, 1985–1994.

39 E. M. Barea, C. Zafer, B. Gultekin, B. Aydin, S. Koyuncu, S. Icli, F. F. Santiago and J. Bisquert, Quantification of the Effects of Recombination and Injection in the Performance of Dye-Sensitized Solar Cells Based on N-Substituted Carbazole Dyes, *J. Phys. Chem. C*, 2010, **114**, 19840–19848.

40 R. Memming, *Semiconductor Electrochemistry*, Wiley-VCH, Weinheim, 2001.

Journal of
Materials Chemistry

Cite this: *J. Mater. Chem.*, 2012, **22**, 1751

www.rsc.org/materials

**COMMUNICATION**

# Enhanced diffusion through porous nanoparticle optical multilayers

**Carmen López-López,[a] Silvia Colodrero,[a] Sonia R. Raga,[b] Henrik Lindström,[c] Francisco Fabregat-Santiago,*[b] Juan Bisquert[b] and Hernán Míguez*[a]**

***Received 13th October 2011, Accepted 21st November 2011***
**DOI: 10.1039/c1jm15202e**

**Herein we demonstrate improved mass transport through nanoparticle one-dimensional photonic crystals of enhanced porosity. Analysis is made by impedance spectroscopy using iodine and ionic liquid based electrolytes and shows that newly created large pores and increased porosity improve the diffusion of species through the photonic crystal. This achievement is based on the use of a polymeric porogen (polyethylene glycol), which is mixed with the precursor suspensions used for the deposition of nanoparticle $TiO_2$ and $SiO_2$ layers and then eliminated to generate a more open interconnected void network, as confirmed by specular reflectance porosimetry. A compromise between pore size and optical quality of these periodic structures is found.**

## Introduction

Recently, different variants of porous one-dimensional photonic crystals (1DPCs) have been proposed and built.[1–12] To create these porous multilayers in which the dielectric constant varies periodically along one direction, numerous methods have been developed in the last few years, such as deposition of supramolecularly templated films,[2,5] glancing angle vapor physical deposition,[1,4,12] sol–gel,[11] or electrochemical etching.[8,10] One of the most versatile techniques is the deposition of nanoparticle suspensions by spin or dip coating.[3,6,7] Although these materials were first proposed by Thomas in the late eighties,[13] and research on them continued in the nineties,[14] it is now when the field is blooming and its technological potential is beginning to be explored.[15,16] The added value of these latter optical multilayers relies on their interconnected porosity, which makes their inner void network accessible to melted or dissolved polymers,[17,18] liquids or gases,[19] as well as on their ease of design and their high versatility for deposition onto a wide diversity of substrates. Actually, these properties have boosted the exploration of applications in fields such as optical sensing[20–22] or photovoltaic devices.[23] The first of these is based on the fact that these films show a different structural color upon infiltration of different guest compounds into the porous network, which alters the effective refractive index of the structure. On the other hand, porous 1DPCs have also been employed as coherent mirrors to improve light harvesting efficiency in dye sensitized solar cells.[23] In this case, their porous mesostructure allows the electrolyte to soak the entire electrode, thus providing high reflectivity and allowing charge transport through the cell. All these applications are highly dependent on both the degree of porosity and the pore size distribution of the films.

Typically, higher dielectric contrast (*i.e.*, wider and more intense Bragg reflections) is attained for multilayers built by alternate deposition of amorphous $SiO_2$ and nanocrystalline $TiO_2$. Up to now, the porosity of nanoparticle 1DPCs has only been controlled through both the degree of aggregation and the particle size of the precursor suspensions,[6,17] which has even made it possible to build periodic multilayers of homogeneous composition.[24] However, the $TiO_2$ nanocrystalline particles typically employed give rise to layers of small pore size, which might impede the proper flow of species throughout the periodic multilayer, limiting their potential application in electrochemical devices.

Herein we demonstrate improved mass transport through nanoparticle 1DPCs of enhanced porosity. Analysis is made by impedance spectroscopy (IS) using iodine and ionic liquid based electrolytes. This achievement is based on the use of a polymeric porogen (polyethylene glycol), which is mixed with the precursor suspensions used for the deposition of the $TiO_2$ and $SiO_2$ layers and then eliminated to generate a more open interconnected void network. A similar method has recently been proposed to improve mass transport in photocatalytic films.[25] This allows controlling both the degree of porosity and the pore size distribution of $TiO_2$ (np-$TiO_2$) and $SiO_2$ nanoparticle (np-$SiO_2$) layers integrated in 1DPCs. We study the changes of the structural properties caused by the alteration of the pore structure in, first, monolayers made of $TiO_2$ nanocrystals and amorphous $SiO_2$ nanospheres and, then, in multilayers containing them. In spite of achieving a large increase in average pore size, the optical quality of the structure is preserved. A reduction of the electrolyte diffusion resistance of above 40% with respect to the starting multilayer is found. These results open the route to optimize the performance of photo-electro-chemical devices in which less porous optical multilayers have already been successfully integrated.

---

[a] *Instituto de Ciencia de Materiales de Sevilla, Consejo Superior de Investigaciones Científicas-Universidad de Sevilla, Américo Vespucio 49, 41092 Sevilla, Spain. E-mail: hernan@icmse.csic.es*
[b] *Departament de Física, Universitat Jaume I, Vicent Sos Baynat s/n, 12071 Castelló, Spain*
[c] *NLAB Solar Laboratories, Drottning Kristinas väg 45, SE-114 28 Stockholm, Sweden*

## Experimental

### Preparation of particle suspensions

The starting materials were suspensions of nanoparticles of $SiO_2$ and $TiO_2$. They were employed in the production of these multilayers due to the high refractive index contrast between them. $SiO_2$ nanocolloids (average size of 30 nm) were purchased from Dupont (LUDOX TMA, Aldrich), while $TiO_2$ nanocrystallites (average size of 10 nm) were synthesized using a variation of a method based on the hydrolysis of titanium tetraisopropoxide followed by a peptization process under hydrothermal conditions.[26] Titanium tetraisopropoxide (20 ml, 97% Aldrich) was added to Milli-Q water (36 ml) and stirred for 1 hour. Once the alkoxide was hydrolyzed, the product was filtered to collect the solid formed and washed several times with distilled water. Then, it was peptized in a Teflon reactor containing 3.9 ml of 0.6 M tetramethylammonium hydroxide ($\sim$2.8 M, Fluka) at 120 °C for 3 h. Later centrifugation at 14 000 rpm for 10 minutes allows elimination of some large aggregates from the dispersion, the concentration of the resultant suspension being typically between 24 and 25 wt%. $TiO_2$ and $SiO_2$ nanoparticles are diluted to 5 and 2 wt% respectively, in a mixture of water, 21 vol%, and methanol, 79 vol%, in order to use as precursors for the spin-coating process. Prior to their deposition each suspension was ultrasonicated for several minutes to re-disperse aggregates.

The polymer chosen to alter the porous network is polyethylene glycol (PEG) because it exhibits good film forming properties, and reduces the density of defects present in the films made by spin-coating.[17] The influence that the addition of different quantities of PEG to the $TiO_2$ and $SiO_2$ precursor suspensions has on the mesostructure of these nanoparticle Bragg reflectors was analyzed afterward. It should be mentioned that there are other methods that allow control of the porosity of nanocrystalline $TiO_2$ films, which involve the synthesis of particles within polyelectrolyte multilayers.[27] Also, the increase of particle size to enlarge the average pore size was discarded since it could give rise to unwanted diffuse scattering, as it has been proven before.[28]

### Preparation of monolayer and multilayer films

Both np-$TiO_2$ monolayers and np-$SiO_2$/np-$TiO_2$ stacks with 1DPC properties made of five bilayers were built by deposition of the diluted $TiO_2$ and $SiO_2$ nanoparticle suspensions by spin-coating (final speed $\omega = 5000$ rpm; acceleration $\gamma = 9180$ rpms$^{-1}$; time 60 s), followed by heat treatment in an oven at 450 °C for 30 min to provide the films with mechanical stability. In order to achieve the desired monolayer thickness, several depositions of the same precursor suspension were carried out. The substrates used to deposit monolayers and multilayers were silicon and glass, respectively. Both substrates were previously treated to enhance their hydrophilicity and, consequently, improve the first layer deposition. The films prepared presented high optical quality and displayed uniform color arising from the interference of the beams reflected by the different interphases.

In order to build the monolayers and multilayers using the np-$SiO_2$/PEG and the np-$TiO_2$/PEG precursor suspensions we also employed the spin coating protocol described above, although in this case it was necessary to perform a thermal annealing at 300 °C for 15 minutes in air after each deposition to eliminate the PEG from the structure and to consolidate the stacking of these layers. Without this intermediate treatment, it was not possible to create a new layer on top, since the deposited film did not adhere properly. Finally, the remaining polymer is eliminated after calcination of the whole multilayer at 450 °C for 1 hour in air.

### Materials characterization

The new porous mesostructure of the $TiO_2$ and $SiO_2$ films was assessed by Specular Reflectance Porosimetry (SRP). This technique is based on the analysis of the shift of the optical response at equilibrium as the vapor pressure of a volatile liquid, first, gradually increases up to saturation and, then, decreases down to the initial value in a closed chamber. In this way, the adsorption–desorption isotherm curves of the np-$TiO_2$/PEG and the np-$SiO_2$/PEG monolayers were obtained. The solvent used to execute this study was isopropanol, which has proven to yield excellent results for the analysis of vapor sorption properties of complex mesostructured and nanoparticle based multilayers.[19,29,30] This technique allows us to obtain the effective refractive index of each one of the films and, by using the Bruggeman equation, analyze the evolution of both the overall porosity and the pore size distribution as the concentration of PEG in the precursor liquid varies. Analysis of the specular reflectance spectra obtained at normal incidence was performed by simulating and fitting the optical response measured at the different solvent partial pressures. To do so, we employed a code written in MatLab based on the transfer matrix method and that has been thoroughly described before.[31] Reflectance spectra were attained using a Fourier transform spectrophotometer (Bruker IFS-66 FTIR) attached to a microscope and operating in reflection mode with a 4× objective with 0.1 of numerical aperture (light cone angle ±5.7°). Please notice that the inadequacy of using standard BET techniques (based on sample weight changes caused by $N_2$ adsorption and desorption from the pore walls) for the study of porous mesostructured films arises from the too low weight of the films. On the other hand, ellipsometry relies on the use of one-side polished silicon wafers as substrates, which would largely affect their optical properties. The images of cross-section were acquired with a field-emission scanning electron microscope (FESEM, Hitachi S-4800 operating at 2 kV).

### Impedance spectroscopy measurements

IS analysis was performed over cells containing a solution made with 0.13 M iodine in 1-butyl-3-methylimidazolium iodide. Each cell was composed of two platinized FTO electrodes, one of them with an np-$SiO_2$/np-$TiO_2$ multilayer, for which different quantities of PEG were employed, deposited over the Pt-coated glass. An area of 1 × 1 cm$^2$ was drawn over conductive glass leaving a 2 mm wide strip on one of the sides to evacuate the charge and make the contacts. FTO out of this area was removed *via* etching with Zn powder and diluted HCl. Then the electrodes were electroplatinized by submerging them into a diluted chloroplatinic acid aqueous solution using a Pt sheet as a counter-electrode and applying a potential of 1.5 V for 1 minute. After this process, dark FTO electrodes were obtained, indicating that a high concentration of Pt was deposited over the surface. The cells were mounted after drop casting the electrolyte in one of the electrodes and fixing the second by pressing it strongly with a clamp. Pressing electrodes together with a clamp ensures to reach a distance between electrodes equal to the photonic crystal thickness. The removal of external FTO avoids both short circuiting of the cells and direct diffusion of iodide between uncovered FTO layers, minimizing edge effects. The conductive strips of the opposed electrodes were oriented in contrary faces also to prevent short circuits. The iodine concentration used in the electrolyte is lower than that found in the literature because the short distance between electrodes makes it more difficult to reach the current saturation regime.[32] Furthermore, a pure ionic liquid is necessary in this experiment both to avoid evaporation during measurements and to be able to appreciate the differences in diffusion due to porosity. Electrochemical measurements were carried out in this two electrode configuration and collected after letting the electrolyte penetrate into the pores of the nanoparticle 1DPC. First, a current–voltage curve between 0 and 1.5 V was made to measure the limiting currents reached. Then galvanostatic IS curves were attained taking 4 different currents starting from 0 mA to near the saturation current for each cell. Analysis of the parameters obtained at the same current density was performed in order to obtain comparable results between the different samples. IS data were fitted to a Randles circuit model.

## Results and discussion

### Analysis of pore size and porosity

The different degree of porosity extracted from the analysis of the specular reflectance spectra of the np-$TiO_2$/PEG and np-$SiO_2$/PEG layers in air is shown in Table 1. On the other hand, the change in the optical response of these porous layers *versus* the gradual increase or decrease of the vapor pressure of a liquid solvent provides us with information on the different pore size distribution. Adsorption–desorption isotherms are presented in Fig. 1 and 2. This analysis reveals that the starting (containing no polymer) np-$SiO_2$ layers present a much larger average pore size than np-$TiO_2$ ones and that the addition of PEG produces more significant changes in both the pore size and average porosity of the second kind of layers. Hence more effort was devoted to improve the pore network of the $TiO_2$ layer since the bottleneck for optimized electrolyte flow must be the narrowest pores of the multilayer, present in the np-$TiO_2$ layers.

First of all, as presented in Table 1, as the PEG : np-$TiO_2$ weight ratios increase from 0 to 0.75, the effective refractive index decreases from 1.70 to 1.50, which implies that the accessible porosity of these layers rises from 47% to 60%. In the case of $SiO_2$ films, the refractive index varies from an already low 1.25 to 1.22 when the PEG : np-$SiO_2$ weight ratio is 0.50, with the porosity changing from 44% to 50%.

Noteworthy, all adsorption–desorption isotherms measured can be classified as type IV[33,34] following a standard classification of the capillary condensation response of mesoporous materials (pore size between 2 and 50 nm). In the curves attained from the np-$TiO_2$ layer (Fig. 1a), the volume of solvent infiltrated within the structure increases as the pressure goes up to a specific value of $P/P_0 = 0.93$, where $P_0$ is the saturation vapor pressure of isopropanol at room temperature, with the filled pore volume remaining constant for higher pressures. This fact indicates that the accessible porosity of the layer is completely filled with the solvent employed. However, this trend is not observed for the case of the isotherms measured from the layers in which the PEG was used to change their internal porous structure (Fig. 1b and c), which is in consonance with the expected effect of the porogen on the mesostructure, namely, the creation of large cavities in which condensation of the vapor is prevented. Pore size distributions of the different np-$TiO_2$ and np-$TiO_2$/PEG films were extracted from the isotherm data, as presented in Fig. 1d–f. The porous structure attained after spin coating the np-$TiO_2$ precursor suspension without PEG is a network of voids whose size is comprised between 4 nm and 18 nm. Broader pore radius ranges, up to 24 nm, are obtained when the different amounts of polymer are employed. For the case of films made of suspensions containing PEG : np-$TiO_2$ weight ratios of 0.25 and 0.50, the larger pore radius created cannot be estimated from the isotherm curves since the plateau at higher partial vapor pressures is not reached. Nevertheless, pore size distributions demonstrate that both the porosity and the pore size are largely increased when PEG is used as porogen.

Similarly, adsorption–desorption isotherms and pore size distributions of both np-$SiO_2$ and np-$SiO_2$/PEG layers are shown in Fig. 2. In this case, the most noteworthy difference is the increase of the radius of necks between nanoparticles of the sample when PEG is used, as it can be seen when Fig. 2c and d (grey circles and lines) are compared. Also, the pore size distribution becomes wider and the average pore size shifts towards higher values. As expected, since layers formed by $SiO_2$ nanoparticles have larger pores than $TiO_2$ films to start with, the effect of porogen on the $SiO_2$ pore size is less noticeable, although in both types of layers the porosity rises with the concentration of porogen used in the precursor suspensions.

### Highly porous layers in Bragg reflectors

Having demonstrated that both the porosity and the average pore size of np-$TiO_2$ and np-$SiO_2$ films are increased when PEG is added to the precursor suspensions, 1DPCs were built in order to prove that these new highly porous layers can also be integrated in a stack that presents photonic crystal properties. For that purpose, np-$SiO_2$ and np-$TiO_2$ precursor suspensions with different concentration of PEG were employed. FESEM images of cross-sections of multilayers made by alternating films deposited from these suspensions are shown in Fig. 3. The samples whose images are displayed were prepared using suspensions containing PEG : np-$TiO_2$ weight ratios of 0 (Fig. 3a) and 0.75 (Fig. 3b), while the same np-$SiO_2$ suspension containing no PEG was used for both samples.

**Table 1** Refractive index and porosity of the different nanoparticle monolayers and multilayers, as estimated from the analysis of the optical reflectance

| Material | PEG/np (wt%) | $n_{eff}$ monolayer | Porosity of monolayer (%) | $n_{eff}$ of np-film in multilayer | Porosity of np-film in multilayer (%) |
|---|---|---|---|---|---|
| $TiO_2$ | — | 1.70 | 47 | 1.69 | 47 |
| | 25 | 1.58 | 55 | 1.59 | 54 |
| | 50 | 1.55 | 57 | 1.54 | 57 |
| | 75 | 1.49 | 60 | 1.49 | 60 |
| $SiO_2$ | — | 1.25 | 44 | 1.27 | 42 |
| | 50 | 1.22 | 50 | 1.22 | 50 |

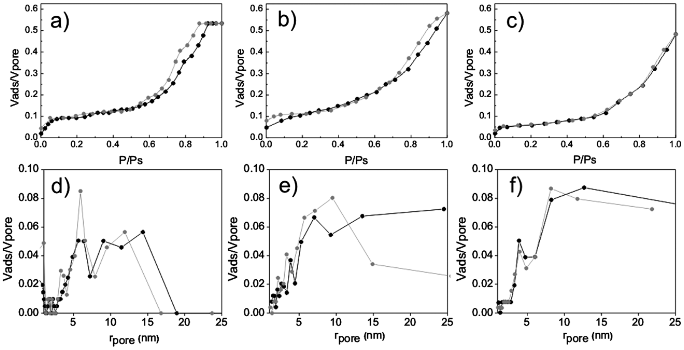

**Fig. 1** Adsorption (black circles and lines) and desorption (grey circles and lines) isotherms and pore size distribution measured by specular reflectance porosimetry from uniform monolayers made of (a and d) np-$TiO_2$ and np-$TiO_2$/PEG mixtures in which the weight ratio between the porogen and the nanoparticles is (b and e) 25% and (c and f) 50%.

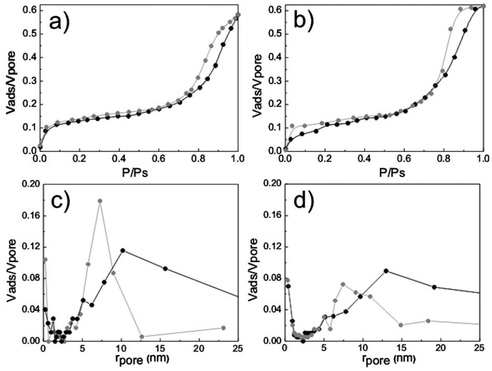

**Fig. 2** Adsorption (black circles and lines) and desorption (grey circles and lines) isotherms and pore size distribution measured by specular reflectance porosimetry from uniform monolayers made of (a and c) np-$SiO_2$ and (b and d) np-$SiO_2$/PEG mixtures in which the weight ratio between the porogen and the nanoparticles is 50%.

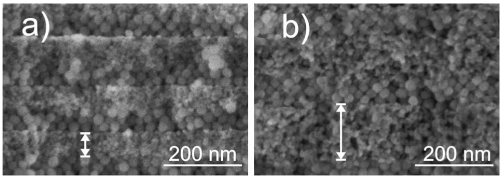

**Fig. 3** FESEM images of cross-sections corresponding to Bragg reflectors made of alternate layers of spherical silica particles and titania nanocrystals. The latter was mixed with PEG in weight relations of (a) 0% and (b) 75% with respect to the weight of np-$TiO_2$ in the precursor suspension.

The different pore structure of the $TiO_2$ layers can be clearly distinguished in these pictures. Furthermore, it can be readily observed that the thickness of the $TiO_2$ layer also increases with the PEG concentration in the precursor suspension, with thicknesses comprised between 60 nm and 130 nm being attained for PEG : np-$TiO_2$ weight ratios ranging from 0 to 0.75. The clear definition between the interfaces of np-$TiO_2$ and np-$SiO_2$ layers present in the originally made nanoparticle multilayers[6] (Fig. 3a) fades when the polymer is used to modify the pore network (Fig. 3b) mainly due to the $SiO_2$ particle interpenetration within the large superficial pores of the $TiO_2$ layers. Long range uniformity is, however, preserved.

In the same way that it was done for the monolayers, the values of the effective refractive index and the porosity of each layer within the periodic stack were also estimated minimizing the difference between the simulated and the experimental reflectance spectra and using the Bruggeman equation, respectively. The results of the fittings are listed in Table 1. It can be noticed that the porosity of the np-$TiO_2$ layers remains practically unaltered after being integrated in the Bragg reflector when compared to that measured for monolayers. It should be remarked that control over the porosity of the films, like the one herein demonstrated, opens the possibility of designing the optical properties of the multilayers built with them with great precision, as it has actually been proven for other optical filters in which porosity, although not accessible, can be tailored to measure.[35] Also, we would like to remark that, although highly reflecting multilayers of controlled pore size distribution can be attained by supramolecular templating,[36] these cannot be easily integrated in photo-electrochemical devices. This is due to the incompatibility of the compounds employed during the preparation of the supramolecularly templated mesostructure with the rest of materials present in the photocatalytic or photovoltaic cell: liquid phase precursors infiltrate the whole device, which yields the uncontrolled formation of metal oxide, drastically reducing the performance of the device. In contrast, when nanoparticle suspensions are used to form the multilayers, the solid phase is retained in the regions onto which it is deposited, while the liquid one evaporates or is easily removed by thermal annealing.

1DPCs of different porosity having their Bragg peaks in the same spectral range were built in order to study the influence that the new pore network structure may have on the control of the photonic crystal properties. This requires that all samples present the same unit cell optical thickness, $d_{uc} = (n_1t_1 + n_2t_2)$, being $n_i$ and $t_i$ the refractive index and the thickness of each type of layer present in the ensemble, since, in a first approximation, the Bragg peak is centred at $\lambda_B = 2d_{uc}$. This condition is achieved by modifying the concentrations of $TiO_2$ and $SiO_2$ precursor suspensions, since, as shown in Fig. 3, the actual thickness of a layer increases when the same concentrations of nanoparticles are mixed with increasing amounts of PEG. The specular reflectance spectra of these samples are displayed in Fig. 4. The comparison between the different spectra reveals that the presence of larger pores does not affect adversely the performance of the multilayers as Bragg reflectors. In all cases, the number of layers deposited is similar ($N = 10$) and primary maxima present intensities above 80%. Slightly higher peaks are achieved for 1DPCs in which the pores are finer. The reason for this effect is the lower refractive index contrast existing between the layers of np-$TiO_2$ and np-$SiO_2$ in those multilayers showing enhanced porosity, which diminishes the scattering strength of the lattice. Also, a clear narrowing of the peak spectral width is observed as the porosity increases. The photonic gap to midgap ratio, $\Delta\omega/\omega_0$, decreases from 25% in the original nanoparticle 1DPC to 20% in those with higher porosity. In fact, it can be shown that $\Delta\omega/\omega_0$ depends on the dielectric contrast, $\Delta n = |n_1 - n_2|$, like $\Delta\omega/\omega_0 = 2/\pi\ \Delta n/n$,[37] where $n$ is the average refractive index, estimated as $n = (n_1t_1 + n_2t_2)/(t_1 + t_2)$. The generation of a more open pore network yields both lower $\Delta n$ and $n$, as it can be estimated from the data shown in Table 1, and thus may lead to spectrally thinner Bragg reflections.

### Enhanced diffusion through Bragg reflectors

To assess the effect that the modified pore network of 1DPCs has on mass transport, curves of current density *vs.* potential (*j*–*V* curves) and impedance spectroscopy measurements were performed over 1DPC samples immersed in a viscous electrolyte, 0.13 M of iodine in 1-butyl-3-methylimidazolium iodide, as schematized in Fig. 5a. As shown in Fig. 5b, the increase of the layer porosity and pore size with the addition of PEG produces a rise both in the slope at low potentials and in the value of the limiting current ($j_{lim}$) plateau (Fig. 5c) of the *j*–*V* curves. These results prove the enhancement of mass transport of an electrolyte embedded in 1DPC as a result of the control of porosity.

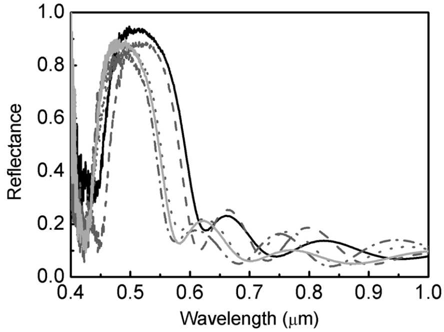

**Fig. 4** Specular reflectance spectra of 1DPCs in which different weight ratios of PEG were added to the precursor suspensions, namely, 0% (black solid line), 25% in $TiO_2$ (grey dashed line), 50% in $TiO_2$ (grey dotted line), 75% in $TiO_2$ (grey dashed-dotted line) and 50% in $TiO_2$/50% in $SiO_2$ (light grey solid line) with respect to that of nanoparticles.

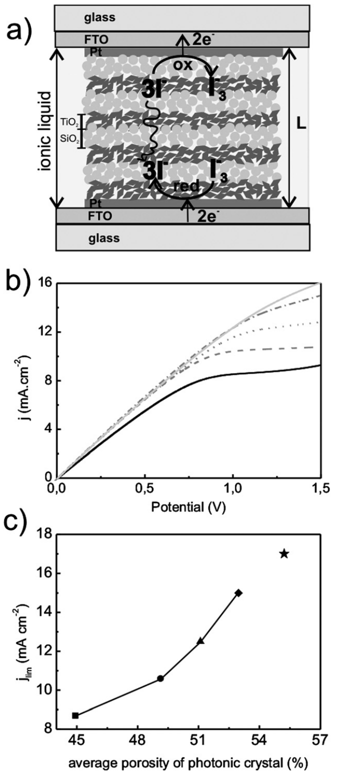

**Fig. 5** (a) Scheme of the sandwich cells measured in this study. (b) *j*–*V* curves for the 1DPCs prepared from precursor suspensions containing different amounts of PEG in the np-$TiO_2$ layer: weight ratios of 0 (black solid line), 0.25 (dashed line), 0.5 (dotted line), and 0.75 (dashed-dotted line) while keeping the PEG : np-$SiO_2$ weight ratio constant and equal to 0. Results for a sample made using both PEG : np-$TiO_2$ and PEG : np-$SiO_2$ weight ratios of 0.5 are also shown (solid grey line) and (c) limit current obtained by extrapolating the values of the plateau on *j*–*V* curves *versus* average porosity of the multilayer.

For a more detailed analysis of these results, each sample was measured by impedance spectroscopy at four different currents between 0 mA and the limiting current. The typical impedance spectrum obtained from the porous 1DPC shown in Fig. 6a was fitted with the Randles equivalent circuit schematized in Fig. 6b. It allows analyzing separately the physical processes of carrier transport and charge transfer that take place in our device where $R_s$ corresponds to the sum of the resistances associated with FTO, contacts and wires, $R_{Pt}$ and $C_{Pt}$ are the charge-transfer resistance and double-layer capacitance from the platinized electrodes, respectively, and $Z_d$ is the diffusion impedance, which represents the resistance to mass transfer through the porous structure. From the expression of $Z_d$ given by eqn (1), where $\omega_d$ is the characteristic diffusion frequency, $\omega$ is the frequency of the measurement and $i$ is the imaginary unit,

$$Z_d = R_d \frac{\tanh\left[(i\omega/\omega_d)^{1/2}\right]}{(i\omega/\omega_d)^{1/2}} \qquad (1)$$

we obtain $R_d$, which is the resistance associated with diffusion of triiodide ions in the electrolyte and is the parameter that will be more affected by variations of the pore network in the multilayers.

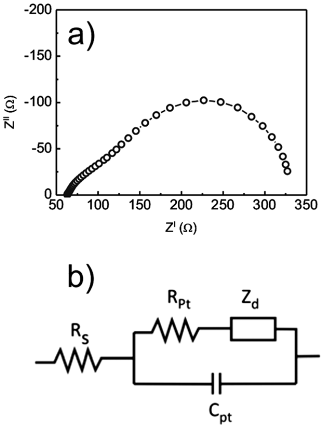

**Fig. 6** (a) Impedance spectrum of a device made by sandwiching a photonic crystal and the electrolyte solution between two platinized electrodes. Galvanostatic measurement was performed at 10 mA over a sample made with 25% PEG in np-$TiO_2$. (b) Randles circuit used to fit experimental data.

From the diffusion frequency and film thickness, $L$, the diffusion coefficient may be obtained using $D = \omega_d L^2$ that yielded values comprised between 1.5 and 2.5 × $10^{-8}$ $cm^2$ $s^{-1}$, in good agreement with data obtained from $j_{lim}$ calculations.[38] These values are one order of magnitude lower than those obtained in the free electrolyte,[32] indicating certain difficulties in the transport of $I_3^-$ through the 1DPC. We associate these low values of $D$ with the increased tortuosity and constrictivity introduced by the 1DPC relative to the free electrolyte.

In practical terms, the diffusion resistance is the most relevant parameter of $Z_d$ since its value determines, together with $R_s$ and $R_{Pt}$, the total series resistance of the device. Thus it may influence its performance, mainly through the loss of fill factor, but eventually also by a drop in short circuit current.[39,40] We thus focus our study on $R_d$ in what follows.

Fig. 7a displays $R_d$ as obtained from the analysis of the impedance spectra measured at several current densities, $j$. The different symbols (lines are just guides for the eye) correspond to photonic crystals possessing different pore networks. In all cases, $R_d$ increases as the current does, reaching rather large values when $j_{lim}$ is approached. It can be readily seen from Fig. 7a that samples with higher porosity present lower diffusion resistance, reaching values similar to those commonly found in optimized devices for $R_s$ (1–5 Ω $cm^2$) and $R_{Pt}$ (1–3 Ω $cm^2$).[40–43] Fig. 7b clearly shows the dependence of $R_d$ measured at 0 mA *versus* the average porosity within the multilayer structure. Again a clear decay of $R_d$ as porosity is increased can be observed while, consequently, the opposite trend is observed for $j_{lim}$, as shown in Fig. 5c. It should also be noticed that this enhanced mass transport must be caused by the combined effect of both larger porosity and average pore size. However, these two effects cannot be analyzed separately: each time porosity is increased (see Table 1), the bottlenecks, responsible for the hindering of diffusion, are also enlarged (see Fig. 1d–f), thus also contributing to a better flow of species through the multilayer.

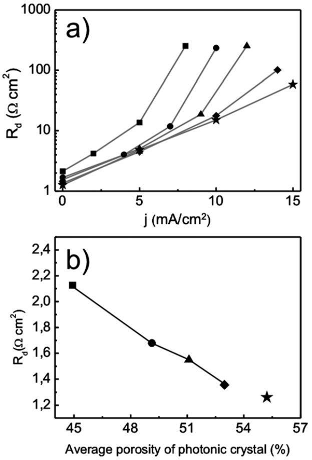

**Fig. 7** (a) Diffusion resistance ($R_d$) *versus* current density ($j$) as extracted from the impedance spectroscopy analysis. (b) Diffusion resistance obtained at $j = 0$ mA $cm^{-2}$ *versus* average porosity of the 1DPC prepared using different PEG : np-$TiO_2$ weight ratios, namely, 0 (squares), 0.25 (circles), 0.5 (triangles), 0.75 (rhombus). Data for the multilayer prepared using both PEG : np-$TiO_2$ and PEG : np-$SiO_2$ weight ratios of 0.5 are also shown (stars).

Impedance spectroscopy analysis confirms that multilayers built using mixtures of nanoparticles and PEG always present larger effective sections for the diffusion of $I_3^-$ species, which results in lower diffusion resistances. This result, combined with the use of optimized electrolytes, allows beating the limitations to efficiency introduced by the addition of the 1DPC extra layers in photo-electro-chemical devices such as dye sensitized solar cells.[23,44]

## Conclusions

In summary, we have presented a method to enhance the mass transport through nanoparticle multilayers displaying one-dimensional photonic crystal properties. Addition of a polymer in the precursor suspensions allows tuning the pore size distribution of the ensemble. Monolayers built from these suspensions have been analyzed by specular reflectance porosimetry to demonstrate that both the total accessible void volume and the average pore size of the film are increased. Stacks of these highly porous layers display intense Bragg reflections as well as improved mass transport, as confirmed by the diffusion resistance obtained for an electrolyte embedded in the structure from impedance spectroscopy measurements. These materials presenting combined optical and transport properties will give rise to improved performance when integrated into photo-electro-chemical devices.

## Acknowledgements

HM thanks the Spanish Ministry of Science and Innovation for funding provided under grants MAT2008-02166 and MAT2011-23593, as well as Junta de Andalucía for grants FQM3579 and FQM5247. HM and JB thank project CONSOLIDER HOPE CSD2007-00007 for funding. UJI team also acknowledges financial support from the Spanish Ministry of Science and Innovation under project MAT2010-19827 and Generalitat Valenciana under project PROMETEO 2009/058.

## Notes and references

1 J. J. Steele, A. C. van Popta, M. M. Hawkeye, J. C. Sit and M. J. Brett, *Sens. Actuators, B*, 2006, **120**, 213.

2 S. Y. Choi, M. Mamak, G. von Freymann, N. Chopra and G. A. Ozin, *Nano Lett.*, 2006, **6**, 2456.

3 Z. Wu, D. Lee, M. F. Rubner and R. E. Cohen, *Small*, 2007, **3**, 1445.

4 M. F. Schubert, J. Q. Xi, J. K. Kim and E. F. Schubert, *Appl. Phys. Lett.*, 2007, **90**, 141115.

5 M. C. Fuertes, F. J. Lopez-Alcaraz, M. C. Marchi, H. E. Troiani, V. Luca, H. Miguez and G. J. D. A. Soler-Illia, *Adv. Funct. Mater.*, 2007, **17**, 1247.

6 S. Colodrero, M. Ocaña and H. Míguez, *Langmuir*, 2008, **24**, 4430.

7 T. Druffel, N. Mandazy, M. Sunkara and E. Grulke, *Small*, 2008, **4**, 459.

8 D. L. Guo, L. X. Fan, F. H. Wang, S. Y. Huang and X. W. Zou, *J. Phys. Chem. C*, 2008, **112**, 17952.

9 B. V. Lotsch and G. A. Ozin, *Adv. Mater.*, 2008, **20**, 4079.

10 K. A. Killian, T. Böcking and J. J. Gooding, *Chem. Commun.*, 2009, 630.

11 P. W. de Oliveira, C. Becker-Willinger and M. H. Jilavi, *Adv. Eng. Mater.*, 2010, **12**, 349.

12 L. González García, G. Lozano, A. Barranco, H. Míguez and A. R. Gonzalez-Elipe, *J. Mater. Chem.*, 2010, **20**, 6408.

13 I. M. Thomas, *Thin Solid Films*, 1989, **175**, 173.

14 M. Mennig, P. W. Oliveira, A. Frantzen and H. Schmidt, *Thin Solid Films*, 1999, **351**, 225.

15 O. Sánchez-Sobrado, M. E. Calvo and H. Míguez, *J. Mater. Chem.*, 2010, **20**, 8240.

16 P. Kurt, D. Banerjee, R. E. Cohen and M. F. Rubner, *J. Mater. Chem.*, 2009, **19**, 8920.

17 D. P. Puzzo, L. D. Bonifacio, J. Oreopoulos, C. M. Yip, I. Manners and G. A. Ozin, *J. Mater. Chem.*, 2009, **19**, 3500.

18 M. E. Calvo and H. Míguez, *Chem. Mater.*, 2010, **22**, 3909.

19 S. Colodrero, M. Ocaña, A. R. González-Elipe and H. Míguez, *Langmuir*, 2008, **24**, 9135.

20 O. Sánchez-Sobrado, M. E. Calvo, N. Núñez, M. Ocaña, G. Lozano and H. Míguez, *Nanoscale*, 2010, **2**, 936.

21 L. D. Bonifacio, D. P. Puzzo, S. Breslav, B. M. Willey, A. McGeer and G. A. Ozin, *Adv. Mater.*, 2010, **22**, 1351.

22 Z. H. Wang, J. H. Zhang, J. X. Li, J. Xie, Y. F. Li, S. Liang, Z. C. Tian, C. A. Li, Z. Y. Wang, T. Q. Wang, H. Zhang and B. Yang, *J. Mater. Chem.*, 2011, **21**, 1264.

23 S. Colodrero, A. Mihi, L. Haggman, M. Ocaña, G. Boschloo, A. Hagfeldt and H. Miguez, *Adv. Mater.*, 2008, **20**, 1.

24 M. E. Calvo, S. Colodrero, T. C. Rojas, J. A. Anta, M. Ocaña and H. Míguez, *Adv. Funct. Mater.*, 2008, **18**, 2708.

25 E. Della Gaspera, A. Antonello, M. Guglielmi, M. L. Post, V. Bello, G. Mattei, F. Romanato and A. Martucci, *J. Mater. Chem.*, 2011, **21**, 4293.

26 S. D. Burnside, V. Shklover, C. Barbé and K. Comte, *et al.*, *Chem. Mater.*, 1998, **10**, 2419.

27 M. Logar, B. Jancar and D. Suvorov, *J. Am. Ceram. Soc.*, 2010, **93**, 3679.

28 T. Druffel, O. Buazza, M. Lattis, S. Farmer, M. Spencer, N. Mandzy and E. A. Grulke, *Proc. SPIE–Int. Soc. Opt. Eng.*, 2008, **7030**, 300.

29 M. C. Fuertes, S. Colodrero, G. Lozano and A. Rodríguez González-Elipe, *et al.*, *J. Phys. Chem. C*, 2008, **112**, 3157.

30 F. Casanova, C. E. Chiang, C. P. Li, I. V. Roshchin, A. M. Ruminski, M. J. Sailor and I. K. Schuller, *Nanotechnology*, 2008, **19**, 315709.

31 G. Lozano, S. Colodrero, O. Caulier, M. E. Calvo and H. Míguez, *J. Phys. Chem. C*, 2010, **114**, 3681.

32 F. Fabregat-Santiago, J. Bisquert, E. Palomares, L. Otero, D. Kuang, S. M. Zakeeruddin and M. Grätzel, *J. Phys. Chem. C*, 2007, **111**, 6550.

33 S. Brunauer, L. S. Deming, W. S. Deming and E. Teller, *J. Am. Chem. Soc.*, 1940, **62**, 1723.

34 S. J. Gregg and K. S. W. Sing, *Adsorption, Surface Area and Porosity*, Academic Press, London, ISBN 0-12-300956-1, 1982.

35 D. P. Partlow and T. W. O'Keeffe, *Appl. Opt.*, 1990, **29**, 1526.

36 N. Hidalgo, M. E. Calvo, M. Bellino, G. J. A. A. Soler-Illia and H. Míguez, *Adv. Funct. Mater.*, 2011, **21**, 2534.

37 A. Yariv and P. Yeh, *Optical Waves in Crystals*, John Wiley and Sons Inc., ISBN 0-471-43081-1, 2003.

38 A. Hauch and A. Georg, *Electrochim. Acta*, 2001, **46**, 3457.

39 F. Fabregat-Santiago, J. Bisquert, G. Garcia-Belmonte, G. Boschloo and A. Hagfeldt, *Sol. Energy Mater. Sol. Cells*, 2005, **87**, 117.

40 F. Fabregat-Santiago, G. Garcia-Belmonte, I. Mora-Seró and J. Bisquert, *Phys. Chem. Chem. Phys.*, 2011, **13**, 9083.

41 T. Hoshikawa, M. Yamada, R. Kikuchi and K. Eguchi, *J. Electrochem. Soc.*, 2005, **152**, E68.

42 Y. Chiba, A. Islam, Y. Watanabe, R. Komiya, N. Koide and L. Han, *Jpn. J. Appl. Phys.*, 2006, **45**, L638.

43 J. Liu, R. Li, X. Si, D. Zhou, Y. Shi, Y. Wang, X. Jing and P. Wang, *Energy Environ. Sci.*, 2010, **3**, 1924.

44 S. Colodrero, A. Forneli, C. López-López, L. Pelleja, H. Míguez and E. Palomares, *Adv. Funct. Mater.*, 2011, DOI: 10.1002/adfm.201102159.